THESE

Présentée à l'Université de Lille
École Doctorale Sciences pour l'Ingénieur
Institut d'Electronique, de Microélectronique et de Nanotechnologie
Higher Institute for Electronics and Digital Training

Pour obtenir le grade de :

DOCTEUR DE L'UNIVERSITE

Spécialité : Electronique microélectronique, nanoélectronique et micro-ondes
Par

Stanislav Didenko

Artificially induced anisotropy of thermal conductivity in 2D Si phononic membranes
Anisotropie de la conductivité thermique artificiellement induite dans des membranes phoniques en silicium

Soutenue le 17 Juin 2019 devant le jury composé de :

Mme. Séverine **GOMES**, *Directrice de recherche CNRS, CETHIL, Lyon*	**Président du jury**
M. Sebastian **VOLZ**, *Directeur de recherche CNRS, LIMMS Director, the University of Tokyo*	Rapporteur
M. Nicolas **HORNY**, *Maître de Conférences, Université de Reims Champagne-Ardenne*	Rapporteur
M. Jean-François **ROBILLARD**, *Enseignant Chercheur, IEMN, Villeneuve d'Ascq*	Co-encadrant de thèse
M. Thomas **SKOTNICKI**, *Directeur R&D, CEZAMAT, Varsovie*	Co-directeur de thèse
M. Emmanuel **DUBOIS**, *Directeur de recherche CNRS, IEMN, Villeneuve d'Ascq*	Directeur de thèse
M. Jean-Marie **BLUET**, *Professeur des Universités, INSA, Lyon*	Invité

Acknowledgements

I am grateful to many people who helped me throughout this thesis project. I would like to address deep acknowledgments to:

- The director of my thesis Prof. Emmanuel Dubois: for giving me the chance to do the PhD project in his research group, for his supervision, support, valuable advices and inspiring motivation.
- Co-director of my thesis Prof. Thomas Skotnicki: for being my scientific supervisor; for the fruitful discussions.
- My supervisor Dr. Jean-François Robillard: for guiding me in my research and being open for the discussions whenever it was needed; for his reasonable advices regarding many aspects of my work; for being friendly and supportive; for his sense of humor and the optimism; his patience and his faith in his student.
- Thank you to my girlfriend Anna Kozina, for all her love and support, and teaching me Python.
- All the colleagues from my scientific group: for their openness to discussions and exchange of the research experience. Thus, many thanks are addressed to Valeria Lacatena, Maciej Haras, Valentina Giorgis, Justine Philippe, Quentin Hivin, Thierno Bah, Di Zhou, Antoine Frappé, Tianqi Zhu, Arun Bahskar and Jun Yin.
- Special thanks are addressed to Valeria Lacatena and Maciej Haras, whose fabrication projects became the foundation for my work.
- Pierre-Olivier Chapuis (CETHIL, Lyon): for discussions and the theoretical support of my work in the domain of Monte Carlo simulation, his efforts and the time spent organizing the collaboration between our lab and INSA-CETHIL colleagues.
- Our colleagues from INSA-Lyon, CETHIL and INL: Jean-Marie Bluet, A. Massoud and R. Orobtchouk, who performed crucial to my work RCWA analysis.
- IEMN engineers Marc Derwitte, Yves Deblock, François Vaurette, Christiane Legrand, Laurence Morgenroth, Guillaume Cochez, Pascal Tilmant, Dimitri Yareka, Garrett Curley, Christophe Boyaval, Isabelle Roche-Jeune, etc., who shared their knowledge and provided me with the technical support, without which this work would not be possible.
- Jean-Michel Droulez: for his technical support and programming advices.
- Maya Marinova (Lille1, Unité Matériaux et Transformations) and David Troadec (IEMN): for their important collaboration, which allowed to obtain fascinating TEM scans.
- Dominique Vignaud: for letting me work in his µRT laboratory; for a great help provided during the work on set-up upgrade; for the technical and theoretical support.
- Florence Alberti: for her great organization and management skills, which helped me to feel a lot more comfortable in France and during the conference missions.
- Our colleagues from Université de Lorraine and INSA-Lyon: Maxime Verdier, David Lacroix and Konstantinos Termentzidis, who provided me with deep fundamental insight into the picture of thermal transport in phononic membranes at the presence of the amorphous oxide.
- Evelyne Martin (IEMN) and Stéphane Monfray (STMicroelectronics): for interesting suggestions and helpful discussions.

List of the added corrections:

Double spaces were deleted

p.110 - Remark was added, regarding the question about the bulk Si and thin-film Si k(T) dependence.

p.127 - Remark was added, regarding the question about k-tensors difference for experiment and simulation

p.119 - attention remark was added in Figure 4.4 concerning 100nm pitch membranes difference among isotropic and anisotropic series.

p.87 - the phrase "utilizing its Raman scattering properties" is added, implying that, indeed, the Laser is not a Thermometer in the direct sense.

Figure 3.12, "Wavelength" was changed to the "Raman Shift" on the plot.

p.102 - Sentence "Non-radians units are in μm, in formulas below" was added.

p.102 - One sentence added into the description of the "knife" method, to make it more detailed.

p.115 - Words "comparing to the bulk value, or 5-fold reduction comparing to the pristine 44nm-thick membrane" were added to make a clear comparison.

p.113 - Figure 4.1 Plot (c): the missing curve for Maxwell-Garnett formula was added.

p.140 - List of the used abbreviations in alphabetic order was added into Appendix.

76th item of Literature was modified.

Around 30 spelling and typo corrections were added around the manuscript.

Table of content

Introduction

As the Moore's law is pushed to its saturation limit, the thermal management becomes the crucial bottleneck of the Integrated Circuits (IC) design. The larger die sizes and more densely-packed IC elements make it harder to sink the heat away from the sensitive areas. The novel 3D integration approach makes IC structures that are even more complex from the thermal point of view, with many interfaces, which thermal contact resistance may be high. The averaged heat power density dissipated in a typical IC is of the order of 100W/cm². Usual thermal strategies treat the overheating issues partially at the expense of the computation speed (additional propagation delay) or the surface footprint, and require sophisticated thermal models. There is a lack of a complementary strategy, based on material properties rather than design and modelling. The directional redistribution of the in-plane heat flow in the silicon layer may become a promising tool in the toolbox of IC thermal management. This approach can be based on the artificially induced anisotropy of the in-plane effective thermal conductivity in Si thin films or IC layers.

In this work, the design, fabrication and characterisation development efforts were directed to resolve the question of the feasibility of such thermal transport anisotropy. Besides being perspective in the thermal management applications, the directional heat guiding can become an important functional element of the thermoelectric generators (TEG) based on thin film silicon membranes, which are CMOS-compatible and possesses low (high) thermal (electronic) conductivity.

Induced anisotropic heat guiding in Si thin films can be achieved via the nanostructuring, e.g. an introduction of the lattice of nanoholes with the rectangular unit cell. The key role is played by the mechanisms of phonon scattering, that allows for artificial modulation of Si thermal transport properties in coherent (wave-like) or incoherent (particle-like) manner. The first chapter of this manuscript is devoted to the review of the fundamental theoretical aspects of the thermal transport in the bulk Si (band structure, Bose-Einstein distribution, dominant wavelength of phononic energy spectrum, Boltzmann transport equation, phonons scattering processes as a function of temperature). Then referring to the bulk properties, the most recent experimental and theoretical studies of the heat transport in low-dimensional and nanostructured silicon are discussed, addressing the question of dominant thermal conductivity reduction mechanisms at room and low temperatures.

Phononic nanostructuring can be realized by the means of state-of-the-art patterning technologies such as e-beam nanolithography (EBL) combined with the plasma etching. Among various Si nanostructures (suspended phononic nanomeshes and nanowires), 2D Si phononic membranes (PhMs) attract the interest since they exhibit ≈20-fold reduction of thermal conductivity as compared to the bulk and at the same time their geometry is closer to IC Si thin layers. This work is the continuation of ERC UPTEG project, during the first stage of which design and fabrication strategies for the beam-like suspended Si membranes were developed by Valeria Lacatena and Maciej Haras. The second chapter describes, how using existing fabrication methodology the new approach, which addresses the question of artificially-induced anisotropy of thermal conductivity in 2D phononic membranes, was elaborated. The thermal transport experiment based on the vacuum micro Raman

Thermometry (µRT) measurements of free-standing beam-like (FSBL) membranes with anisotropic lattices of nanoholes was proposed. FSBL topology allows for direct measurements of effective thermal conductivity eigenvalues in principle orientations of 2D anisotropic phononic lattice. The vacuum-based µRT implies the non-invasiveness and the elimination of both convection losses and interface resistance due to the absence of the metallic probes. Details concerning the improvement of the processing steps, that were only partially successful in previous methodology work or had a limited functionality, are given: obtaining a decent quality of the nanoholes etching; implementation of a new test-probe method allowing the fast assessment of the profiles of the etched nanoholes; finding optimal EBL writing method for anisotropic phononic patterns; etc.

The measurement of thermal properties of fabricated PhMs and interpretation of the experimental results require the knowledge of geometrical (width, thickness) and structural (holes diameter, roughness, surface oxide thickness) characteristics. Chapter 3 describes how those characteristics were estimated, using scanning and transmission electron microscopy (SEM and TEM), electron dispersive x-ray spectroscopy (EDX), ellipsometry, laser interferometry, optical microscopy and statistical image analysis. The issues connected with the measurement methodology and data analysis are discussed: laser beam profile estimations, the installation of continuous variable filter and reference Si photodiode detector (which allowed to conduct the power-variation µRT experiment with a bigger set of measurement points). By the combined use of µRT, Rigorous Coupled Wave Analysis (RCWA), performed by colleagues from Institut des Nanosciences de Lyon (INL) and Centre d'Energétique et de Thermique de Lyon (CETHIL), and Finite Element Modelling (FEM) it was possible to measure the thermal gradient and membranes' effective thermal conductivity κ.

Chapter 4 is devoted to the obtained results and their possible application. Based on the new experimental methodology, a graphical isotropic/anisotropic visualisation of the heat flow was proposed. The ratio of effective κ principal components was found: 2.2 for the pitch ratio of anisotropic lattice of holes (r) equal to 2.5 and 1.9 for r=2. Besides, 25-fold reduction of the thermal conductivity was observed for r=2.5 pattern: k_{yy}= 6±0.6Wm^{-1}K^{-1}. This experiment confirms the possibility to induce artificially high anisotropy of κ in Si PhMs almost not changing the filling fraction (*ff*) and the diameter of the holes. At last, parameterized FEM Comsol model had been used for the purpose of demonstrating the possible implementation of induced anisotropic effects in the area of IC thermal-management.

Chapter 1 Thermal transport in nanostructured membranes

The recent developments in micro- and nanofabrication have made possible the synthesis of semiconductor materials with nanoscale modifications. New classes of materials with reduced dimensionality have emerged: quantum dots, nanowires, thin films (including Si phononic membranes). Such materials exhibit new properties in both electronic and phononic heat transport. The characteristic length of these functional materials is comparable to or shorter than the mean free path or wavelength of the heat carriers, which include molecules, photons, electrons, phonons, and magnons[1]. Accurate theoretical and experimental treatment is required for this class of material. This chapter reviews some fundamental phononic theoretical aspects of the bulk Si: dispersion relation, band structure, statistical treatment of phonons with Bose-Einstein distribution, Wien's displacement law and the dominant wavelength of phononic energy spectrum, kinetic model based on Boltzmann transport equation, Matthiessen's rule and phonons scattering processes as a function of temperature. Then the most recent experimental and theoretical studies of the heat transport in low-dimensional and nanostructured silicon are discussed, addressing the question of dominant thermal conductivity reduction mechanisms at a room and low temperatures: incoherent and coherent effects.

1.1 Heat transport in Bulk Si

The crystal materials comprise the periodical lattice of atoms. At non zero temperature atoms are displaced from their equilibrium positions, i.e. from the minimum potential energy of their interaction forces. Displaced atoms vibrate around the equilibrium position due to unbalanced forces. Collective atomic vibration motions can be viewed as a series of harmonic and anharmonic waves, that can propagate the energy from the hot spots of the material to the cold ones. The energy levels of vibrational waves are quantized. A single quanta of the lattice vibration is called phonon. Phonons can be viewed as both waves and particles. In this section the main theoretical models that account for wave-like and particle-like aspects of phonons, are reviewed.

1.1.1 Dispersion curve and phononic band structure

Let's consider the simplest case of atomic vibration: one-dimensional chain of atoms which move only along x axis (longitudinal motion). Silicon crystal has a two-atomic basis[2], it means that its primitive cell in each point contains two atoms. Therefore, in our simple model the chain consists of atoms of two kinds. In a real crystal each of the two atoms experiences different interatomic force. In order to simplify the problem, we take an assumption that difference of interatomic forces can be viewed as difference of atomic masses or effective masses (M_1 and M_2 on the figure below). In this case the chain comprises two kinds of atoms connected with the springs of the same constant.
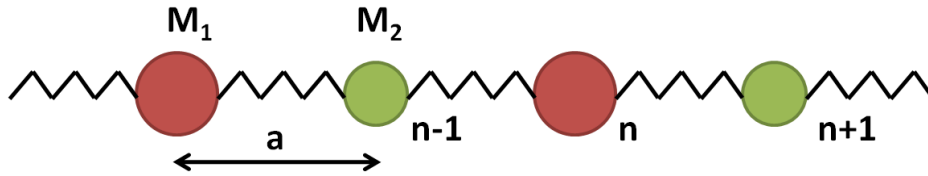
Figure 1.1
One-dimensional chain of atoms, with masses M_1 and M_2. Constant a is the interatomic distance.

Finally, taking the assumption that vibrations are harmonic (no damping forces), we can describe the motion of the atoms with the following equations:

$$M_1 \frac{d^2 u_n}{dt^2} = -C(2u_n - u_{n+1} - u_{n-1})$$

$$M_2 \frac{d^2 u_{n+1}}{dt^2} = -C(2u_{n+1} - u_{n+2} - u_n) \tag{1}$$

where C is the spring constant, u_i is the displacement of an atom from its
equilibrium position.

The solutions are expected to be in a form:

$$u_n = A_1 e^{i(qna - \omega t)}$$

$$u_{n+1} = A_2 e^{i(q(n+1)a - \omega t)} \tag{2}$$

where A is the amplitude of the displacement, q is the wave vector, a is the interatomic distance, and ω is the frequency.

Substituting (2) into (1), and solving the system of two linear equations[3], one can derive the dispersion relation:

$$\omega^2 = C(\frac{1}{M_1} + \frac{1}{M_2}) \pm C\sqrt{(\frac{1}{M_1} + \frac{1}{M_2})^2 - \frac{4\sin^2 qa}{M_1 M_2}} \tag{3}$$

The two curves for respective sign of the dispersion equation are plotted below. The curve, which starts at q=0 and ω=0, is called "acoustic branch", it corresponds to elastic waves of sound. Another curve is called "optical branch". The largest contrast between the two branches can be seen if we compare the lattice vibration at q = 0 (infinite wavelength). According to the equations, the acoustic branch has $A_1 = A_2$ if q=0. It means that the amplitude and the phase of both atoms is the same, in other words, the whole chain oscillates as a rigid body.
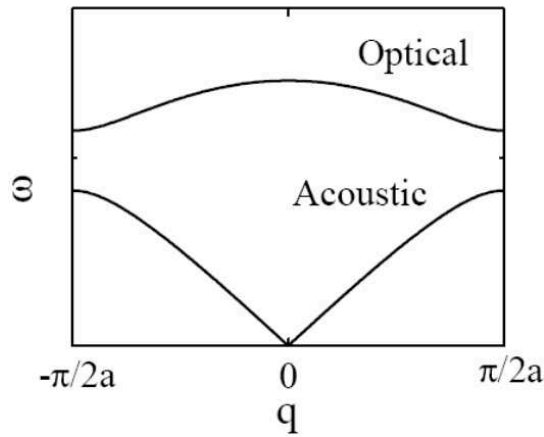
Figure 1.2
Optical and acoustic branches of one-dimensional chain of atoms.

One can show that atoms in the optical branch have antiphase oscillations, thus the centre of mass of the chain does not change. Optical oscillations occur at the infrared frequency. This property is of particular importance in this work, because the experiment is based on the Raman (light) scattering form the optical phononic modes (see Paragraph 3.2.3).

In the next paragraph it will be shown that the group velocity of phonon wavepacket, which is the derivative of the dispersion curve $\upsilon_g = d\omega/dq$, is proportional to thermal conductivity. Conventionally the group velocity is calculated only from the dispersion of acoustic phonons, for the reason that their contribution to κ is the largest (derivative of the

optical branch is much lower than the acoustic one). Acoustic phonons are often called thermal.
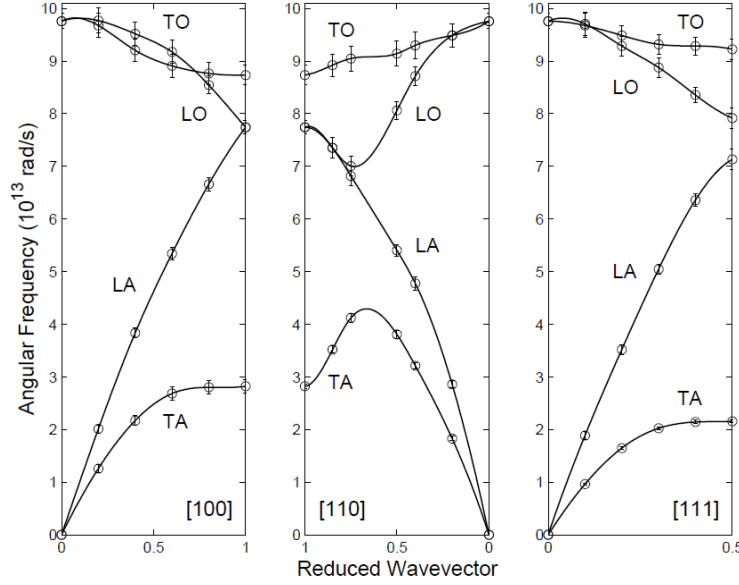
Figure 1.3
Phonon dispersion curves[4] for the [100], [110], and [111] directions in silicon based on neutron scattering data. The two transverse phonon branches are degenerate in each of the directions.

In the three-dimensional crystals the atomic vibrations also split into the optical and acoustic branches. The figure above demonstrates Si phononic band structure for three high symmetry crystal directions. In modes' abbreviations (LA, TA, LO, TO), the first letter indicates the polarisation of atomic displacement (transverse or longitudinal) and the second indicates the branch (optical or acoustic). As for 1D chain example, for 3D Si crystal we observe the same situation for υ_g, which is high for LA and TA modes.

1.1.2 Towards dominant phonon calculation

According to Debye model, atomic oscillations are quantized[2]. Because any crystal has a finite size, there is a finite number of possible energy levels for oscillations. The phonon is a quantum of particular vibration energy ($\varepsilon = h\omega/2\pi$). There are two main assumptions which allow to treat phonons statistically. The first is that any number of phonons can occupy the same energy state. The second assumption is that there are many more energy levels than phonon particles. If g_i is a number of energy levels in a small i^{th} energy interval and n_i is the number of phonons that occupy this interval, then the total number of all possible arrangements of the energy states in all intervals[5]:

$$\Omega = \prod_i \frac{(n_i + g_i)!}{n_i! g_i!}$$
(4)

Maximizing Ω with Lagrange multiplier method, putting the constraint of the constant energy at 0K, and substituting Lagrange multiplier with the measure of entropy ($-1/K_B T$, where KB is Boltzmann constant), one can derive the distribution of phonon energy with respect to the temperature.

$$\frac{n(\varepsilon)}{g(\varepsilon)} = \frac{1}{e^{\frac{\varepsilon}{K_B T}} - 1}$$

(5)

The last expression is called Bose-Einstein distribution. In order to estimate the total energy U, the density of states function $g(\varepsilon)$ is needed. One can show that for 3D crystal, accounting for 3 modes of polarisations, $g(\varepsilon)$ is expressed as:

$$g(\varepsilon) = 3\frac{V\omega^2}{2\pi^2 v^2}$$

(6)

where V is the volume, $v=\omega/q$ is the velocity of a phonon .

Expressing everything in terms of angular frequency, and integrating over $\hbar\omega n(\omega)d\omega$, we obtain:

$$U = \frac{3Vh}{4\pi^3 v^3}\int_0^{\omega_D}\frac{\omega^3 d\omega}{e^{\hbar\omega/2\pi K_B T} - 1}$$

Where ω_D is the Debye cut-off frequency, which is related to the fact that the wavelength cannot be shorter than interatomic distance. $v=\omega/q$ is the velocity of a phonon.

(7)

At a low temperature U is proportional to T^4, which is the same as for Stephan-Boltzman law of photon radiation[6]. This is the reason why heat transport by phonons is often called phonon radiation. From the mentioned proportionality of U and T^4 it follows that the expression under the integral is an analogue to Plank distribution for phonons. Hence similarly to photonic distribution for black body radiation, we can differentiate phononic Plank distribution to obtain Wien's displacement law for phonons: $\hbar\omega_{dom} = K_B T$, where ω_{dom} is the dominant frequency for phonons. Figure 1.4[7] demonstrates the distribution of phonons with respect to the wavelength and the T, where the dominant wavelengths λ_{dom} correspond to the maximum of the curves. λ_{dom} is of the order of 1nm at a room temperature (RT) and 100nm at 1K.
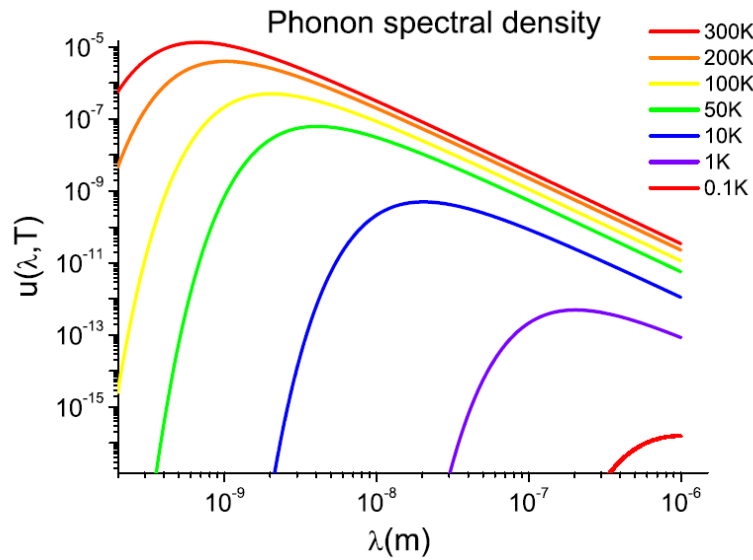

Figure 1.4
Phonon spectral density[7] as a function of the wavelength for different equilibrium temperatures of a black body.

1.1.3 Boltzmann transport equation, Fourier's law and scattering processes

Boltzmann transport equation (BTE) treats phonons as particles, which are described by the nonequilibrium distribution function u(**r**, **k**, t), that can be interpreted as the probability of finding the particle at position **r** with wavevector **k** at a time t. In the case of a collision at a time $t+dt$ the differential of the distribution function is:

$$du = u(\vec{r} + d\vec{r}, t + dt, \vec{k} + d\vec{k}) - u(\vec{r}, t, \vec{k}) = dt\left(\frac{\partial u}{\partial t}\right)_{coll} \tag{8}$$

Under the assumption that no external force exerts on the system, and applying the single relaxation time approximation, one can derive the equation describing particle diffusion :

$$\frac{\partial u}{\partial t} + \vec{V_g} \, \nabla_{\vec{r}} u = -\frac{u - u_0}{\tau} \tag{9}$$

In this expression u_0 is the equilibrium distribution, v_g is the velocity of heat carriers (or group velocity in the wavepacket picture), τ is the relaxation time. Solving for heat flux current q_y [J/(m² s)] in particular direction, one obtains the Fourier law:

$$q_y = -\frac{\partial T}{\partial y}\frac{1}{3}\int_0^{\omega_{max}} C_p(\omega)\, V_g(\omega)\, \Lambda(\omega) d\omega$$

where $C_p(\omega)$ [J s / (m³K)] is the volumetric modewise heat capacity. Λ is the mean free path of the phonon. ω_{max} is the maximum frequency (Debye frequency) $\tag{10}$

Fourier law relates the temperature gradient to the heat current via thermal conductivity.

Simplifying (9) for the specific heat, averaged values of the group velocity and the mean free path one can obtain:

$$q_y = -\kappa\frac{\partial T}{\partial y}; \quad \kappa = \frac{1}{3}CV_g\Lambda \tag{11}$$

As we can see, the thermal conductivity depends on the knowledge of dispersion curves (group velocity), specific heat, and the mean free path (or relaxation time). For the bulk material the mean free path can be expressed according to Matthiessen's rule, which combines boundary (B), impurity (I) and Umklapp (U) scattering contributions:

$$\Lambda^{-1} = \Lambda_B^{-1} + \Lambda_I^{-1} + \Lambda_U^{-1} \tag{12}$$

The boundary and impurity scattering processes are dominant extrinsic scattering mechanisms[8]. The first is attributed to the scattering of the phonons on the surface of the material. Hence, the surface roughness plays a crucial role because the dominant phonon wavelength at RT is of the order of 1nm (as was shown in the previous paragraph), and this value is the same for the roughness on the typical Si surfaces. In low-dimensional nanostructured materials, the boundary scattering contribution to the mean free path is usually a fitting parameter[9]. Impurity scattering is proportional to the dopant concentration and can be found in literature. The last term in Matthiessen's rule accounts for the dominant intrinsic scattering process called Umklapp scattering. It is an anharmonic quadratic (four

phonons) or cubic (three phonons) process (three/two phonons can collide forming the third/forth one). In the case when the wave vector of created phonon falls outside the first Brillion zone, the total phonon momentum changes according to the addition of the reciprocal lattice vector G. This creates a flux in the opposite direction to heat propagation. The Umklapp processes become more dominant with the temperature. At a low T, the boundary scattering dominates because the MFP is longer than the sample size. The figure below summarizes the dominant scattering mechanisms' contribution into the bulk Si thermal conductivity at different T.
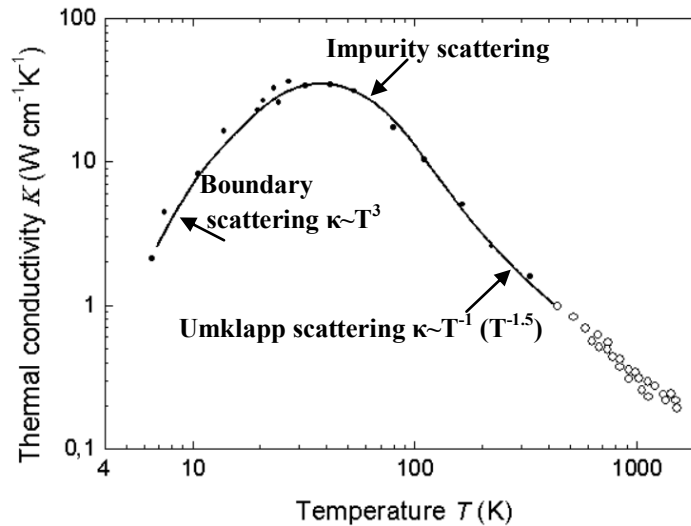
Figure 1.5
Thermal conductivity of Si as a function of T measured with radial heat-flow method[10] and remarks for dominant scattering mechanisms' contributions[8].

1.2 Literature review of thermal conductivity modulation experiments

In this chapter, some recent experimental and simulation studies for low-dimensional Si materials will be reviewed. As was shown in the previous chapter, phononic properties, such as the mean free path and the dominant wavelength, are both temperature dependant. Now we are interested in the question, how do the phononic properties regulate the thermal conductivity in nanostructured Si systems.

1.2.1 Coherent and incoherent effects in different transport regimes

Conventionally there are two types of phononic effects that can dominate in the reduction of thermal conductivity: incoherent and coherent. The first type of effects is connected with the particle-like picture of phonons, which can experience boundary and impurities scattering. Kinetic BTE model is used to describe incoherent phonons. To the contrary, coherent phonons are viewed as the waves, which can interfere or Bragg scatter. This implies that the reduction of thermal conductivity for coherent phononic transport can be initiated by the reduction of the group velocity (phononic band gap modification) or destructive interference.

Depending on the T, the size of the sample and the roughness of the surface, the contribution from these two effects into thermal transport can change. Different transport regimes are distinguished, each of them is described with specific model. In the work of O. Bourgeois et al[7] a good summary of these regimes is given (Figure below).

relevant length scales	transport regime	models	relevant formulae
$\lambda_{dom}(T) < \Lambda_{ph}(T) < L$	Diffusive regime (incoherent)	Kinetic model	$K = \dfrac{1}{3}C\upsilon_s\Lambda_{ph}$
$\lambda_{dom}(T) < L \sim \Lambda_{ph} < \Lambda_{ph\text{-}bulk}$	Casimir regime (incoherent)	Casimir model	$K_{Cas} = \beta\Lambda_{Cas}T^3$
$\lambda_{dom}(T) \sim L < \Lambda_{ph}$	Ziman regime (partly coherent)	Ziman model	$\Lambda_{ph} = \dfrac{1+p}{1-p}\Lambda_{Cas}$
$L < \lambda_{dom}(T) < \Lambda_{ph}$	Ballistic regime (coherent)	Landauer model	$T = \dfrac{1}{1+3L/4\Lambda_{eff}}$

Figure 1.6
Classification of the different regimes[7] of phonon transport in nanoscaled systems at low enough temperature, typically below 30K for silicon. L is the sample length, Λ_{ph} is the inelastic phonon mean free path, and λ_{dom} is the dominant phonon wavelength. K_{cas} is the thermal conductance in Casimir regime. Concerning the Landauer limit, the parameter T denotes the transmission coefficient between a nanowire and its heat reservoir. Other important lengths are explained in the text.

The diffusive regime is described by the kinetic model, and is mostly attributed to the bulk material. Incoherent effects are dominant. Thin-film membranes at a RT also can be attributed to this regime if both MFP and λ_{dom} are smaller than the length of the sample.

Decreasing the T and/or the length of the sample, we approach the Casimir regime, when MFP for the bulk is bigger than the reduced MFP inside the sample. Even though this limit is reached[7] at a low enough T, only the boundary scattering mechanism, linked to the surface roughness, dominates.

In the Ziman regime the T drops even further, hence the λ_{dom} becomes larger than the roughness amplitude[7] and specular reflections of phonons on the surface cannot be neglected. p in the Ziman model is the probability parameter of a phonon to be specularly reflected on the surface, which depends on the wavelength of a phonon and the roughness.

Basically, the same formula from the Casimir model conductance can be applied for Ziman and ballistic regimes, if the Λ_{cas} is replaced by an effective MFP Λ_{ph} from the Ziman formula. Specularity parameter p=1 means that all the phonons scatter coherently and ballistic transport limit is reached (elastic MFP is diverging to infinite). The ballistic regime has to be described with Landauer formalism[11] where the transport is determined via the transmission coefficient with the assumption of zero temperature gradient within the sample. According to Fourier's law, for zero T gradient the thermal conductivity cannot be prescribed. In the ballistic regime, the heat transport can be explained only in terms of the thermal conductance.

1.2.2 Diffusive and ballistic transport in thin-film membranes as a function of T

Many experimental measurements of the thermal conductivity showed that, as the thickness of the Si sample decreases below 1µm, κ reduction is observed. In the work of E. Chávez-Ángel et al[12] , large-scale Si membranes of different thicknesses were studied by micro-Raman Thermometry (µRT) at a RT. 16-fold reduction of κ with respect to the bulk value (148W/mK) was achieved for 9nm-thick membrane.
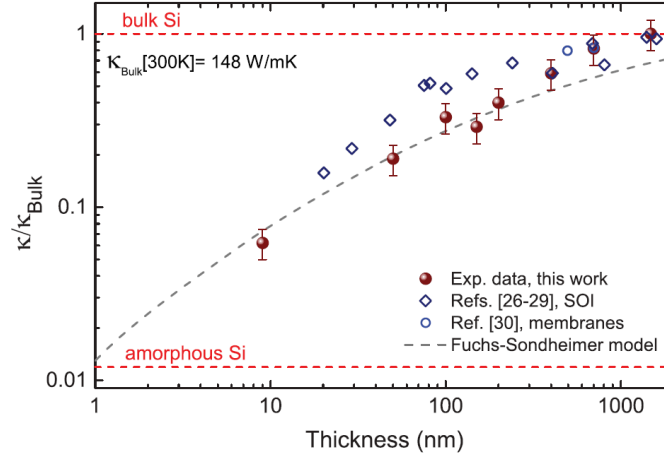
Figure 1.7

Normalized thermal conductivity[12] of Si large-scale membranes as the function of thickness. The fitting dashed line is according to Fuchs-Sonheimer model in a purely diffusive regime (p=0).

Sondheimer-Ziman[4,13] model fitting performed with zero specularity parameters indicates purely diffusive regime of phonon scattering. This model (at p=0) implies that the reduction of thermal conductivity is attributed to the shortening of the phonon mean free path due to diffusive boundary scattering. This outcome is in agreement with the formalism for diffusive transport regime described in the previous paragraph, which requires at least one size of the membrane to be much larger than phonon MFP.

An interesting experiment addressing the question of coherent effects contribution into the thermal conductivity, was performed by Maire et al. from the group of M. Nomura[14]. Beam-like suspended membranes with the phononic lattices of a different disorder level were fabricated. Measured at a RT the effective thermal conductivity did not reveal any response to the change of the lattice disorder. Whereas at a low temperature (3.7K), the effective thermal conductivity was suppressed as the phononic structure became more ordered. This is the sign of the coherent effects. The size of the dominant wavelength near 1K is of the order of 100nm, which is comparable to the pitch of the lattice in Maire's work. Coherent wave scattering might occur on the ordered phononic lattice, which could lead to the group velocity reduction due to the modification of the dispersion relation.
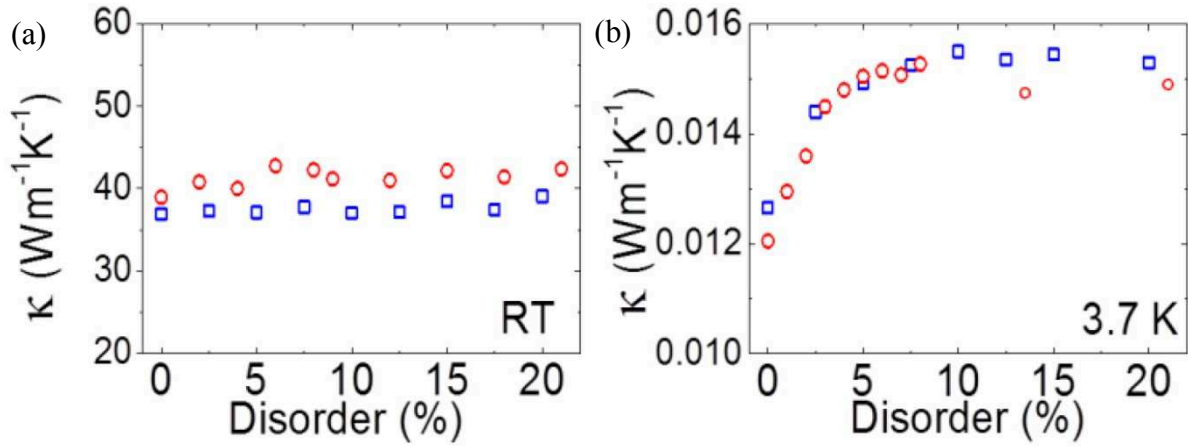
Figure 1.8
Effective thermal conductivity[14] as a function of phononic lattice disorder for 145nm-thick thermocrystals with hole diameters of 135nm (red) and 170nm (blue) at (a) a room temperature and (b) 3.7K.

1.2.3 Thermal conductivity of phononic membranes at a room temperature

As we saw in the previous paragraph at sufficiently low T coherent effects become significant due to phononic waves interference with the periodic structure in 2D phononic membranes (PhMs, i.e. thin-film membranes with the lattices of holes). The key parameter here is the temperature. Some authors argue that coherence can occur at room temperature in 2D PhM (for example, the work of Alaie S. et al[15]). In this paragraph, experimental and computational work of J. Lee et al.[9] is summarized. The authors give reasonable arguments that the thermal conductivity reduction in 2D phononic structures has a diffusive nature.

In the first part of the experiment of J. Lee work, periodic and aperiodic silicon nanomeshes with a pitch down to 100nm were studied. Both types of membranes had identical thickness (100nm), neck size (≈30nm) and transverse pitch (100nm). The pitch along the direction of heat flow varied from sample to sample by up to ±20% around 100nm. The authors investigated thermal transport in the temperature range from 14K to 325K. Their experimental results[9] show that periodic and aperiodic silicon nanomeshes yield identical (within ±6% experimental uncertainty) thermal conductivity, indicating (according to the authors) the wave nature of phonons is not important in the regime where $\lambda \ll$ pitch$\ll \Lambda_U$ and $\lambda \sim$ roughness.

In the second part of their experiment (see Figure 1.9), κ of nanomeshes with different pitches were measured. Fixing the pitch in y axis, and varying the pitch along the direction of the heat flow, it was possible to estimate the level of thermal conductivity reduction due to so-called backscattered phonons, i.e. the phonons which x-axis velocity component changes from positive to negative due to the boundary scattering[9]. The results show, that increasing the number of bridging necks (i.e. the necks that are lateral to the direction of the heat flow) decreases κ, as predicted by the phonon backscattering effect. Their experiment were supported by the ray tracing simulation, which provided a rigorous particle model

predictions, successfully explaining all experimental results without invoking coherence effects.
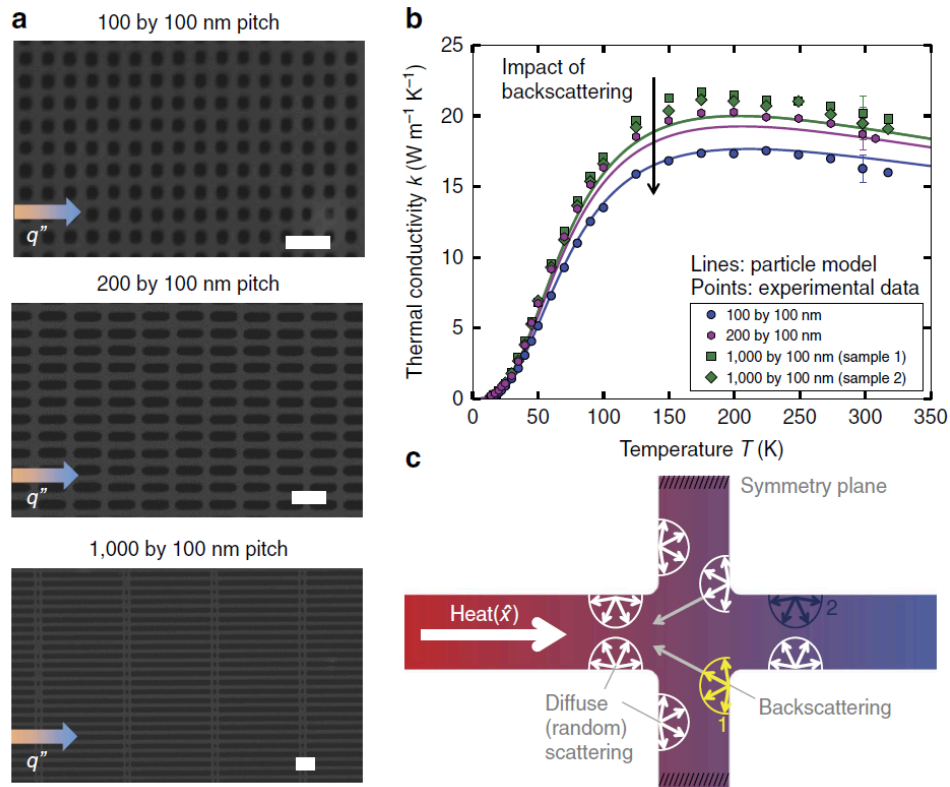
Figure 1.9

From J. Lee[9] et al. Investigating thermal conductivity and backscattering effects with variable-pitch Si nanomeshes. (a) SEM images of nanomeshes with varying pitch size (100nm – 1μm) along the direction of heat flux. Scale bars, 200 nm. (b) Experimental results and particle ray tracing model predictions for κ(T) of four samples. Decreasing the pitch decreases κ, as predicted by the diffusive backscattering effect. In the particle model all surfaces are fully diffuse. (c) Illustration of backscattering for diffuse surfaces. The intersection neck backscatters a larger percentage of incident phonons, which leads to increased backscattering from short pitch nanomeshes. For example, 100% of the phonons are backscattered at point 1 (indicated in yellow) while the backscattering percentage is only 50% at point 2 (indicated in dark blue).

1.2.4 The role of the native oxide and the roughness

In this paragraph, we will review the studies that show the native oxide (grown in the ambient atmosphere SiO_2) and the surface roughness play an important role in thermal conductivity reduction for both ultra-thin plain membranes and PhMs.

The native oxide is omnipresent on the surface of Si wafers. XPS (X-ray photoelectron spectroscopy) study[16] shows (Figure below) that the thickness of the native oxide on (100) Si n-type (10^{15} cm^{-3}) wafer surface reaches 2 Å during the first 120 min, 5.3 Å after 17 h and 6.7 Å after 7 days of exposure to the air of the clean room with 1.2% concentration of H_2O. 2Å initial SiO_2 was grown during the water rinsing preceded by ($H_2SO_4+H_2O_2$) chemical cleaning and ($HF+H_2O$) deoxidation. If the wafer is immersed into the water the growth rate is higher and the thickness can reach several nm within days. To conclude, many parameters, doping concentration, the fabrication conditions (exposure to the air or long time water immersion) and the storage conditions (moisture and pressure), affect the thickness of the native oxide. Therefore it is hard to predict the oxide thickness relying on the literature estimations that may vary and reach values up to 2nm[17].
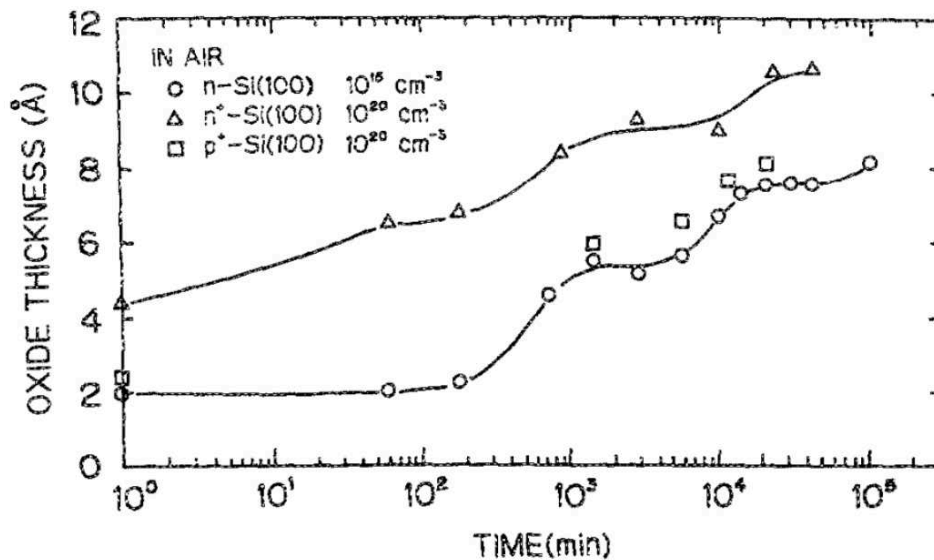
Figure 1.10
Thickness of the native oxide[16] as a function of exposure time to the air for different types of the dopant and doping concentration.

Neogi et al.[18] fabricated ultrathin 9nm and 27nm-thick Si membranes. Their experimental goal was to see how the properties of the surface affect κ. Three samples for each thickness were measured with 2 lasers μRT: samples with thin layer of native oxide, samples with thick layer of native oxide and additional roughness, and samples without oxide but with additional roughness. Based on their observations, the authors' conclusion[18] was that the dimensional reduction greatly enhances surface effects (both roughness and oxidation), and hence, surface scattering plays the dominant role. The authors pointed out that this scattering limits the phonon mean free path. At the same time, their equilibrium molecular dynamic (EMD) study suggests that dimensional reduction directly affects the phonon dispersion relations by flattening the phononic modes. However, the modification of phononic spectrum alone does not hamper thermal transport to a great extent.
.
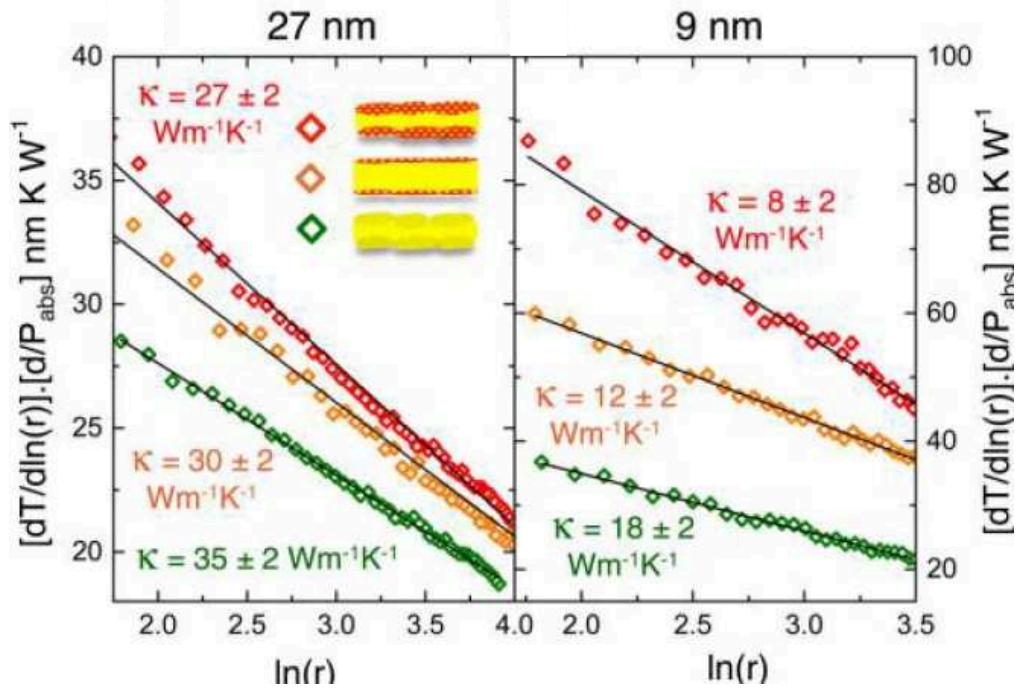
Figure 1.11
Temperature decay[18] obtained by μRT in logarithmic scale for 27nm (left) and 9nm (right) membranes. The red, green, and orange diamonds represent membranes with native oxide, with oxide removed, and with 6h of oxidation after etching, respectively; ln(r) is the logarithm of the distance r from the center of membrane.

In the recent EMD study by M. Verdier et al.[19], κ of Si PhMs at RT was estimated as a function of the size of silicon and silica amorphous phases placed on the walls of the holes and membranes horizontal surfaces. Membranes with a thickness of 8.145nm, different diameters (1-6nm) and neck sizes (1.6-7nm) were modelled. The results show that the reduction of κ due to silicon dioxide is greater than that due to amorphous silicon. For the scale of the simulation model, increasing the thickness of the amorphous shells of holes (exposure of the membranes to nonprotective conditions) leads to an important decrease of the thermal conductivity, even to ultralow subamorphous thermal conductivity keeping a large fraction of crystalline material. From MD data the authors extracted information about the density of frequencies of phonons and calculated phononic density of states (DOS) function. DOS analysis has shown that, when increasing the thickness of silicon amorphous shell, TO and TA modes became redshifted (toward lower frequencies). For silica shells all the modes of crystalline silicon became less populated and TA mode was redshifted. Besides, three high-frequency peaks, characteristic to the presence of SiO_2, appeared in DOS spectrum.
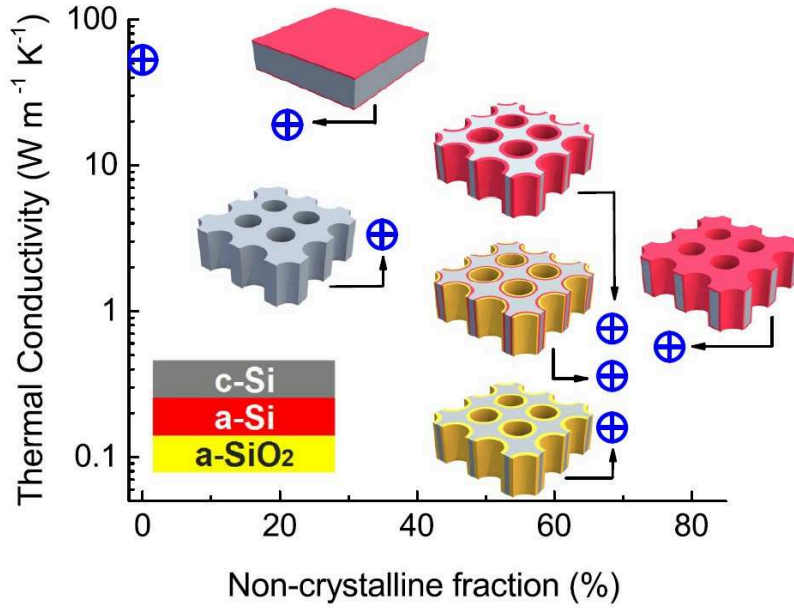
Figure 1.12
Thermal conductivity[19] of plain membrane and PnMs with and without amorphous shells and edges as a function of the noncrystalline fraction. The height of each membrane is h = 8.145 nm. The diameter of the hole for each PnC is d = 5.43 nm. The thickness of amorphous shells for PnCs with shells is t_s~1 nm and the thickness of amorphous edges for the membrane and the PnCs which have amorphous edges is t_e ~ 1 nm.

It is notable that in both EMD studies reviewed in this paragraph, the modification of phononic band structures at RT was observed. In the first case it was shown that bands modification becomes pronounced with the membrane thickness reduction. And the second study showed that the roughness and, most importantly, the oxidation, change the dispersion relation configuration when the neck size of phononic patterns is at least as small as 7nm.

1.2.5 Free-standing beam-like phononic membranes fabrication at Silicon Microelectronics group

The current work is partially based on the fabrication methodology developed by M. Haras and V. Lacatena[20]. The project UPTEG, in which both authors were involved, aimed to investigate electric and thermal conductivity of low-dimentional nanostructured silicon, estimating if this material can be efficient as thermoelectrical generator. Two types of measurement devices (platforms) were designed in order to estimate κ using 1) electro-thermal method (Figure below, a) which applies the Joule heating for probes and sensors (details are give elsewhere[20]), and 2) μRT characterisation (plot b).
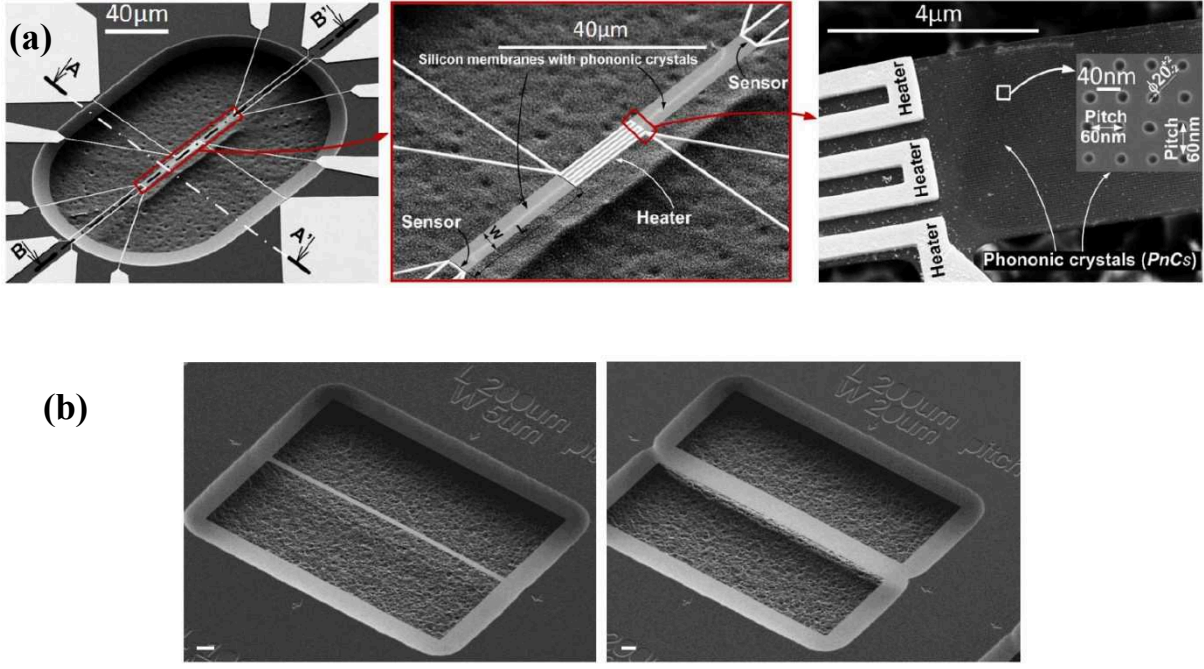
Figure 1.13
(a) SEM images[20] of electro-thermal measurement platform with free-standing beam-like PhM. The lattice has 60nm pitch and 20nm hole diameter. The small scale picture (on the left) shows 12 electrodes for 2 sensors and one heater, attached to the suspended membrane. (b) SEM images[21] of 5μm and 20μm-thick free-standing beam-like PhMs for μRT measurements. The scale bar is 10μm.

Both methods report similar values for the thermal conductivity of 54nm-thick silicon plain membranes[22]. During the project, phononic membranes were also fabricated, however the holes of the phononic lattices were only partially etched (see Paragraph 2.3.3). The authors reported of κ=59±10W/mK in 54nm-thick Si plain membrane and κ =34.5±7.5W/mK in the membrane with integrated underetched phononic lattice, both measured with electro-thermal method. The comparison of electro-thermal, μRT and other main characteristic techniques, used for the nanoscale thermal transport study, is given in Paragraph 2.1.2.

1.3 Conclusions

Fundamental theoretical aspects of phonon heat transport in the bulk crystalline material were reviewed. At first, the dispersion curve and phononic band structure of the bulk silicon were discussed. Di-atomic basis of Si defines the presence of optical branches. Due to a high group velocity, mostly acoustic modes contribute to the heat conduction. Like the photons, the phonons are described by Bose-Einstein statistical model which leads to photonic-like (black-body radiation) picture in the energy distribution of the phonons. Hence, the phononic analogue of the Wiens displacement law can be applied to calculate the dominant phononic wavelength as a function of T: λ_{dom} is of the order of 1nm at a room temperature and 100nm at 1K. Kinetic model based on Boltzmann transport equation shows that the thermal conductivity depends on the knowledge of dispersion curve (group velocity), specific heat, and the averaged mean free path (or relaxation time). Different scattering processes affect the

averaged mean free path. The proportion of the Umklapp and boundary scattering contributions to κ changes with temperature.

Coherent (wave-like) and incoherent (particle like) phononic effects can dominate in the thermal transport, depending on the temperature, the size of the sample and the roughness of the surface. Different transport regimes are distinguished depending on the proportion between these two types of effects. Each regime is described with specific model. If ballistic (coherent) transport dominates, the heat transport cannot be estimated in terms of the thermal conductivity. The recent studies suggest that when the scale of phononic patterns in silicon membranes is of the order of 100nm, the diffusive regime (or incoherent effects) processes dominate in the heat transport at RT, while the coherent effects become dominant at very low temperatures (3.7K). At the same time EMD modelling shows that when either the thickness of the membrane or the neck size of phononic lattice approach 10nm, the modification of both dispersion relation or DOS can occur. However, the quantitative estimation of any meaningful coherent effects contribution into the thermal conductivity reduction at a RT and 10nm size of the critical feature (the lattice pitch, or the thickness) is still an open question. Finally, EMD research done for phononic lattices at sub-10nm size of both critical features shows that the reduction of κ due to silicon dioxide is greater than that due to amorphous silicon.

Chapter 2 Design and fabrication of the experimental PhM devices

The following tasks were pursued at the design stage and during the fabrication work:

1) Based on the existing fabrication methodology (briefly introduced in Paragraph 1.2.5), to develop a new approach to address the question of artificially-induced anisotropy of thermal conductivity in 2D phononic membranes (PhM). Give justifications for the choices of a particular design element or fabrication method. The design of experiment has to account for the specificity of possible anisotropic heat transport, allowing the measurement of thermal conductivity components and the study of their dependence on structural parameters: pitch, neck size, pitch aspect ratio.

2) Improve some processing steps, that were only partially successful in previous methodology work or had a limited functionality: a) obtain a good quality of the nanoholes etching; b) develop a test-probe method allowing for the fast assessment of the quality (and structure) of the etched nanoholes.

3) Find the optimal fabrication solution for EBL (electron-beam lithography) machine writing of anisotropic phononic patterns.

4) Adjust EBL doses and spin-coating recipe to the requirements dictated by the design of experiment.

This chapter gives a detailed description of the development addressing all the-above-mentioned goals.

2.1 Membrane geometry and the alignment of phononic patterns

This section is devoted to the justification for the choice of the topology and measurement method for experimental membranes which have to facilitate the study of induced anisotropic heat transport in Si planar nanostructures.

2.1.1 Directionality of the measurements.

We start with the problem description in a general form, without particular measurement method in mind, just assuming that we can apply some heat gradient along the straight line and measure the heat current along this line or perpendicular one. Our goal is to see what alignment of the measurement devices and the sample is preferable for the effective thermal conductivity tensor $\bar{\bar{\kappa}}$ estimation. The word "effective" points out, that in some cases, the creation of phononic patterns in the membrane changes only the thermal conductance (compared to pristine membrane level), due to the volume decrease (increase of phononic patterns filling fraction), and the host material κ stays the same or slightly changes. Effectiveness of κ will be discussed in Chapter 4, therefore for now this term will be omitted.

a)

$$\kappa^S = \begin{pmatrix} \kappa'_{11} & \kappa'_{12} \\ \kappa'_{12} & \kappa'_{22} \end{pmatrix}$$

$$\overline{\overline{\kappa}}^D = R^T \overline{\overline{\kappa}}^S R$$

$$R = \begin{pmatrix} \cos(\theta) & -\sin(\theta) \\ \sin(\theta) & \cos(\theta) \end{pmatrix}$$

$$\kappa^D = \begin{pmatrix} \kappa_{11} & 0 \\ 0 & \kappa_{22} \end{pmatrix}$$

b)

$$\begin{pmatrix} \kappa'_{11} & \kappa'_{12} \\ \kappa'_{12} & \kappa'_{22} \end{pmatrix} \begin{pmatrix} \dfrac{\partial T}{\partial x} \\ 0 \end{pmatrix} = -\begin{pmatrix} J'_x \\ J'_y \end{pmatrix}$$

$$\begin{pmatrix} \kappa_{11} & 0 \\ 0 & \kappa_{22} \end{pmatrix} \begin{pmatrix} \dfrac{\partial T}{\partial x} \\ 0 \end{pmatrix} = -\begin{pmatrix} J_x \\ 0 \end{pmatrix}$$
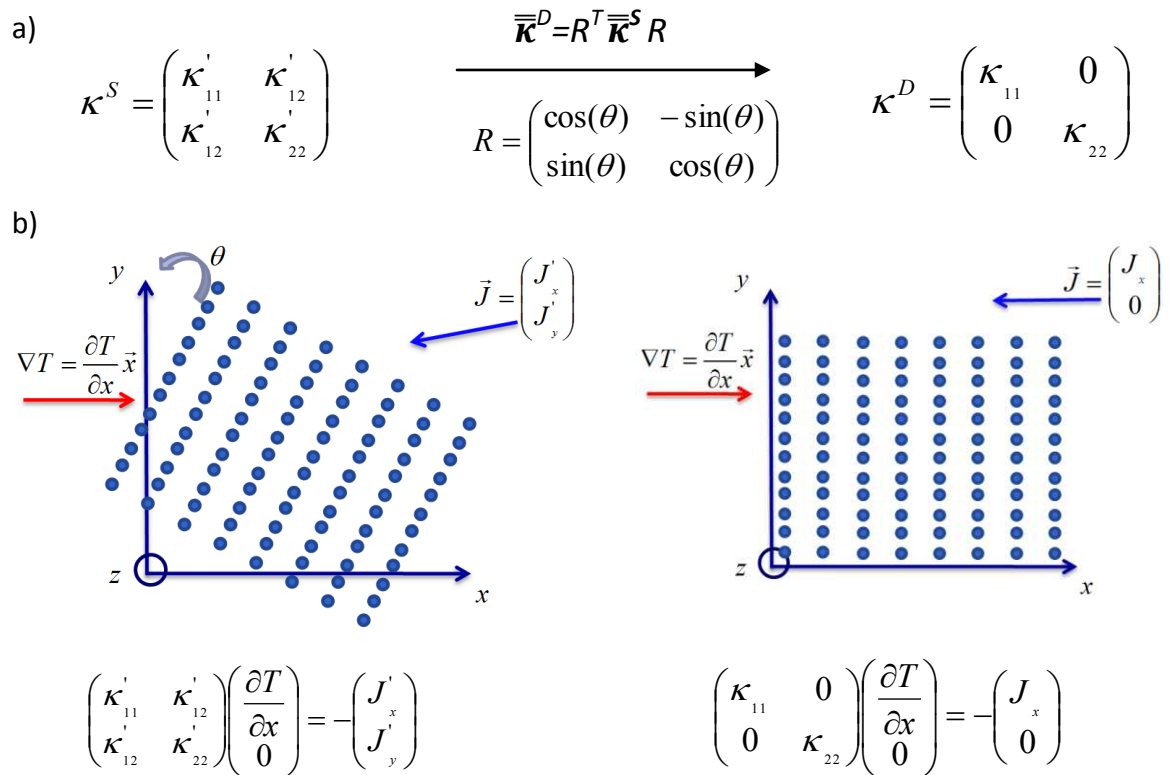
Figure 2.1
(a) Symmetric matrix κ^S can be diagonalized by the rotation operation with **R** matrix. (b). schematic example of non diagonalized and diagonalized $\bar{\bar{\kappa}}$ measurements. Note: it is assumed the material on the sketch has an in-plane anisotropy of the crystal (or phononic) structure and of $\bar{\bar{\kappa}}$ as a result. The lattice on the sketch is assumed to be infinite.

Tensor $\bar{\bar{\kappa}}$ is a symmetric matrix with distinct eigenvalues (Figure above, a). In a Cartesian space such matrix is diagonalizable by the real orthogonal eigenvector matrix (for example by the rotation matrix **R**, as shown on the figure above), thus it is possible to align the lattice principal axis (axis of orthorhombic phononic or crystal lattices) and experimental probes

(heat source/sink connectors and the temperature probes) in such a way, that one can obtain the eigenvalues of $\bar{\bar{\kappa}}$ (Fig above, b) applying Fourier law:

$$\vec{J} = -\bar{\bar{\kappa}}\nabla T,$$ (13)

where ∇T is a temperature gradient, $\vec{J}$ is a heat current vector.

We want to work with very thin, quasi 2D, membranes, where the thermal gradient is applied strictly in-plane, besides both crystal and phononic lattices (phononic voids) aligned in parallel with z axis (thickness direction). Therefore, off-plane and in-plane thermal properties can be viewed as decoupled and we can focus only on the in-plane heat vector that does not have the out-off plane components. Hence, we are legitimate to reduce $\bar{\bar{\kappa}}$ to 2D in-plane dimensions.

Experimentally the diagonalization is useful because it makes the measurements of $\bar{\bar{\kappa}}$ easier (and more accurate). As one can see on the left sketch (Fig above b), one-component temperature gradient vector ∇T nonparallel to the principal axis of the phononic anisotropic lattice produces the heat current vector $\vec{J}$ with two components. Such misaligned experimental scheme would require to do an additional measurements applying ∇T in y direction in order to find all elements of nondiagonalized symmetric tensor κ'_{ij} (or two in-plane eigenvalues κ_{ii} after diagonalization). In total for the measurements of two eigenvalues in nondiagonalized case, one needs to apply ∇T and measure heat current 2 times (in two directions). Besides, other things being equal, these measurements can lead to a higher experimental error. To the contrary, the measurement of κ_{ii} in diagonalized case (Fig above, b, right), is straightforward and more accurate. Thus, the first conclusion is that we would like to measure the thermal transport in principle orientations.

2.1.2 Heat current and measurement techniques.

In practice, ∇T can be easily obtained by temperature measurements (for example, via electrical resistance probe or a light probe[23]), whereas the heat current cannot be directly probed. Usually, it is estimated from the absorbed power at the high T spot or interface. Therefore, experimentalists need to guarantee the absorbed power localisation inside the heat channels: it implies the absence of convection (otherwise its precise knowledge), thorough check for any heat leakages (irradiation, or substrate heat sink) and the losses due to the interfaces with metals and oxides. Vacuum chamber utilisation perfectly addresses the first problem. The second and the third problems are addressed by nanofabrication, the task here being to isolate physically and thus thermally membrane from the substrates and buried oxide layers. In the next paragraph, the main geometries of the suspended (or free-standing) membranes are discussed. However even with the suspension, many experimental techniques require specially deposited metallic layers for the temperature probe. This poses a question of the heat losses estimation at the interfaces. For example, the following electro-thermal methods highly depend on the properties of metallic probes and the interfaces they form: Direct Current (DC)[24,25] and 3ω[26,27] methods. A similar problem arises in Time Domain Thermo Reflectance TDTR[23]. Scanning Thermal Microscopy SThM[28–30] requires precise

knowledge of geometry and thermal properties of the probe tip, which needs accurate FEM analysis. In this regard, the contactless µRT technique (one of the two techniques available in our lab; the second is DC method) has an advantage because it implies direct membrane heating by light absorption.

The table below summarizes drawbacks and merits of the main thermal transport characterization techniques, some of them have already been mentioned. Noninvasiveness and the absence of heat losses make the µRT method very promising. The third argument in favor of this method over the DC electrothermal method is a shorter fabrication process (no need for NO_2 and metallic heater/probes deposition). However, as will be seen in this manuscript, µRT limitations leads to higher errors and difficulties in the analysis: wide laser spot size (which is dependent on the lens resolution) requires careful estimation prior to experimental design; the need for theoretical absorption estimation adds to the final experimental uncertainty.

Table 2.1
Comparison of the main characteristic techniques used in thermal transport research. Table courtesy: P.-O. Chapuis, CETHIL.

Optical techniques

Method	Advantages	Limitations	
Flash	Ease of application	Laser spot size	Thickness > µm
Thermoreflectance	Time resolution down to picosecond		Metal deposition, heat capacity, invasive
µ-Raman thermometry with one laser	Ease of application, heater = thermometer, non-invasive		$A = 1 - R - T$, modelling
µ-Raman thermometry with two lasers	Non-invasive, direct access to λ		$A = 1 - R - T$

Electrical techniques

Method		Advantages	Limitations
DC	Electrothermal deposited device	Ease of application	Heat losses, invasive
3ω (harmonic)		Resolution down to 10^{-4} K	Metal deposition, electrical insulation, invasive
Scanning thermal microscopy (SThM)		Non-invasive, spatial resolution ~ 100 nm, resolution down to 50 mK	Standards, probe modelling, contact

2.1.3 Membranes shape

Based on the observations from the last two paragraphs, we conclude, that it is preferable to work with the fully suspended membranes in a vacuum (to localize the heat flow) and use µRT method as a measurement tool. Last but not least, since we work with anisotropic thermal conductivity, we would like to measure thermal transport in principal orientations of phononic pattern.

Mainly, two types of suspended membranes topology are possible: beam-like (introduced in Paragraph 1.2.5) and large-scale (Figure 2.2a).
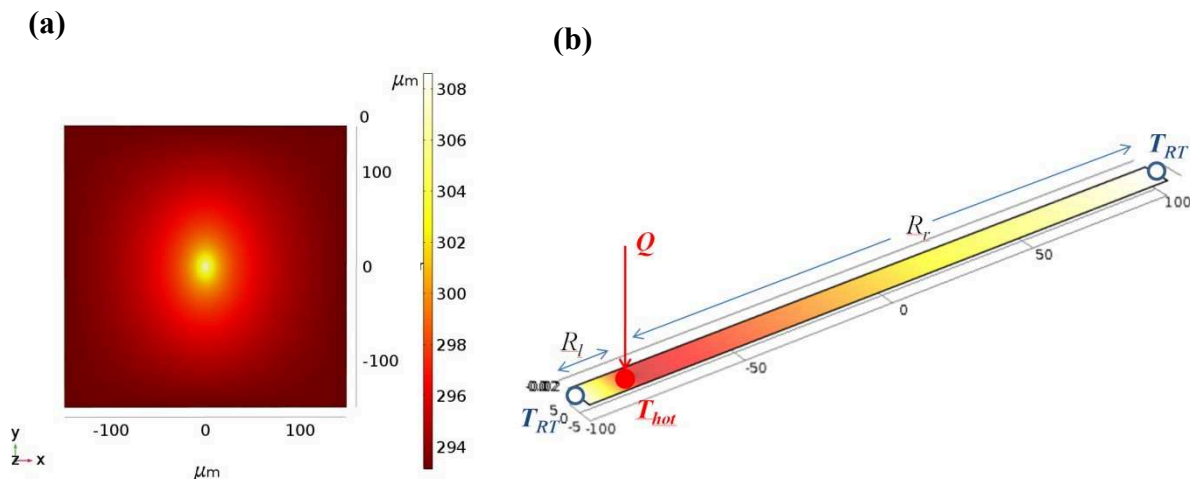

Figure 2.2

FEM-simulated equilibrium anisotropic temperature profile induced by the heat absorption at a spot (laser beam spot) of thin membrane with in-plane *κ*-anisotropy. (a) Large-scale membrane with anisotropy of thermal conductivity, input heat flux is at the centre and has symmetrical Gaussian power distribution with standard deviation σ=1.5µm. (b) Beam-like membrane (colours are inverted). Both configurations imply µRT measurements, where the laser is a heater and a probe at the same time.

If the heat flow is anisotropic, the large-scale membrane would require the measurement of the temperature profile: directly with a two-laser approach (details are given in Paragraph 3.2.1), or indirectly using only one laser. In both approaches for the large-scale membrane, there is an additional work needed (in comparison to the beam-like membrane): either the installation of the second laser (probe laser) or more sophisticated analysis in the case of indirect profile measurements. Advantage of the large-scale µRT method is that there is no need for the perfect (diagonalized) alignment described in the paragraph 2.1.1. The main task for large-scale membranes with thermal anisotropy, when measured by µRT, is to obtain T-profile along the principle orientation.

In comparison to large-scale shape, beam-like membrane advantage is that there is no need for the temperature profile scan, which is a time consuming process. Instead, it is enough to vary the power at a laser spot. This approach is called P-variation, and details can be found in Section 3.2, but the main idea that it allows faster and more accurate (due to elimination of membrane curvature influence) measurements.

In the beam-like membrane the heat current is forced to flow only in one direction. We are free to choose this direction in the principal orientation of the nanopattern (i.e. to fabricate the

membrane accordingly), as needed for the direct eigenvalues measurements. In this way we are able to measure eigenvalues with fast P-variation method.

Notwithstanding the advantage of direct eigenvalues measurements in beam-like configuration, the large-scale membranes experiment can be extremely helpful. Comparison of the large-scale membrane anisotropic T-profile with the one reconstructed from the localised measurement of κ could increase reliability of the experiment. A novel method of large-scale membranes fabrication was under development until recently (see Paragraph 2.2.3) in our lab. Therefore, only beam-like configuration was used in this work for PhM with and without anisotropic patterns.

2.1.4 Design of phononic anisotropic patterns

The final PhM layout is described in this paragraph. It was planned to work with elongated beam-like Si membrane of standard width $w = 10$ µm and lengths $l = 200$µm. These sizes are reasonable since they are large enough not to affect averaged phononic MFP at RT ($\approx$100-500nm) [31], and small enough to localize the heat. The thickness t is below 100nm, which is comparable to the thinnest IC layers used nowadays, and small enough to reduce thermal conductivity 3 times compared to the bulk value[12]. Our minor goal is to achieve higher reduction of κ introducing the phononic structure. The major goal is to induce thermal anisotropy. Lattices of nanovoids are a versatile approach for anisotropic nanopatterning, since they span a big space of configurations': for example it is easy to design a series of lattices, which would have the same filling fraction (or unit cell area) but different pitches in orthogonal direction. The shape of voids (holes) is cylindrical because we aim to work at the bottom of EBL resolution, where square shapes with angles are almost not achievable. Schematic representation of the membranes with anisotropic hole patterns and physical quantities is given on the figure below.
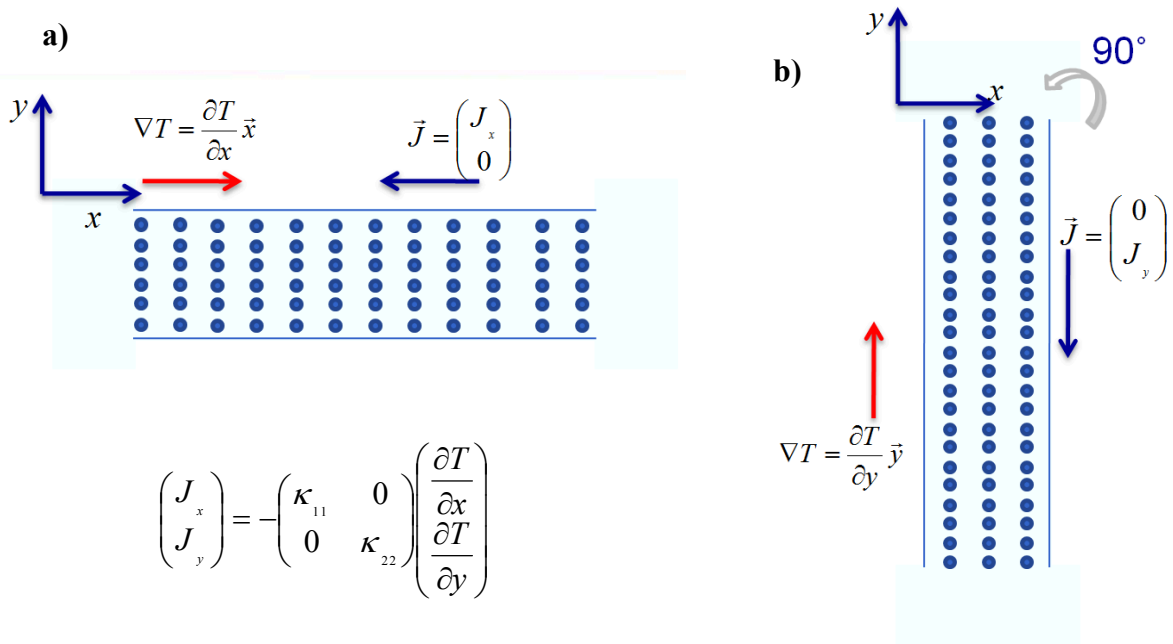

Figure 2.3
Schematic representation of the proposed experiment, when $\overline{\overline{\kappa}}$ eigenvalues corresponding to particular anisotropic nanopatterns can be measured.

Analytically, the picture is the same as the one described in paragraph 2.1.1. The main difference is that now we localise the heat flow. It is important to mention, that according to experimental conditions the heat current J (defined by the absorbed laser heat Q_A) is the known quantity and the heat temperature gradient is the estimated quantity (defined by the Raman Shift). Details on how $T(J)$ or $T(Q_A)$ is measured are in Section 3.1.

The proposed experimental topology, is analogue to the situation when one would have a film of anisotropic material, and by isolating two pieces of it in orthogonal principal orientation, is able to measure κ_{ii} eigenvalues[32]. In order to make the experiment more reliable, it was planned to perform the measurements on the isolated "tilted" membranes with the same phononic patterns (see Figure below). In other words, we would like to cut three more beam-like pieces (with 3 different angles) out of our 2D material. There are two possibilities of matching the data for different orientation pictures (tilted and principle). The first is to plot measured gradient ∇T vs. angle of membrane orientation, which could be approximated with elliptical curve (similar to isotherms from Figure 2.2a). In the isotropic case ∇T vs. angle trend has to be approximated by the circle curve. The second approach is to reconstruct symmetric matrix (tilted case) using orthonormal rotation operator R (figure below). This will allow to obtain corresponding gradient $\nabla T^{Model}(\theta)$ via FEM model and compare it to experimental gradient.

$$\kappa^S = R\kappa^D R^T$$

$$R = \begin{pmatrix} \cos(\theta) & -\sin(\theta) \\ \sin(\theta) & \cos(\theta) \end{pmatrix}$$

$$\kappa^S = \begin{pmatrix} \kappa'_{11} & \kappa'_{12} \\ \kappa'_{12} & \kappa'_{22} \end{pmatrix}$$

$\nabla T^{Model}(\theta)$

$\nabla T^{Exprm}(\theta)$
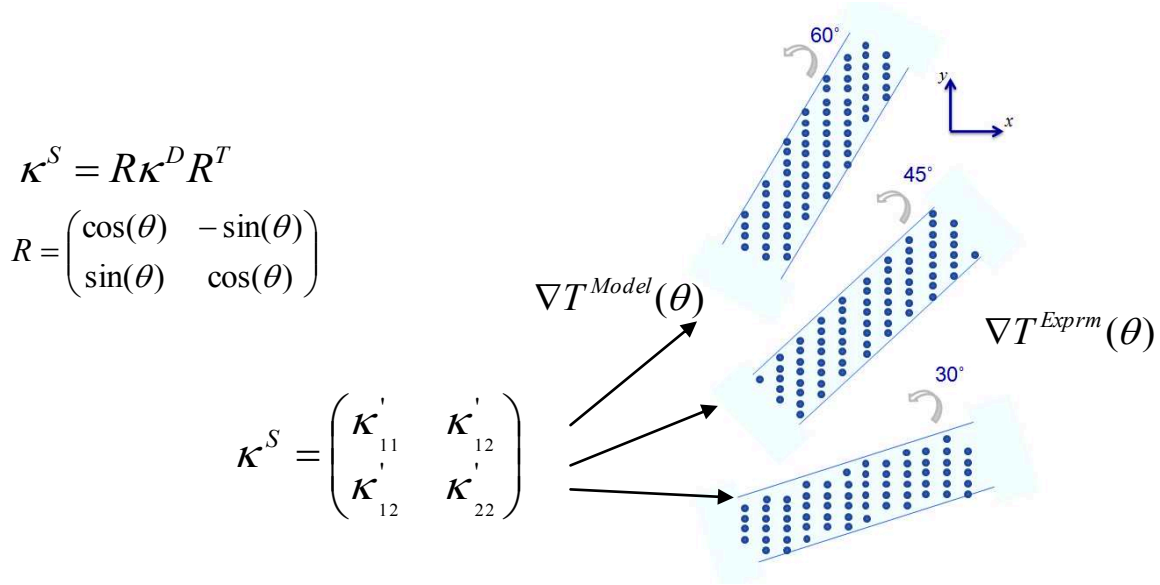
Figure 2.4
Schematic representation of the proposed experiment for tilted PM. Formulas demonstrate analytical approach predicting temperature gradient of tilted PhM from the known thermal conductivity eigenvalues.

Two principles are put in the experimental layout design for the series of anisotropic PM:
1) It is interesting at what ratio of the pitches the eigenvalues difference becomes pronounced, and how this difference changes with the increase of the pitch ratio.
 2) This comparison can be valid only if the filling fraction of the voids is the same (or similar) for different anisotropic patterns. Otherwise it is necessary to calculate contribution of the filling fraction into thermal conductivity. This is not a trivial task because the effective

medium models, which are conventionally used for the estimation of filling fraction factor (more details are in paragraph 4.1.4), do not account for the fundamental changes in phononic properties that occur at the scale when the obstacles of the heat propagation are close to the averaged MFP.

In order to make a valid quantitative comparison among the patterns, we have to design them being of different pitch aspect ratio but having the same filling fraction. For this we keep the unit cell (UC) area of the lattice constant, squeezing it in one dimension and stretching in orthogonal one (as can be seen in a Table below).

Table 2.2
Layout of the anisotropic series of µRT experimental platforms for the estimation of anisotropic heat transport. All 25 suspended Si membranes designed to be of 200µm long, 10µm wide. Membranes have to be perforated with lattices of holes in different configurations, characterized by the aspect ratio of the pitches in y- and x- directions and the angle of the membrane orientation to the principle axis of the phononic lattice. Unit cell area of the lattice (as well as the filling fraction) is designed to be constant

x pitch, nm	y pitch, nm	UC Area, nm²	90°	0°	45°	60°	30°
100	100	$\kappa_{11} = \kappa_{22}$ 10000					
90	111	$\kappa_{11} \neq^? \kappa_{22}$ 9990					
80	125	$\kappa_{11} \neq^? \kappa_{22}$ 10000					
70	143	$\kappa_{11} \neq^? \kappa_{22}$ 10010					
63	159	$\kappa_{11} \neq^? \kappa_{22}$ 10017					

Besides the series of anisotropic membranes experimental platforms, the other series were planned for fabrication. In order to demonstrate the reliability of the proposed experiment, it was decided to prove predicted absence of any meaningful in-plane anisotropy in pristine Si membrane of the same surface orientation[33] (which is true at room temperature and higher). For this purpose, 5 platforms with plain membranes (no patterns) were added to the layout with five different angles (similar to any row of membranes from the figure above).

Additional series of isotropic membranes were prepared, with pitches ranging from 60nm to 500nm, in order to find $\kappa(ff)$ trend and try to estimate if, and within what range of ff, thermal conductivity is effective (i.e. real thermal conductivity is constant, see Chapter 3).

2.2 Overview of the fabrication methods and experimental devices design

The section will give a brief description of the fabrication procedures relevant to this work. Then we will focus on the most recent techniques and approaches used for nanopatterning and suspended thin-film membranes fabrication. We will compare beam-like and large-scale membranes fabrication processes.

2.2.1 Clean-room fabrication procedures

In order to justify the choices made in this work during the fabrication stage, it is crucial to give a review of conventional clean-room micro- and nanofabrication techniques. All fabrication operations described here were involved in the process of the measurement platforms creation in this work.

The wafer

We use commercially available SOI wafers by Soitec[34] produced with the use of the smart-cut process[35]. The name "SOI" stands for "Silicon On Insulator" and stresses the role of monocrystalline semiconductor Si layer (Figure 2.5) electronically insulated from the substrate (also: the handler or the "rest of the silicon wafer"). Smart-cut process allows to obtain ultra-thin insulated Si films (layers) of 50-200 nm thickness, that are suitable for IC manufacturing. Insulation layer is called BOX (Buried Oxide) and is made of SiO_2.

(a)

SOI (55nm)
BOX (145nm)
Si Substrate (845μm)

(b)
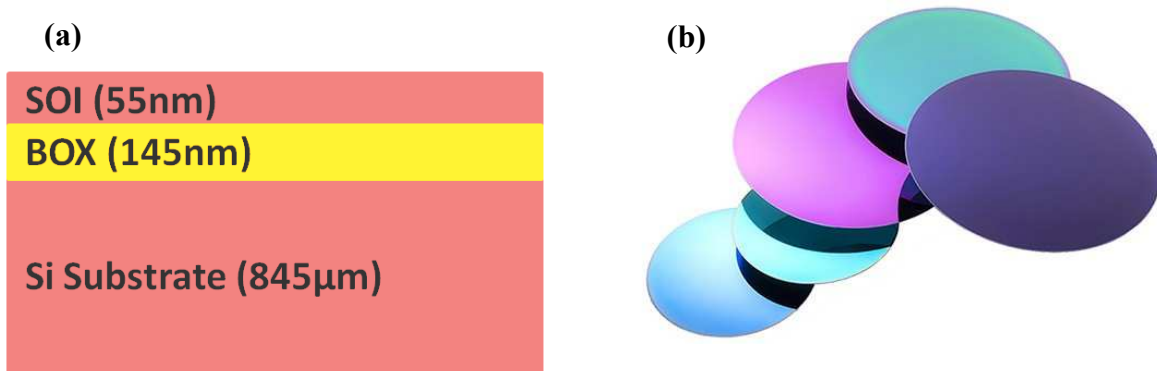
Figure 2.5

(a) SOI wafer cross-section with the layers' thicknesses (this work values). (b) Industrial quality SOI wafers [34].

Five main operations shown on Figure 2.6 (except the oxidation) constitute the most common top-down process line in microchip fabrication. Process starts with the spin-coating, which, together with the lithography and the development, can be considered as preparatory steps for the key operation, the etching. The etching allows to remove the insulator or semiconductor materials, creating patterns of voids and cavities according to the layout

designed by a researcher or an engineer. Many different etching gases and liquids are able to interact effectively (chemically or physically) with the wafer materials[36]. Those substances are called etchants (examples are in the "**Etching**" part). However, in order to make the etching process feasible, the mask or a stencil has to be deposited on top of the wafer sample. This mask has to protect the wafer parts that we don't want to etch and open-expose the parts that we would like to etch.

Spin-coating and resists

In most cases, special polymers are used for masking. They are called "resists" (the term "mask" or "photo mask" usually applies to photolithography stencil). The process of liquefied resist deposition (coating) is called "spin-coating" because a fast rotation (spinning) mechanism is used during this process. In order to transfer a circuit pattern onto the resist, making it a stencil for the etching, the resist has to be exposed to the light or e-beam radiation. This induces chemical changes throughout the exposed volume of the resist layer. For instance, chemical bonds may be formed or destroyed, initiating a change in solubility. Depending on the type of radiation, resists are subdivided mainly into two groups: photoresists (optical resists) or e-beam resists (see **Lithography** part). The last type is used in this work. There are many different brands of e-beam resists. The following are e-beam resists related to this work: PMMA, ZEP, CSAR. Details about their characteristics and justification of the choice for particular fabrication operation is given in Section 2.3.

The crucial part of the spin-coating process is the prebaking (pre-exposure baking). The purpose is to remove solvent (up to 15% in concentration) from the deposited resist and release the stress. This procedure significantly improves the adhesion to the substrate. However the over-baking may easily destroy photoactive substances in a photoresist and cause bad lithographic sensitivity. Typical baking parameters are in the range of 75–100°C for 1-10min of the hot plate (non vacuum) baking. Both parameters vary with the type of resist and the desired thickness. In order not to trap the solvent inside of the resist, which can happen during convective oven heating, the hot plate is used in most cases. Otherwise, convective baking has to be done with a slow ramping.

Lithography

As mentioned before, the radiation-induced change of solubility of the resist is a key feature. One can induce or mute the ability of a resist to be soluble in particular solvents (developers) by exposing it to the light or electron radiation. If the radiation makes a resist soluble, we call such polymer a "positive resist". In the alternative case, it is called "negative resist", because the wafer post-developed surface area is negative (opposite) to the surface area that was exposed during lithography. The sketch below demonstrates the fabrication process performed with the use of a positive resist. The mechanism of resist exposure depends on the type of radiation used. In the optical case, a specially manufactured photomask is used, which allows an instant exposure of the whole wafer. The photolithographic mask approach has led to a high-volume production of IC devices. It is a predominant technique in the semiconductor industry.

E-beam lithography (EBL) is a maskless technique (direct-write): the focused beam of electrons step by step covers the patterns' area during exposure, therefore the whole process is

time-consuming, compared to photolithography. EBL is called a "sequential" method as opposed to photolithography, which is called "parallel". However the small scale of research laboratory or prototyping projects makes it acceptable to utilize slower but more versatile EBL method. Besides, the high cost of an optical mask and the time, spent on its fabrication, often make EBL a more flexible and preferable tool in R&D laboratory projects. Interesting recent highlights about the **lithographic efficiency contest** can be found in **Appendix**.
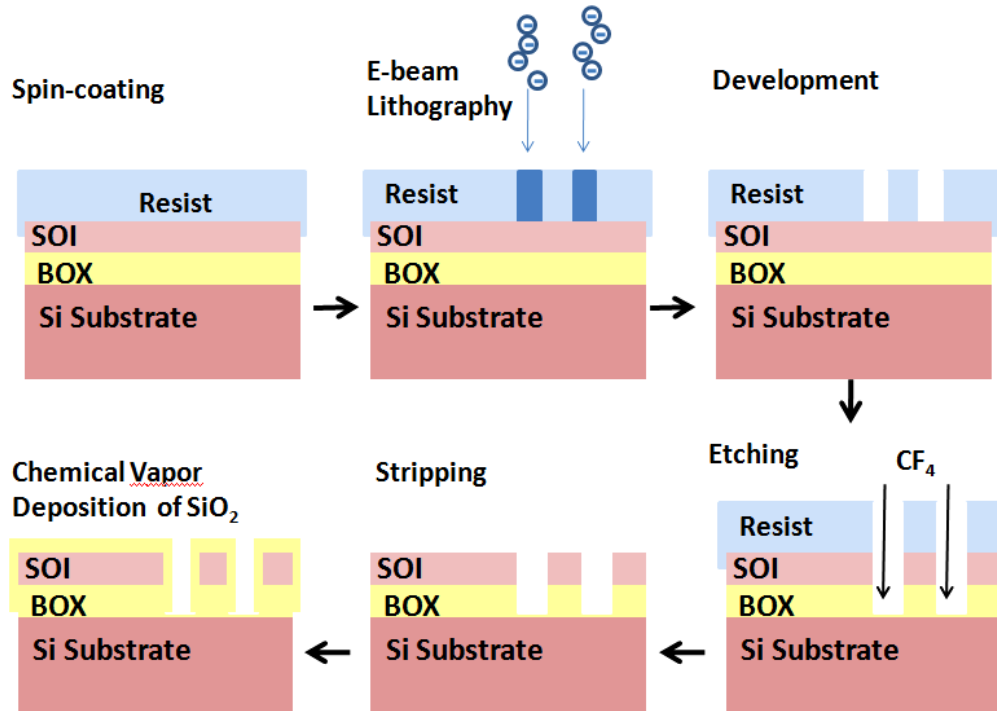
Figure 2.6
Typical top-down process line in micro- nanofabrication.

Development

A typical consequence of a positive e-beam resist interaction with electron irradiation is the chain scission. In this process molecular bonds break up and lower molecular weight fragments get formed in the exposed regions. The task of a solvent developer is to wash away those regions of fragmented chains, leaving the unexposed resist volume untouched. This selective process occurs in a conventional EBL resist, PMMA (Polymethylmethacrylate). Usually, PMMA is developed with MIBK (Methyl isobutyl ketone) solvent. MIBK is too strong[37] and can remove unexposed polymer's parts. For this reason it is diluted with non-solvent alcohol IPA. Some techniques (ultrasonic agitation or cold development) have enabled PMMA resolution patterning down to 10nm. Postbaking procedure can follow the development. It can help to remove the post-development solvent residue from the resist and improve the resist-substrate adhesion and coater hardness. Sometimes, postbaking has significant limitations, such as stress increase, resist melting and feature walls' degradation.

Etching

There are many types of the etching techniques. A few of them are described in paragraphs 2.2.2, 2.2.3, where some relevant processing examples from literature will be discussed.

Dry etching

Here, we will focus on the etching type that was applied in this work, namely the conventional RIE (reactive ion etching) method. It is a dry etching technique, that enables the transfer of lithographic patterns onto semiconductor (insulator) bulk material with the use of a plasma. RIE makes the control of the etching profile feasible, i.e. the control over an anisotropy or an aspect ratio of the etched trenches. This is possible thanks to the synergistic combination of the chemical reactions of neutral particles and physical ion sputtering (bombardment)[38]. The figure below demonstrates different modes (extreme cases) of plasma etching[39]. Ideally perfect vertical trenches' sidewalls with no lateral undercut are possible at the micro-scale, however at the nano-scale things become trickier and obtaining good etching anisotropy is a challenging task even with RIE. Luckily there is a special extension of RIE called ICP-RIE (ICP stand for "inductively coupled plasma"), which in some cases helps improving anisotropy significantly. ICP-RIE enables better control of directionality because the ions can be accelerated towards the target electrode controlled by a separate electric circuit. Mainly halogen or halogenated gases (such as Br, Cl_2, SF_6, CF_4) are used for RIE.
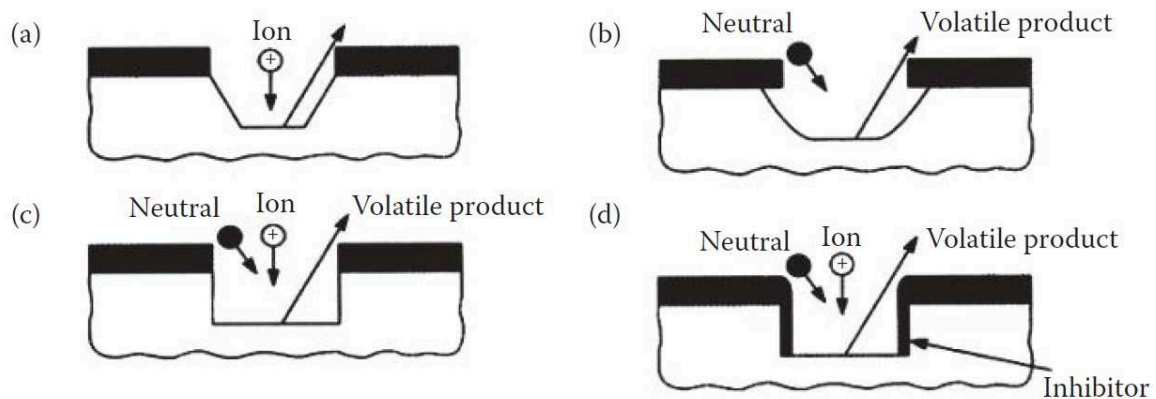

Figure 2.7
Comparison[39] of possible RIE regimes. (a) Partially-anisotropic sputtering profile obtained in directed plasma (similar to ion beam etching IBE case) with low pressure (10^{-3}- 10^{-4} Torr) and low etching rate. (b) Almost isotropic profile resulted by low ionisation voltage and high pressure (1 Torr), mostly chemical etching. (c) Ideal anisotropic case via combined physical and chemical etching, high voltage and pressure. (d) Same as previous, but with the use of sidewall protection.

Wet etching

Wet chemical etching is generally isotropic. The common isotropic wet etchants are either acids (hydrofluoric acid HF) or mixtures of acids (hydrofluoric acid, nitric acid, and acetic acid forming HNA mixture). When etching crystallographic materials, like Si, some wet etchants (potassium hydroxide KOH and tetramethylammonium hydroxide TMAH) have different etching rates in different crystal orientations, which leads to partial anisotropy (comparable with Figure 2.7a).

Besides being the generally more isotropic method, wet etching has another crucial drawback, which is the surface tension. At the scale of sub-100-nm features this drawback makes the wet etching utilisation very problematic.

Stripping

The final basic top-down fabrication step is the selective etching of resists. This process is called the stripping. Strong acids (example: H_2SO_4), acid-oxidants (example: H_2SO_4-Cr_2O_3) or alkaline solvents are used as strippers (removers). The efficiency of some liquid strippers depends on the postbake status of the resist. For example, tough resist skin formed during 20min of 140°C postbaking, makes acetone stripper useless[37]. The other wet strippers are stronger (yet toxic) and able to etch very thick and tough volumes of resist: for instance, PG remover (N-methyl-2-pyrrolidinone) used with PMMA, PMGI, SU-8 resists. High stripping rate ($\approx$1μm/min) methods such as wet exothermic Piranha solution (H_2SO_4 mixed with water) and ozone-water (dry ozone injection) are often used for both stripping and cleaning.

Dry stripping, and particularly dry reactive plasma resist stripping, has reached big popularity in the industry due to the high etching rate and such advantages as: controllable processing, low metallic parts' corrosiveness, less by-product (polymer residue) is left on the surface after the etching, no undercutting and broadening of the etched features. The key mechanism of the plasma stripping is the splitting of molecular oxygen into atomic form via electrical discharge. As a result, more reactive isotropic etching occurs. Finally, the combination of UV and ozone gas is used for dry etching. UV facilitates ozone etching efficiency by breaking resist chains' bonds. The advantage of ozone plasma stripping over the oxygen is the absence of the plasma side effect damage to the sample surface.

Oxidation

The last procedure from Figure 2.6 (oxidation) may not be included into the set of the conventional microcircuits fabrication steps, but as the sizes of the etching features decrease down to sub-100nm scale, the importance of oxide thin films' deposition increases.

Firstly, an oxide layer may serve as a protection (passivation) shield material, covering the small and fragile Si nanofeatures. A case example of oxide passivation, related to this work, can be found in the next chapter. There are two kinds of oxidants possible typically: O_2 and H_2O for the dry and wet oxidations respectively. Both substances interact chemically with the Si surface creating SiO_2. However at room temperature the growth rate of the oxide is very small and exponentially drops with oxide thickness. High temperatures[40] (700-1300°C) substantially expedite the growth rate. One of the most popular techniques of oxide (and nitride) thin film formations is the low-pressure chemical vapour deposition (LPCVD). It comprises gaseous phase deposition with low pressure and high temperature conditions. A typical LPCVD chamber is a tubular shaped furnace with gas inlets and vacuum pump passages. Further enhancement of the growth rate is possible with the utilisation of a plasma discharge mechanism. This method is called PECPD (plasma-enhanced CPD). The oxide growth occurs in two phases: a linear phase (up to 30nm), where reaction growth rate defines the main rate; and a square root phase, when diffusion rate limits the overall rate. Regardless of the etching rate phase, almost half (0.44) of the silicon volume is consumed for a growth

of oxide unit volume. This property makes the thermal oxidation, followed by removal of the grown oxide, a fabrication process used to thin down the Si layer.

2.2.2 Nanopatterning

Nowadays, different fabrication approaches are used for the creation of phononic nanostructures. Focused ion beam milling (FIB)[20,21] can be applied to nanopattern a large-scale made of materials that may not be easily processed by wet or dry etching (Figure 2.8a,b). For Si PhM the most widespread approach is a combination of optical or electron beam lithography (EBL) with the reactive ion etching (RIE) or inductively coupled plasma (ICP)[9,21,23] (Figure 2.8c,d). Wherein etchant gases and their parameters may vary: SF_6/O_2, HBr, CF_4/He, Cl_2. RIE(Cl_2) method is used in this work, and the detailed description of the fabrication process is in paragraph 2.3.
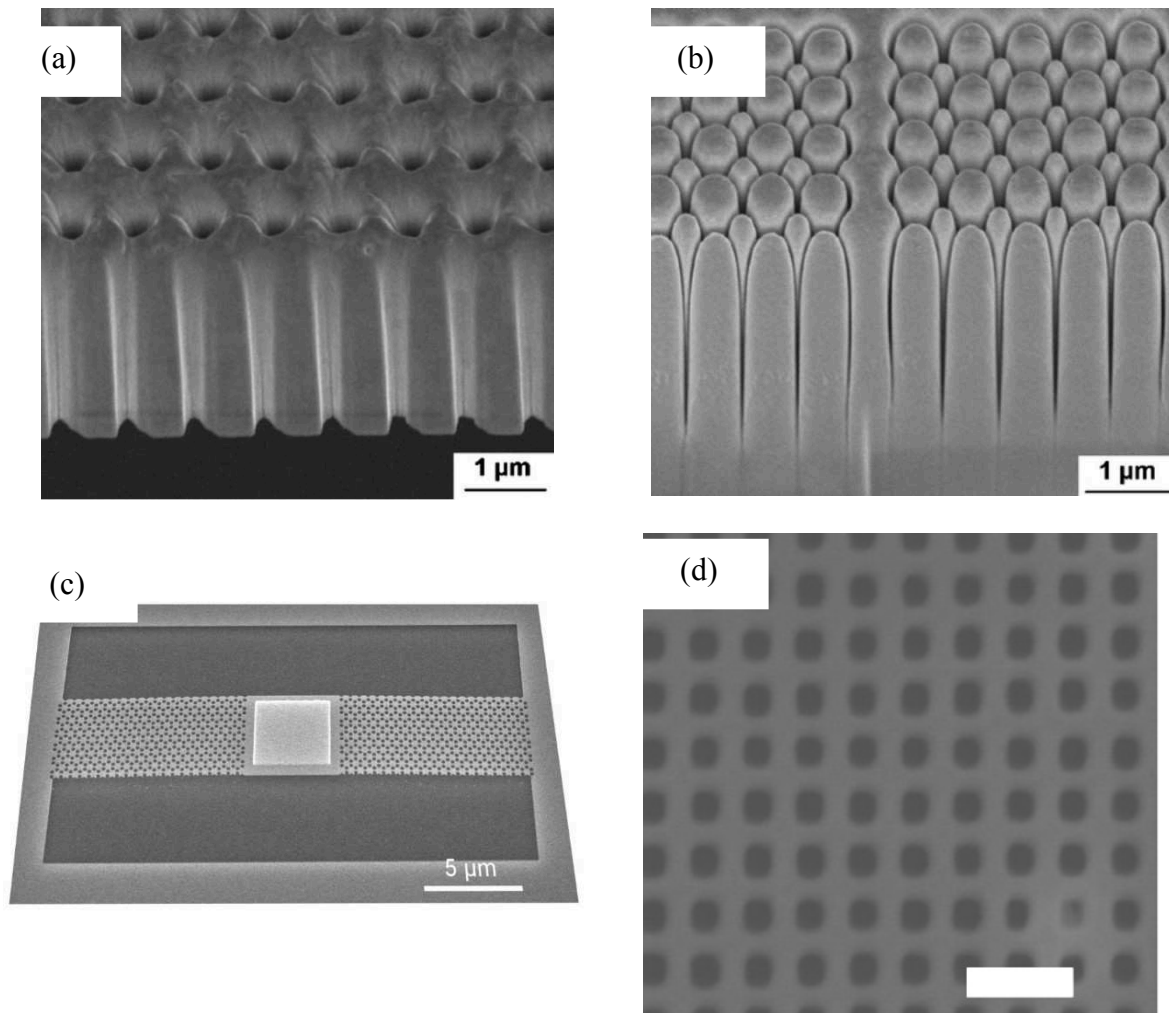

Figure 2.8
SEM images showing cross-section of $LiNbO_3$ PhM patterned with (a) the lattice of holes and (b) hexagon-shaped lattice of nanorods produced by FIB milling[21], Si PhM with honeycomb holes lattice[23] (c) and Si nanomesh[9] (d, scale bar is 200nm) produced by EBL/ICP(RIE) method using SF_6/O_2 and HBr gases respectively.

For relatively thick membranes (250nm and more), the alternating Bosch process can be applied for the etching[41], which is preferable for the patterns with a high aspect ratio. Bosch process, also known as pulsed or time-multiplexed etching, performs alternately the etching (by SF_6) and the deposition of a passivation layer (for instance, C_4F_8), creating highly anisotropic etching profiles. However, this process may lead to a bigger roughness[41] (8 nm vs. 1.5-2 nm with EBL/ICP[19]) or even corrugation on the surface of the etched nanoholes. In some cases, such a situation may complicate the analysis of the experiment, particularly if the nature of the heat transport is under study. On the other hand, if accurately estimated with SEM/TEM techniques, varying roughness (or corrugation) can serve as a useful parameterisation addressing the issue of T-dependant dominant phononic wavelengths in nanostuctured region[7].

Most of the nanopattern processes described above (except the FIB method) have one common feature: the use of e-beam resist (polymer-based) mask layer, such as CSAR or ZEP 520 resists. The main requirements to e-beam resist in nanopatterning applications are high resolution and sensitivity, high stability in time and good plasma etching resistance[42]. Later in this chapter (paragraph 2.3.4), it will be explained in more details why CSAR[43] is preferable over ZEP and conventional PMMA, and some main challenges in e-beam resist usage will be covered.

Resist spin-coating is not the only solution to the etching mask implementation in a nanopatterning process. Due to the rapid development in nanofabrication during the last two decades, new classes of low-scale materials have emerged (quantum dots, nanowires, superlattice thin films). In particular metal nanowires (NW) opened a new possibility of creating a non-conventional (not resist-based) etching mask layer. Superlattice nanowire pattern transfer (SNAP) techniques translates nanoarray pattern from $GaAs/Al_xGa_{(1-x)}As$ superlattice into Pt nanowires array, and then Pt array as a mask gets deposited into silicon epilayer. In the simplest case the array of Si nanowires can be produced by a single SNAP. The other possibility is to overlap with some angle two SNAP arrays. This creates a nanolattice etching mask. In principle, a big variety of different lattice patterns are possible. On the figure below one can see how the square lattice of holes in Si can be produced with the help of Pt mask, obtained by overlapping of two SNAP Pt nanowires arrays.
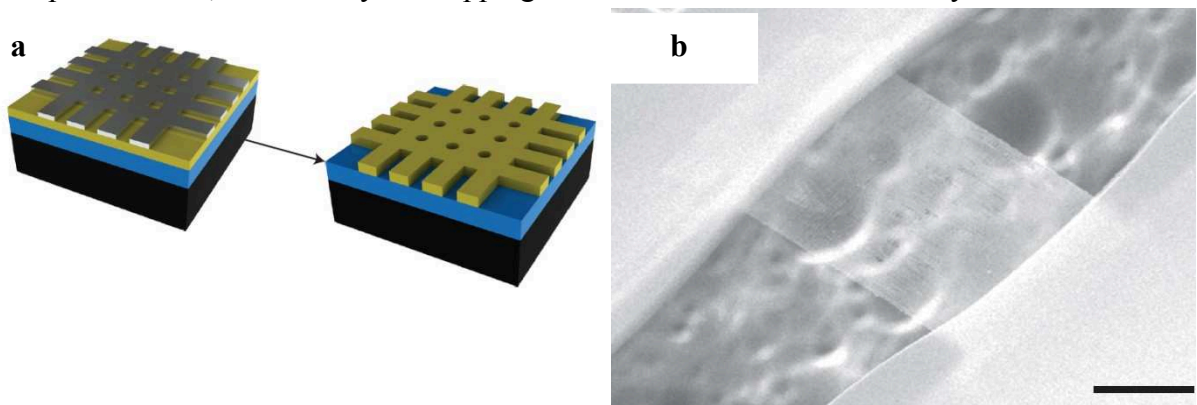

Figure 2.9
(a) Sketch of SNAP-fabricated Pt nanolattice mask (silver) on top of the SOI layer (yellow), on the left. Post-etching SOI layer on the right. (b) SEM image of fabricated nanomesh (NM) thin film with cylindrical holes of 11-16nm, scale bar is 200nm[44].

At this point it is important to note the following. Many practical applications may require phononic structures (like the ones presented in this paragraph) being produced inside of the SOI layer stacked on top of the BOX and handler layers (like in IC). However, most of the measurement techniques (and some applications as well) rather deal with suspended membranes due to the necessity of thermal isolation as was discussed in Section 2.1. The combination of nanopatterning and membrane suspension processes adds an additional complexity. In the next paragraph we will see some reliable techniques for plain and phononic membranes suspension.

2.2.3 Membrane fabrication techniques

The design of the experimental PhM platform (or device) can significantly depend on the type and configuration of the measurement technique. Moreover if we focus on particular methods of measurement, for example micro Raman thermometry (μRT), we will find different approaches regarding the choice of PhM's device geometry and structure. For example, considering μRT technique (see paragraph 3.1), the experimentalists may favour working with the beam-like membrane (for the purposes of thorough $\bar{\bar{\kappa}}$-elements characterisation discussed in Paragraph 2.1.1) or free-standing large-area PhM[41,45] (Figure 2.11). Large-scale membranes are easier in fabrication in terms of the processing steps, but require accurate treatment of the residual stress which manifests itself as a bulky surface. Good quality of the large-scale membranes are present below (Figure 2.10).
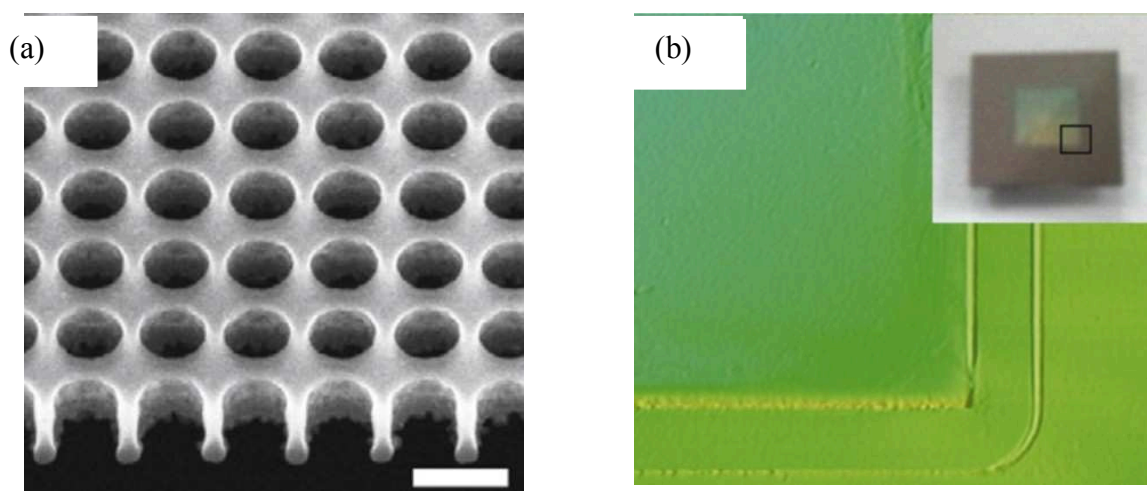
Figure 2.10
Taken from M. Sledzinska[41] et. al, laboratory of C.M. Sotomayor Torres (ICN2, Barcelona), scale bar is 300nm. (a) SEM image of a PhM (holes diameter = 220nm) produced by FIB on (b) free-standing large-scale membrane.

The other reasons, why one may prefer to work with large-scale PhM exploiting μRT are: (1) direct measurements of induced anisotropic temperature profile with two-lasers Raman setup (see paragraph 3.2.1; reconstruction of this profile is also possible with a one laser scheme, however requires additional modelling); (2) feasibility of direct absorption measurement due to back-side suspension geometry; (3) large-scale membrane has a potential to be used for demonstration of Si PhM applicability to thermoelectricity (See Appendix).

Figure 2.11
(a) 200 µm-long beam-like membrane (this work) and (b) 500x500µm large-scale membrane, fabricated by Di Zhou[46].
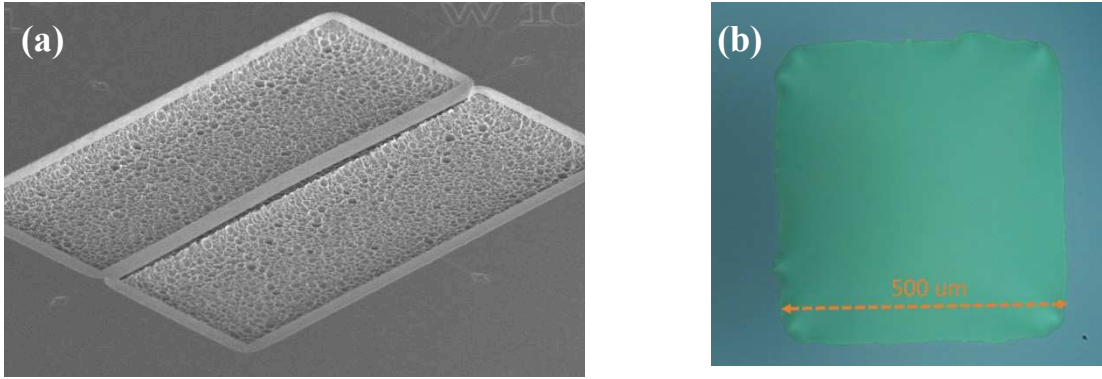
This thesis is dedicated to the fabrication and measurement of front-side suspended beam-like PhMs. Detailed comprehensive descriptions and instructions of fabrication processes for beam-like membranes are in the next section. In this paragraph we focus more on the large-scale membranes, that were just introduced above. This kind of membranes were fabricated in our lab by D. Zhou, and thermally characterized by the author (κ=58.8±12.4Wm^{-1}K^{-1} at the thickness of 157.5 ±0.3nm). These membranes are planned to be used in the perspective study in our group related to the anisotropic heat flow and its applications.

Until recently the release of large-scale membranes could be achieved via deep dry etching (Bosch process)[47] or wet etching[48] (with the use of common anisotropic Si etchants) from the backside surface of the SOI wafer, going through the handle wafer and the BOX layer. Anisotropic wet etchants, such as potassium hydroxide / Isopropyl alcohol (KOH/IPA) and tetramethylammonium hydroxide (TMAH) produce anisotropic trapezoidal-like cavities, whereas Bosch process is able to create highly anisotropic features. However for the relatively large cavity of suspended membrane, the anisotropy criteria is not crucial. The crucial property for membrane release is fabrication process speed, or a number of fabrication steps required for suspension (see table below). Backside suspension methods are generally faster (2-3 times in total fabrication time) than the front side membrane release, mainly due to the fact that just one mask-lithography step is sufficient for all etching operations. But the front side method (not counting the need for alignment markers fabrication) requires plus 1 lithography step and additional wet oxidation protection step (the details can be found in the next section).

Remark: an additional oxidation step (with 2 oxidation in total) for front side suspension was used for electrothermal device fabrication[49] in the preceding project. The main purpose of a double oxidation was to facilitate the control over the precision and the size of the membrane's thickness decrease. In the current work, wet oxidation for front side suspension is done only once due to a small initial thickness of the SOI layer.

Compared with conventional MEMS process	Number of fabrication steps					In total
	Wet oxidation process	Spin-coating	lithography (optical /e-beam lithography)	Plasma etching or KOH wet etching	XeF$_2$ etching and HF etching	
Front side suspension [1]	2	2	2	2	1	~4-5 weeks
Backside suspension [2]	1	1	1	1	1	~10 days
Our work	1	1	0	0	1	~4 days

Table 2.3 Fabrication process map
Figure courtesy: D. Zhou[46]. Conventional MEMS processes comparison for parameters of fabrication steps.

The novel approach of membrane release with femtosecond (400fs) laser ablation technique was developed recently (D. Zhou[46]). The need of 400fs pulses (of Diode-pumped solid-state DPSS laser in 343nm-mode) was motivated by the aim to have a good anisotropic etching profile, high resolution step and an absence of cracks inside the cavities' walls. Sub-ns (ps, fs) generation is capable of performing such a delicate ablation. This ablation mechanism involves the low heat penetration[50] (small heat-affected zone in sub-μm scale), that occurred at a high-power (0.1-3W) and short-pulse exposure[51]. The biggest part of the photons wave-packet gets absorbed by the atoms via multiphoton excitations. Such a process is also called "atomized vapor" or "cold ablation process" due to a very low heat penetration and a low temperature developed in the region around ablation spot (or microcavity).

The etching based on the cold laser ablation approach allows for even faster processing than conventional backside suspensions. The precision of the laser set-up motion mechanics combined with fs pulse time make possible the creation of the cavities from the back side of the membrane without any use of the mask layer, i.e. no lithography step at all (including auxiliary spin-coating and stripping steps). Only two passivation layers (resist and SiO$_2$) were deposited and one etching step was performed for the full suspension. Preliminary study shows the possibility of creating large-area Si membranes with the desired geometrical properties (thickness, surface area, different shapes) using fs-pulsed laser milling. The only drawback found during the characterisation of the first generation membranes was the slight buckling (with maximum amplitude 3μm) which occurred due to the lack of stress. This issue can be easily solved[20] by releasing additional strain (increasing the mechanical strength of membrane) via LPCVD-deposited Si$_x$N$_y$ frame[47].

2.3 Overview of the fabrication process

This section is devoted to the fabrication of the experimental phononic platforms (the design of which was described in Section 2.1). The focus is on experimental justification of the chosen fabrication techniques, and the main highlights of the quality improvements of phononic membranes. But before delving into the details of experimental platforms engineering, it is worth to take a brief overview of the whole fabrication process in its final tested version, indicating the most problematic parts of its development.

State-of-the-art "top-down" approach for experimental nanopatterned membranes consist of several steps, described in Figure 2.12 (Most of the processes on Figure 2.12 were introduced in paragraph 2.2.1). It comprises conventional clean-room laboratory techniques of Electron-beam lithography (EBL), Reactive-ion etching (RIE) and Low Pressure Chemical Vapour Deposition (LPCVD). The main challenges in fabrication arose in connection with anisotropic nano holes' patterns. At the design stage, two different e-Beam Lithography (EBL) machine modes were tested with the purpose of choosing an appropriate lithography method for nanoarray anisotropic patterning. It turned out that the advantageous fast DOFL (dots-on-the-fly)[52,53] technique, that was used efficiently for the writing of isotropic hole patterns, has a drawback for anisotropic patterning: the absence of specific algorithms in EBL set-up software which would allow for the design of smooth tilted geometrical shapes combined with anisotropic beam steps' sizes in DOFL-compatible modes (see paragraph 2.3.4). However, this drawback can be overcome in the future and requires some minor modifications from the side of the set-up manufacturer.

A search for optimal spin-coating thickness was performed. The experimental aim of keeping the diameter of the holes as similar as possible over the patterns (to maintain the same filling fraction) posed the need for EBL dose tests for each individual phononic pattern. These adjustments were needed to mitigate the difference in lithographic proximity effects occurred due to the variation of distances (pitches) between holes over the patterns. Cl_2 RIE etching recipe (step 2) and oxidation recipe (step 4) were thoroughly studied and calibrated in order to fully etch the holes and find an optimal protection layer. Special probe patterns were fabricated and processed with the aim of TEM structural characterization of nanoholes profiles.
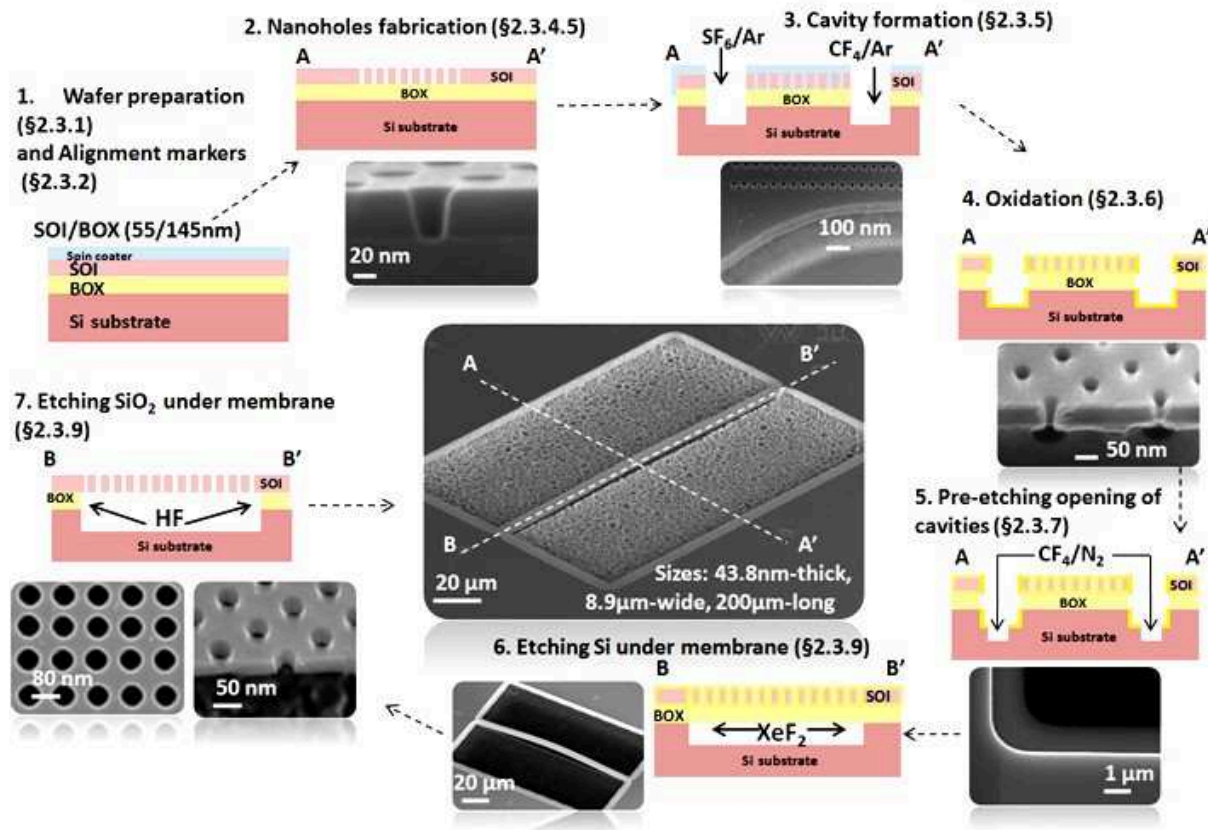
Figure 2.12
Fabrication process map of experimental platforms for the estimation of isotropic and anisotropic thermal conductivity. The references to particular paragraph, where the process is described, are given in parenthesis. Processes in short: 1) 55nm/145nm SOI/BOX wafer cut into the wafers of appropriate sizes (1' wafers in this work), small wafer is covered with a thin layer of CSAR resist (≈200nm) and processed with EBL (where each dose was adjusted for particular phononic lattice pattern); 2) RIE etching with Cl_2 gas of the holes pattern in Si SOI layer. 3) RIE etching of the cavities around the membrane; 4) LPCVD-oxidation of all Si surfaces with the aim of protection. 5) Oxide layer opening at the bottoms of the cavities. 6) XeF_2 etching of Si substrate under the membrane. 7) Final suspension of nanomembrane via HF etching.

2.3.1 The wafer preparation (cutting and layout).

Commercial SOI wafer was used (see table below for details) fabricated by Soitec (Commercial part: G8P-131-01).

Property	Value	Units
Si crystal orientation	(100)	
Diameter	200	mm
SOI thickness	55±7.5 (±3σ)	nm
BOX thickness	145±2 (±σ)	nm
Wafer thickness	725	μm
Doping type	p (Boron)	
SOI resistivity	8.5-11.5	Ω cm
Carrier concentration	0.7-1	10^{15} cm^{-3}
Manufactured	Soitec	

Table 2.4
SOI wafer characteristics.

According to the general process line in our lab, 200mm SOI wafers are usually cut into 4 standard 3" (d=76.2mm) wafers, which geometry fits clean room fabrication equipments (EBL set-up mainly). The cut was done with the use of nanosecond laser (351nm; cutting parameters: 6W, 50% attenuation, speed = 30mm/s, 18 cycles).

An unfortunate quality problem occurred during RIE-Cl$_2$ nanopatterns etching, when 3" wafers were used. This situation will be discussed in Paragraph 2.3.4.4. The problem limited the wafer sizes that can be processed without inacceptable defects. For this reason 1" wafers were used for processing dose tests and the fabrication of working samples. The figure below demonstrates combined multilayer lithographic layout for 1" wafer design. The layout includes 4 identical experimental cells described in Figure 2.14.
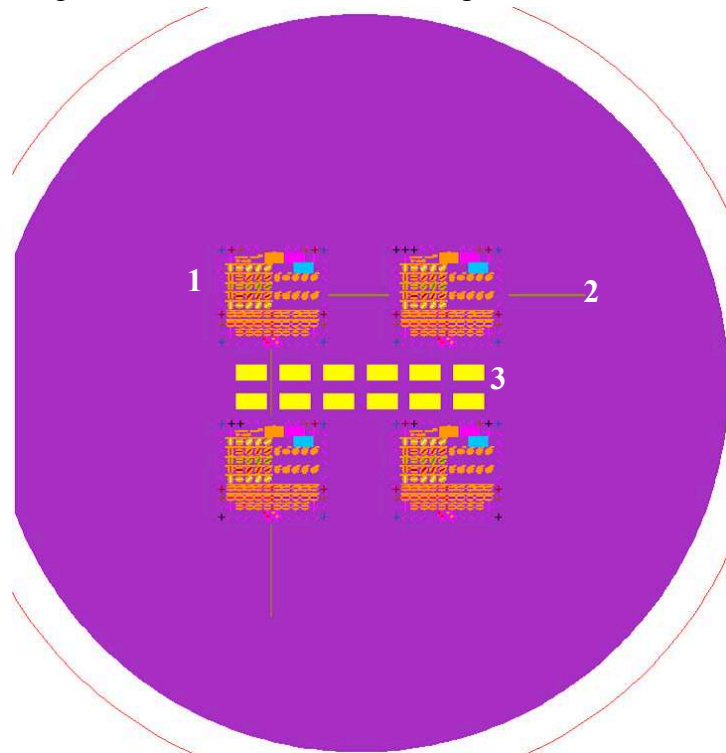

Figure 2.13

Combined EBL layout of 1' wafer consisted of 4 experimental cells (№1) paved with phononic measurement platforms, 3 probe lines (№2) for phononic profiles SEM quality test, array (№3) of end point detection (EPD) cavities for nanopatterning RIE-Cl$_2$ etching.

Large area end point detection (EPD) cavities (№3 in Figure 2.13 and №1 in Figure 2.14) are used as reflection platforms for monitoring the thickness of the etched layer (layers). Monitoring is based on laser reflection signal analysis. The intensity of reflected light vs. etching time is the combination of the multilayer interference patterns' changes. It is possible to analyse the change of reflection signal combined with the layers dielectric and geometrical parameters, in order to estimate the thickness of the upper layer during the etching. Characteristic EPD patterns for particular etching process can be found in the following paragraphs. The concept of the probe lines (№2 on Figure 2.13), that facilitate SEM monitoring of the holes profiles, is discussed in the next chapter.
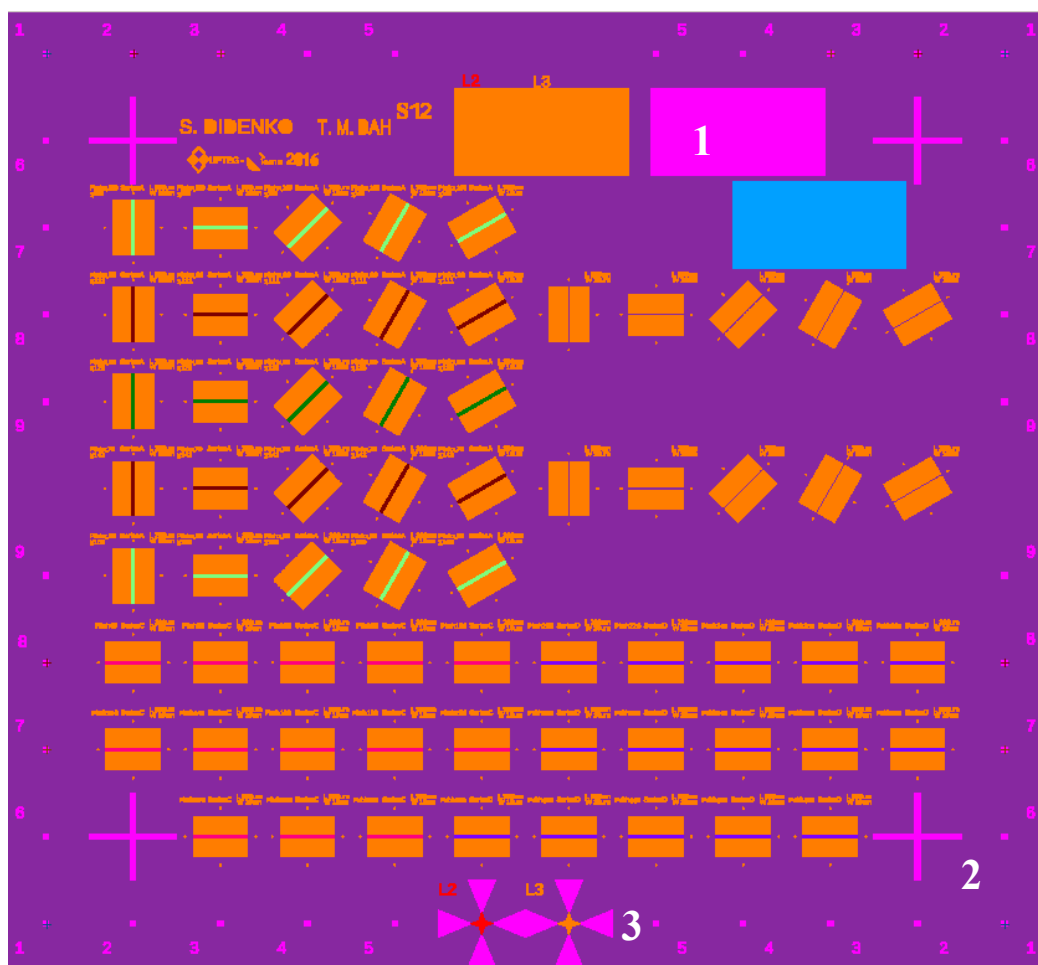
Figure 2.14

Combined (over 4 etching processes) EBL layout of a single fabrication cell containing phononic measurement platforms with beam membranes perforated by anisotropic and isotropic nanoholes lattices. Layers correspond to 4 etching processes: 1) alignment marks etching (violet marks around the border (№2) of the cell; 2) nanolattices etching over the area of the membranes (narrow stripes between orange rectangular shapes, different colours correspond to different EBL doses, discussed in the paragraph 2.3.4); 3) cavity openings (coincide with orange rectangular shapes); 4) oxide passivation layer opening at the bottoms of the cavities combined with membranes labels' etching (all orange features). Membranes lattice patterns were described in paragraph 2.1.4. Three end point detection EPD (№1) rectangular cavities (correspond to four etching procedures). №3 indicates alignment quality indicators patterns.

2.3.2 Alignment markers

Alignment markers are auxiliary etching patterns (seen as violet features around the cell perimeter in Figure 2.14). Mainly they are needed for the sample alignment during EBL processing. The alignment procedure is crucial for fabrication processes requiring more than 1 fabrication step. The sensitivity of EBL localisation method defines markers geometry. In our case, EBL contrast localisation was used. This method requires deep alignment markers, at least 1.5 μm. The second purpose of the alignment markers is to check how precisely the successive etching steps were performed. For this, the alignment quality indicators (Figure 2.14, №3) of the first (alignment markers') layer are designed in such a way that the etching of the next layers creates complimentary indicators (red and orange inners diamond patterns). Sharp endings of indicators allow for optical and SEM tests, to assess the mismatch size. In this work acceptable indicators mismatch threshold was around 200nm.

The table below includes all the principal procedures for alignment markers fabrication. As usual, the first step is a spin-coating. Used "COPO EL-13% MMA 8.5" spin-coater is based on PMMA resist. Polymethylmethacrylate (PMMA) is a conventional positive-tone resist widely used in the industry, it has a high-resolution in EBL. The large number of options was developed for its usage. Some modifications have been proven to be more stable: for example, copolymer of MMA (methylmethacrylate) and MAA (Methacrylic acid) which have a higher sensitivity[54] (i.e. lower dose, and faster exposure) were used in our fabrication processing. Typical clean-room PMMA developer and stripper were applied for MMA copolymer resist: MIBK (Methyl Isobutyl Ketone) and PG-remover (based on N-Methyl-2-pyrrolidone (NMP) solvent) respectively. The same combination of resist, developer and remover (with some minor recipe modifications) was utilised prior to the etching of the cavities and bottom SiO_2.

Some EBL doses (for MMA 8.5 copolymer) were calculated in Sceleton™ (Synopsis®) software which uses Monte Carlo simulation. The idea is to find optimal EBL doze accounting for proximity effects, whereby electrons from closely packed exposed resist regions penetrate into the neighbouring regions enlarging their area and decreasing the contrast of the etched features.

The end point detection mechanism, mentioned in the previous paragraph, allows for the monitoring of the reflection signal change during the etching. This signal has specific features that correspond to the etching of a particular layer. The features help to know when the recipe has to be switched for the one of the next layer. For instance, a sharp drop of the signal (Figure 2.15, left) indicates that Si (SOI) layer is almost etched. Another important indicator is that when the SiO_2 (BOX) layer is consumed, the signal becomes constant (saturated line).

Table 2.5
Alignment markers fabrication.

№	Procedure	Specifications
1	**Spin-coating**	Resist: COPO EL-13% MMA 8.5. Expected thickness ~ 2 μm. Pre-processing: hot plate preheating at T= 80°C for 1 min; cooling to RT for in 1-2min. Speed=1000rpm; acceleration = 1000rpm/s; duration=12s. Temperature ramping: 80°C-180°C with 8°C/min changing rate, with 1min waiting stops at each 20°C step; final stop at 180°C for 10min. Hot plate is closed.
2	**Profilometry**	Thickness check with mechanical profilometer. Values: thickness at the top of the wafer = 1840 nm; thickness at the bottom = 1945 nm.
3	**EBL exposure**	Dose = 450 μC/cm², Current = 25 nA, Resolution = 25 nm
4	**Development**	Developer: MIBK+IPA (30ml/60ml). Time = 1min with 100rpm agitation. Post-development: 30s IPA rinse, nitrogen blow dry.
5	**Dry-Etching**	1) Etching of ≈50nm SOI layer: SF_6 flow = $10cm^3$/min, Ar flow = $10cm^3$/min, Pressure = 10mTorr, Power=30W, t ≈ 1min. 2) BOX Etching (≈145nm): CF_4 flow = $40cm^3$/min, N_2 flow = $40cm^3$/min, O_2 flow =$5cm^3$/min, Pressure =10mTorr, Power=100W, t≈14.5min. 3) Etching of Si Substrate: SF_6=$10cm^3$/min, Ar flow =$10cm^3$/m, Pressure=10mTorr, Power=30W, t≈10min. Expected depth ~ 1.5 μm.
6	**Stripping**	UV exposure for 20mins. Wafer immersed in preheated PG-remover at 65°C for 2h. Cleaning: acetone rinse; IPA rinse; nitrogen dry blowing.
7	**Profilometry**	Depth check with mechanical profilometer. Cell №1 thickness = 1600nm; Cell №4 thickness = 1630nm.

The etching recipes utilised here were verified by M. Haras[49]. It was shown that, despite the fact that SiO_2 etching rates (ER) for SF_6 and CF_4 are similar (≈10.5 nm/m), the use of CF_4 has advantages such as: 1) CF_4-based recipe yields more anisotropic etching; 2) SF_6-based recipe for SiO_2 etching does in parallel noticeable and unnecessary lateral etching of SOI layer (due to high SOI sensitivity to SF_6: $ER_{SF_6}^{Si} \approx 7 ER_{CF_4}^{Si} \approx 70 nm/m$. Thus, CF_4 gas is used in this and following processing steps as the main BOX etchant.
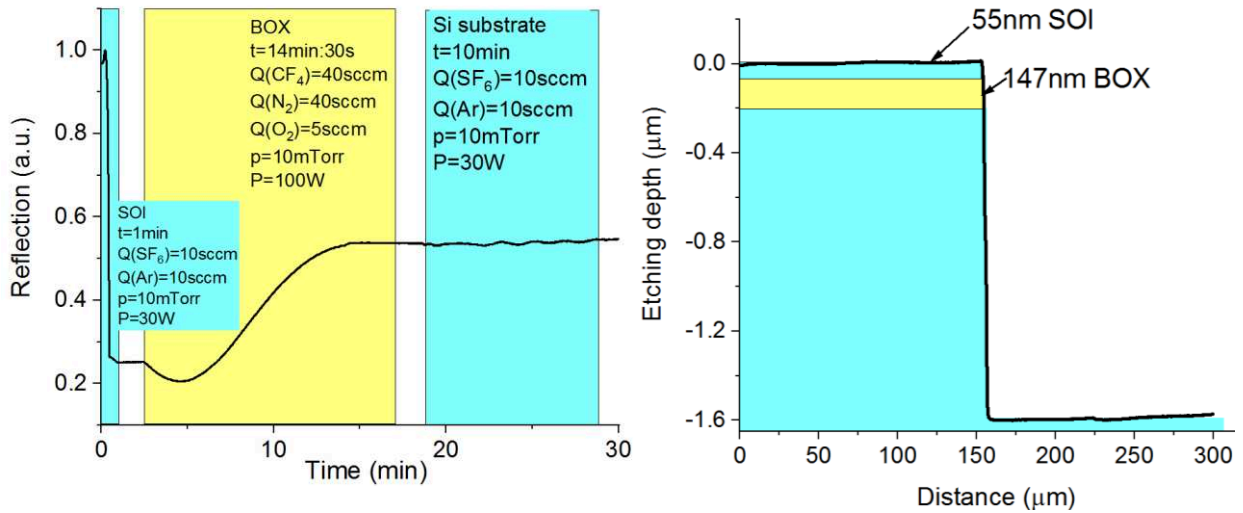
Figure 2.15

EPD reflection signal vs. etching time (left) with colour blocks indicating specific layer during the RIE etching of the alignment markers in SOI, BOX and substrate layers. Layers' borders are defined by specific patterns of the signal. Blank spaces between the blocks indicate gas venting procedure, when plasma circuit is not active. Corresponding etched profile (right, solid thick curve) of the alignment marker cavity (EPD platform) obtained as a result of the etching.

2.3.3 New method for the quality assessment holes with the tilted lattices cleaving

The fabrication of suspended beam-like membranes (using front side etching) is a long process, it goes through dozens of fabrication operations. In the case of phononic membranes, it is not reasonable to proceed with membrane suspension, if the quality of the perforated holes, processed at the very beginning, is not known. The practice has shown that the fabrication of holes is the most difficult step, since it involves the highest resolution of electron beam lithography and there is no way to obtain the direct end point detection signal during the etching on a feature smaller than 300nm.

Unfortunate fact of non-satisfactory hole quality was obtained *a posteriori* membrane fabrication in the preceding work[21]. It was discovered with the help of TEM (transmission electron microscopy) scans (Figure 2.16c). Applied TEM characterisation requires auxiliary FIB (focused ion beam) cut of the microsample (lamela). TEM-FIB is a powerful technique for roughness estimation, native oxide and contamination monitoring, because the images can be atomically resolved. However if one needs to assess holes profiles quality many time during the dose tests etching, this approach is not well suited. Another technique, AFM (atomic force microscopy), was not able to estimate holes profiles (Figure below, d).

There was a strong need for a novel method which allows fast and reliable checking of the quality of phononic nanovoids right after their fabrication.

Observing a fragment of phononic membrane on Figure 2.16b, it is reasonable to suggest as a solution the removal of membrane margins. In principle, some hole profiles can be seen even right after the cavities etching in this case. But still the approach requires at least one EBL-RIE cycle. Moreover, this idea was considered as objectionable due to oxidation difficulties that could arise when sharp features are formed on the edges of the membranes. It was decided to ignore this suggestion. However during the fabrication, due to slight

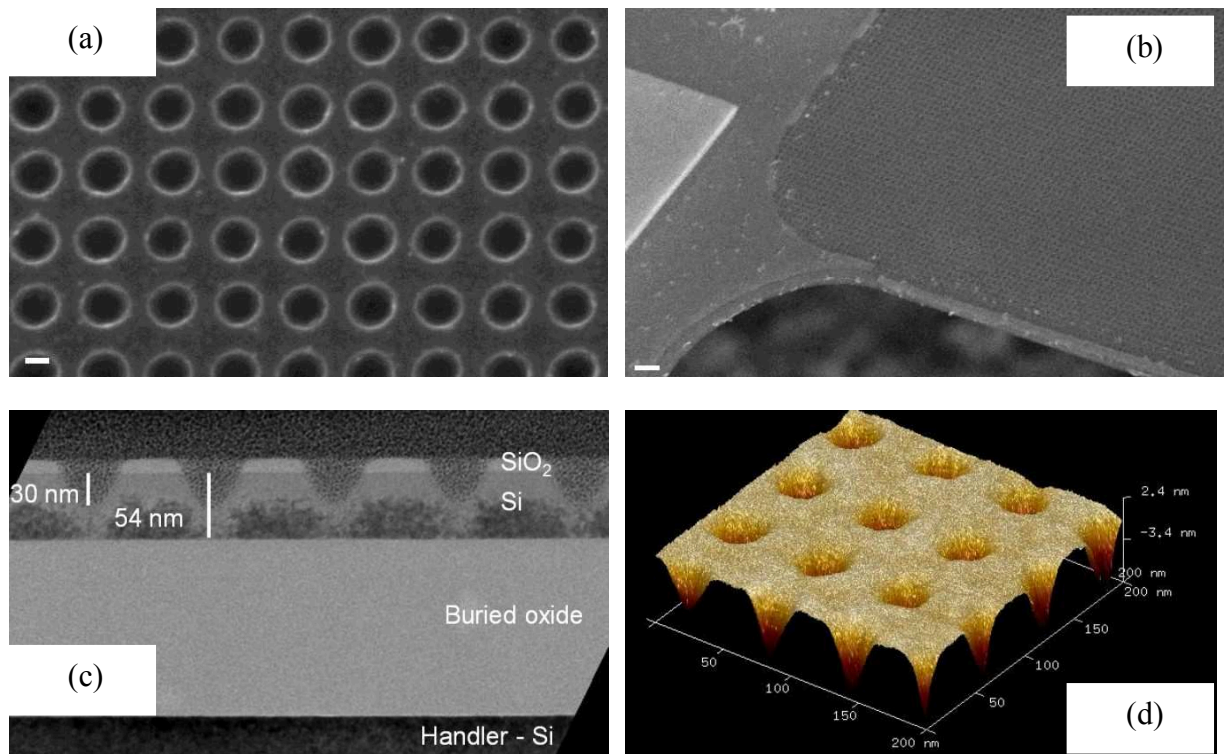unintentional overetching, this idea was proven to be feasible, as will be shown in the next paragraphs.

Figure 2.16

SEM images of 60 nm pitch isotropic PhM created by V. Lacatena[21] during the first stage of UPTEG project: a) top view scale bar = 20 nm; b) side view of the suspended PM, scale bar = 200 nm. c) TEM scan (obtained by STMicroelectronics) of non-suspended membrane fragment demonstrating that holes are not fully etched. d) AFM image of surface topography, defined the roughness of 0.20nm, but not the hole profile depth.

Fortunately, a fast and reliable method was found. It was tested and utilised. It is based on the cleaving of the Si SOI sample along crystallographic planes (110) or (100). The key idea is to design the stripes with phononic lattices, when the lattice axis is at a sharp angle (Figure 2.17b) to the cleaving plane (30 degree proved to be a good choice). Tilted orientation of the lattice and the cleaving plane makes it highly possible that there is a handful of holes on the edge of the SOI layer, and what is more important the cleaving plane cuts some of those holes along their diameter (Figure 2.17d). Thus we can estimate the diameter of the etched holes at the top and at the bottom. Although it is a little chronological over jump in the narration, it is worth to see the final result based on this methodology to grasp the idea. The point is that the verification of many EBL and etching dose tests, which were preceding to successful outcome shown on Figure 2.17cd, was based on multiple profile checks obtained with the help of the presented approach. The next paragraph is a short story about how the etching and EBL doses were derived via experiment.
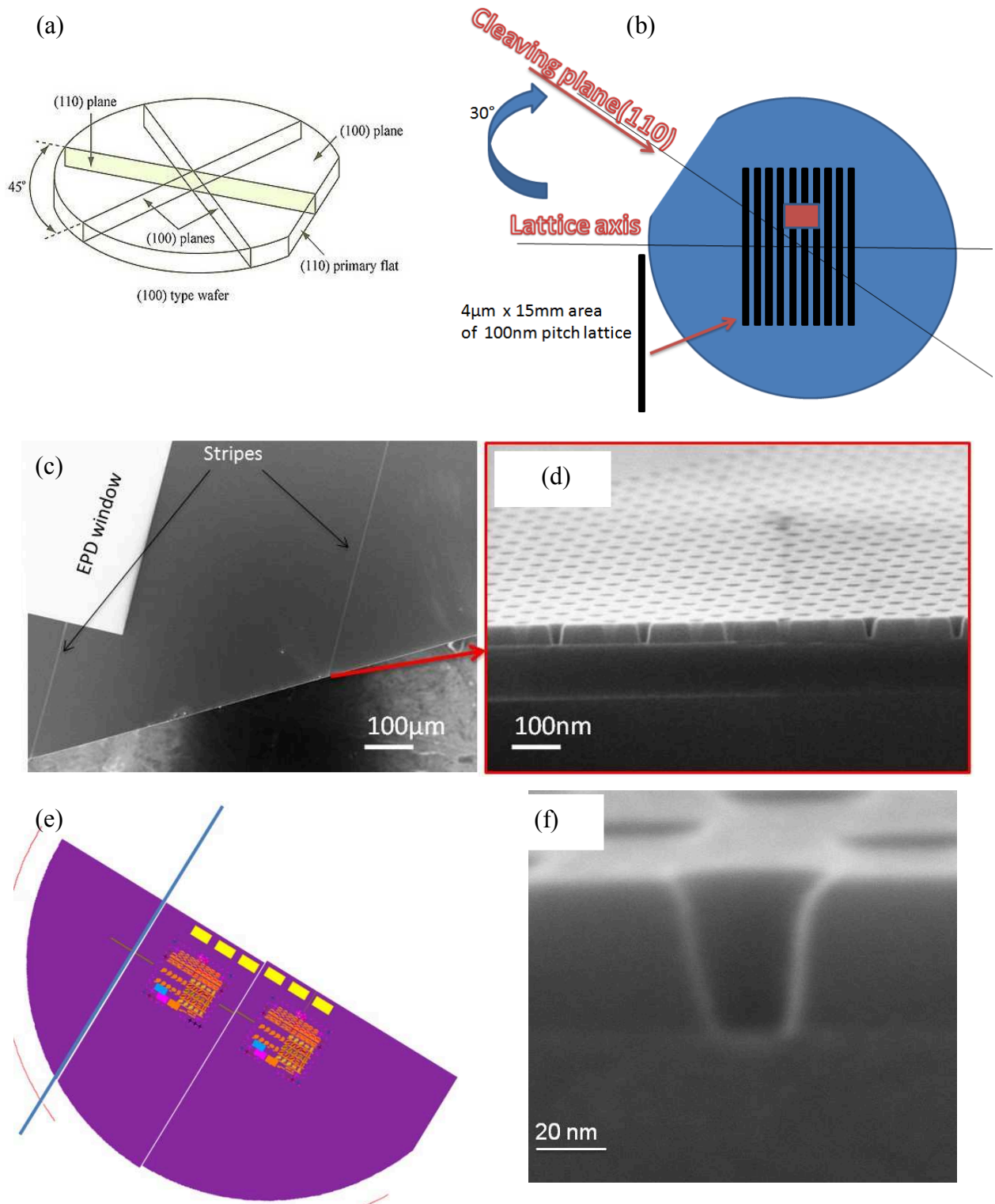
Figure 2.17

The method of the etched holes quality monitoring: a) main Si crystal planes related to the (100) SOI; b) key principle of the method: stripes of phononic wholes are etched with a 30° angle to the cleaving plane (big red feature at the centre is EPD platform); SEM images with c) the etched stripes of holes' lattice; d) close view of the holes at the cleaving edge with their well observed profiles and diameters, notice that the principle axis of the holes' lattice form a sharp angles (30°) with the cleaved edge. (e) Layout demonstrating how this idea is implemented in a wafer, which is cut along the blue line, across the stripe with the holes. (f) SEM high resolution image of one of the holes seen in the image(d).

2.3.4 Nanopatterns engineering.
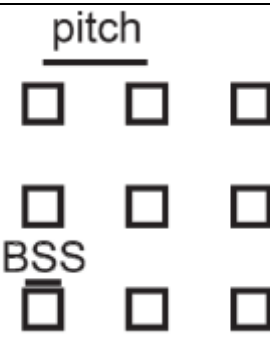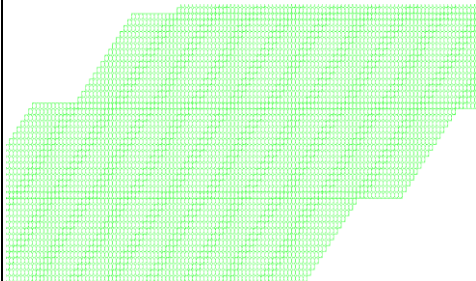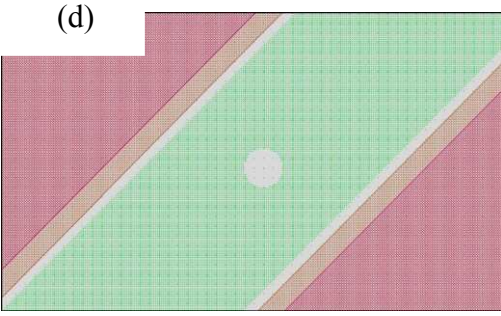
2.3.4.1 Choosing appropriate EBL technique

An important preliminary task for anisotropic nanoarrays patterning is the choice of an appropriate lithography method. Different EBL modes (regimes) can be applied for nanodots arrays exposure[52]. An emerging technique called "Dots on the fly" (DOTF) drew attention recently, allowing the increase of the writing speed by up to 3 orders of magnitude compared with the conventional approach. The key idea is to decrease or get rid of the overhead time, which is the delay caused by pattern generator (EBL instructions processor) readjustment between two successive features. An example is shown on (Figure 2.18b), each square can be viewed as a smallest possible feature, it is a smallest resolution which is equal either to machine Beam Step Size (BSS) or to the smallest pixel in a layout program. If one, for example, needs to write a small lattice of 9 holes, the pattern generator has to readjust 9 times. Whereas for the DOFL approach this lattice is written as a single feature, with a single pattern generator launch. The lattice writing is possible in this mode because actual beam size is around 10 nm regardless of what BSS is. The formula below clarifies this idea. Overhead term in the conventional approach can be by order of magnitude higher than the actual writing time (left term).

$$t_{\text{exp/dot}} = \frac{(dose * area)}{current} + t_{\text{overhead}} \quad (14)$$

It turned out that the advantageous fast DOFL technique, that was used efficiently for the writing of isotropic hole patterns[53], has a drawback for anisotropic patterning: one has to create the layout with different x and y beam step sizes (BSS). Such an option is not supported by the Beamer software (which interprets layout design as the e-beam machine code), thus one has to design manually the features with unequal BSS modifying machine code. At the time of this fabrication work the so-called "trapezium" mode was the most feasible option for the tilted membranes layout (Figure 2.18c), and its outcome was not satisfactory compared to the smooth layout obtained by the conventional methodology (easily done using Boolean operations in LayoutEditor software). Besides the unwanted rough edges of the tilted membranes (designed with the purpose discussed in Section 2.1) it was difficult to obtain a symmetrical unpatterned platform (white round zone with diameter of 2μm) seen on Figure 2.18d. This platform is placed in the geometrical centre of the membrane. It was planned that the laser heating beam during the μRT measurements shines directly onto the platform. The purpose is to avoid absorption being perturbed by the presence of phononic holes lattices (details are in Paragraph 3.2.7).

The first conventional EBL dose tests performed for anisotropic phononic patterns showed that the writing time per membrane is around 3 seconds, and varies slightly depending on the charge dose. This timing is satisfactory for my experimental layout. Thus it was decided to proceed further with the conventional method. To reach high pattern resolutions, the "overdosing" approach was used which implies high dose (test range: 90000 - 340000 $\mu C/cm^2$) and low current (300 pA) combination. This ensures high pattern resolutions for the smallest square features with the size equal to BSS (2 x 2 nm^2). Resultant holes diameters are proportional to the impinging dose.

EBL → modes	DOFL	Conventional
Writting principle	(a)	(b)
Layout of expected result	(c)	(d)

Figure 2.18

Comparison of DOFL (a, c) and Conventional (b, d) EBL writing principles (upper row) and their layouts' smoothness (bottom row) for the same tilted membrane (45°), where c) "Trapezium" mode anisotropic layout is done by manual coding for DOFL method; d) conventional anisotropic layout done in a graphical interface of LayoutEditor.

Thanks to lithography tests, it was confirmed that the EBL machine (Vistec EBPG 5000+[55]) is able to write anisotropic phononic patterns in DOFL mode using different BSS in x and y directions. It is important to note that the geometrical drawbacks described here, which are attributed to tilted anisotropic features, generated for DOFL approach, seems to be a solvable software problem, that requires the involvement of the manufacturer. There is yet another perspective approach called "Sequence" (its development requires deep software modifications and was under development at the time of PhM fabrication), which combines in itself both high writing speed of the DOFL method and the layout flexibility of the conventional method.

2.3.4.2 Preliminary CSAR62 resist tests

Fabrication of nanoholes lattices demands thin resist with high plasma etching stability (for higher contrast) and low EBL sensitivity (for a faster EBL writing). Until 2014 ZEP520[56] polymer (by Japanese manufacturer ZEON) was the best choice for EBL low resolution tasks. Due to high prices of ZEP520 the need for a cheaper and more efficient competitor led to the development of a novel powerful resist, synthesised by Allresist.

CSAR62 (AR-P 6200)[43] is based on the copolymer composed of chloromethyl methacrylate and methylstyrene, dissolved in a safer solvent called anisole. Like ZEP520

CSAR62 is twice as sensitive as PMMA-based resist, and has a higher etching resistance compared to PMMA. Comparative study[57] of CSAR62 and ZEP 520A in respective native developers showed, that both reveal excellent structural resolution and comparable dose sensitivity (although CSAR62 is more sensitive). However, the contrast was twice higher for CSAR62 when developed with AR600-546. This concludes that CSAR can compete with ZEP resist.

The first test for holes fabrication was aimed at defining the etching rate of CSAR resist V_{CSAR}. This value depends on many parameters of the etching plasma. But for the starting point the test was done for the set of values, used with the ZEP520 resist for nanopatterns of the previous work (Figure 2.16): Cl_2-RIE with 30 sccm, 5 mTorr, 30 W. It turned out that the etching rate (taken as a ratio of initial and final thickness difference and etching time $V_{CSAR} = (T_{after} - T_{before})$/etching time) is ≈ 39 nm/min, which were confirmed by EPD signal (detecting the time of half oscillation of interference EPD signal ($\lambda/2n$)/etching time, where n is CSAR refractive index) estimation equal to ≈ 38 nm/min. It is important to note that this was done for a large 3" wafer. Taking into account the etching rate of the Si SOI V_{SOI} (for the same set of parameters and the same wafer), being of 50nm/min, and the thickness of SOI ≈ 55nm, one may target for 120nm thickness of the CSAR layer: when at least $\approx 2/3$ of the resist thickness (≈ 80nm) remains as a protection until the end of the etching. Thicker resist is harder for EBL and developer processing because the sizes designed features are below 50nm.

Spin coating thickness of CSAR62 depends on spincoater parameters and concentration of diluent. Optimal concentration of Anisole (1:0,5) was chosen and the thickness as a function of spincoater frequency at constant acceleration (1000rpm) and time (15s), was estimated and shown on figure below.
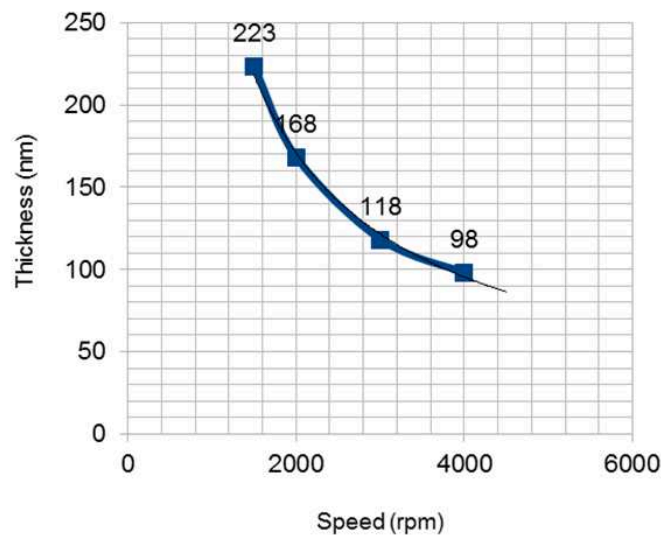

Figure 2.19
Plot courtesy: Pascal Tilmant (IEMN). Reflectometry measured CSAR62/Anisole(1/0.5) thickness as a function of spincoater speed (rotations per minute). Experimental points fitted with hyperbolic function.

2.3.4.3 **EBL dose tests. Anisotropic dose choices.**

3" SOI wafer covered with 120nm CSAR62 layer was planned to be EBL-exposed according to the dose test layout (Figure 2.20a). Each cell consists of identical series of stripes with phononic patterns. Green stripes correspond to anisotropic pattern (Figure 2.20b) designed according to specifications present in Table 2.2 (Paragraph 2.1.4). The blue stripes are anisotropic series analogous to the previous one, but with 150nm basic patterns instead of 100nm. Other patterns are isotropic, having a range of pitch from 60 to 500nm.

After resist development by AR600-546 solvent (which ensures the highest contrast according to the specifications) SEM observations (Figure 2.20c) were performed, which demonstrated, that the charge effect accumulated on the resist surface does not allow for the accurate assessment of the feature sizes, making the images blurry. The Figure shows the same fragment of 60nm pitch pattern that was scanned with half a minute time interval and the same settings. To the contrary, when stripped, SOI surface is well suited for SEM analysis (Figure 2.20d), which is comprised of two stages. The first is a visual estimation of SEM scans with different doses. We select doses which lead to the smallest neck size (smallest distance between two holes), but without overlapping of holes.

Figure 2.20d demonstrates comparison SEM images for two kinds of anisotropic series patterns: the dense patterns, identical to the series from Table 2.2 with 100nm pitch in the isotropic basic pattern, and the sparse patterns, where the basic pattern pitch is 150nm and all the anisotropic patterns pitches are scaled proportionally. For the dense patterns the range of acceptable dose spans from 200 to 320 mC/cm^2. At this point, it was decided to choose anisotropic series with the denser patterns, since the sparse patterns (with 150nm basic pitch) require doses higher than the limit of the performed test, and hence longer writing time.
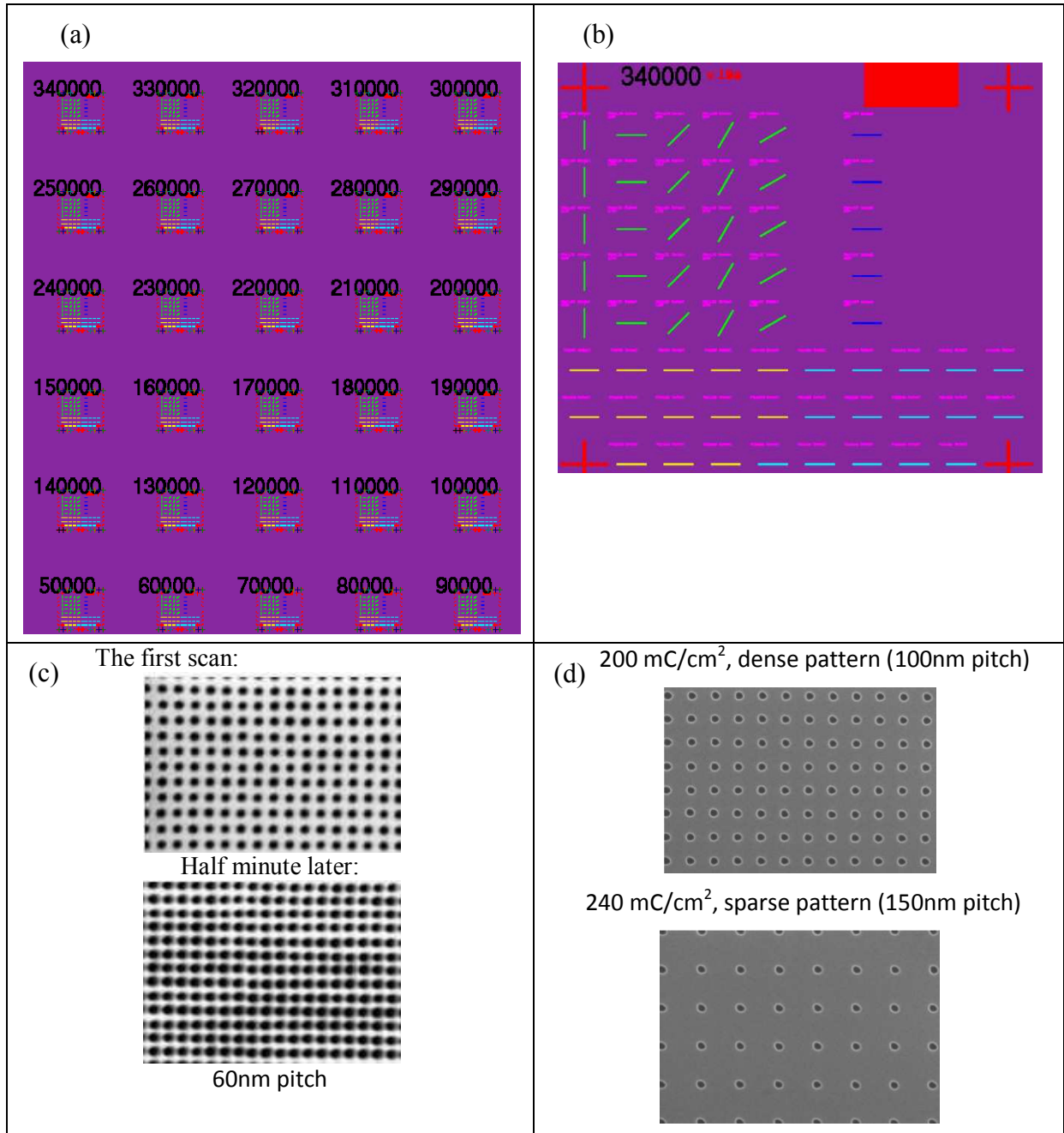
Figure 2.20
EBL dose test layout for all planned configurations of the membranes' patterns: a) 3" SOI wafer cells for different exposure values from 90000 to 340000 $\mu C/cm^2$; b) Anisotropic (green and blue stripes) and isotropic (all others) patterns in one cell. c) Post development SEM scans of 60nm pitch patterns exposed with 240 mC/cm^2, demonstrating charging effect distortion over time due to resist d) Dense and sparse patterns after Cl_2 etching, resist is stripped.

The second stage of SEM patterns analysis deals with anisotropic patterns. As was discussed in Section 2.1, the purity of experimental comparison requires the filling fraction to be constant (or as similar as possible) for different anisotropic configurations. With this in mind statistical estimation of the radiuses of the holes was done using SEM scans of stripped SOI surface. The figure below demonstrates screenshots of the same 100nm pattern with statistical filters applied to it in ImageJ[58] program, which helps to evaluate averaged radius of the holes: the first inner radius is attributed to the black circles and the second one

corresponds to the circles formed by the outer rims of the white shells. It will be shown later that these circles correspond to the openings at a bottom and a top of SOI layer (for the case when the holes are fully etched). In what follows in this paragraph for simplicity we take only radius of the big circle (white shell rim) into consideration.
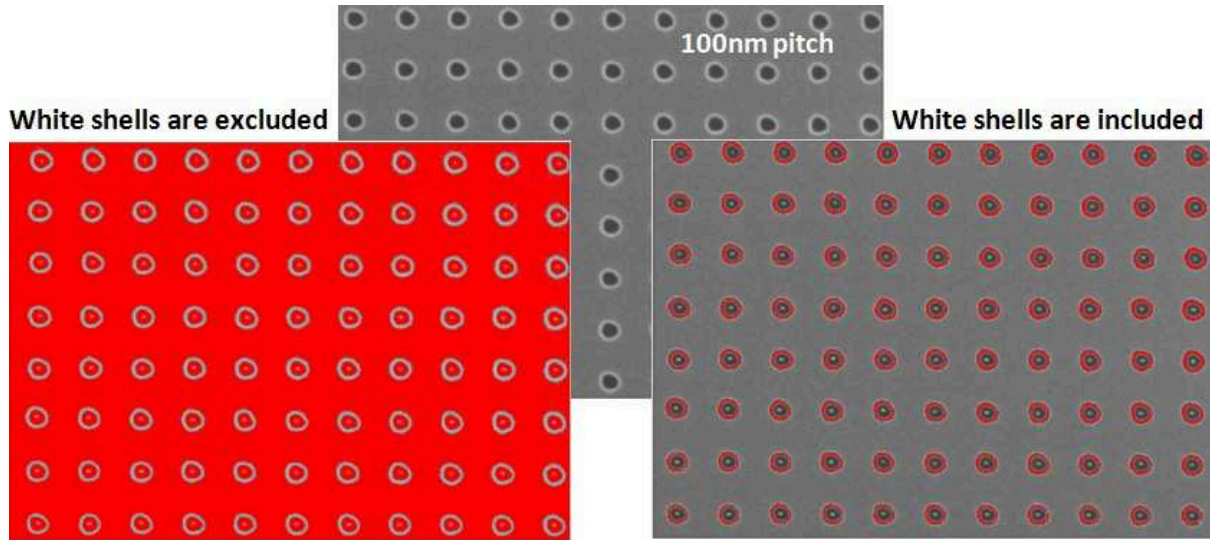
Figure 2.21
Statistical estimation of inner and outer holes diameters with the use of ImageJ[58] software for 100nm pitch phononic lattice. Averaged inner (black cycle) radius = 14.7 ± 0.2 nm, and outer (white shell is included) radius = 20.9 ± 0.4 nm.

Figure 2.22
Radius vs. pitch ratio for 200 mC/cm^2 dose and corresponding SEM images used for statistics. The line is a guide to the eye. Patterns were produced by conventional EBL writing on 55/145 SOI wafer with the use of CSAR resist, and Cl$_2$ RIE. EBL parameters: lattice of 2x2 nm squares in layout, low current (300pA), V=100kV.

Although the current sample was not fully etched, the comparative statistical dose analysis based on the top radiuses (white shell rim) will be valid for fully etched membranes.

Following the same approach we estimated radius mean and standard deviation in the dose range of interest (200-320 mC/cm^2) for 5 pitch ratio. Statistics shows that anisotropic membranes with different ratio (Figure 2.22), when exposed to the same dose, have different radius. We observe the same W-shaped pattern for each dose. Radius increases in proportion to the dose. Finally, for each pitch ratio appropriate dose was chosen in such a way that all the patterns can have the same radius (within statistical error).
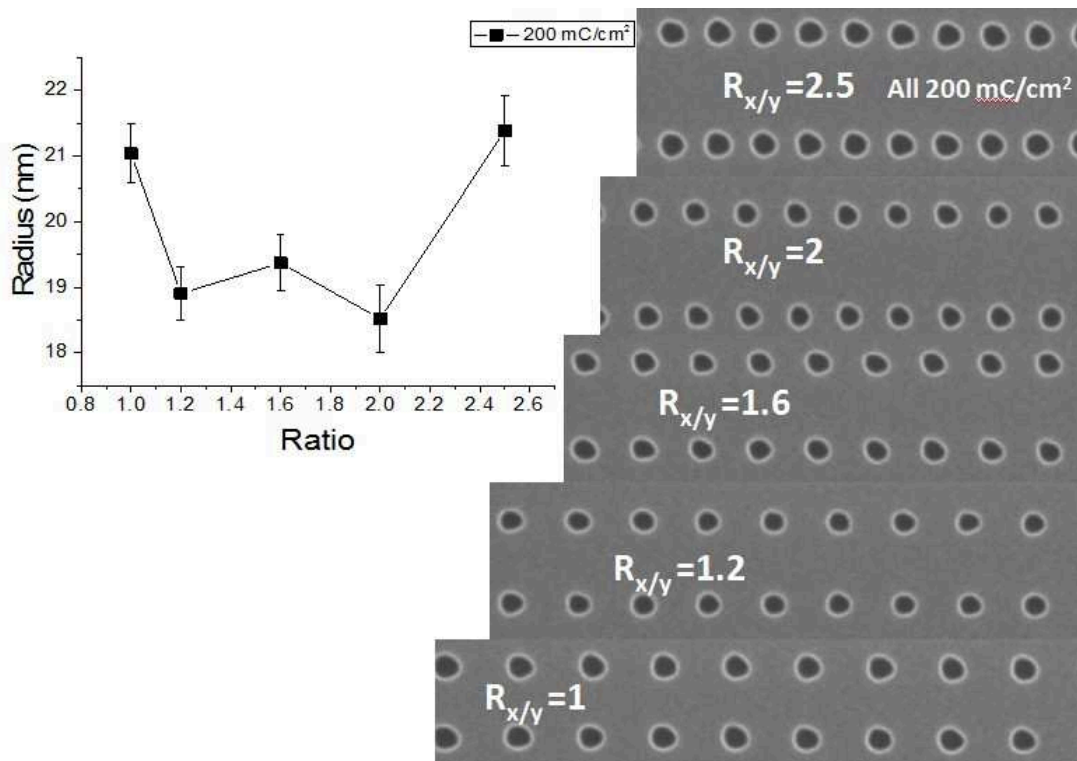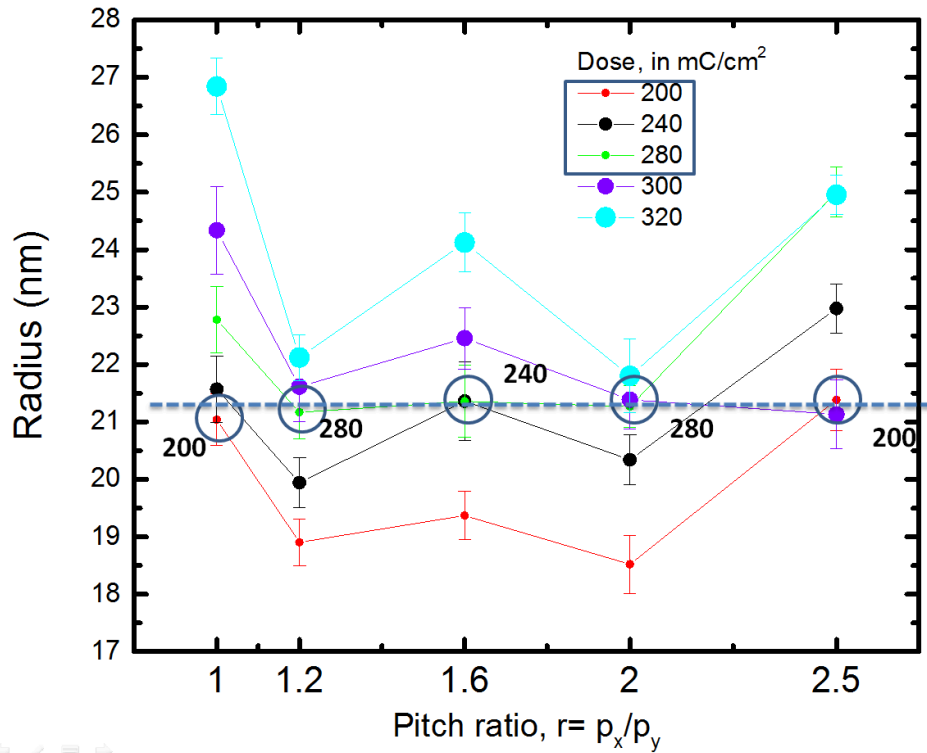

Figure 2.23
Statistical results of EBL dose test for five anisotropic lattice patterns (lines are guides to the eye), produced by conventional EBL writing on 55/145 SOI wafer with the use of CSAR resist, and Cl$_2$ RIE. EBL parameters: lattice of 2x2 nm squares in layout, low current (300pA), V=100kV, varying high doses. Favourable doses are highlighted with hollow circles and the frame on the legend. Error bars are equal to one standard deviation value.

Figure 2.24 demonstrates the mixed dose set of anisotropic membranes, where both visual and statistical picture show improvement (compared to Figure 2.22): radius can be approximated to be the similar within the error bar of ±1nm.
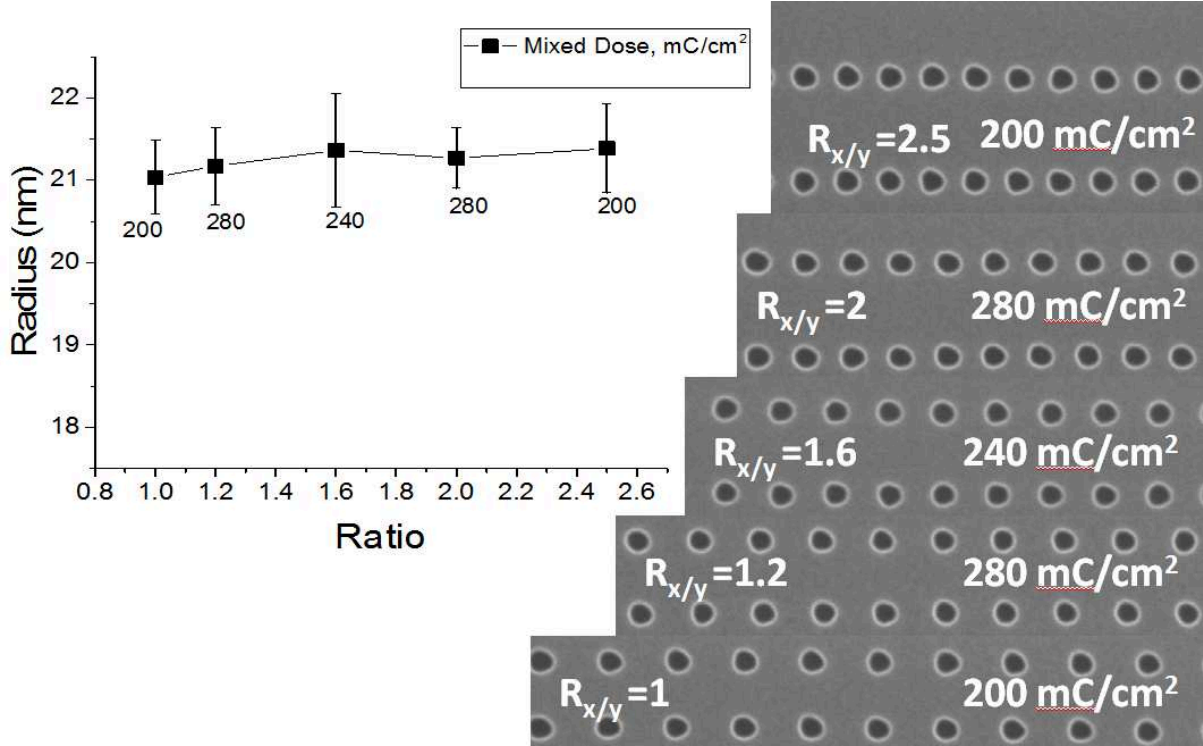
Figure 2.24
Radius vs. pitch ratio for the mixed dose and corresponding SEM images used for statistics. The line is a guide to the eye. Patterns were produced by conventional EBL writing on 55/145 SOI wafer with the use of CSAR resist, and Cl_2 RIE. EBL parameters: lattice of 2x2 nm squares in layout, low current (300pA), V=100kV.

2.3.4.4 Holes etching improvement.

The final experimental step in the recipe derivation of nanopatterns was dedicated to the improvement of the holes profiles. The cleaving methodology presented in Paragraph 2.3.3 was utilised as a probing technique. In order to save SOI wafers surface, 1" wafers were used for the etching dose tests. It turned out that the same set of parameters of the etching machine lead to different etching outcomes for the wafers of varying sizes. Thus, the etching rate of CSAR62 ($V_{CSAR} \approx 38nm/min$) estimated on 3" wafer (Paragraph 2.3.3) did not match the rate found after switching to 1" wafer ($V_{CSAR} = 87$ nm/min). This huge discrepancy made it impossible to apply the successful configuration of parameters for 1" wafers directly to 3". Therefore, final experimental samples (for μRT characterisation) were created on the basis of 1" wafers.

Mentioned change in the resist etching rate required the increase of its thickness up to 200nm. Four main parameters were varied during the etching dose tests: the power of RF bias P_{RF} applied to the substrate Si wafer, power of the ICP coil (which increases the etching rate), gas flow V_{Cl}, pressure p, and etching time t. Particular obstacle of this testing is the deceiving nature of EPD signal, which was obtained on a large resist-free platform of the wafer (Figure 2.17b), which etching rate several time as small as the etching rate of the nano features. Figure below demonstrates this problem, when EPD signal indicates the depletion of SOI layer, nanoholes are still not fully etched. ICP power was off because whatever other combinations of parameters we tried, it led to overetching or too fast depletion of the resist

59

(which is reasonable since ICP signal increases plasma density in a gas). Finally, a satisfactory set of parameters was found: P_{RF} =30W, P_{ICP} = 0, V_{Cl2}=30sccm, p =10mTorr,   t =2m:45s. Narrow time window (≈30s) of successful etching was observed in correspondence to the mentioned set of parameters. As seen on the figure below, the borders of this time slot (±15s around t=2m:45s) are underetched and overetched (when resist layer is depleted) cases.
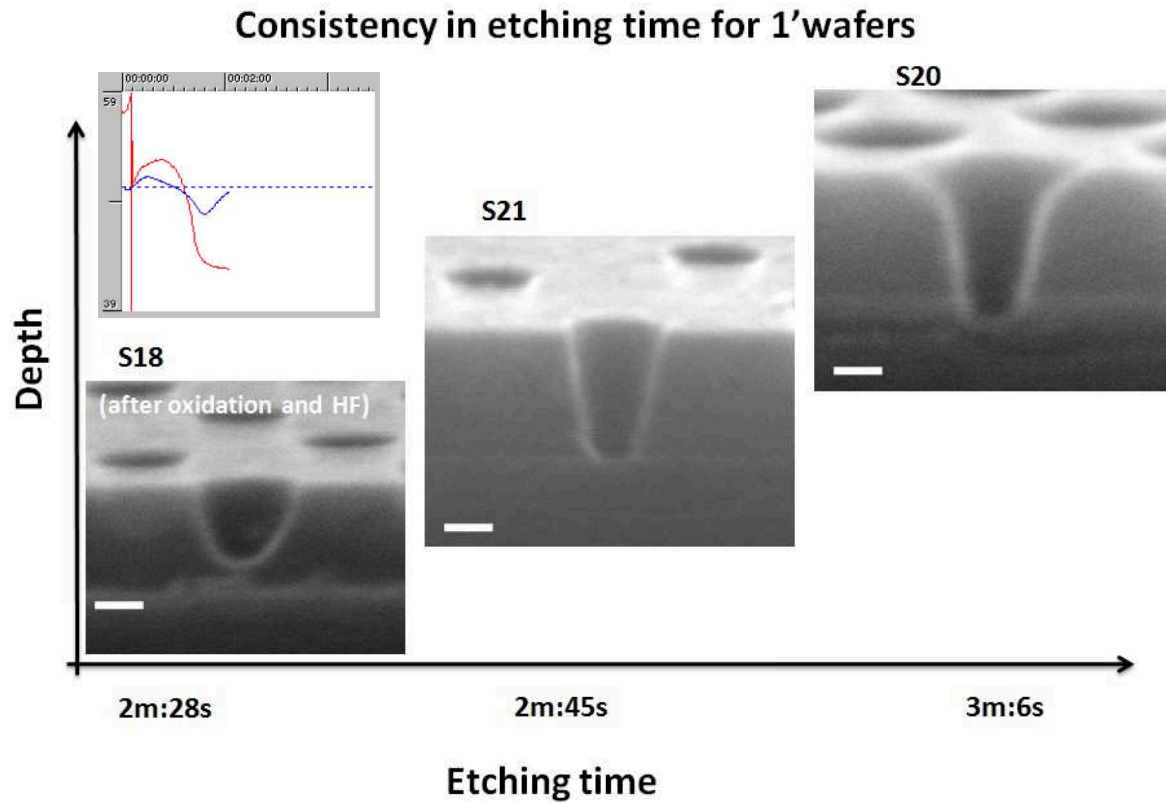
Figure 2.25
SEM images' illustration of the depth of holes profile etched with the same set of parameters   (P_{RF} =30W, P_{ICP} = 0, V_{Cl2}=30sccm, p =10mTorr) vs. the etching time. The etching was done in RIE-ICP machine by Cl_2 plasma. All samples have the same ≈55nm SOI thickness. EPD detection signal (at the top left corner) corresponds to the underetched case (SEM below). Scale bar is for all images =20nm.

The more detailed SEM analysis of the holes profiles proved that the diameter of the white shell rim around the holes (from the top view) correspond to the biggest diameter of the hole (top diameter), whereas the diameter of the dark area is identical to the bottom hole diameter. These estimations are shown on the figure below. Truncated cone shape of the holes is quite a big improvement compared to the previous study, when holes were not fully etched. However non perfect anisotropic profiles lead to some systematic error in absorption estimation via RCWA (rigorous coupled-wave analysis) computation. This method will be described in the next chapter. The averaged diameter/radius (averaged over the top and the bottom hole's diameters) will be used in this work as structural characteristics in experimental data analysis.
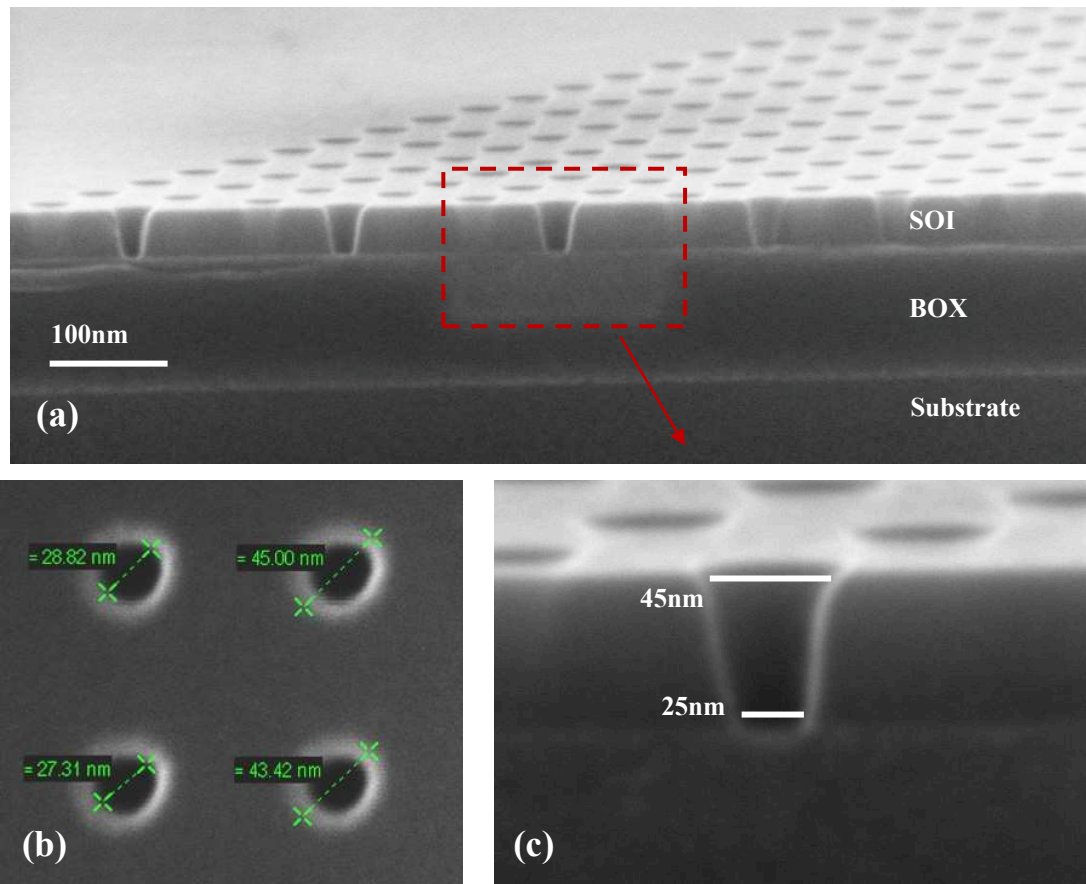
Figure 2.26
SEM estimation of the top and the bottom diameters (c) of the etched holes' profiles concluded that they correspond to the diameters of the dark circle and the rim of the white shells (b) from the top view images. (a) shows the small-scale view of the same SOI layer.

2.3.4.5 Combined recipe of nanoholes fabrication

After EBL and etching dose tests for the holes fabrication, successful probing by cleaving and SEM estimation of the holes profiles on the test samples, 1" wafer with 4 identical cells of PhM devices was processed with the combined recipe of nanoholes fabrication. The table below summarises the steps.

Table 2.6
Nanoholes fabrication.

№	Procedure	Specifications
1	**Surface cleaning**	1) H_2SO_4 (pure 96%) : H_2O_2 (50%) (45ml :15ml) for 10 min 2) HF (**5%**) for 30s. N-aired.
2	**Spin-coating**	Resist: CSAR 62/Anisole(1/0,5). Expected thickness ~ 200 nm. 1) Adhesion and wetting promotion with HMDS. Closed coater. Speed=2000rpm; acceleration = 1000rpm/s; duration=20s. 2) Resist spin-coating. Closed coater. Speed=1500rpm; acceleration = 1000rpm/s; duration=15s 3) Baking at 150°C for 1min
3	**Profilometry**	Thickness check with mechanical profilometer: 185nm
4	**EBL exposure**	Anisotropic patterns: Holes patterns of 2x2nm squares in layout. Low current (300pA), V=100kV, High Dose varied according to the patterns. Doses: 1) for r=1 and r=2.5: D=200mC/cm²; 2) for r=1.2 and r=2.0: D=280mC/cm²; 3) for r=1.6: D=240mC/cm²; Isotropic patterns: Same, but D=260mC/cm²; Small EPD pattern: D=300μC/cm², I=10na; Big EPD pattern: D=450μC/cm²; I=25na;
5	**Resist Profilometry**	The depth on small EPD features inside the cells: 1st cell - 192nm; 4th cell - 192nm; Big EPD feature: 190nm.
6	**Development**	Developer: AR600-546. Time = 1min, without agitation. Post-development: 30s IPA rinse, nitrogen blow dry.
7	**Holes Etching**	RIE-ICP etching: P_{RF} = 30W, P_{ICP} = 0, V_{Cl2} = 30sccm, p = 10mTorr, t=2m:45s
8	**Resist Profilometry**	The height of the remaining resist right after the etching. On scratches. At a flat side: 44nm; right side: 55-60nm.
9	**Stripping**	UV exposure for 30mins. Wafer immersed in preheated PG-remover at 65°C for 2h. Cleaning: acetone rinse; IPA rinse; nitrogen dry blowing.
10	**Cleaving and SEM check.**	Cleaving the probe lines of holes at the bottom of the sample and a study of the quality of the etching looking at the holes profiles with SEM. Results are shown on Figure 2.28.

The last step is a cleaving of the probe line with the lattice of holes. The figure below demonstrates the layout of the planned cleaving and its implementation. As can be seen from the picture on the right, the PMMA resist (needed for the further processing) deposited by spin-coating on the cleaved sample covers the cells area. However, for the sake of precaution

it was concluded to modify the future designs, making the probing line longer, thus performing the cleaving closer to the border of the sample.
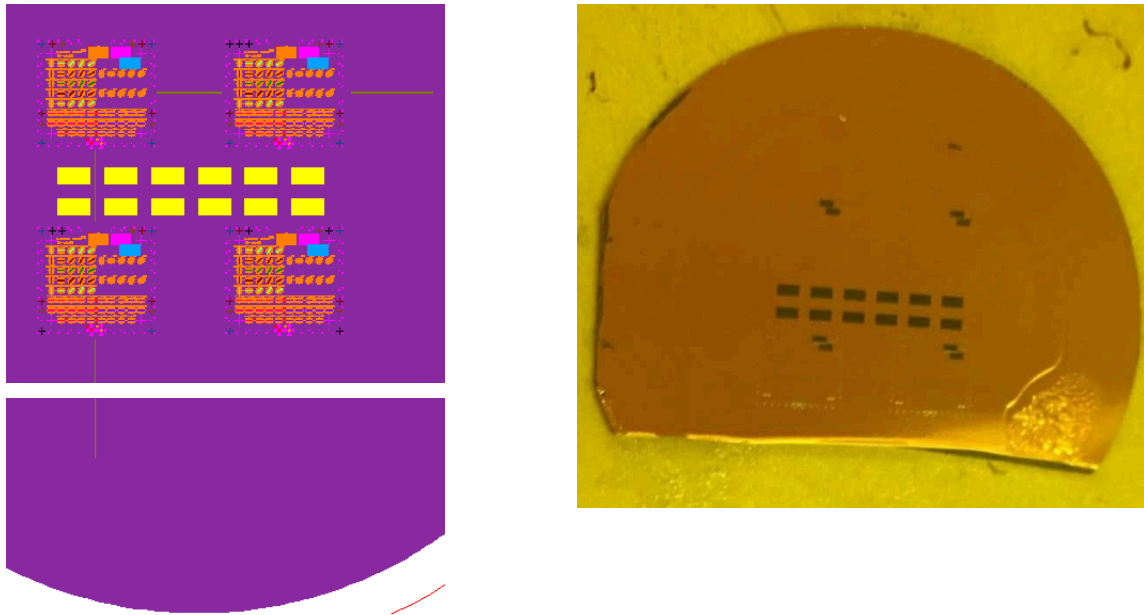
Figure 2.27
Layout (left) split along the cleaving plane (110) in the middle of the probe line with the tilted lattice of holes. Photo of the sample (right) done after the cleaving and PMMA spin-coating as a preparatory step for the cavities etching.

Further SEM estimation had proven a good quality of the holes etching on the current sample.
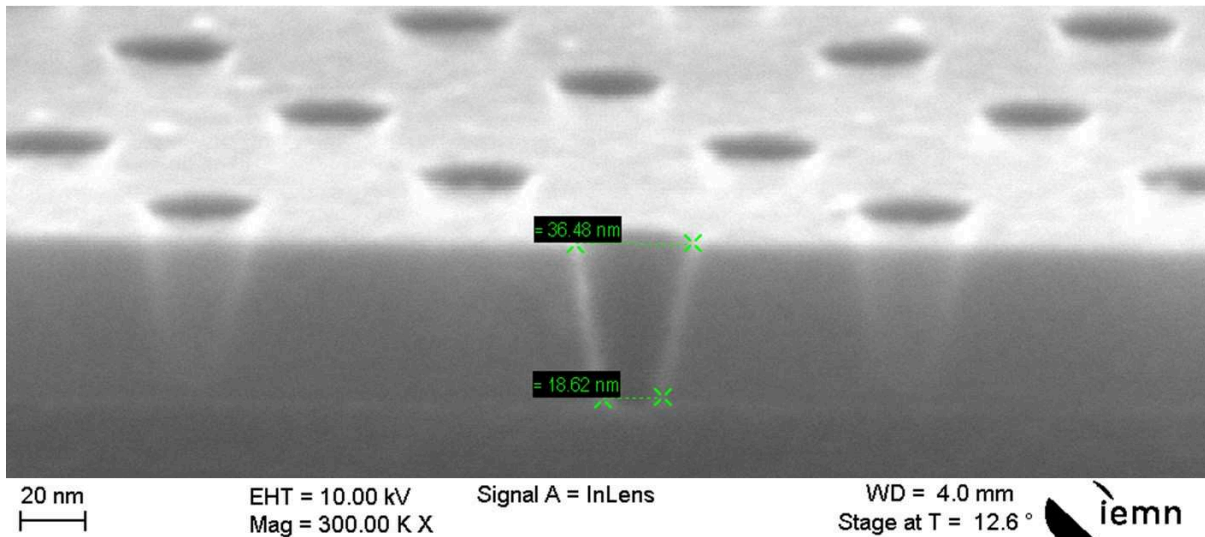

Figure 2.28
SEM estimation of nanoholes etching in the sample processed with the aim of beam-like PhM fabrication.

2.3.5 Cavities formation

The aim of the next fabrication set of procedures (Table 2.7) is to create cavities from both sides of the beam-like membrane. This will prepare us for the next steps: the passivation (oxidation) of membrane and suspension etchings. The set of the current procedures is similar to what was done for the alignment markers.

Table 2.7

Cavities formation.

№	Procedure	Specifications
1	**Spin-coating**	Resist: COPO EL-13% MMA 8.5. Expected thickness ~ 2 µm.
		Pre-processing: hot plate preheating at T= 80°C for 1 min; cooling to RT in 1-2min.
		Speed=1000rpm; acceleration = 1000rpm/s; duration=12s.
		Temperature ramping: 80°C-180°C with 8°C/min changing rate, with 1min waiting stops at each 20°C step; final stop at 180°C for 10min. Hot plate is closed.
3	**EBL exposure**	Dose = 450 µC/cm², Current = 25 nA, Resolution = 25 nm
4	**Development**	Developer: MIBK+IPA (30ml/60ml). Time = 1min with 100rpm agitation. Post-development: 30s IPA rinse, nitrogen blow dry.
5	**Profilometry**	Height of the resist measured with profilometer: 1850nm
6	**Dry-Etching**	1) Etching of ≈50nm SOI layer: SF_6 flow = $10cm^3$/min, Ar flow = $10cm^3$/min, Pressure = 10mTorr, Power=30W, t ≈ 50sec. DC bias = 145V.
		2) BOX Etching (≈145nm): CF_4 flow = $40cm^3$/min, N_2 flow = $40cm^3$/min, O_2 flow =$5cm^3$/min, Pressure =10mTorr, Power=100W, t≈14.5min, DC bias = 316V.
		3) Stop when the substrate is reached (see horizontal feature of EPD signal on Figure 2.29)
		Expected depth ~ 200 nm (SOI plus BOX layers)
7	**Stripping**	UV exposure for 30mins. Wafer is immersed in preheated PG-remover at 65°C for 2h. Cleaning: acetone rinse; IPA rinse; nitrogen dry blowing.
8	**Profilometry**	Depth check with mechanical profilometer. At EPD features in each cell: D_{cell1} =199nm, D_{cell2} = 211nm (Figure 2.29) D_{cell3} = 208nm. At a membrane (cell №1): 202nm.
		Conclusion: everywhere Si substrate is reached: 55 ± 7.5 (SOI) + 145 ± 2 (BOX) ≈ 200 ± 10 nm (SOI and BOX values are according to manufacturer specification file).
9	**SEM inspection**	Looking at the membranes borders. Due to the overetching and not perfect spin-coating, the edges of the membranes were additionally etched by ≈200nm-300nm from both sides, which led to smaller width of the membranes: 8.7-9.2 µm instead of planned 9.5-10 µm.

One of the few differences here from the fabrication of alignment markers is the stop of the etching upon reaching the substrate. The idea is to open the substrate surface slightly etching inside of it for a few nm. During the next procedures substrate Si will be removed by

XeF$_2$ gas, which will require additional protection of the Si membrane with the oxide deposition.
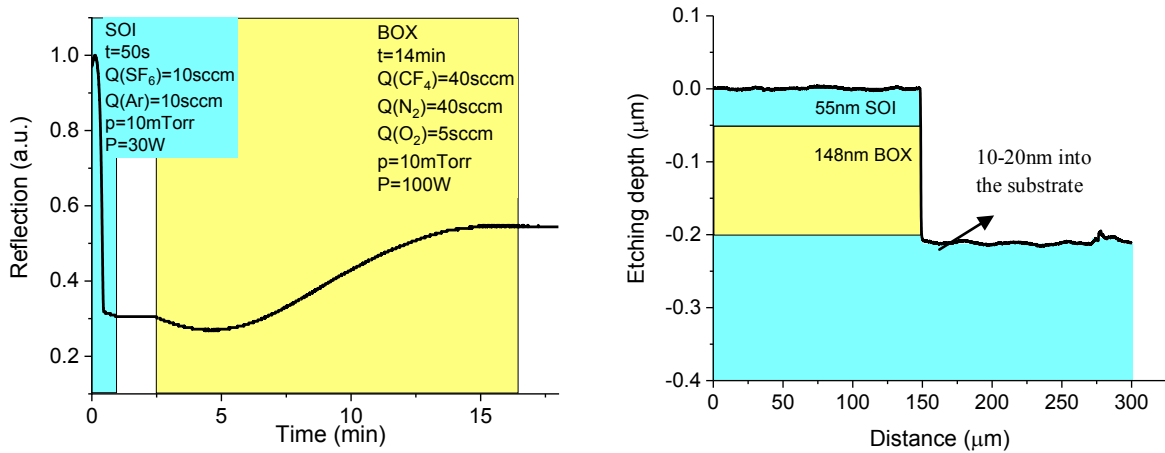
Figure 2.29
EPD reflection signal vs. the etching time (left) with colour blocks indicating specific layer during the RIE etching of the cavities in SOI and BOX layers. Layers' borders are defined by specific patterns of the signal. Blank spaces between the blocks indicate gas refill procedure, when plasma circuit is not active. Corresponding profile (right, solid thick curve) of membrane cavity obtained as a result of the etching. Etching depth is measured by mechanical profilometer. The thickness values of SOI and BOX layers are taken from the averaged ellipsometry estimation.

SEM scans showed that due to the overetching, the holes-free margins along membranes edges were depleted (Figure 2.30ab), which led to the situation when membranes are completely covered with holes. This can be considered as an interesting opportunity to produce high quality PMs fully covered with the lattices of holes, however an additional challenge arose in connection with the oxidation procedure, which is explained in the next paragraph.

(a)

=9.224μm

(b)   (c)

SOI

BOX

400nm   70nm
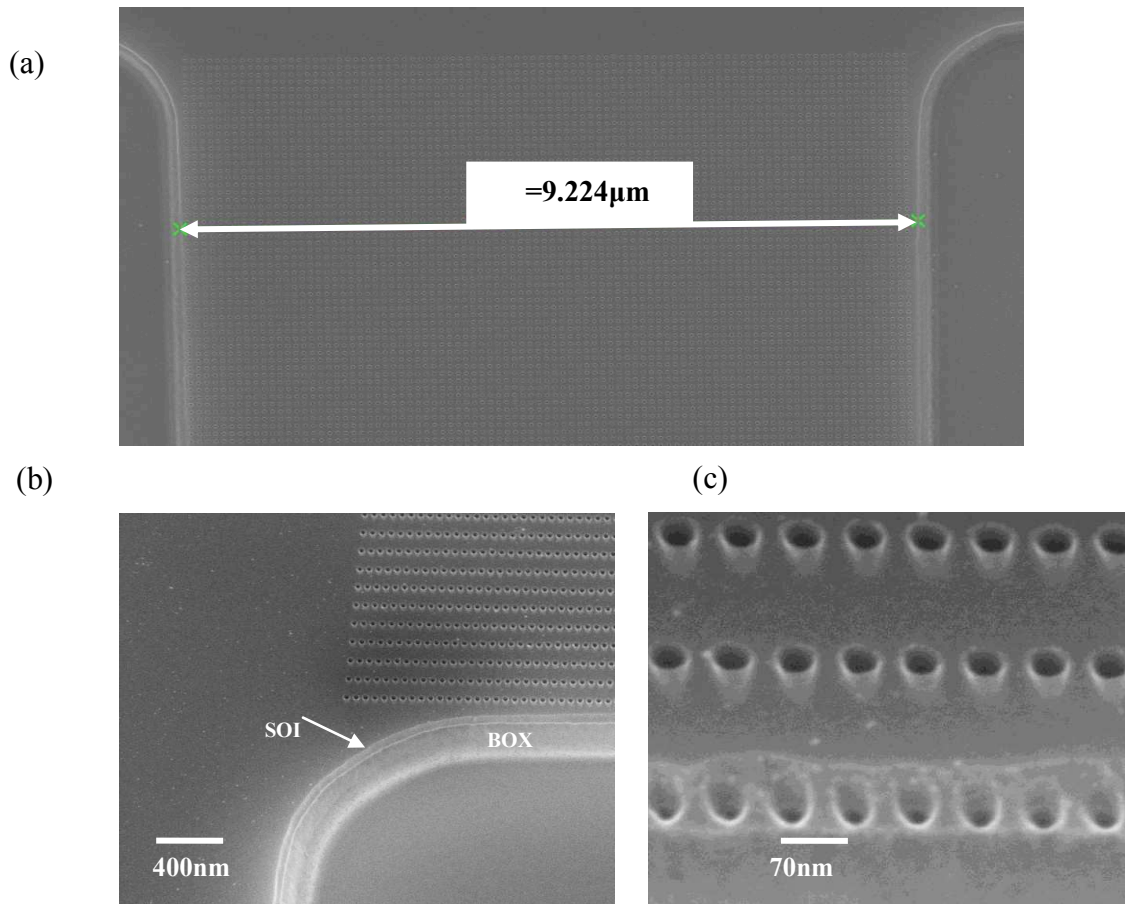
Figure 2.30

SEM images demonstrate the outcome of cavities etching around the membrane. (a) Top-view of the membrane shows that the holes-free sides (margins) were etched. (b) Tilted (angle = 40°) view of the membrane shows 200nm deep cavity border formed around the membrane. (c) Close view shows the fragment of the membrane's edge with a line of holes, which is cut by half forming sharp features, which will require higher thickness of oxide.

2.3.6 Oxidation

Rough features on the membrane edges formed by the partially etched lines of holes (Figure 2.30c) require additional oxidation. The rougher the edges, the higher the risk of forming low thickness oxide spots during the oxidations. Those spots, even if they are 2-5 nm in size, can lead to a bad protection during XeF_2 etching, which may lead to the membrane destruction. To overcome this risky situation, it was decided to increase the oxidation thickness. Wet low-pressure chemical vapour deposition (LPCVD) was used. Wet oxidation has a higher growth rate than dry oxidation, due to the fact that the ability of hydroxide (OH⁻) to diffuse through the grown layer is better[59] than that of O_2. Targeting for a twice thicker passivation layer (20nm) compared to the previous PMs generation, we chose the wet oxidation.

Table 2.8
Wet Oxidation

Procedures and gases	Temperature (°C)	Duration (min)	Flow rate (liter/min)
Purging with N_2	500		2
Heating with N_2	500 - 850	35	2
Oxidation with O_2 and H_2	850	15	1.5 (O_2) and 2.5(H_2)
Purging with O_2	850	15	1.5
Cooling with N_2	850 - 500		2

Standard cleaning procedure was performed prior to oxidation. The specifications can be found in the first row of Table 2.6. HF cleaning was necessary in order to remove the native oxide formed on the Si surface. Native oxide complicates the even growth of silica during LPCVD.

After introducing the sample into LPCVD preheated oven with N_2 atmosphere, the temperature was raised with the ramping rate of 10°C/min. The smooth temperature increase moderates mechanical stress in the sample. During the next stage, the inlet gases O_2 and H_2 form the water vapour, which reacts chemically with the Si surface, oxidising it: $Si + 2\ H_2O \rightarrow SiO_2 + 2H_2$. The thickness of the passivation oxide layer depends on the oxidation time. The target thickness of 20nm was estimated to be achieved for 15min of oxidation. After the oxidation step was done, the oven tube was purged of H_2 with O_2. Finally, the cooling was performed with the same temperature ramping.

Table 2.9
Layers' thickness estimation by ellipsometry

	Layers			
Location	SiO_2	SOI	BOX	R^2
1	19.3	42.5	147.9	0.84
2	17.3	44.4	147.8	0.9
3	17.9	43.8	147.9	0.93
Mean	18.2	43.6	147.9	
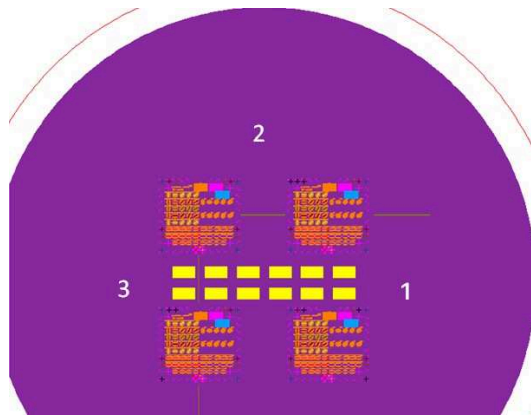
Figure 2.31
Estimation (table on the right) of the layers' thickness at three different location (left) on the oxidised SOI wafer.

In order to estimate the thicknesses of the grown SiO_2 layer, thinned SOI layer, and verify the thickness of the BOX layer, near-IR ellipsometry was used. Spectroscopic ellipsometry is one of the most reliable experimental optical techniques due to its almost century-long development history and the diversity of practical realizations with respect to geometry. It is successfully used for the characterization of thin films and multi-layer semiconductor structures. All types of ellipsometry techniques have one common basis: from the change of the probe light polarization one can obtain information about an optical dielectric response of the system[60]. Dielectric and polarisation information is entangled with the thicknesses of the

samples layers. Si and SiO$_2$ dielectric functions are well-studied, therefore using literature data[61], and ellipsometry measurements, it is possible to estimate thicknesses of all three mentioned layers (Figure 2.31).

Measurements revealed that the BOX layer is 3nm thicker than the average value given in the specification. Obtained thickness values of the grown silica (≈18nm) and thinned SOI layer (≈43.6nm) correspond to predicted empirical estimate: 47nm = 55nm-18.2nm*0.44. This estimate implies that on average during the oxidation the silicon layer is getting thinned down by a factor of 0.44.

Post-oxidation SEM analysis (Figure 2.32ab) of the membrane parts showed that the native oxide evenly covers Si surface, including the walls of the holes. However observed nanocavities under membranes' holes added some worries. Nanocavities in the BOX layer under the holes were formed during important HF cleaning (removing of the native oxide). This outcome was not predicted in advance, mainly because this was the first series of samples with the fully etched holes in SOI layer. To minimize or eliminate this effect it is recommended to adjust HF concentration in the cleaning solution to lower level and decrease the time of the sample immersion.
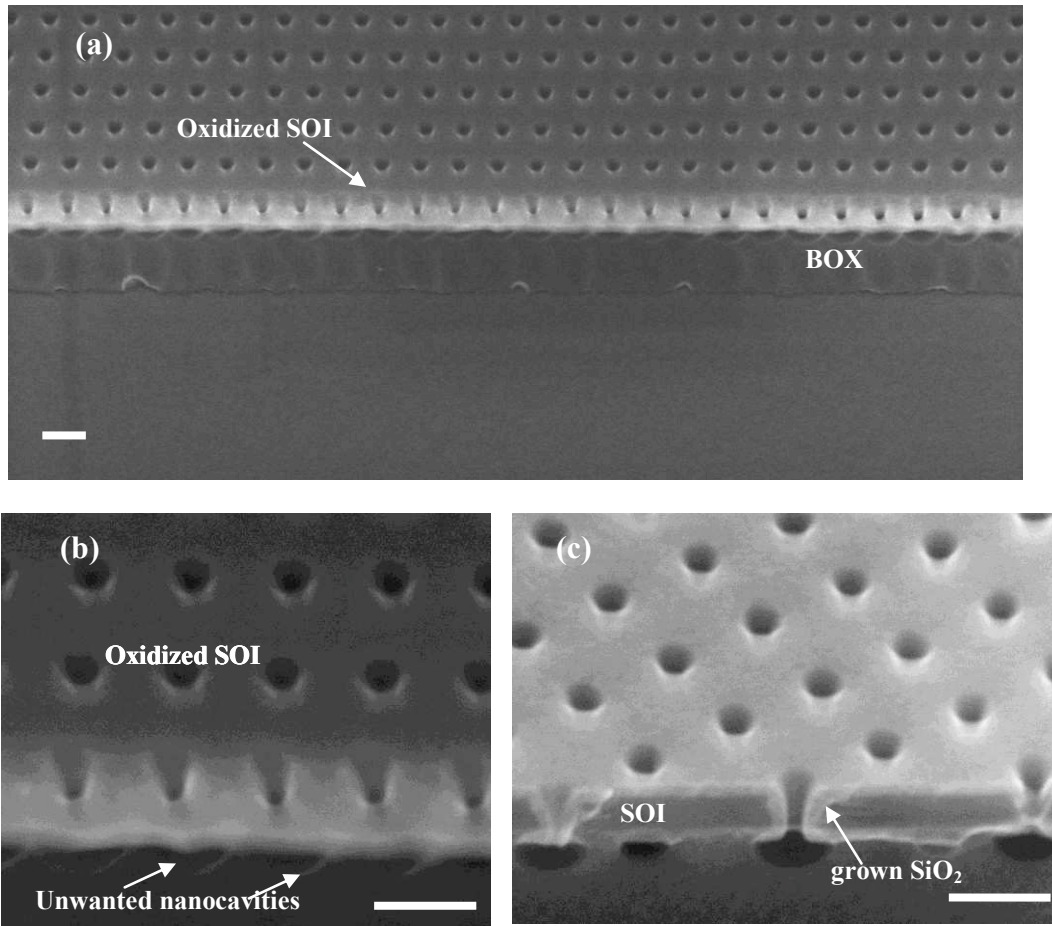
Figure 2.32

SEM images show the quality of SiO$_2$ passivation layer grown during LPCVD oxidation. (a) Tilted top view of the membrane SOI layer covered with the grown silica. (b) The same zoomed view where nanocavities formed by HF cleaning are well seen. (c) Cleaved edge (in (110) orientation of Si) of the probe line with the identical lattice of holes. The image allows to see that silica completely covers SOI surface. Scale bar is equal to 100nm everywhere.

In order to develop a confidence in the quality of passivation layer at the presence of nanocavities, a special cleaving was done on another probe line with holes, located outside experimental cells. The edge of this cut was studied with SEM (Figure 2.32c). It is clearly seen from the image that the silica covers not only the walls of the holes, but also the top part of the nanocavities, where Si was opened by HF. This concludes that the SOI perforated region of the future membrane is protected and XeF_2 etching of the silicon substrate can be performed without causing any damage to suspended Si membranes.

2.3.7 Pre-etching opening of cavities

After the oxidation procedure, the surface of Si substrate cavities became covered with SiO_2 layer of ≈18nm. The goal is to suspend the SOI part making it a membrane. This can be done via substrate etching with XeF_2. This gas does not react with protective silica. Therefore it is important to get rid of the Si passivation layer at the bottom of the cavities. This is achieved with the help of selective plasma RIE at the bottom regions. The procedure is similar here to the fabrication of alignment markers and cavities. At first by the means of PMMA spin-coating and EBL lithography we protect sample surface selectively leaving uncovered almost whole surface area at the bottom of the cavities. We leave protected only 1µm margins around the surface (they can be seen in post-etching SEM scan on Figure 2.33bc). The purpose of these silica margins is to secure the silica layer around membrane part as much as possible during RIE etching

Table 2.10
Cavities opening.

№	Procedure	Specifications
1	**Spin-coating**	The same procedures as for the "cavities formation" (See Table 2.7)
3	**EBL exposure**	
4	**Development**	
5	**Profilometry**	Height of the resist measured with profilometer: 1768nm
6	**Dry-Etching**	1) Passivation SiO_2 etching (19.3nm): CF_4 flow = 40cm³/min, N_2 flow = 40cm³/min, O_2 flow = 5cm³/min, Pressure = 10mTorr, Power = 100W, t ≈ 2min, DC bias = 316V. 2) Si substrate etching, continuing the process from step 1 for 1min.
7	**Stripping**	The same procedures as for the "cavities formation" (See Table 2.7)
8	**Profilometry**	Depth check with mechanical profilometer. At EPD features in each cell: D_{cell1} =230nm (+31nm), D_{cell4} = 246.5nm (Figure 2.33b). At a membrane (cell №4): 233nm. Conclusion: silicon substrate is well open even on the least deep profile (Cell 1). Based on ellipsometry and profile estimations: 18(SiO_2) + 44(SOI) + 148 (BOX) ≈ 210 (nm). D_{cell1} - 210nm = 20nm, which is more than averaged SiO_2 thickness estimation.
9	**SEM inspection**	Looking at the membranes borders (see figure below)

According to the previous study[49], the etching rate (ER) of Si by CF_4 plasma (under conditions from Table 2.7): ER(SiO_2 by CF_4) =10.5nm/min. This implies that 2min have to

be enough to etch SiO_2 at the bottoms, considering that the highest observed silica thickness ≈ 19.3nm. In order to get rid of SiO_2 etching residues, the etching goes for 1min more. Substrate etching rate is almost the same ER(Si by CF_4) =11.6nm/min.
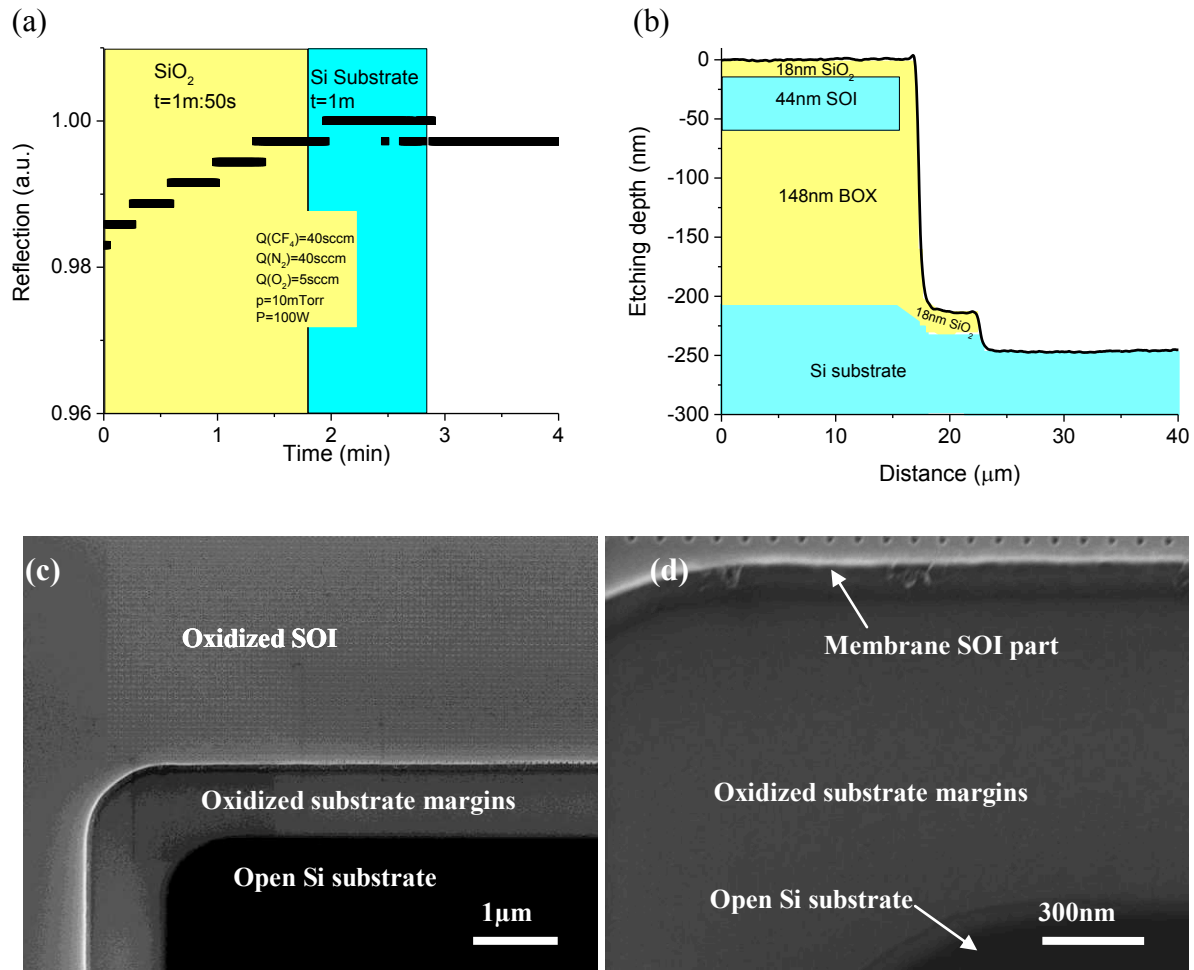
(a) EPD signal during CF_4 etching with highlighted layers, defined by the EPD signal characteristics. Structural post-etching characterisation: (b) profile (black curve) of the cavity done by stylus profilometer, SEM scans showing the contrast between silica covered regions and opened Si substrate ((c) top view, and (d) zoomed tilted view.

Characteristic EPD signal and resultant post-etching profile of the cavity close to the membrane part of SOI (Figure 2.33ab) conclude that the current fabrication step goal was achieved and the sample was ready to be processed for Si substrate etching below the membrane. SEM scans (the same Figure 2.33cd) confirmed that the silica protective layer remained of a good quality and the selected bottoms area was released.

2.3.8 Die singulation

This is the last procedure, preceding the final fabrication step "Membranes releasing". The final step is challenging since it involves gas and dry vapour etchings. XeF_2 etching is a delicate step because one has to etch a big amount (comparing to membrane thickness of 44nm) of the substrate bulk, cavity depth $\approx 11\mu m$. The recipe used for previous generation of plain and not well-perforated PhMs, was planned to be tested on prepared well-perforated

SOI beams of 44nm thickness. The process might work well, or could be too strong for the sharp features located at the edges of the membranes or underneath the nanoholes. For this reason the wafer was split into 4 samples (dies) containing individual cells and one sample (die) with the probe lines of holes. The first cell sample had to be separately processed and structure characterised. On the basis of these observations the necessary etching recipe modifications ought to be done (if needed).

The sharp diamond stick was used for the hand cleaving. This method is faster than the laser cut procedure for small samples with few cells. It is necessary to perform the substrate etching right after the cavities opening (in the same day), because the grown native oxide might require additional XeF_2 etching cycles (or time). S-probe sample (Figure 2.34) was used for the SEM structural check of the oxide deposited by LPCVD (Figure 2.32c).
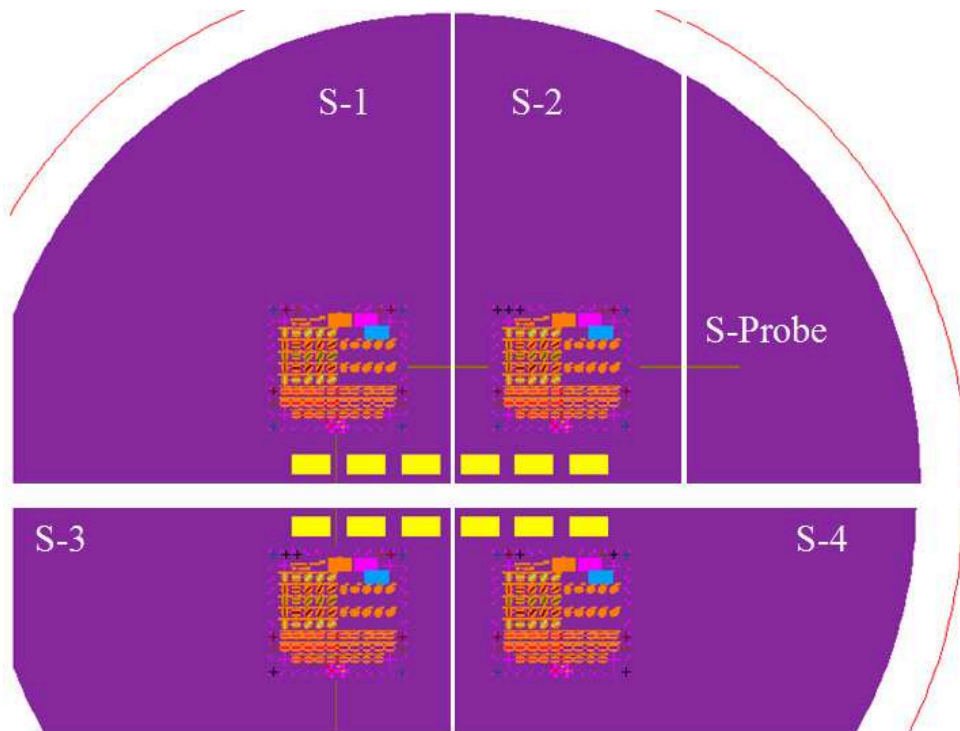
Figure 2.34
Layout of the processed wafer split into samples indicating the cleaving lines along Si principal orientations (110).

2.3.9   Membranes release

In order to remove Si substrate under the membrane (which comprises now SOI+BOX+Mask layers) isotropic etching process is required (Figure 2.35). Moreover, the thickness (≈210nm) of SOI+BOX+Mask implies the necessity for the soft etching, which does not impose mechanical stress in the suspended double layer membrane. For these two reasons commonly used wet substrate etchants (KOH[62], TMAH[63]) were not applied: their etching rate is anisotropic (depends on the crystal orientation), mandatory post-etching

cleaning rinsing procedures can induce stiction and capillary forces while removing the wet etchant, even the nitrogen dry blowing can cause membrane damages.
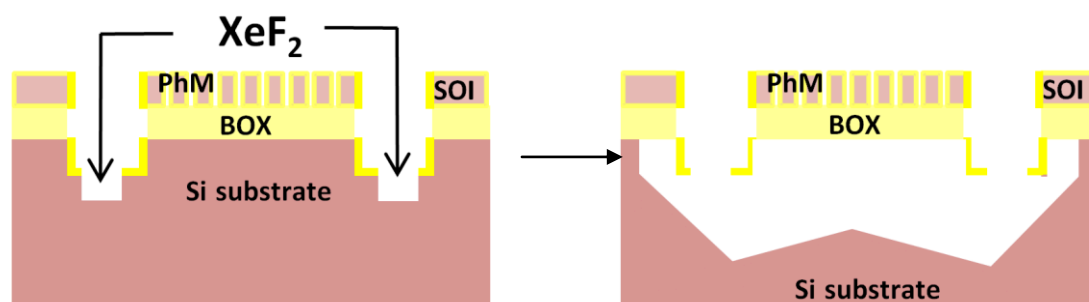
Figure 2.35

Schematic representation of the PhM device in cross-section view and the substrate etching procedure (proportions are not respected). Etchant gas exposes the substrate surface open at the cavities bottom, all SOI parts (including PhM part) are protected by 18nm passivation silica layer. On the right the desired outcome of the etching: PhM is released, no damages in PhM part.

To the contrary dry XeF_2 etching is more isotropic, offers high selectivity (with respect to silica) 1:10000, and does not apply strong forces[64,65]. The etching reaction occurs according to the formula: $2XeF_2$ (g) + Si → $2Xe$ (g) + SiF_4 (g), where (g) denotes the volatile substance. Thus the etching product can be easily evacuated. Theoretical etching rate corresponding to the used set of operating parameters (room temperature, Pressure = 3Torr) is ≈1.25µm/10s. The process goes in 10s cycles, needed for the iterative evacuation of the volatile by-products (Xe, SiF_4) and the remnants of XeF_2. Pump-out pressure is 0.8Torr. Assuming perfect isotropy of the process and the absence of native oxide on top of the Si substrate, 4 cycles could be enough for the membrane suspension. However, both assumptions are not correct. The native oxide grows rapidly on the pristine surface[16] during the first days (reaching 0.4 nm in 16h), this adds an additional barrier to the etchant in the 1st cycle. The second assumption (isotropy) had been disproved by step-cycle optical analysis. Figure 2.36 demonstrates images from the optical inspection of the same sample non-perforated membranes that were etched during 6 and 8 cycles. The yellow region on the membrane (Figure 2.36a) signifies the bulk substrate presence. Green parts are suspended. This observation implies that the etching is not perfectly isotropic since the lateral cavity depth (green membrane parts) is ≈3.5µm, whereas the vertical cavity depth, that was achieved for 8 equivalent cycles, is ≈11µm (laser interferometry estimation). Only vertical depth is close to the theoretical estimation (1.25µm/10s · 8 ·10s =10µm), while the lateral depth estimation (1.25µm/10s · 6 ·10s =7.5µm) is more than twice as much as the real experimental value (3.5µm). This concludes that the etching is anisotropic.
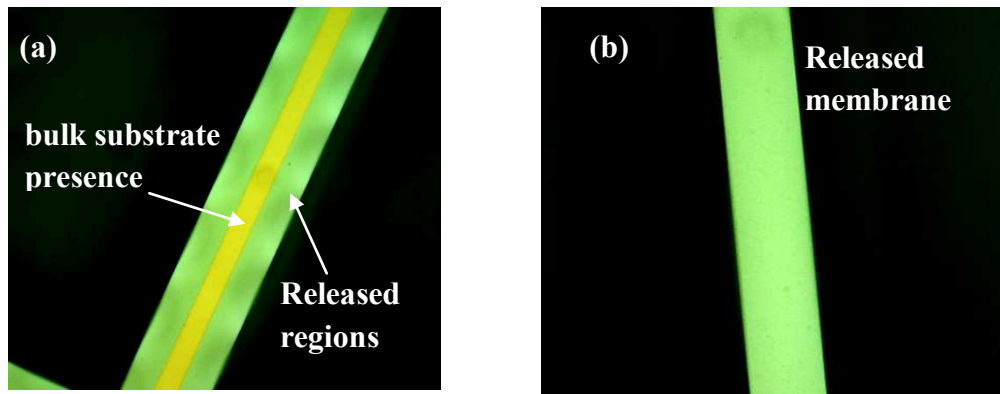
Figure 2.36

Optical images of 9µm-wide non-perforated membranes (the stack of SOI+BOX+Mask layers) after (a) 6 cycles and (b) 8 cycles of XeF$_2$ etching. Green regions correspond to parts of the membrane released from the substrate.

After concluding that 8 cycles is optimal for the suspension using the testing wafer with non-perforated membranes, one of 4 cleaved samples with PhMs was chosen for the same recipe processing.

Besides the aforementioned delicate etching procedures the final fabrication step involved thorough structural characterisation, including SEM and laser interferometry[66] (non-contact and quick method). The latter was used as a profilometer tool instead of a mechanical stylus, for the reason of fragility of the suspended membranes. The triple layered suspended membrane is very light and the stress is substantially released in it, compared to SOI layer. This low stress causes a big membrane curvature. Figure 2.38 shows the combined picture of the curvature of the membranes and the measurements of the cavity depth performed after XeF$_2$ and HF etching (HF removes BOX and grown silica protective layer). While optical inspections after XeF$_2$ etching allow to verify if the triple layer (SOI+BOX+Mask) membrane is fully suspended, interferometer gives a quantitative estimation of the suspension, measuring ΔZ height at the membrane centre with respect to the sample top surface. A reliable reference value of ΔZ(SOI+BOX+Mask)≈7.5µm was obtained with non-perforated test membrane (of the same layer thicknesses), the suspension quality of which was confirmed by both optical (Figure 2.36) and SEM inspection (Figure 2.37).
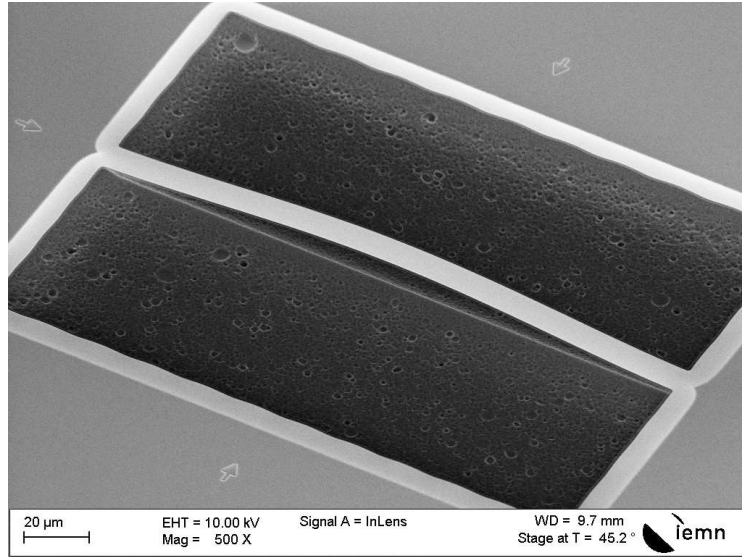
Figure 2.37
SEM scan of non-perforated membrane (SOI+BOX+Mask) after XeF_2 etching, showing good quality of suspension and high curvature due to the low stress (high strain).

After XeF_2 (substrate etching)   After HF (silica etching)
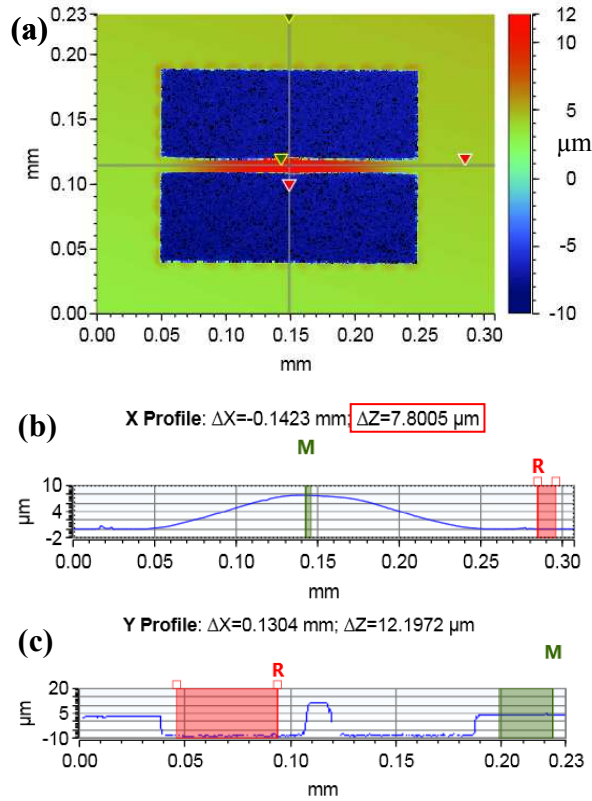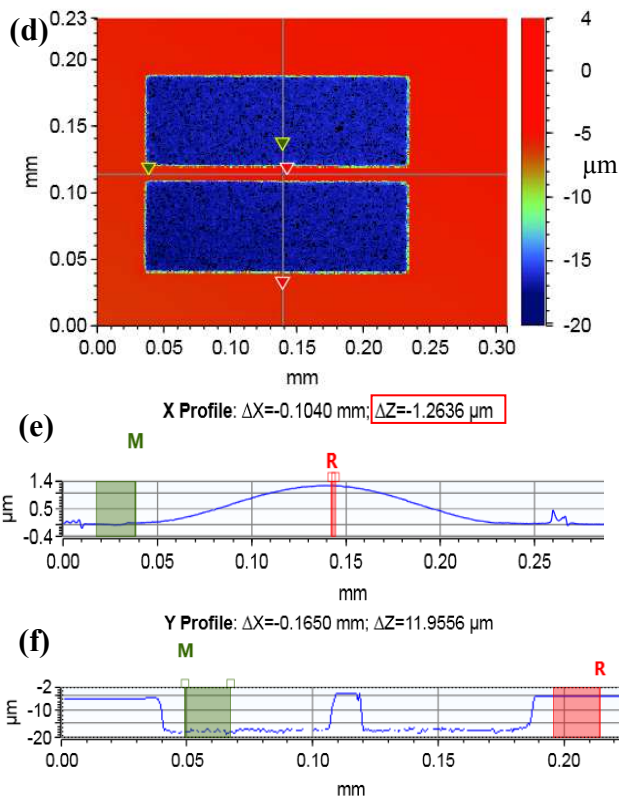
Figure 2.38
Laser interferometer estimation of the membrane curvature height and cavity depth after (a-c) XeF_2 and (d-f) HF etching. The top row shows the depth colour plots, the second (curvature estimation) and the third (cavity depth estimation) rows are ΔZ profiles vs. the distances along the lines indicated in the colour plots.

Post-XeF$_2$, the triple-layered perforated membrane revealed similar curvature height $\Delta Z_{curvature} \approx 7.8\mu m$, which ensured good suspension (Figure 2.38b). In parallel, the depth of the Si substrate cavity under membrane was estimated: $\Delta Z_{cavity} \approx 12\mu m$ (Figure 2.38c).

The very final PhMs fabrication step was HF (Hydrofluoric acid)[67] vapour etching of the protective silica and the BOX. As in the previous etching, the fragility of the membrane dictates the preference of the gaseous phase over the liquid. Reaction goes as follows: $4HF(g) + SiO_2 \rightarrow 2H_2O$ (g) + SiF_4 (g). Volatile by-product is an advantage again, due to the possibility of performing non-destructive cleaning by gas(vapour) evacuation. At first, the sample is heated for 2min @260°C in order to evacuate residues from the previous cleaning and etching processing. 1 cycle (7min) with the composition of etching and purging gases was performed. Gases entering the chamber have the following flow rates: 310cm^3/min (HF), 350cm^3/min (C$_2$H$_5$OH), 1250cm^3/min (N$_2$). The etching rate according to the set-up specifications is 37.4nm/min. However, the thickest SiO$_2$ layer (148nm BOX) is located below SOI layer. Under-etching requires longer time, therefore time = 7min was chosen.

Post-HF interferometry (Figure 2.38e) revealed a curvature of the membrane 7 times smaller ($\Delta Z_{curvature} \approx 1.1\mu m$). The presence of the curvature indicates the membrane is less stressed than SOI layer. The $\Delta Z_{curvature}$ value corresponds to the reference obtained on the non-perforated membrane. The depth of the cavity was not changed.

SEM structural analysis has confirmed complete removal of the silica from the surface of PhMs. The images can be found in the first section of the next chapter, where the other important geometrical estimation of the PhMs and structural TEM analysis of the holes surfaces are discussed. Three more samples were processed (separately) for the membrane release with the same recipes that were present in this paragraph.

2.4 Conclusions

On the bases of the results on design and fabrication of experimental platforms with 2D Si PhMs having potentially anisotropic thermal properties, the following conclusions are drawn.

The thermal transport experiment based on vacuum μRT measurements of free-standing beam-like (FSBL) membranes with anisotropic lattices of nanoholes was proposed. The approach was motivated by the following arguments: 1) FSBL topology allows for direct measurements of effective $\bar{\bar{\kappa}}$ eigenvalues in principle orientations of 2D anisotropic phononic lattice, eliminates the contribution of substrate heat sink; 2) vacuum-based μRT implies noninvasiveness, direct membrane heating by the light absorption, elimination of both convection losses and interface heat transport perturbation from metallic probes.

Additional research questions were formulated and corresponding design of PhMs was done: (1) To see at what ratio of anisotropic lattice pitches the difference of $\bar{\bar{\kappa}}$ eigenvalues become pronounced, 5 phononic patterns with rectangular unit cell lattices were designed. Patterns are characterized by the pitch ratio r, with the values: [1, 1.2, 1.6, 2, 2.5]; (2) in order to visualize graphically the heat flow (or obtain directional dependence of effective κ each patterns was implemented in five membranes with different PhM orientation angle (0°, 30°, 45°, 60°, 90°); (3) to minimize *ff* difference (increasing comparison reliability) among the patterns, unit cell of phononic lattices is kept the same ≈ 10000nm^2.

An optimal fabrication solution for EBL based on the conventional approach was applied for anisotropic phononic pattern writing.

EBL dose tests were performed in order to overcome lithographic proximity effect and obtain similarity in holes sizes and *ff* for the patterns. The result sets filling fraction variation from 17.5% to 23.3% (estimation details are in the next chapter).

A fast and reliable test-probe method for the assessment of the quality (and structure) the etched nanoholes was proposed and extensively utilized in the fabrication process at multiple steps.

The increase of wet oxide thickness improved the quality of passivation.

All aforementioned results combined with the known processing recipes led to the successful fabrication of the designed series of anisotropic PhMs, isotropic PhMs series (with the pitch variation from 80nm to 500nm), and plain membrane reference series (with the angle variation).

Chapter 3   Characterisation Methods

3.1 Post-fabrication structural characterisation

Relying on the fabrication methodology described in the previous chapter, a series of new micrometer measurement platforms were created, with the aim of an experimental study of the feasibility to artificially induce anisotropy of κ in Si phononic membranes (PhMs).

The measurement of thermal properties of fabricated PhMs and interpretation of the experimental outcome requires the knowledge of geometrical (width, thickness) and structural (holes diameter, roughness, surface oxide thickness) characteristics. This section describes how those characteristics were estimated.

3.1.1 SEM observation of the fabricated membrane

Multiscale SEM images (Figure 2.1A-D) shows one of successfully fabricated perforated (phononic) membranes (PhMs) with isotropic (pitch =100nm) lattice of holes. For comparison, the large scale scan of anisotropic lattice is given (E), which concludes that both types of lattices have similar circular shapes of holes. At last, the membrane edge with the hole profile (F) ensures full holes etching and the absence of residues.

Figure 3.1
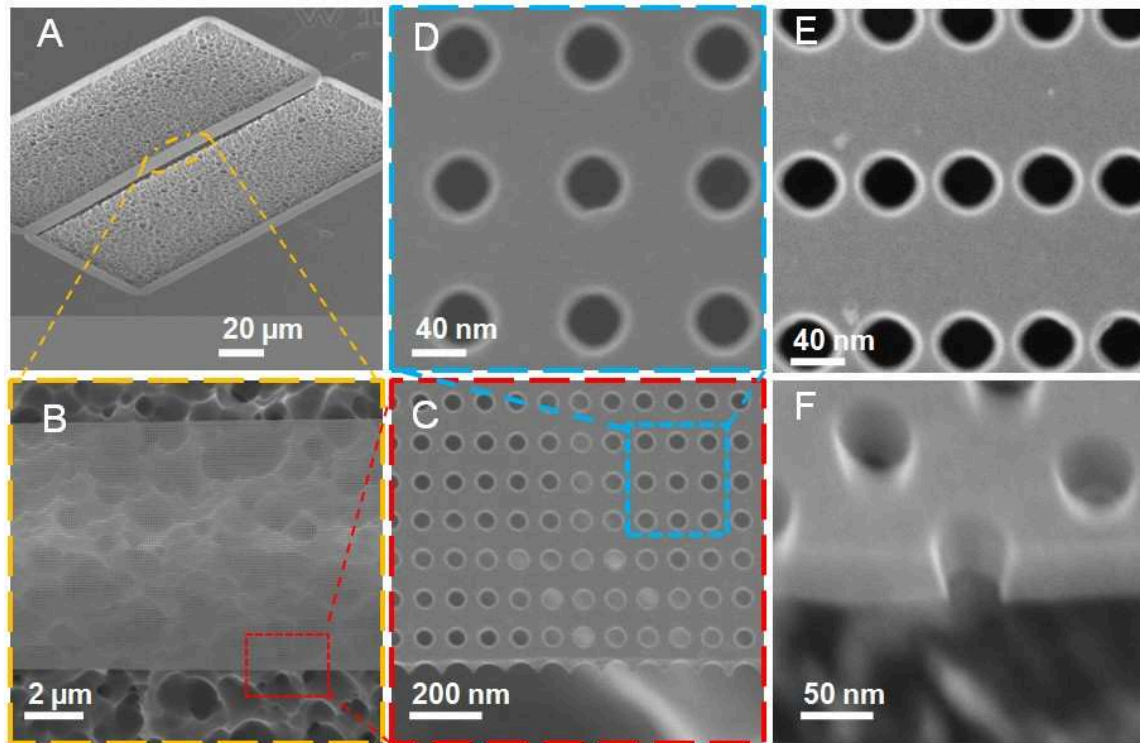SEM images of a 43.8nm-thick nanostructured silicon suspended membrane (length = 200μm, width=8.9±0.1μm (estimation is given in the next paragraph)) with (A-D) isotropic (period $P_x = P_y = 100$ nm) and (E) anisotropic ($P_x = 70$ nm; $P_y = 143$ nm) lattices of holes. (E) SEM cross-section view (tilt angle 43.5°) of the edge of nanostructured SOI suspended layer, identical to the membrane.

3.1.2 Membrane width

The overetching and following depletion of membranes margins, which occurred during RIE of the cavities, left the membranes fully covered with the phononic lattices. This is an accidental but positive outcome of the fabrication. However, it requires additional estimation of membrane widths. 8 well-fabricated different membranes were randomly chosen for SEM analysis, where the width of each membrane was measured at three locations (at the ends and the centre of the membrane). Results (Table 3.1) show that the middle width is shorter than the width at the ends is by ≈170nm. This difference comprises 2% from the total average of all measurements (width ≈8.9μm). This difference is negligible since it does not induce noticeable change in thermal calculations, which were tested in Comsol simulation (this approach will be introduced in the next section). The final width estimation concludes in 8.9±0.1μm, where the error interval is half of the difference between the highest and the smallest measured width value.

Table 3.1
Membranes' width estimation at the ends (left, right) and at the middle (centre) parts (all in μm), using SEM scans of 8 membranes randomly chosen in the cell.

membrane	left	centre	right
1	8.837	8.724	8.854
2	8.965	8.763	9.013
3	8.981	8.774	8.981
4	9.045	8.843	8.933
5	8.981	8.837	8.981
6	8.997	8.832	9.030
7	8.901	8.758	8.917
8	8.885	8.737	8.901
mean	8.949	8.784	8.951
std	0.068	0.047	0.06
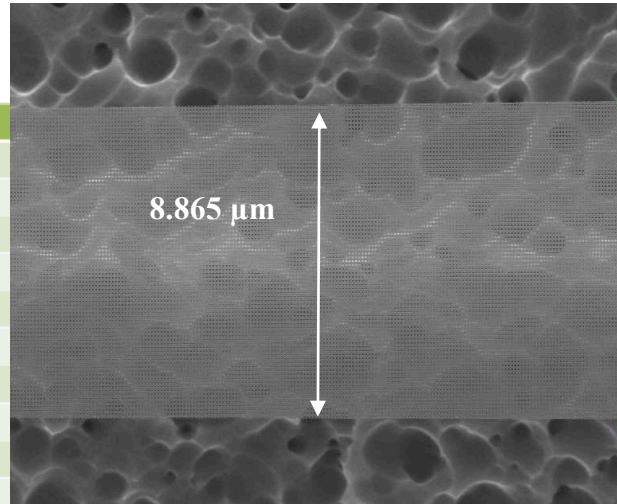
Figure 3.2
One of the estimated width values at membrane's centre obtained thanks to SEM scans (right) and corresponding table with the data for 8 membranes (left) and 24 measurements.

3.1.3 Thickness estimation

There are two possible approaches for the estimation of thickness. The first is to apply ellipsometry again, measuring the stack of native oxide, SOI and BOX at various spots of the membranes (Figure 3.4). High selectivity of HF etching implies that the SOI and membrane thicknesses have to be the same. The second way is to try to look directly at the membrane sides by tilting the sample in SEM (Figure 3.5). However, direct membranes observation detects mostly unevenly cut edges (Figure 3.4), which is the expected outcome of the etching due to the holes being located right at the edges. It is a tedious task to find many spots at different part of the membrane where the edge is even. However, some spots were found. SEM estimation can be used just as auxiliary information, since the resolution does not allow the precise sub-nm estimate that ellipsometry does.
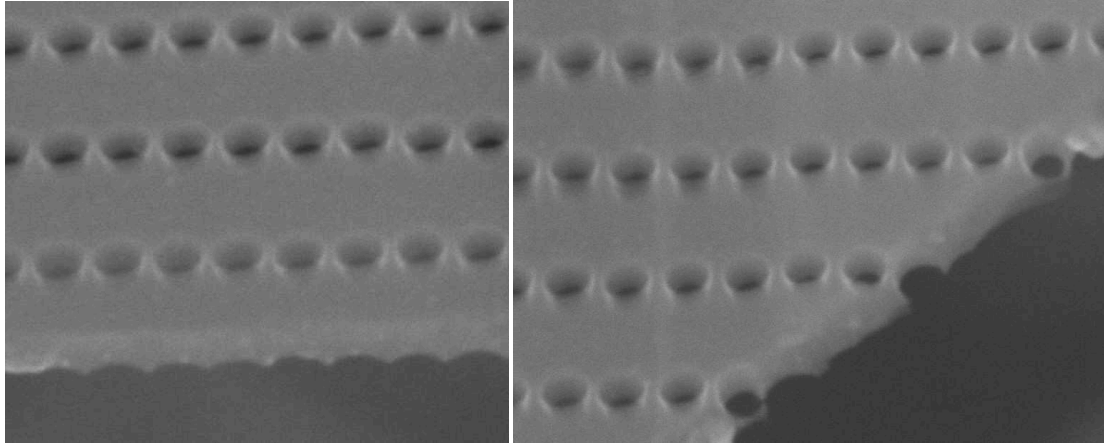
Figure 3.3
SEM scans of irregularities at membranes' edges caused by the phononic lattice. Smallest neck sizes between pores are around 16nm

Ellipsometry done at free spots yielded values (Table 3.2, after complete fabrication), that are similar to the previous estimation ("After oxidation"). Therefore, the average over all 6 points gave a thickness estimate for the membrane: w=43.8nm. Besides, a rough estimate of a very thin native oxide layer was obtained: 1.3nm. This value is of the order of typical wafer roughness, therefore the native oxide layer gave the highest contribution to the error, which was manifested in lower coefficient of determination, compared to the previous measurements done with much thicker grown SiO_2.
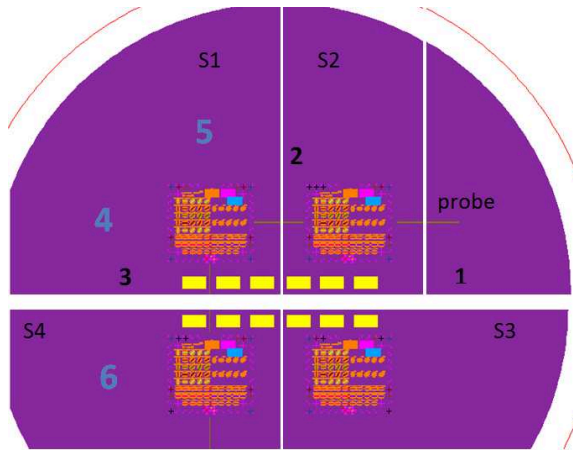
Table 3.2
Layers' thickness estimation by ellipsometry

Positions	SiO_2 grown	SiO_2 native	SOI	BOX	R^2
After oxidation					
1	19.3		42.5	147.9	0.84
2	17.3		44.4	147.8	0.9
3	17.9		43.8	147.9	0.93
After complete fabrication					
4		1.28	44.1	146.7	0.57
5		1.23	44.2	147	0.61
6		1.5	43.6	146.4	0.8
Mean	18.2	1.3	43.8	147.3	

Figure 3.4
Ellipsometry estimation (table on the right) of layers' thickness at different spots done after oxidation (black numbers) and after complete membranes fabrication (blue numbers). Averaged values are calculated from both measurement sessions.

It was possible to ensure the validity of out-of-membrane ellipsometry estimation using SEM at the even edge of membrane. The image was done in the tilted orientation of the sample. Obtaining the image estimated value T_{image}, one can calculate the real thickness, dividing T_{image} by cosine of the tilt angle $T_{real}=T_{image}/\cos(43.5°)$. This rough SEM-estimation

gave the thickness: T_{SEM}= 44.7nm, which is very close to the value obtained by elliposometry.
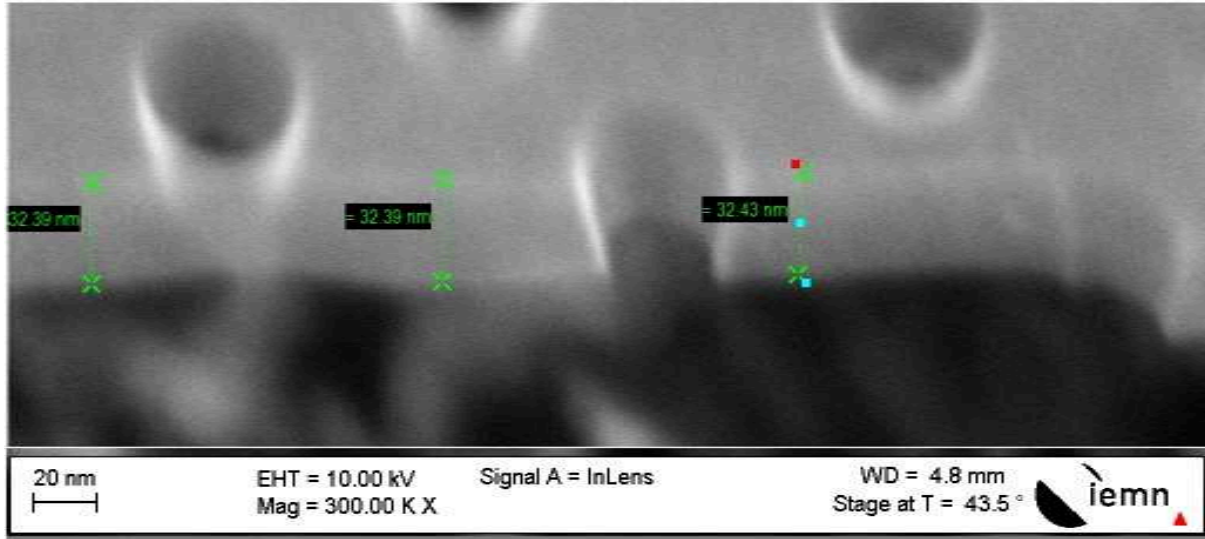
Figure 3.5
Membrane thickness estimation using SEM image. The measured intervals are in the plane, which is tilted by 43.5° to the plane where real width intervals lie.

3.1.4 Hole pattern characteristics and experimental goals

The same statistical approach, that was used for holes characterisation in Paragraph 2.3.4 was applied here. For five patterns from anisotropic series the average over big and small radiuses was estimated using statistical image tool and SEM scans of the membrane surfaces. The averaged radiuses vary slightly (by 2nm) around 25nm value.
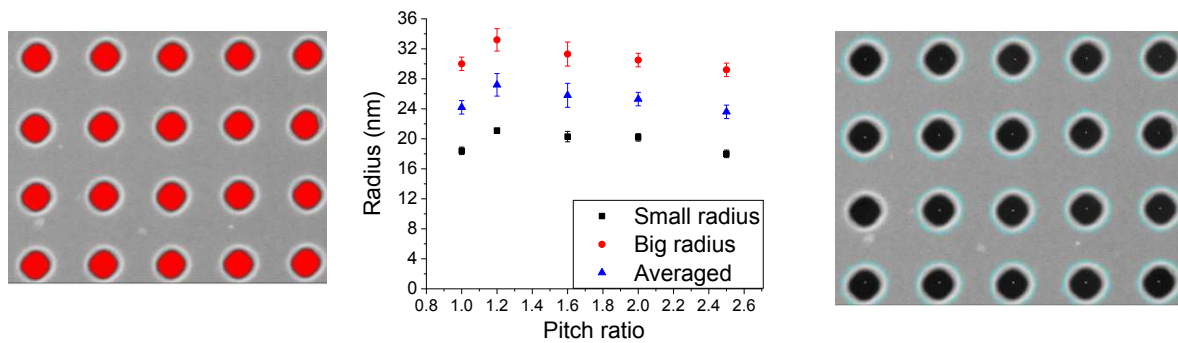
Figure 3.6
Hole radiuses for lattice patterns from anisotropic membranes series vs. the pitch ratio (r=pitch$_y$/ pitch$_x$) of the pattern. Corresponding small (left) and big (right) radiuses estimation SEM scans from statistical image tool (ImageJ).

Prior to summarising all the structural characteristics for anisotropic series of membranes, it is worth to review once again the whole picture of the planned experiment. This time (Figure below), it can be done using the experimental images, rather than design layout (Table 2.2). The main idea is that we want to study the heat transport in 5 phononic patterns

(realized in 2D ≈44nm-thick membrane). 4 patterns are anisotropic (which is characterized by the pitch ratio r = pitch$_y$/pitch$_x$ >1) and thus we expect to observe different heat propagation in different directions.
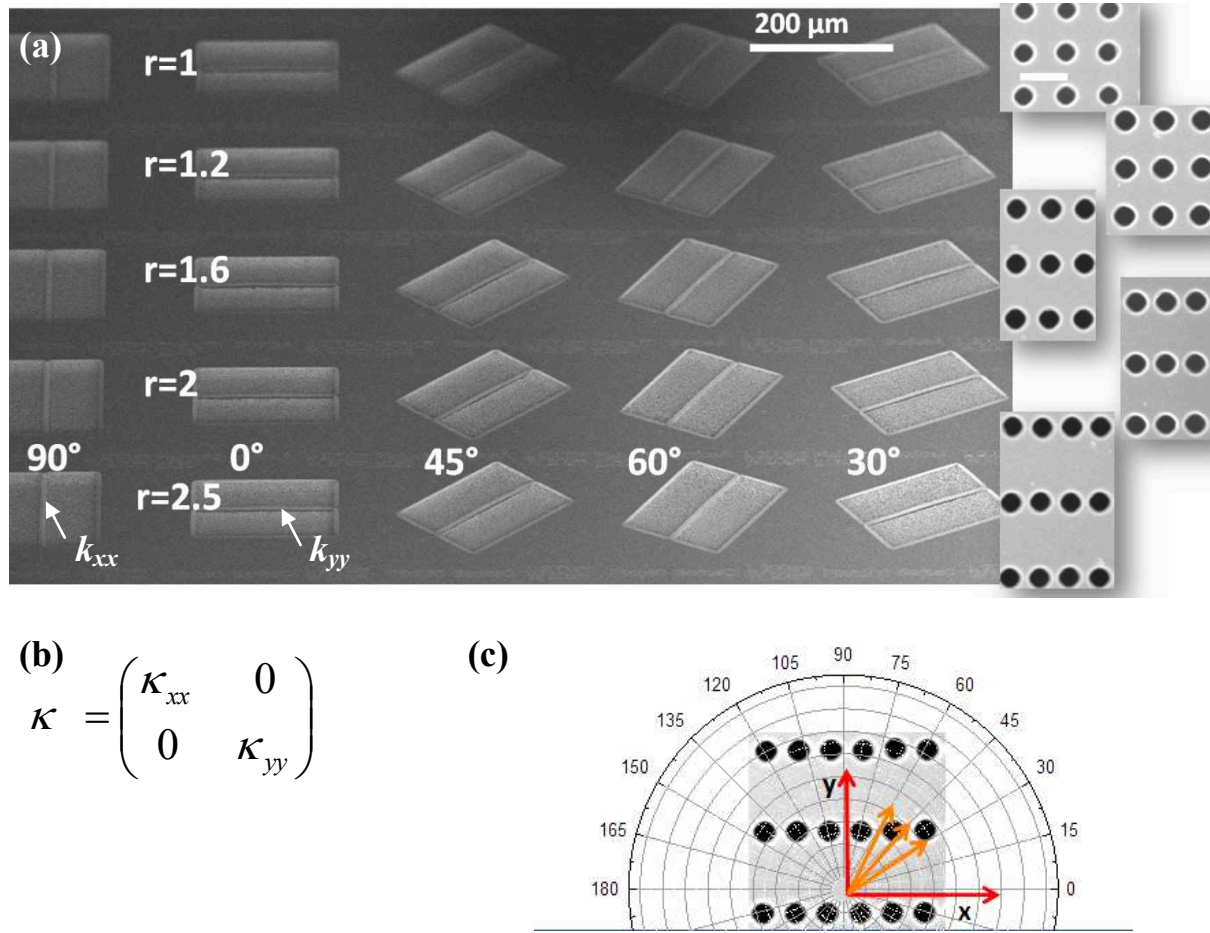
Figure 3.7
(a) SEM image of fabricated experimental platform consisted of 25 suspended Si PhMs with isotropic (r=1) and anisotropic (r=1.2 : 2.5) patterns of the hole lattices (SEM images on the right, the scale bar is 100nm for all) in 5 angular orientations. (b) Diagonalized in-plane matrix of thermal conductivity, expected to be obtained via measurements on phononic patterns in principal orientations (90°, 0°) and high pitch aspect ratio r=pitch$_y$/pitch$_x$. (c) Auxiliary sketch of the heat propagation directions with respect to the pattern orientation, for which thermal gradient and effective kappa were planned to be studied .

In order to eliminate the need for non-trivial calculation of the filling fraction (*ff*) or porosity contribution into the effective thermal conductivity, it is necessary to make the filling fraction (i.e. both unit lattice cell and the hole radiuses) as similar as possible over membrane patterns. The averaged unit cell area (**A** (r1, .., r2.5) = 10003 ± 10 nm^2) differs from pattern to pattern by 0.1%. A slightly higher ±8% deviation is observed in hole radiuses for the patterns. This leads to *ff* (calculated as *ff*=100%πR^2/A) variation from 17.5% to 23.3%, which concludes that fabricated phononic patterns have close, but not identical *ff*. Thus, quantitative comparison of thermal properties between different patterns can be valid only if this difference is well pronounced.

The table below summarises all geometrical structural characteristics of the membrane patterns. Pitches and radiuses were used to calculate the neck sizes. It is interesting that it was

possible to create a pattern with quiet small neck feature (15.8nm for r=2.5), close to state-of-the-art limits.

Table 3.3
Summary table of geometrical characteristics for anisotropic phononic patterns.

r	X-pitch, nm	Y-pitch, nm	Averaged Radius, nm	ff %	X-neck, nm	Y-neck, nm	Neck ratio
1	100	100	24.2 ± 0.9	18.4	51.6	51.6	1.0
1.2	90	111	27.2 ± 1.5	23.3	35.6	56.6	1.6
1.6	80	125	25.8 ± 1.6	20.9	28.4	73.4	2.6
2	70	143	25.3 ± 0.9	20.1	19.4	92.4	4.8
2.5	63	159	23.6 ± 0.9	17.5	**15.8**	111.8	7.1

In a similar manner geometrical characteristics were estimated for membranes with isotropic pitches. In the table below only membranes with the valuable experimental outcome are given. Despite the fact that membranes with multiple pitches were fabricated (up to 500nm), the experiment (as will be shown in this chapter) reveals that thermal properties (ΔT and κ) for membranes with the pitch > 140nm are similar to plain membranes.

Table 3.4
Summary table of geometrical characteristics for isotropic phononic patterns.

Pitch, nm	Averaged Radius, nm	Hole averaged surface, nm^2	Lattice unit cell, nm	ff %	Neck size, nm
80	26.7 ± 0.6	2240	6400	34.99	26.6
100	25.4 ± 0.5	2027	10000	20.27	49.2
120	24.9 ± 0.9	1948	14400	13.53	70.2
140	24.3 ± 0.4	1855	19600	9.46	91.4

3.1.5 TEM study of the surface roughness and oxidation

In order to evaluate the quality of the holes and membrane surface, STEM (scanning transmission electron microscope) and EDX (electron dispersive x-ray spectroscopy) were applied. FIB (focused ion beam) helped to prepare TEM lamellae. Prepared SOI layer with phononic lattices was sent for analysis to STMicroelectronics laboratory. The STEM and EDX images were made by R. Bon and F. André (requester: S. Monfray).
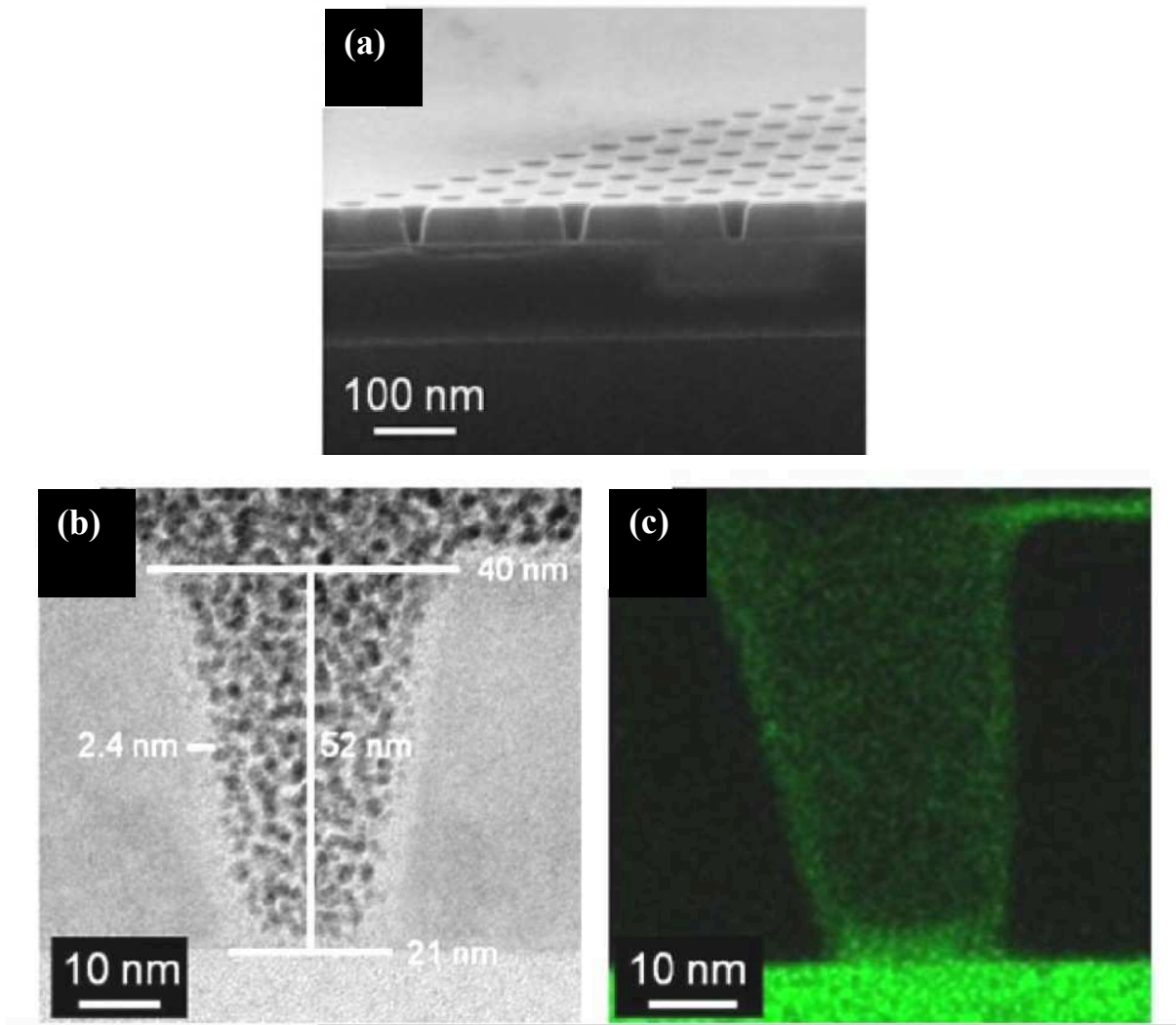
Figure 3.8
(a) SEM scan of the cleaved cross-section perforated with phononic holes, which were fabricated for preliminary STEM study. 55nm SOI layer was not oxidised, holes etched with Cl_2. (b) STEM cross-section view of the fabricated hole, the rough surface formed by the etching. (c) EDX scan with silicon (black) and oxygen (green) content. (b) and (c) images were done by R. Bon and F. André (requester: S. Monfray), STMicroelectronics.

From the a cross-section view of a single hole (Figure 3.8b), where the actual silicon thickness is 52 nm, it is seen that a thin 2- to 3-nm rough layer is present on the membrane's upper side as well as on the hole surface. By EDX scan, it was confirmed that the layer is at least partially composed of silicon oxide. This investigation concluded that the amorphous oxide layer of at least 1nm forms within a period of one month. This finding was used as an experimental reference[19] in computational study of the roughness and amorphous silica impact on the thermal properties of PhM.

The last work was performed for non-oxidised SOI layer. But it is crucial to repeat this study at the final stage of membrane fabrication. Besides, big improvement was planned: prepare lamellae sample in such a way that TEM scan can atomically give resolved images. For this purpose, the FIB cut (prepared by David Troadec, IEMN) was done along (110) crystal orientation (primary flat plane). To ensure that a hole cross-section can be obtained,

the lattice of holes was tilted by 35° with respect to (110) plane. TEM and EDX scans (prepared by M. Marinova, Lille1, Unité Matériaux et Transformations).
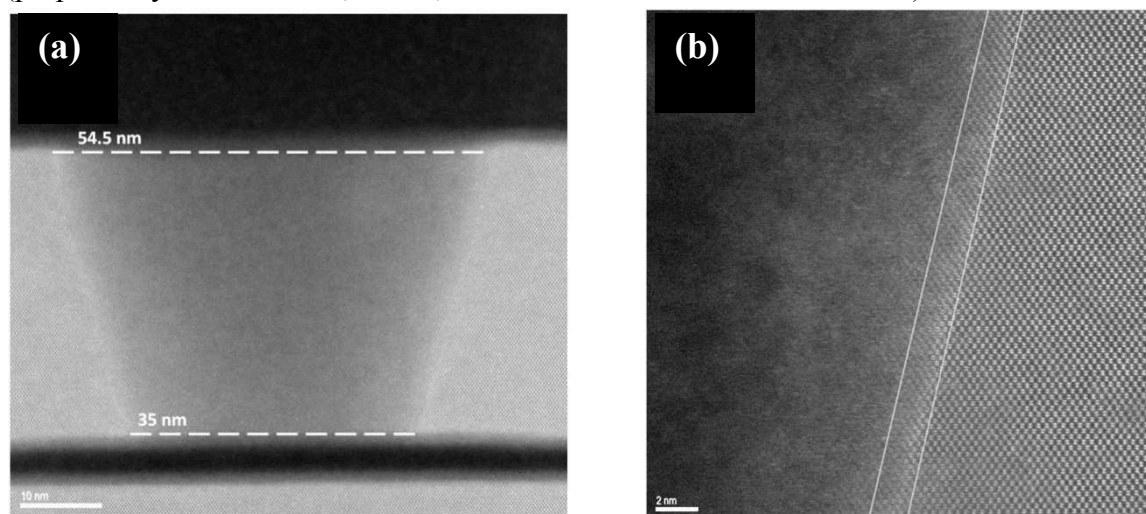
Figure 3.9

(a) High-angle annular dark-field imaging image of the cleaved cross-section of phononic hole at a final stage of fabrication. (b) Hole edge, atomically-resolved by HAADF showing the crystalline phase irregularities due to the roughness and/or amorphous phase presence. Images are courtesy of M. Marinova and David Troadec.

STEM extension, HAADF (High-angle annular dark-field imaging) was able to atomically resolve the hole profile (Figure 3.9). This technique detects high-angle electrons that are incoherently scattered from the atoms' nucleus (Rutherford scattering). Electrons that are scattered this way (in contrast to Bragg scattering) are sensitive to variations in the atomic number Z, which yields to Z-contrast images[68].

The probed sample was processed in a similar way as fabricated PhMs, however due to slightly higher oxidation, it is thinner by $\approx$10nm. The images show irregularities of the surface within 2-3nm. The high resolution image from Figure 3.11b demonstrates the transition of the crystalline phase into amorphous that occurs over the distance of 2nm. This transition is irregular, indicating the crystalline phase roughness presence of at least 2nm.

It can be concluded (Figure 3.10b) that the crystalline roughness on the walls of the holes is more pronounced than on membrane surfaces. This may be attributed to the fact that the holes were etched by Cl_2 at first and then the following oxidation process reproduced the surface irregularities formed by the etching.
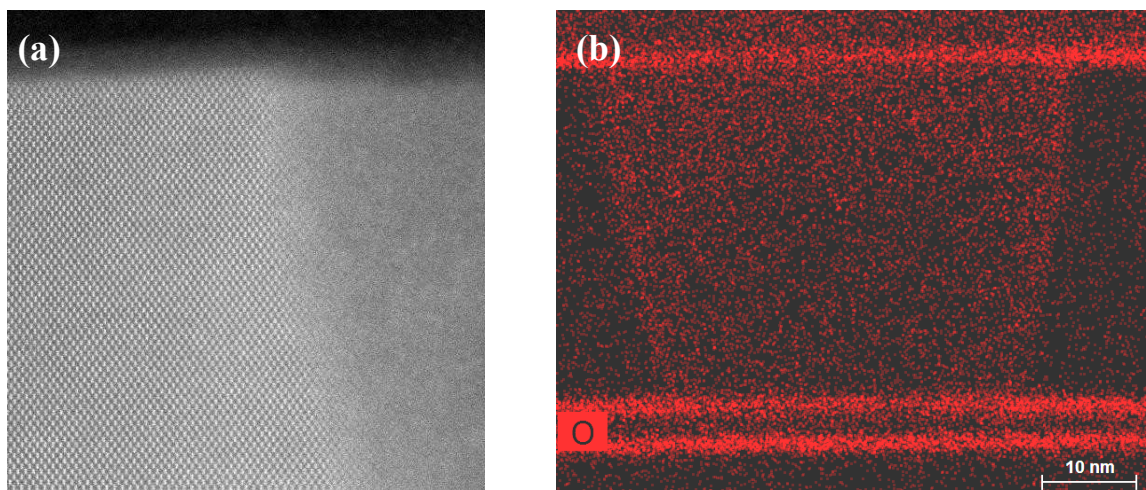
Figure 3.10
(a) Hole edge and top membrane surface, atomically-resolved by HAADF highlighting the contrast of irregularities on different surfaces. (b) EDX scan of the same hole, showing the presence of oxygen. Images are courtesy of M. Marinova.

The EDX analysis confirmed the presence of the native oxide layer on the walls of the holes. However, due to the different lamella preparation approach, the surface of the hole profile was open-exposed. This did not allow to obtain as good a contrasted picture of the hole edges as was demonstrated in the previous study, where the platinum filler was introduced into the hole volume. Therefore, it is hard to estimate the thickness of the oxide directly on the wall. At the same time the top and bottom surfaces are confirmed to have a 2-3nm layer of oxide. The brightness of the oxygen layer on horizontal surfaces is high on the image due to cumulative detection of oxide molecules over lamella width.

3.2 Micro-Raman Thermometry

A relatively novel contactless technique for thermal conductivity determination[12,21,22] was used in this work: micro-Raman Thermometry (μRT). Concerning anisotropic heat flow measurements, the main advantages of this method were discussed in Paragraphs 2.1.2, 2.1.3. Here is a brief summary of the advantages of this method: μRT allows for the better accuracy due to the elimination of errors related to the thermal resistance at the interfaces and heat losses in the metal sensors; the method is based on the simplicity of experimental configuration, which allows to measure the temperature noninvasively thanks to direct proportionality between the temperature and the Raman shift; μRT combined with FSBL (free-standing beam-like) topology of the membrane allows for the measurements of the κ eigenvalues in a simple way. The limitation may vary depending on particular implementation of the Raman Thermometry experiment (see 3.2.1). In our case, the main limitation is attributed to the requirement of the accurate estimation of the absorption, which depends on simulation reliability and literature refractive index values.

This section mainly describes the development of experimental methodology, including some details about the upgrade and installation of crucial elements for the μRT set-up. The author addresses in details the issues of data analysis, error estimations and minor design drawback, which require a careful treatment.

3.2.1 Experiment general overview

The main idea of the Raman Thermometry experiment is the utilisation of laser radiation as a heater and a thermometer (utilising its Raman scattering properties). Incident laser beam heats suspended membrane creating the steady-state heat flow (radial or in one direction depending on the sample configuration), which manifests itself by the temperature gradient. Depending on the geometry of the problem, structural and convective conditions, one can solve a heat equation analytically or numerically and thus formulate the relation between absorbed power P_{abs}, temperature at the heating spot T_0 (or the whole T-profile) and the thermal conductivity κ.

P_{abs} can be found via absorption A, which can be found via transmission and reflection measurements done in parallel with the μRT or by doing the numerical correction to the literature dielectric constant (3.2.4). T_0 or T-profile can be measured by the Raman excitations in μRT (3.2.3). When T is measured and P_{abs} is estimated, one can apply numerical simulation to find κ, or, if geometry allows, directly use analytical expression. For example, in the case when the large-scale membrane in vacuum is heated by the laser, 2D radial heat propagation is described by the expression (15)[69], which is a modification of Fourier law. Its integrated form (16) gives the expression for the T-profile, that can be found experimentally and then fitted in order to obtain κ.

$$\frac{P_{abs}}{2\pi rd} = -\kappa \nabla T \tag{15}$$

$$T(r) = T_0 - \frac{P_{abs}}{2\pi d\kappa} \ln(r/r_0) \tag{16}$$

where d is the thickness, r is the radius from the heating spot centre, r_0 is a spot radius (where the field intensity drops to $1/e^2$).

Both tasks (heating and temperature probing) can be combined by one laser source (Figure 3.11a). In such a case, only T_0 is measured. Then it is possible to estimate κ analytically for beam-like membranes, or numerically using FEM (see Paragraph 3.2.5). For better accuracy many ΔT_0 points have to be calculated, either as a function of P_{abs} at a constant location or as a function of position at a constant temperature.

A more difficult in terms of experiment, but very reliable approach is the two-laser scheme [69,70] (Figure 3.11b), which does not require complex modelling since T-profile can be directly measured. However this method can impose systematic uncertainty due to temperature fluctuations induced by the probe laser.

Another important design feature is the detection of transmitted beam power (Figure 3.11c), that allows for experimental determination of the amount of the absorbed radiation and thus increase the reliability of the experiment. However, free-standing beam-like topology of fabricated PhMs makes the opening of the bottoms of the cavities almost not feasible. Therefore, absorption values were estimated analytically.

(a)

(b)

(c)
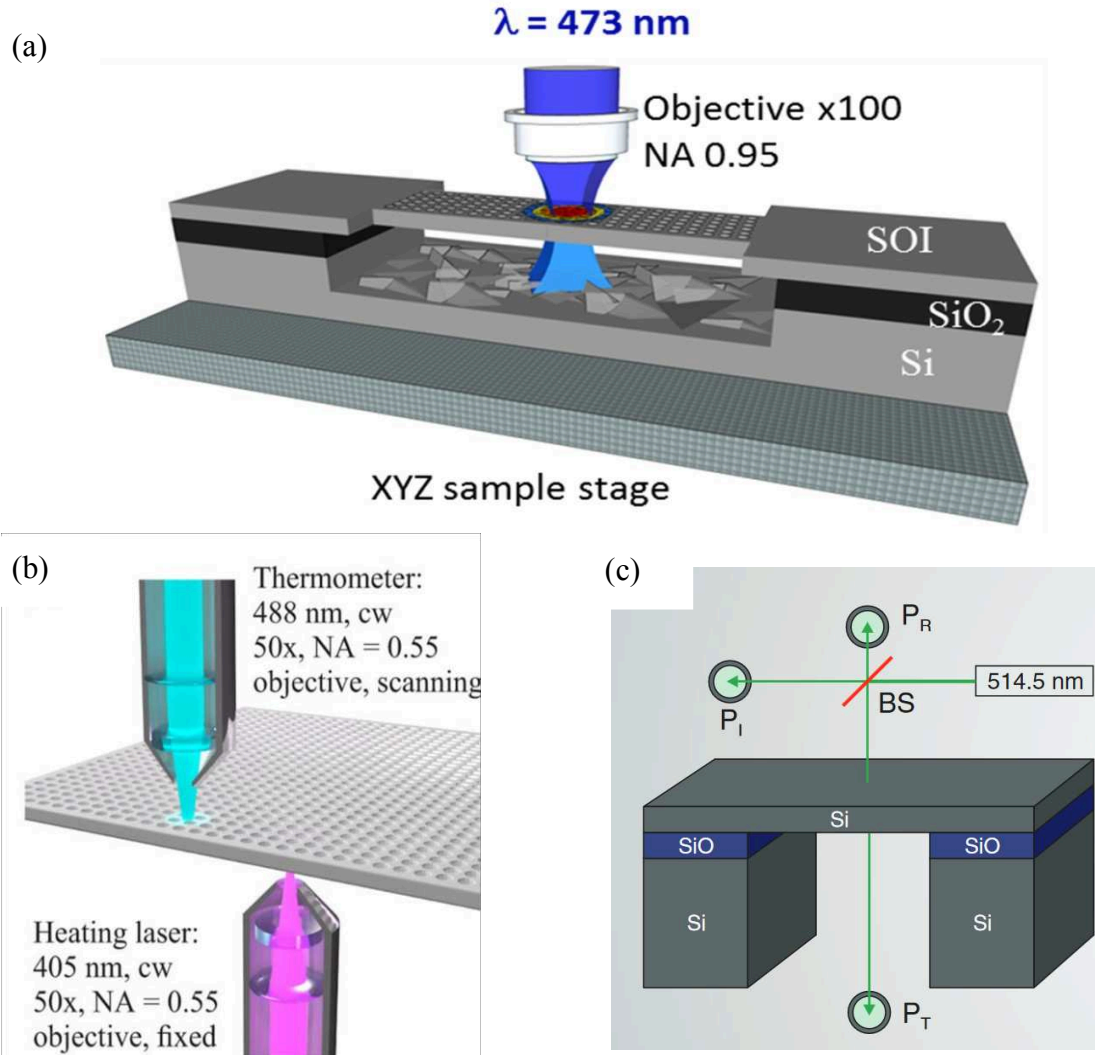
Figure 3.11

Schematic representation of the PhM measurement process in two different configurations of the μRT experiment: (a) current work method utilising one laser source[22] (image is courtesy of M. Massoud), (b) two-laser μRT[70] and one-laser μRT with power meters used to determine absorption coefficient of the membrane.

3.2.2 Set-up

Inelastic second order scattering (Raman) is profoundly smaller in intensity than the first order effects (like elastic Rayleigh scattering)[71], in terms of the number of scattered photons the ratio of these processes is $1:10^{12}$. Typically, double monochromator is used to ensure good rejection of elastically scattered photons. According to the selection rule, only LO phonon mode is a source of backscattering from (001) Si surface if incident light has (100) polarisation. Therefore, only one peak in the Raman shift spectra is detected in our experiment where (100) plane is a wafer surface and the laser beam has a normal incidence.
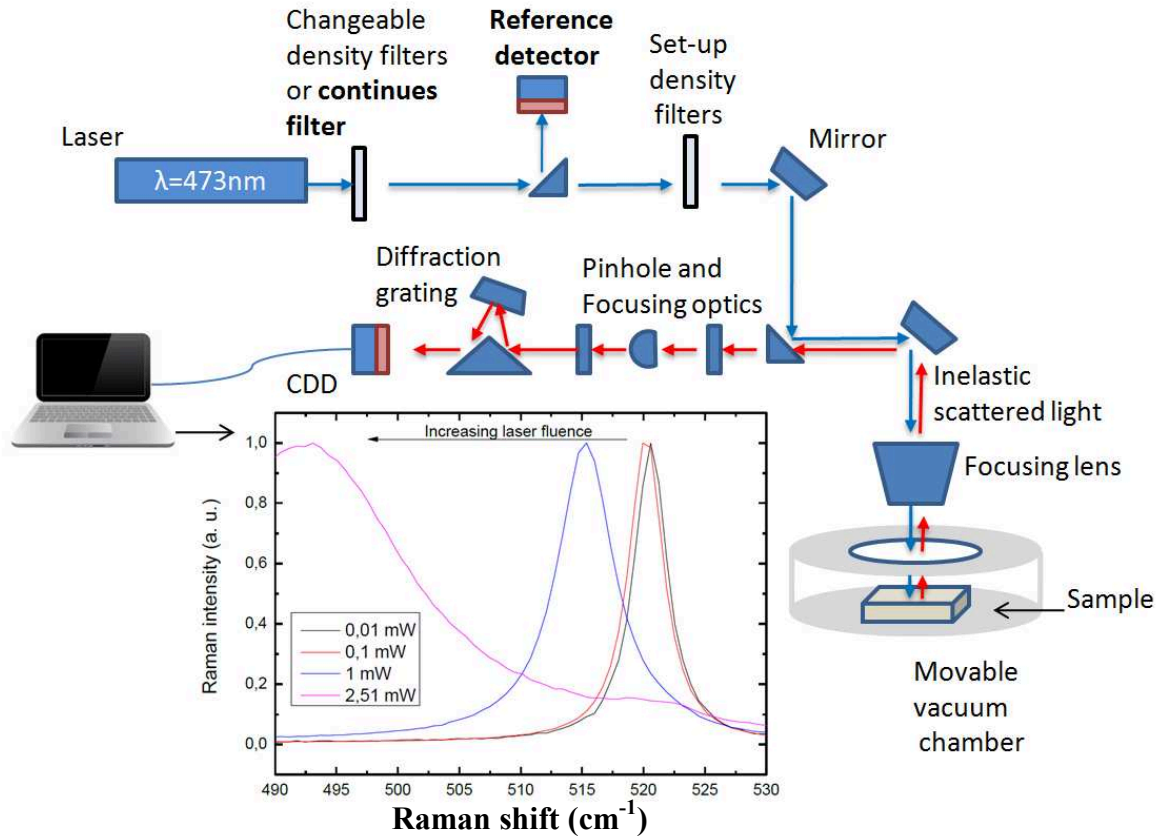
Figure 3.12
Schematic representation[22] of Raman microscope analogous to LabRAM HR confocal system from Horiba Jobin-Yvon[72] used with 473.11 nm continuous-wave diode-pumped laser. The parts indicated in bold were purposefully installed (Paragraph 3.2.9) to improve the experiment. The plot shows the typical Lorentz distributions (obtained on the plain Si membranes) of the measured Raman Shift signal. Distribution shifts to the left as the T (and incident power) increases.

The figure above demonstrates typical measurement procedure of a bulk Si Raman shift. It is important to note, from what follows all μRT measurements are done in vacuum in order to eliminate convective heat losses. Laser beam ($P_0 \approx 8$mW, $\lambda_0 = 473.11$ nm) is attenuated by two filters (from changeable and set-up series). Each filter is characterised by the optical density number $OD = \log(P_0/P)$ with $OD_R = [4, 3, 2, 1, 0.6, 0.3]$ for set-up and $OD_C = [0.1, 0.5....]$ for changeable filters. Thus, using combinations of OD_R and OD_C , one can obtain different incident powers. The beam is focused with strong lenses x100 (NA=0.5, $r_0 = 1.22\lambda_0/(2NA) = 0.58$μm) or x50 (NA=0.42, $r_0 = 0.69$μm), where r_0 is a theoretical beam radius at a focal plane, assuming diffraction limited case of the beam and perfect parts of the system. High resolution defines the name "micro-Raman Thermometry". For bulk thermal conductivity, the Raman shift ($\omega = 1/\lambda_0 - 1/\lambda$, where λ is reflected wavelengths) is constant at least up to 0.5mW[73]. This is due to a strong heat flow that leaves the spot of incidence at the ambient level, and T is linearly proportional to ω (which is explained in the next paragraph). Thus, the frequency of the red shifted reflected light defines the Raman shift for a room temperature (RT), which is typically $\omega \approx 522$ cm^{-1} for Si. In order to obtain the wavelength of the red-shifted signal, high-selectivity diffraction grating (monochromator) is used. The signal measured by CCD camera has a Lorentz distribution (Figure 3.12).

Another important part of the set-up is the vacuum chamber. All the measurements were performed at a vacuum pressure ≈ 5 10^{-4} Pa, which avoids convective heat losses from the membrane and ensures the localisation of the absorbed heat inside the membrane.

3.2.3 Temperature of the heating spot determined by μRT

In the fundamental work of Balkanski *et al.*[74], cubic and quadratic anharmonic contribution into Raman shift and optical (LO) phonon was studied. The approach which is based on the Klemens[75] model, accounts for three and four anharmonic phonon interactions, which allows for an accurate treatment of experimental results at high temperatures: 800-1400K (see Figure 3.13). It was shown, that both Raman shift (Δ) and damping constant (Γ) temperature dependence can be expressed as a sum of cubic, quadratic (plus higher orders) terms of anharmonic Hamiltonian.

$$\Gamma = A\left[1+\frac{2}{e^x-1}\right] + B\left[1+\frac{3}{e^y-1}+\frac{3}{(e^y-1)^2}\right],$$ (17)

where $x = \hbar\omega_0/2k_BT$, $y = \hbar\omega_0/3k_BT$, and anharmonic constants $A = 1.295$ and $B = 0.105$.

At a high-T limit factors multiplying A and B change as T and T^2.

Another way to express this anharmonicity is to derive the Raman shift $\Omega(T)$ as a function of contributions from three and four phonon processes, which have analogous T-dependence:

$$\Omega(T) = \omega_0 + \Delta(T),$$ (18)

where ω_0 is the shift at 0K.

$$\Delta(T) = C\left[1+\frac{2}{e^x-1}\right] + D\left[1+\frac{3}{e^y-1}+\frac{3}{(e^y-1)^2}\right],$$ (19)

where free-phonon and four-phonon constants: $C = -2.96$ cm^{-1}, $D = 0.174$ cm^{-1}.

This concludes that the anharmonicity of vibration potential energy allows to probe the local temperature in the crystal through Raman spectrometry.

In the range between room temperature and high-T limit, the dependence can be approximated as linear. For example, when expressing the Raman shift in terms of thermal expansion and anharmonic phonon-phonon coupling[73], taking Maclaurin series and cutting off at linear terms, it is possible to obtain the slope for linear approximation.

$$\left(\frac{d\omega}{dT}\right) = -3\omega_0\gamma\alpha + \frac{k_B}{hc\omega_0}\left[4A+9B\right]$$ (20)

where γ is Gruneisen parameter, α is the coefficient of linear thermal expansion.

Another way of finding the slope is by expressing (18) through (19) for the room temperature value (300 K). The slope obtained is equal to $\chi_T = -0.022$ cm^{-1}K^{-1}, which is in good agreement with other literature estimations.
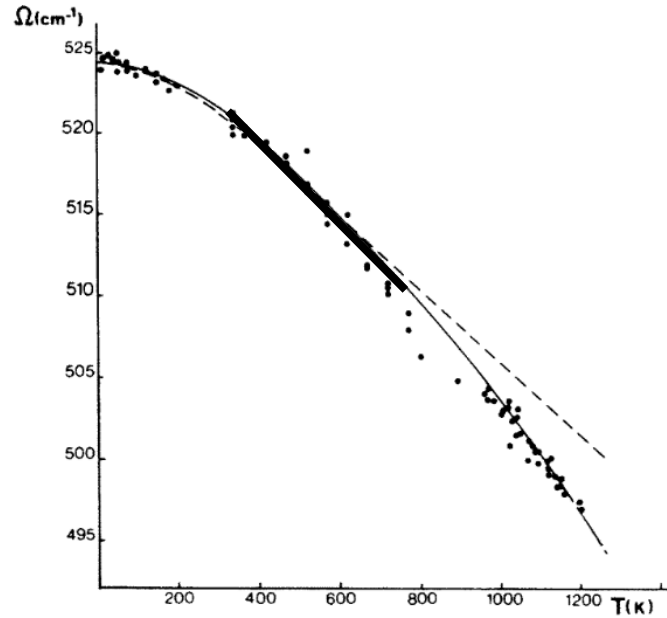
Figure 3.13
From Balkanski *et al.*[74]: Raman shift as a function of temperature. The solid and dashed curves are model fit accounting for free- and four-phonon and only free-phonon processes respectively. Thick line is a guide to the eye highlighting the idea of linear approximation between 300K and 800K

The figure above demonstrates the fit of measured Raman shift vs. T. Below high-T limit (<800K) in the range from 300K to 800K linear fit (theoretical model that does not include four-phonon contribution into anharmonicity) well approximates the data. This makes the use of the Raman shift feasible as a linear response to temperature change.

3.2.4 Estimating the absorption

In order to model the heat transfer in the membrane, one has to know precisely the amount of heat absorbed by the material, which is equal to P_{abs}. This value can be estimated by measuring the power of the incident laser beam P_{in} and calculating the absorption coefficient A of the membrane: $P_{abs} = AP_{in}$. During the experiment the power was measured with Si power meter (Thorlabs[76]).

Fabricated plain Si membrane can be viewed as a single-layered thin film optical resonator, or Fabry-Perot interferometer. By applying transfer-matrix formalism[77], one calculates coefficients of reflection and transmission. We assume that there is no light absorbed at the bottom side of the membrane because the bottom surface of the device cavity is very rough and scatters the light. The calculation was done iteratively for thicknesses varying from 10 nm to 200 nm (Figure 3.14). The index of refraction was taken from the COMSOL5.1 Optical module, which constructs an interpolation using data obtained by Vuye et al[78]. This index was chosen in the previous works[21,22] in FEM analysis of experimental data (Paragraph 3.2.5). Now we use this index again, but only as a test input parameter for the new version of FEM model, which was constructed independently and had to be referenced for the output with the previous version of the model. As shown in the plot below, there is a drop of more than two-fold in the absorption as the thickness decreases from 55 to 45 nm (similar situation effects occur with other refraction index values from the literature). Later in this work, the optical constant from another source[79] is used.
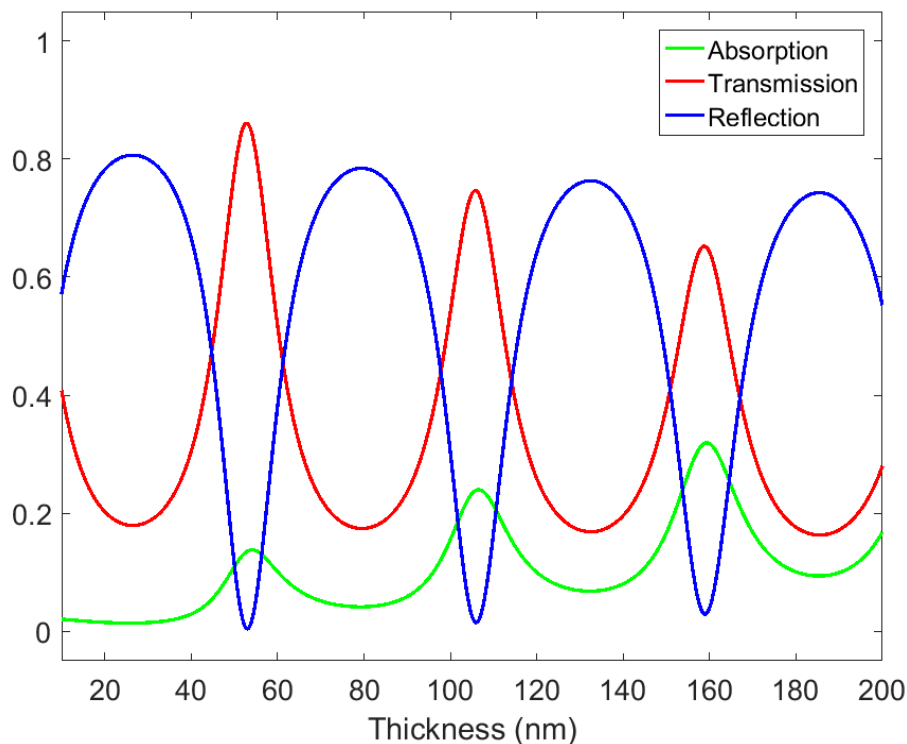
Figure 3.14

Coefficients of absorption, reflection and transmission of 473.11 nm laser light in single-layered Si thin film with complex index of refraction n = 4.4644 + i0.0471 (@20C° Vuye).

Vuye et al[78] showed that both parts of refractive index are slightly T-dependent close to and above room temperature. This dependency might not be negligible and affect the absorption. Using the same Matrix formalism, the absorption coefficient as a function of the thickness was calculated at 20 C° and 100 C°. The clear 1% difference in the absorption for 55-65-nm-thick membranes, created by 80 C° temperature rise, had to be taken into account for Raman Thermometry analysis. However, the absorption of new fabricated 44-nm-thick membranes can be considered as T-independent in 20-100 C° range.

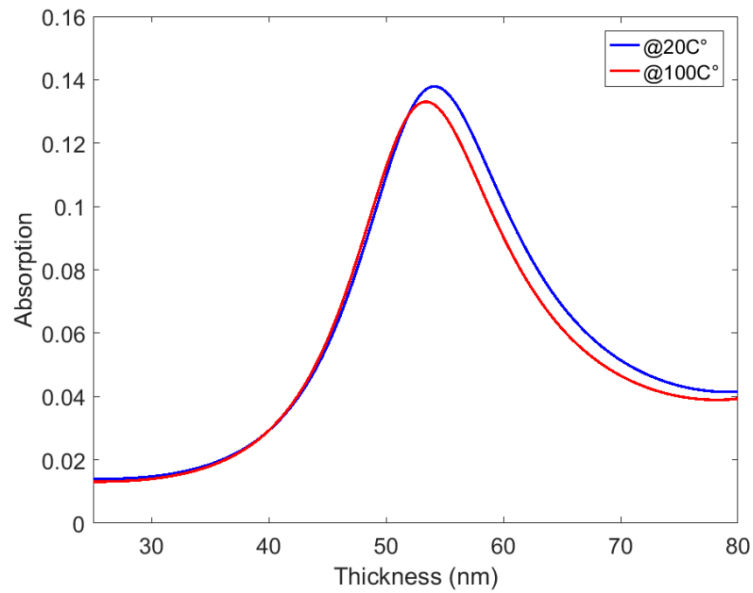**Figure 3.15**
Absorption at 473.11nm in a single-layered Si thin films with complex indexes of refraction n (Vuye, @20C°) = 4.4644 + i0.0471 and n (Vuye, @100C°) = 4.5221 + i0.0453.

3.2.5 Modelling the thermal conductivity

In order to get a quick insight into the problem, let us use the electrical analogy for the heat transfer model in the studied membranes. In the case of zero convection and the simplest slab-like geometry, according to the Fourier's law, the thermal resistance R[K/W] relates the temperature difference to the heat flux ($\Delta T = P_{abs}R$) same way as the electrical resistance relates the voltage to electrical current: U=IR. Figure 3.16 (left) illustrates this analogy for two parallel thermal resistors. The idea is that the left and right heat paths from the laser hot spot (heat source spot) to the cold membrane's ends (see sketch on the right) can be viewed as two parallels resistors, which resistance varies with the position x of the laser spot:

$$R_{l/r} = \frac{R_k(\frac{L}{2} \pm x)}{wt},$$ (21)

where L, w and t are length, width and thickness of the membrane slab respectfully, R_k is thermal resistivity [Km/W].

In this simplified model the thermal conductivity can be generally expressed as [remark: $\Delta T(x)$ is a parabola (Figure 3.18) therefore there is no parabolic dependence of κ vs. x, which seems to be appeared in a formula]:

$$\kappa = \frac{1}{R_k} = \frac{P_{abs}}{\Delta T(x)} \frac{L}{4wt}(1 - \frac{4x^2}{L^2})$$ (22)

If the laser spot is at the centre:

$$\kappa_{x=0} = \frac{P_{abs}}{\Delta T} \frac{L}{4wt}$$ (23)
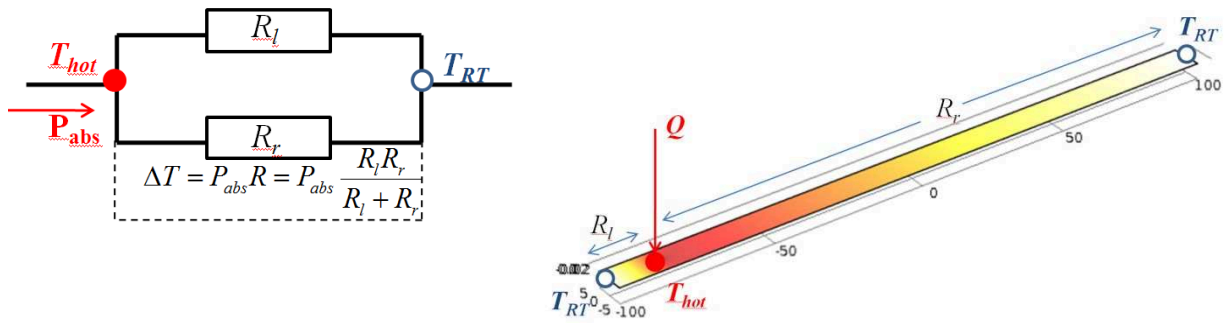
Figure 3.16
Plain Si membrane (on the right) in the form of a slab with spots of laser heating and room temperature heat-sink at the ends. Electrical analogy of two thermal resistors that correspond to the right and left heat paths, when the hot spot at the centre.

In principle, we could use equations (22,23) to fit the κ in the T-profile method or P-variation methods (in a vacuum). But the real device geometry is a bit more complicated than that of a simple slab. In addition, the heat source distribution is not uniform. It has a Gaussian shape (24), where σ=0.6μm is a standard deviation, taken from the work[22] of M. Massoud, where he used it for the same experimental data as we do here to verify that the model is correct (Figure 3.18). For this work experiments, σ for different lenses was measured (Paragraph 3.2.8). Accounting for these factors, a Comsol model was constructed (Figure 3.17).

$$P_{abs}(x,y) = \frac{AP_{in}}{2\pi\sigma^2} e^{\frac{-(x^2+y^2)}{2\sigma^2}} \qquad (24)$$
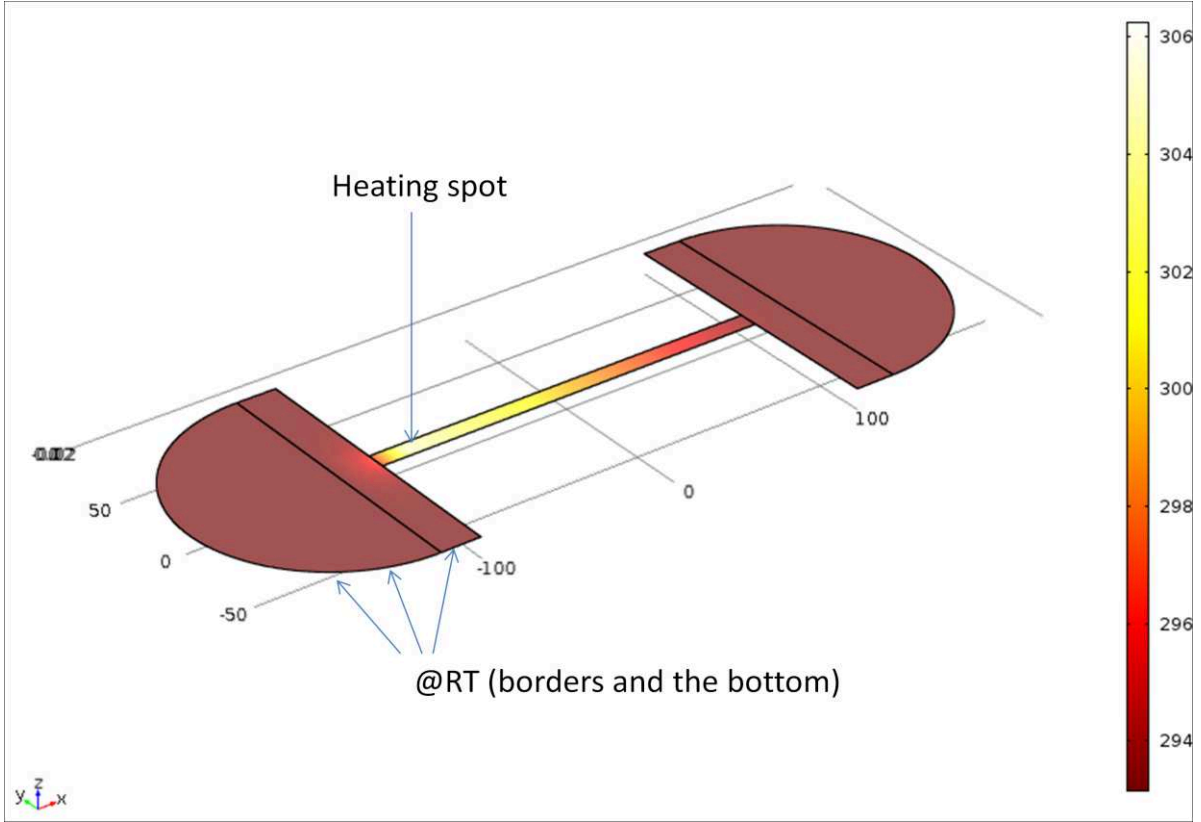
Figure 3.17
COMSOL model for thermal conductivity fitting using experiment geometry and Finite Element Model analyses for heat transfer.

The key fragment of the device geometry, that makes a big difference in heat propagation relative to the slab case, is 10-20μm-wide SOI "wings" that are formed as a result of the etching around the cavity (as seen in the centre image of Figure 2.12). They can be viewed as membrane extensions. The analysis done in COMSOL shows some difference in the temperature profiles envelope between the slab and the device geometries (Figure 3.18) for the same value of fitted k. From what follows, the device geometry will be used in this work when experimental data has to be fitted by FEM model. The width of the SOI "wing" is found by the SEM study. In the figure below, the experimental results were obtained by the T-profile method for a membrane of the generation fabricated in the previous research[21]. Those membranes have a thickness of about 60nm and were suspended over the cavity that is surrounded by 20nm-wide SOI wings.

Using parameterisation of the laser spot position and thermal conductivity value, it is possible to fit the experimentally obtained data of the profile envelope. The fitting curve from the figure below yielded κ = 58 W/mK, which matches with the findings obtained independently by our colleague[22] who used the same data in the similar and independently constructed COMSOL model.
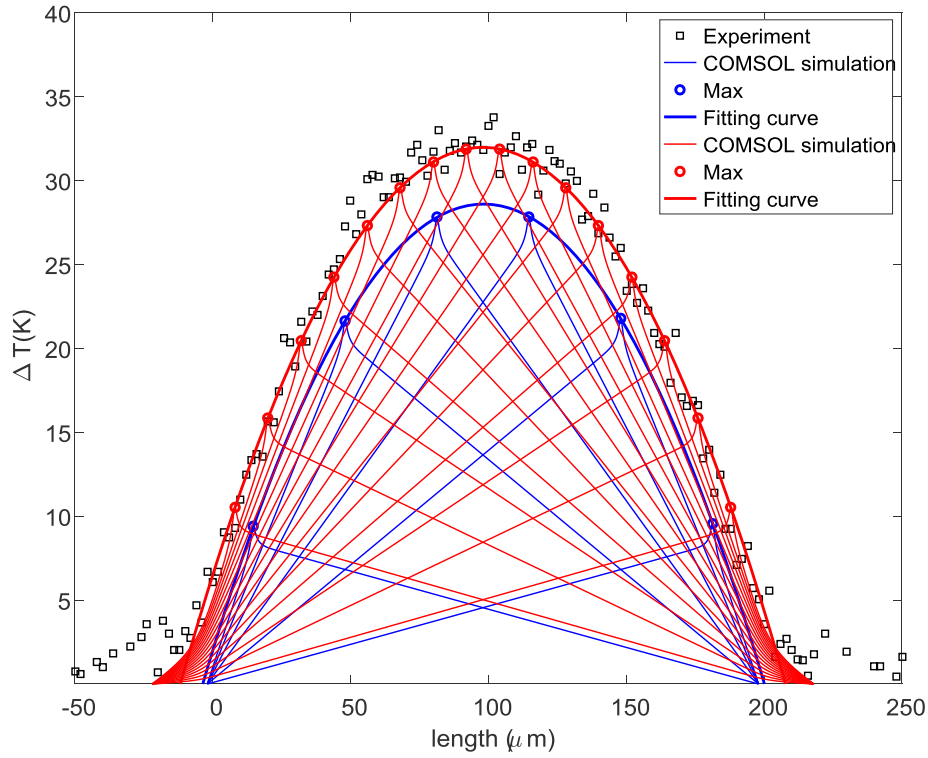
Figure 3.18

Temperature profiles (thin lines) in the Si plain membrane for parameterized laser spot positions (along the membrane length), calculated by COMSOL solver with the simple slab (blue) and device (red) geometries. Scatter points are profile's maximums, measured experimentally. Thick lines are second degree polynomials which are used to fit the maximums' points. Experimental data points of the profiles envelope were obtained by the Raman micro thermometry measurements[22]. Both geometries were simulated for the membrane with the thickness th=59.4 nm, length = 200 µm and width w = 10 µm, laser power P_{in} = 185 µW, absorption A = 10.63% according to (Vuye[78], @20C°, @473.11nm). Wings size for the device geometry equals 20 µm.

The COMSOL model was also tested with earlier data for the same plain membrane obtained by power-variation method (Figure 3.19). Experimentally we are looking for the same physical quantity as in the temperature-mapping method: $\Delta T(\Delta\omega(P_{abs}))$. The only difference is that, now, we vary the laser power, or the power absorbed by the membrane. In the experiment for data tested here, the laser was always focused at the middle of the membrane. According to the model fit thermal conductivity value is close to 56.5W/mK, which is also in agreement with the outcome of the previous model. Another conclusion is that both types of measurements lead to similar estimations of κ.
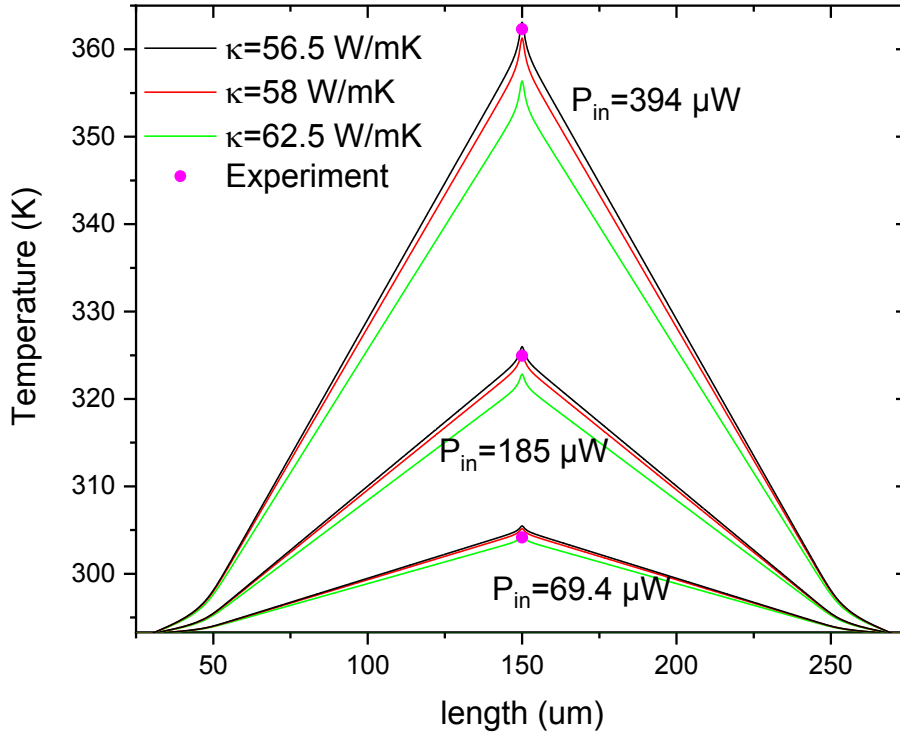
Figure 3.19

FEM-simulated temperature profiles (solid lines) of the heat propagating in the Si plain membrane for parameterized power of the laser light incident into the middle of the membrane, and for different values of thermal conductivity. Pink points are µTR experimental values. Membrane has the thickness t=59.4 nm, length = 200 µm and width w = 10 µm. Absorption A = 10.63% according to (Vuye[78], @20C°, @473.11nm). Wings size for the device geometry equals 20 µm.

3.2.6 Absorption estimation for new phononic membranes

In the presence of the holes lattice, the absorption slightly changes due to photonic effect, which arises as a result of a light scattering on periodic structures. Numerical technique called Rigorous Coupled-Wave Analysis (RCWA) helps to define corrections for structure-modified optical properties, applying Fourier-space formalism[80] (electromagnetic field is represented as a sum of spatial harmonics) and Floquet theorem. Solutions for electromagnetic modes with particular wave vector of the incident plane wave and periodicity of the dielectric material can be obtained by the differential Maxwell's equations and the boundary conditions, expanded by the Floquet functions and turned into infinitely large algebraic equations[81]. RCWA analysis was done by R. Orobtchouk and M. Massoud, in the frame of a collaboration with the Institut des Nanosciences de Lyon (INL) et Centre d'Energétique et de Thermique de Lyon (CETHIL).
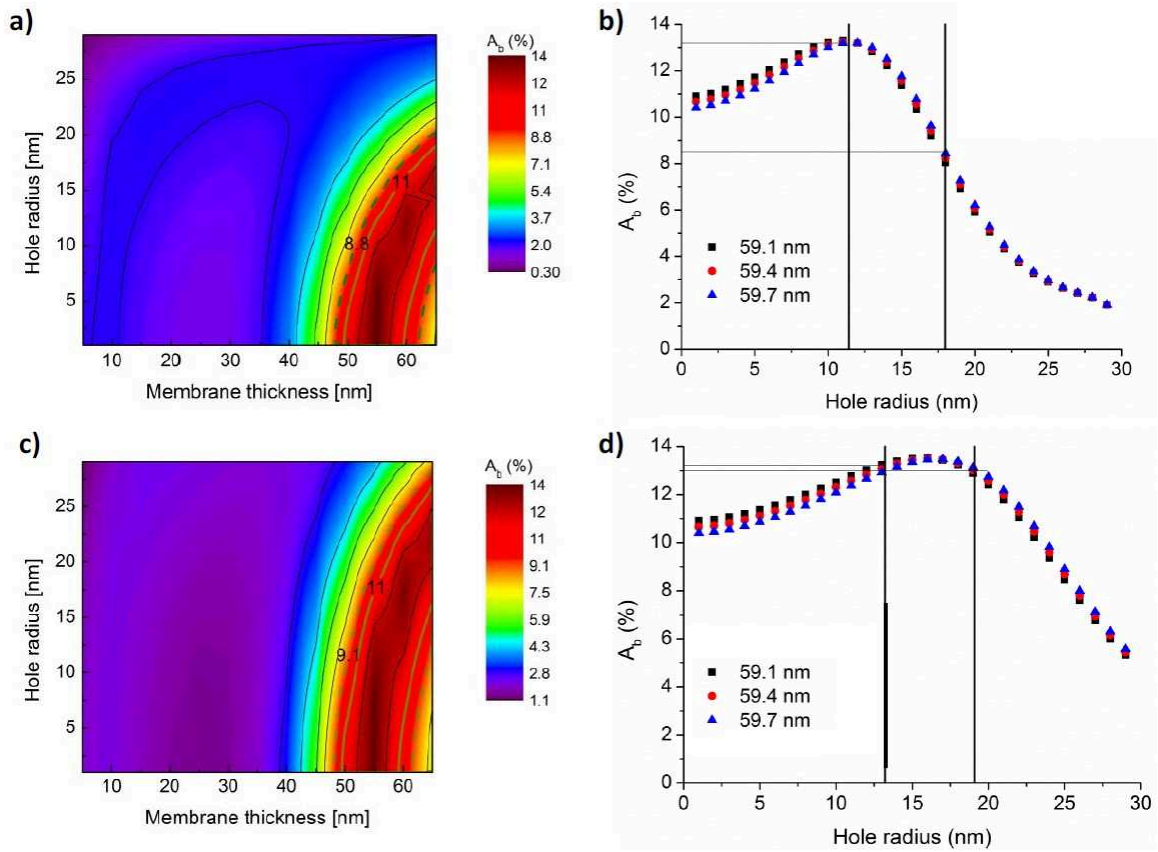
Figure 3.20
Figure courtesy of CETHIL, A. Massoud *et al*. RCWA-calculated absorption as a function of (a,c) holes' radius and membrane thickness, (b,d) holes' radius for different thicknesses. Upper row corresponds to 60nm lattice pitch, the bottom row is for 80nm pitch. Refractive index according to Vuye[78] @20C°, @473.11nm.

RCWA absorption corrections (figure above) have revealed that for ≈60nm-thick membranes at some pitches (the case of 60nm pitch on the figure, upper row), the absorption is very sensitive to the hole radius. This gives rise to big absorption error, even at moderate error of radius. These observations make RCWA a crucial step in our analysis. For this reason a more careful choice of optical constants was done. Palik[79] constants were chosen as they seem to be more reliable in RCWA model tests. New RCWA simulation based on new refractive constants for 43.8nm-thick membranes showed way less absorption change with respect to the radius and the pitch (Table 3.5).

.

Anisotropic		Isotropic	
Pitch ratio	A, %	Pitch, nm	A, %
Plain	3.73	80	2.39
1	2.42	100	2.98
1.2	2.26	120	3.32
1.6	2.39	140	4.31
2	2.5	160	3.53
2.5	2.67	180	3.58

Table 3.5

RCWA absorption corrections from CETHIL (by R. Orobtchouk and A. Massoud) for anisotropic and isotropic PhMs with characteristic lattice parameters. Refractive index from Palik[79] (n = 4.463 + i0.0367) and 43.8nm thickness were used.
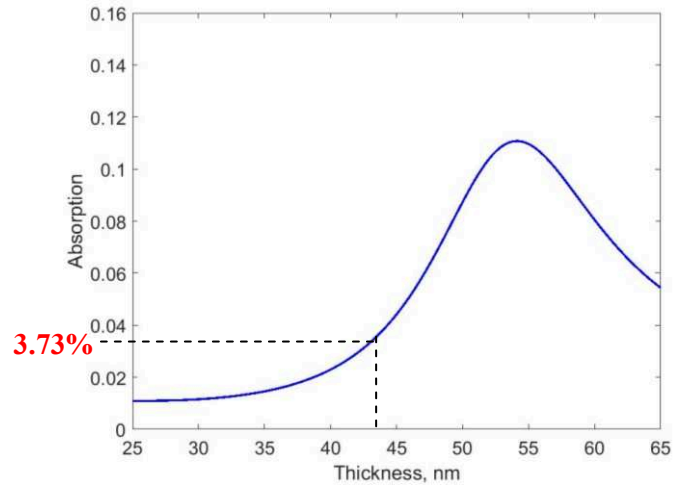
Figure 3.21

Absorption at 473.11nm in a single-layered Si thin film as a function of thickness calculated by transfer-matrix method, using refractive index from Palik[79] (n = 4.463 + i*0.0367).

In the analysis for anisotropic patterns, a cylindrical holes shape was modelled with the radius value as the mean of top and bottom radiuses for the real truncated-cone shape (Paragraph 3.1.4). Whereas for isotropic patterns all three values (top, bottom and mean radiuses) were checked for comparison. It was shown that the averaged error or difference between absorption values corresponding to high (top) and low (bottom) estimations of the holes' radius constitutes not more than 1.3% of the absorption values. This error contribution is negligible compared to 10% error for the incident power measurement.

3.2.7 Attempt to eliminate photonic effects

As was shown in the previous paragraph the estimation of the optical properties by RCWA for the previous generation of perforated membranes revealed that the absorption is strongly related to the radius. Expecting a similar picture for the new generation of anisotropic PhMs, we decided to introduce non-perforated platform at the centre of the membrane, the area of which was supposed to be the host spot for incident laser beam (Figure 3.22). For the P-variation measurement, the use of the non-perforated platform could eliminate the photonic effect. However, the fabrication of the membranes was done before the thorough check of the beam profile size at the focal plane of Raman set-up microlenses (see next paragraph). It will be shown that a big amount of the beam profile extends the borders of the platform, which means that RCWA corrections are still crucial. The analysis has to account for the two regions with different absorption at the membrane centre and a very precise beam positioning is needed (down to 100nm accuracy), which extends the resolution of the microscope system. Though the platform design was not successful, it did not affect the experimental results, but it added work in data treatment.
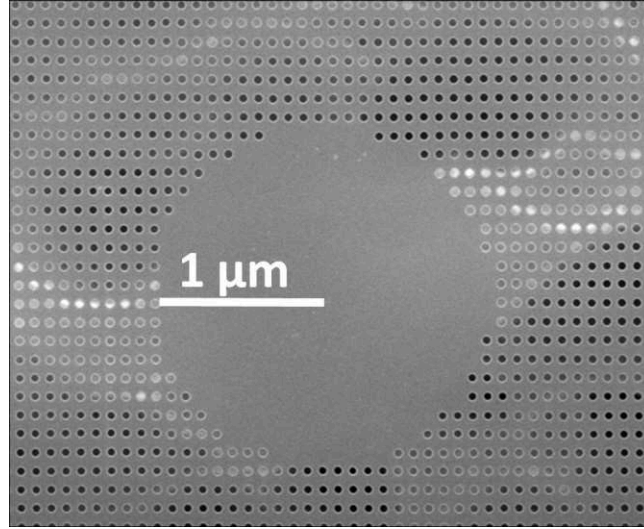
Figure 3.22
SEM image of fabricated 43.8nm-thick Si PhM with 100nm pitch and the plain 1μm radius platform located at the membrane's centre.

3.2.8 Determination of the laser beam size

In order to determine which lens gives the optimal shape and size of the incident beam, the intensity profile distribution (normal distribution) of the beam had to be studied. Two microscopy objectives were available: 100x (NA=0.5, r_0=1.22λ_0/(2NA)=0.58μm) or x50 (NA=0.42, r_0 = 0.69μm), where r_0 is the theoretical beam radius. One has to take into account that these long-range objectives were chosen because the measurements (and focusing) were performed through the cryostat window. The commonly used knife method[82] was applied to characterize the beam profile. The idea was to measure the sample of the beam power profile along the major or minor axis (or along any direction, in the case of symmetrical beam), then fit the data to the theoretical cumulative distribution function (CDF) curve. It is handy for computation to define CDF with the error function erf(x) :

$$F(x) = \frac{1}{2} + \frac{1}{2} erf\left(\frac{x-\mu}{\sigma\sqrt{2}}\right) \tag{25}$$

$$erf(x) = \frac{2}{\sqrt{\pi}} \int_0^x e^{-t^2} dt \tag{26}$$

Where μ is the centre of profile maximum, σ is the standard deviation of
the profile distribution, x is a coordinate along the axis of the measurement.

We relate the beam size to standard deviation for convenience, whereas the profile distribution can be expressed in terms of radius r_0, defined as r_0 from: $I(r_0) = I_c e^{-2}$, where I and I_c are the beam intensity at point r_0 and the centre of profile distribution respectively. For a perfect Gaussian beam, in the absence of noise in the measurement system, the beam diameters in $1/e^2$ and D4σ definitions are identical[83]. The experiment went as follows. A Si power meter (Thorlabs[76]) was partially covered with a thin Si sample that had a sharp and

101

even edge (the knife). The purpose of the knife is to changing the level of attenuation of the normally incident light: from 0 to 1 of the measured normalized light power. Thus at the beginning the beam was fully attenuated, i.e. the measured power was zero. The beam was focused on the knife. The platform was moving together with the detector and the knife along the same axis, increasing the exposure of the uncovered area of the detector to the beam. Cumulative intensity of the beam was rising slowly from zero to maximum value, where it became saturated (Figure 3.23a,d). With CDF fitting for 50x lens (plot a), we obtained $\sigma=1.5\mu m$ and then reconstructed the Gaussian profile (plot c). Standard deviation helped to estimate what fractions of the incident power correspond to the platform area F_{pl} (Formula 27), the whole membrane surface F_{membr} (Formula 28) and membrane area out-of-platform $F_{out-of-pl}$. All calculations imply that the beam is localized at membrane centre. The first two values were estimated via integrating symmetrical Gaussian distribution of the beam intensity over the area of interest using radial or Cartesian coordinates (the units are in μm). $F_{out-of-pl}$ was found as the difference between membrane and platform fractions. The limits of F_{membr} integration correspond to the sizes of the membrane (length=$200\mu m$, width = $8.9\pm0.1\mu m$). Non-radians units are in μm, in formulas below.

$$F_{pl} = \int_0^{2\pi} \int_0^1 \frac{1}{\sigma^2 2\pi} e^{-\frac{r^2}{2\sigma^2}} r\, dr\, d\theta \tag{27}$$

$$F_{membr} = \int_{-100}^{100} \int_{-4.45}^{4.45} \frac{1}{\sigma^2 2\pi} e^{-\frac{x^2+y^2}{2\sigma^2}} dx\, dy \tag{28}$$

The table at the left top of the Figure 3.23 lists all the calculated values for x50 lens. It concludes that the size of the non-perforated platform has to be much bigger in order to localize 99% of the beam on its surface: for example for the square platform area with $4.45\mu m$ side, F = 0.994. Another conclusion is that 99% of the beam can be easily localized on the surface of the membranes, which makes the measurement possible. Making $\approx 10\mu m$ step from the centre of the membrane along the length axis allows to localize the beam spot in the region of the phononic pattern, where the measurement error will be smaller.

Analogous experiment and the fitting were done for x100 lens. However, with the cumulative curve for the single Gaussian distribution (Formula 25) it was not possible to obtain any satisfactory approximation. The stronger lens implies a narrower profile of the beam, however the data showed unexpected slopping regions at the top and the bottom near the very steep centre. This feature suggests the presence of a secondary beam distribution.

50x lens:

Model σ	F_{membr}	F_{pl}	$F_{out\text{-}of\text{-}pl}$
1.48µm	0.997	0.199	0.798

100x lens:

Model σ_1, σ_2,	F_{membr}	F_{pl}	$F_{out\text{-}of\text{-}pl}$
0.56µm, 8.96µm	0.692	0.401	0.291
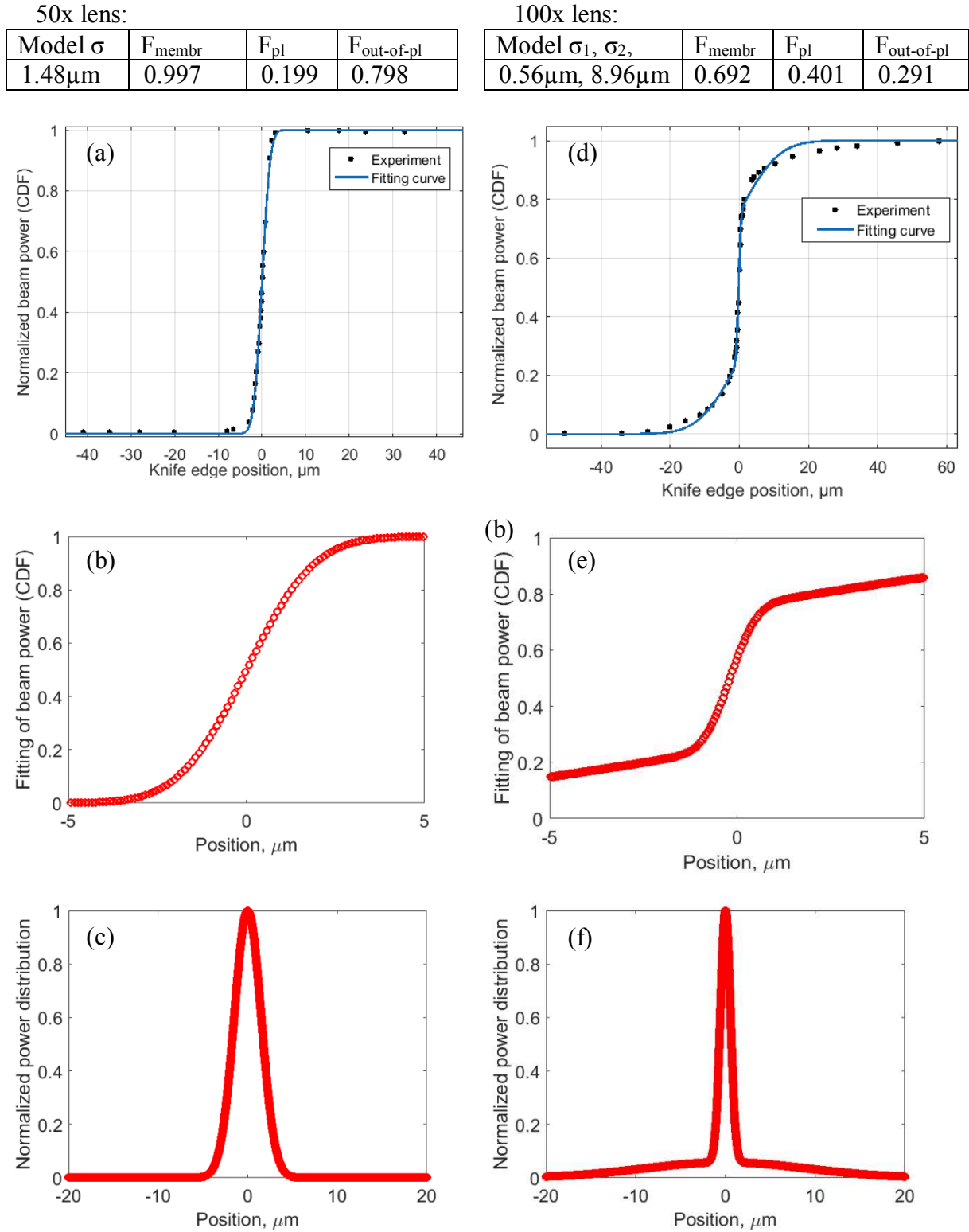
Figure 3.23

Analysis of the knife-edge experiment done for two lenses: (a-c) 50x(NA=0.42) and (d-f) 100x(NA=0.5). (a, d) Normalized beam power and a fitting curve (CDF). (b, e) Large-scale plot of the fitting curve. (c, f) Normalized beam power distribution obtained as a derivative of the fitting CDF curve. The table at the top summarized estimated values for the standard deviation, calculated fractions of the beam power with respect to membrane surface F_{membr}, non-perforated platform F_{pl} and out-of-platform membrane $F_{out\text{-}of\text{-}pl}$ surfaces.

Indeed, when only applying the CDF with two weighted erf functions, it was possible to fit the data for a 100x lens. However the cause of the second beam artefact had not been established. Reconstructed beam profile (Figure 3.23f) clearly shows the overlap of the narrow and wide distributions. According to the fitting results, they are equally weighted ($\omega \approx 0.5$ in formula below).

$$F(x) = \frac{1}{2} + \frac{\omega}{2} \, erf\left(\frac{x - \mu}{\sigma_1 \sqrt{2}}\right) + \frac{(1 - \omega)}{2} \, erf\left(\frac{x - \mu}{\sigma_2 \sqrt{2}}\right) \tag{29}$$

The calculation of the area fractions (Formulas 27 and 28) were done as the summation of two integrals for respective standard deviations of the beam profiles: $F = F(\sigma_1) + F(\sigma_2)$. The results are summarized in the figure table (above the plots d-f). Due to a very large deviation of the artefact beam formed by 100x lens, the analysis of the absorbed heat distribution becomes more complicated. Besides, low-T heating due the secondary beam adds the noise to the Raman shift spectrum. For this reason, only 50x lens was satisfactory for the Raman experiment.

3.2.9 Experiment upgrade

The experimental set-up introduced in paragraph 3.2.2 had one limitation which concerned the reliability of the power-variation measurement. The available combinations of stationary and removable filters did not allow for more than 3-4 measurement points in the acceptable range of powers (Figure 3.19). Thusly, it was not possible to statistically estimate the quality of $\Delta T(\Delta P)$ data. In order to increase the number of experimental points per membrane and obtain meaningful error of linear regression fitting, continuous neutral filter was installed (Figure 3.24a). Its optical density changes from 0 to 2 in the range of 270° sector of the rotational wheel. The last quadrant is transparent. The attenuation curve of the filter was obtained in order to verify the noise level of the measurement when the wheel was rotated by hand, i.e. without automated precision mechanism (the installation of which may decrease the noise). When measurements are performed in the chamber, it is not possible to measure the incident power directly. This limitation together with the found undesirable outcome of 10% errors (in terms of single σ) of the attenuation points (Figure 3.24b) motivated the installation of the reference detector, which can measure the ratio of attenuation. This is a reasonable idea since the signal that has passed the fixed filter wheel is stable. Once calibrated to the power meter in experimental conditions, the reference detector is able to give us the value of incident power on the sample.
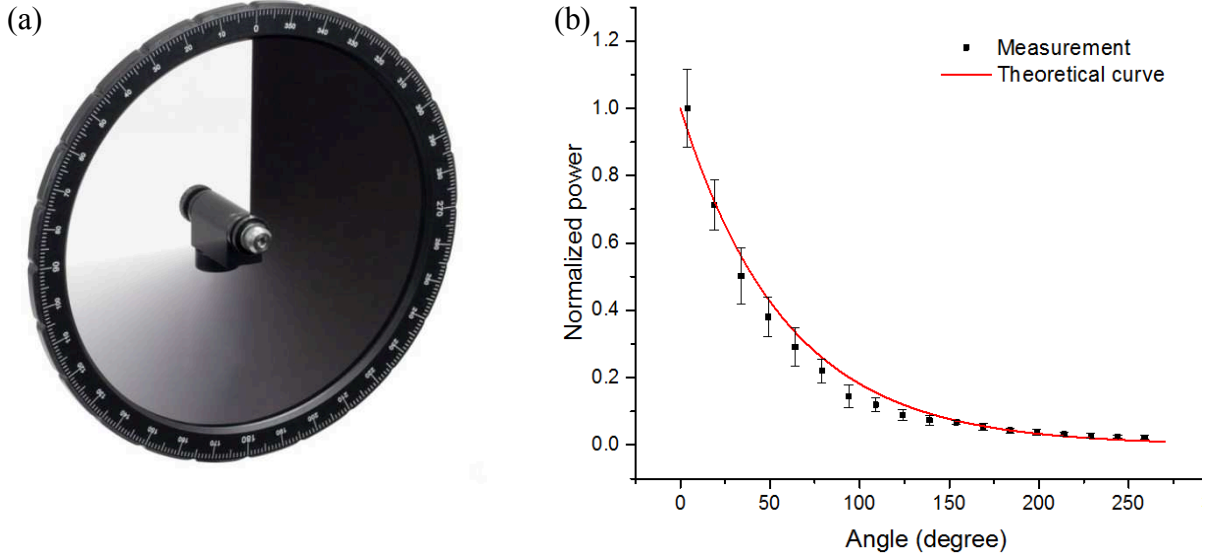
Figure 3.24
(a) Continuous variable filter (Thorlabs, NDC-100C-2M[84]) and (b) its characteristic attenuation curve, power vs. the angle (in 0°-270° range) measured with 473nm laser. Error bars are standard deviations over 5 measurement samples. Theoretical curve is according to Formula 30.

$$\frac{P(\theta)}{P_0} = 10^{\frac{OD_{Max}\theta}{270^\circ}},$$

(30)

where OD_{Max} is maximum optical density ($OD=\log(P/P_0)$), which equals to 2, P_0 and P are the constant beam and attenuated powers, θ is the filter angle.

A silicon photodiode[85] was installed into the reference optical path of the Raman set-up in order to measure the level of light attenuation by the continuous wheel filter. Photovoltaic mode (at zero voltage bias) was chosen since it is appropriate for low light levels detection. For the constant signal, low thermal noise and the absence of the dark current (due to zero bias), the noise filter may not be needed. The produced current is a function of the incident light power, and proportional to the voltage drop across the resistor (Figure 3.25b). Estimating the resistor voltage, we obtain the reference signal. Detectors responsivity (which is the ratio of photocurrent and incident light power, $Rs=I_P/P$) for λ=473nm is equal to 0.15[85]. Expecting to measure the values of the incidence power P on the photodiode in the range of 5-1000µW, we considered 10kΩ resistor as an optimal choice, since it is not too strong (no thermal noise issues) and the level of the voltage signal is measurable: V=0.0075-1.5V (according to the output voltage expression: V=P·Rs·R, where R is resistance). The calibration curve (Figure 3.25b) shows the chosen parameters led to high resolution measurement along the linear response interval of the photodiode, with minimal signal fluctuations. Thus, the installation of a continues variable filter combined with the reference photodiode detection let us conduct a power-variation Raman experiment with a bigger set of measurement points.
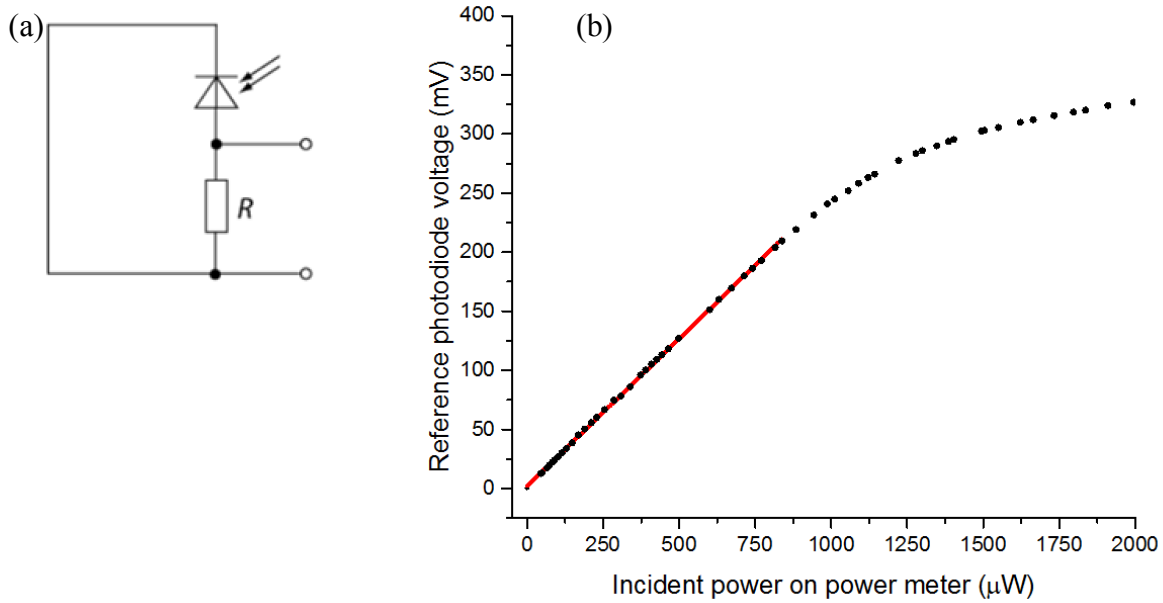
Figure 3.25
Simple scheme of unbiased Si photodiode connected to 10kΩ resistor, which voltage drop detection gives a reference signal. (b) Reference voltage as a function of the main beam power measured at the experimental conditions (at a focal plane behind the cryostat window). Red curve is a linear fitting from 0 to 800μW.

The figure plot above shows the reference voltage signal as a function incident power P_{Inc}, i.e. the power of the main beam focused with the x50 lens onto the detector placed behind the cryostat window. The linear response of the photodiode is in the range of 0-800μW. This suits our experimental requirements well, since P_{Inc} equals to 300μW is a threshold above which even a plain membrane can be burnt (tested empirically). The fitting across the linear interval gives a slope constant that is used to reconstruct P_{Inc} value during the Raman measurements. Even though the reference line fitting gives a minimal error, there is a systematic error for P_{Inc} ($\varepsilon(P_{Inc}) \approx 10\%$) developed due to the procedure of power meter detection. Combined with a small relative error of absorption estimation (1.3%), the total error for absorbed power propagates as $\approx 10.1\%$ (Formula 32).

3.2.10 New measurement approach

Besides the aforementioned improvement of the set-up (which increase the number of experimental points for the power-variation method), some other modification were introduced. The first one is the way the data has to be fitted. According to the anharmonic phononic model (Paragraph 3.2.3), the Raman shift ω is linearly proportional to T in the range of 300-800K, where the slope $\chi_T = d\omega/dT = -0.022$ cm^{-1}K^{-1}. Determining the ω at different values of absorbed power P_{abs}, we can deduce the T. However, the absolute measured ω value does not guarantee precise correspondence to some T value, since the literature estimations even for bulk Si are different[73]. Therefore, without a thermometer system that would allow for the determination of ambient temperature on the SOI wafer surface, we do not have any known reference point for T(ω) dependence. In this situation only the relative change of temperature (ΔT) obtained via the Raman shift change ($\Delta\omega$) is

known from the experiment. Thus, taking the intersection parameter to zero in the fitting of ΔT vs. P_{asb} can lead to a big error increase in the fit. The figure below demonstrates the typical µRT outcome for the phononic membrane. The blue dots are experimental values of the temperature change vs. P_{abs}. The fitting curve (green line) is not constrained to zero. ΔT intercept corresponds to the ambient temperature, which remains unknown. In other words, only the slope matters.
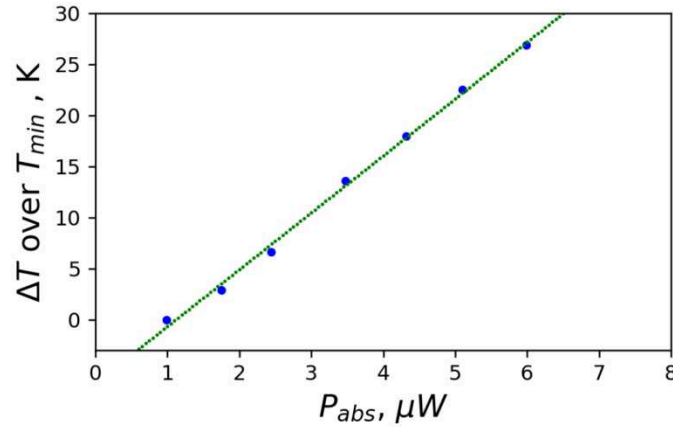
Figure 3.26
Experimental ΔT as a function of absorbed laser power P_{abs} (blue points) obtained by µRT for PhM with the pattern [r=1, tilt angle = 60°] from the sample №2. The beam was focused by x50 lens. Green curve is a linear regression fit with intercept = 6.23K and a slope = 5.57K/µW.

Estimating the quality of the fit with root mean square error (RMSE) function, we come up with the statistical error for the T value (Formula 31). Another contribution to T error is attributed to the relative power error $\varepsilon(P_{abs})$, which is mainly systematic. Taking into account the fact that the final estimated ΔT value is obtained via the fitting equation $\Delta T = a + bP_{abs}$ (where a and b are the intercept and the slope), we can propagate the error according to Formula 32): $\sigma_{\Delta T,sys} = b\sigma_{Pabs} = bP_{abs}\varepsilon(P_{abs})$. The final error is calculated according to Formula 33. For the membrane which data is shown on the plot above the estimated $\Delta T_{fit}@8.45µW = 47.08 \pm 4.9K$ with $\sigma_{\Delta T,stat} = 1.4K$ (n=7) and $\sigma_{\Delta T,sys} = 4.7K$.

$$\sigma_{\Delta T,\, stat} = \sqrt{\frac{\sum(\hat{\Delta T} - \Delta T)^2}{n - 2}}$$

(31)

Where ΔT is the experimental value and ΔT with the hat is a predicted value at the same argument. n is the number of experimental points. The summation goes over n points.

$$\sigma_f = \sqrt{\sum(\frac{\partial f}{\partial z_i})^2 (\sigma_{z_i})^2}$$

(32)

Where f is a quantitiy which depends on parameters z_i. Each z_i has its own experimental error $\sigma(z_i)$.

$$\sigma = \sqrt{\sigma_{stat}^2 + \sigma_{sys}^2}$$

(33)

Another modification concerns the analysis of the thermal conductivity. There is no need to make multiple FEM model runs for each experimental point of $\Delta T(\text{P}_{asb})$ to predict different κ values and then average them. Instead a single temperature value obtained from the μRT fitting can be used, allowing us to reconstruct a single κ value. This approach is reasonable since κ in this case is obtained from statistically averaged ΔT_{fit}, which has its own error. The T value for the thermal conductivity fitting at a particular value of the absorbed power is expressed as: $\text{T}_{Comsol}=\text{T}(\text{P}_{abs}=0)+b\text{P}_{asb}$, where the first term is the ambient T in the model and the second term is a predicted temperature shift (ΔT_{fit}) at some P_{asb}. The final error of κ can be obtained via error propagation calculations. This procedure will be explained in this paragraph.

The next Figure demonstrates the same Comsol model for the membrane device as in Paragraph 3.2.5, with some added changes relevant to the new PhMs design. First of all, the thickness of the membrane and the SOI layer as well as the membrane width were changed accordingly to the new PhM's characterisations. The wings extensions are two times smaller (width=10μm). A non-perforated platform was introduced at the centre, the thermal and absorption properties of which are the same as for plain Si and SOI parts. Prior to PhM modelling, the plain membranes (of the same 43.8nm thickness) had to be analyzed. Then, their averaged thermal conductivity was used as an input for the centre platform part, the wings and the SOI part. In our case, 4 plain membranes (from the same sample №2) with tilted angles [30, 45, 60, 90] were measured and analysed by the model: the averaged κ_{plain}=31.7±3.6 W/mK. The tests showed that the modelled PhM thermal conductivity changes negligibly (<0.3%) when thermal conductivity input (κ_{plain}) for the plain parts takes the limit error values.

Figure 3.27c,d shows the model-reconstructed thermal gradient (green curve) for the same PhM characterized by the pattern [r=1, tilt angle = 60°]. The thermal conductivity was obtained via fitting the gradient maximum at a hot spot position 160μm (where 150μm is a centre of PhM) to experimental temperature value (blue dot) at 8.45μW of absorbed power: $\text{T}_{Comsol}=\text{RT}+\Delta T_{fit}(@8.45\mu W) = 340.23\pm4.9K$. Fitted PhM thermal conductivity $\kappa_{PhM} = 23.65$ W/mK. We also tested two cases for the fitting, including and excluding the non-perforated platform. The values of κ_{PhM} were the same in both scenarios. Finally, the temperature at the centre-located hot spot T_{centr} was reconstructed (using the value of κ_{PhM}) with disabled non-perforated platform. In other words, we wanted to obtain the hot spot T at the centre as if our membrane was fully covered with the holes. From the plots below, we can clearly see (blue curve) that T_{centr} is just slightly different from the temperature measured at the spot shifted by 10μm. Subtracting RT from T_{centr}, we estimate ΔT_{centr} value =47.61±4.9K, which is the temperature rise (or the gradient) established at the centre of the ideal (non-perforated) phononic membrane. We assume that the error ΔT_{centr} is the same as for ΔT_{fit}. ΔT_{centr} quantity will be used in the next chapter when multiple anisotropic PhM will be compared in terms of ΔT_{centr} as a function of the phononic pattern and direction of heat propagation.
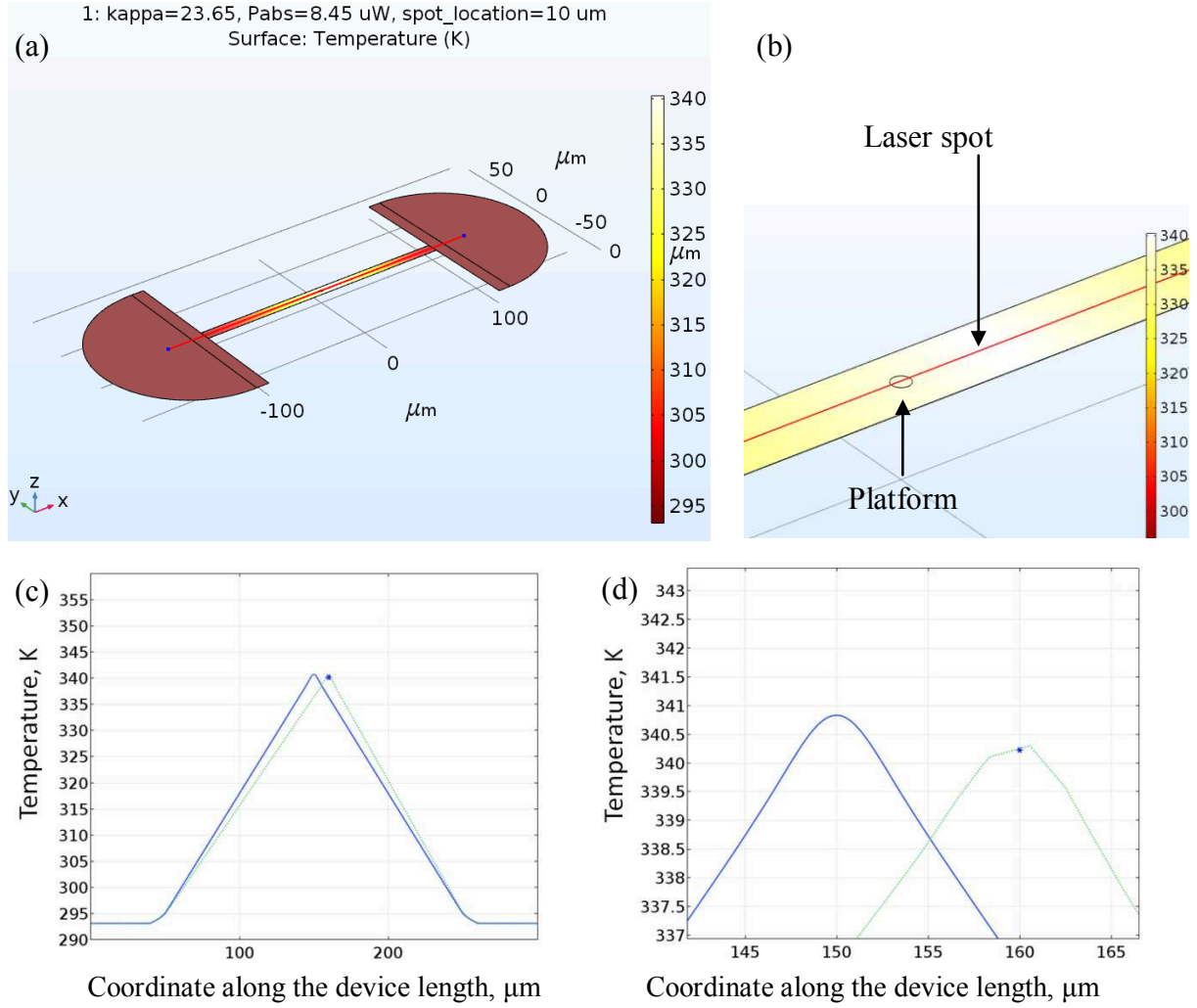
Figure 3.27

FEM modelling of PhM (r=1, tilt angle = 60°) device. (a,b) Colour maps of the temperature distribution in PhM device established due to the heat absorption (P_{abs}=8.45μW) at a hot spot 10μm apart from the centre of the membrane (green line in (c) and (d) plots). The red line is a cross-section along which the gradients are plotted (c,d). Blue dot is a temperature inferred from the experiment: T_{Comsol}=RT+ΔT_{fit}(@8.45μW) = 340.23K. Blue curve is a gradient established for the same absorbed power when the hot spot is located at the centre and non-perforated platform is disabled. (b) Zoomed section of (a) around the centre, where the contour of the platform is shown.

For the fabricated PhM's, with smaller thickness and the width of the wings, the value of the model κ_{PhM} is very close to the one calculated with Formula 22 (which is given below for convenience). For example, for the PhM studied above, the model predicts κ_{PhM}= 23.65 Wm^{-1}K^{-1}, whereas the formula yields κ_{PhM} = 23.08 Wm^{-1}K^{-1}. This correspondence allows us to use this formula for the error propagation.

To simplify the differentiation we express partial derivatives in Formula 32) through the logarithm of the main function[86] (Formula 34). In our case, logarithm unfolds according to expression (35). The final equation (Formula 36) for the thermal conductivity error σ_κ depends on the set of already estimated errors for geometrical parameters (width w, length L, thickness d), experimental quantities of absorbed power and measured temperature rise at a

hot spot, and finally the position, with an accuracy $\sigma_x=2\mu m$ (this value is due to possible lateral shift of the sample in the vacuum chamber).

$$\kappa = \frac{P_{abs}}{\Delta T}\frac{L}{4wd}(1 - \frac{4x^2}{L^2})$$

where d, L, w are the width, the length and the thickness of the membrane, x is the location of the hot spot.

$$\sigma_\kappa = \kappa\sqrt{\sum(\frac{\partial ln(\kappa)}{\partial z_i})^2(\sigma_{z_i})^2} \quad (34)$$

$$ln(k) \approx ln(P_{abs}) - ln(\Delta T) - ln(4) - ln(w) - ln(d) + ln(L) + ln(1 - \frac{4x^2}{L^2}) \quad (35)$$

$$(36)$$

$$\sigma_\kappa \approx \kappa\sqrt{(\frac{1}{P_{abs}})^2(\sigma_{P_{abs}})^2 + (\frac{1}{\Delta T})^2(\sigma_{\Delta T_{stat}})^2 + (\frac{1}{w})^2(\sigma_w)^2 + (\frac{1}{d})^2(\sigma_d)^2 + (\frac{L^2 + 4x^2}{L^3 - 4x^2L})^2(\sigma_L)^2 + (\frac{8x}{4x^2 - L^2})^2(\sigma_x)^2}$$

Where L, w, d are membrane's length, width and thickness, x is the location of the hot spot, P_{asb} is the absorbed power, ΔT is the established temperature shift, σ_i is the corresponding to each variable absolute error. The largest contribution comes from ΔT and $P_{asb.}$

Taking into account all parameters which contribute to the error, we concluded that the effective thermal conductivity in the direction, tilted by 60° from the axis of the phononic lattice, in isotropic (8.9±0.1µm-wide, 200µm-long and 43.8nm-thick) Si PhM with 100nm pitch and 24.2±0.9nm holes radius, is equal to 23.65±2.4 Wm^{-1}K^{-1}. When 8.45µW of the laser power is absorbed at the centre of the membrane, the temperature at a spot rises by 47.61±4.9K (in short: $\Delta T_{centr}(@8.45\mu W) = 47.61\pm4.9K$).

Remark: the highest experimental temperature in this work was about 350K (all the values above it, that can be found in the next chapter, are fit extrapolation). According to the literature[87] thermal conductivity of the pristine 50nm-thick membrane changes by 11% when temperature rises from RT to 350K. However in our experiment this effect was not taken into analysis since the Raman shift (and Temperature) response vs. light power was found to be linear (which indicates the absence of noticeable $\kappa(T)$ dependence).

3.3 Conclusions

On the basis of the results on structural PhMs characterisation and development of experimental methodology, the following conclusions are drawn.

SEM observations confirmed the good quality of both fabricated isotropic and anisotropic series of PhMs, that are fully suspended. The absence of etching and oxidation residues was confirmed. Only a small fraction of PhMs were damaged during the fabrication. For the first time it was possible to obtain the full coverage of the membranes area with phononic lattices. The slight variation of membrane width within 0.2µm was detected. The average value (over 8 randomly chosen membranes and 24 locations) estimation is ≈8.9µm. In total, 25

membranes of anisotropic series, 10 membranes of plain series, and 10 membranes of isotropic series were fabricated per 1' wafer sample. 4 samples were created. Around 10% of the membranes were damaged during the fabrication process, they were not used in the experiment.

Other geometrical parameters were studied. Ellipsometry measurements, roughly confirmed by SEM images, concluded that the thickness of PhM is ≈43.8nm. Statistical analysis of the holes radiuses showed that anisotropic phononic patterns have similar hole sizes (varied from 23.6 ± 0.9nm to 27.2 ± 1.5nm). Consequently the filling fraction among the patterns varies within the small range from 17.5% to 23.4%, which makes the comparison of the heat properties of different anisotropic patterns possible. SEM study showed that the smallest neck feature size is ≈15.8nm (for the pattern with r=2.5), which is close to state-of-the-art fabrication limits.

Irregular transition over 2nm interval from the crystalline to amorphous phase was observed by TEM scan on the holes wall. In parallel, EDX study showed the presence of oxide on the wall, and gave quantitative estimation of 2-3nm oxide layer presence on the membrane surface.

The independently constructed COMSOL FEM model reproduced the thermal conductivity estimations for PhM of the previous generation. New RCWA corrections were used to modify the absorption of membranes with different phononic patterns.

The issue connected with the mismatch of the sizes of the non-perforated platform and laser beam profile was carefully studied. The shape and the characteristic sizes of the beam power distributions formed by x50 and x100 lenses were analyzed. Artefact secondary beam, formed by 100x lens and with large standard deviation, was found. Its presence leaves at least 30% of the beam power outside the membrane. To the contrary, the beam formed by x50 fits membrane sizes and makes the power-variation measurements close to membrane centre possible.

The installation of a continuous variable filter and a reference Si photodiode detector allowed to conduct a power-variation μRT experiment with a larger set of measurement points. The issues of data analysis were addressed. The fitting procedure and the methodology of error estimations for both temperature measured by μRT and effective thermal conductivity modelled by FEM were elaborated.

Chapter 4   Results and discussion

In this chapter, the experimental outcome of the work is presented. Plain and phononic membranes with isotropic and anisotropic lattice patterns were studied by means of micro-Raman Thermometry (μRT). Anisotropic heat propagation is visualized in both $\kappa(\theta)$ and $\Delta T_{centr}(\theta)$ representations. FEM modelling, which demonstrates the possible implementation of induced anisotropic effects, is introduced in the second section of this chapter.

4.1 Experimental results

At first, we discuss the results in terms of thermal conductivity picture for the set of membranes with isotropic lattices. The question of κ effectiveness is addressed by the theoretical model which accounts for porosity (filling fraction) contribution into the thermal conductivity. Paragraph 4.2.1 is dedicated to the results and discussions for PhMs with isotropic lattices. In the last paragraph, a special attention is focused on the found effect of unexpected reduction of the thermal conductivity in patterns with the highest anisotropy (r=2.5) when the heat flux propagates in the direction of a relatively wide transverse neck.

4.1.1   PhMs with isotropic lattices

The series of PhMs with isotropic lattices of holes (geometrical parameters are in Figure 4.1a) were studied by μRT, the data was analysed in Comsol FEM solver following the methodology described in Paragraph 3.2.10. All the membranes studied are from the sample №2, which has the smallest proportion of damaged membranes. It is important to compare membranes from the same sample, because the etching was applied individually to each sample (hence different roughness level is possible). Besides, different exploitation/storage atmospheric conditions may lead to the variation in native oxidation level and the size of contamination. All isotropic PhMs were designed in such a way that the heat propagates along the axis of the phononic lattice. Figure 4.1b demonstrates measured thermal conductivity as a function of the lattice pitch. The data for the plain membranes is included for comparison. All four plain membranes have different angles of the orientation (30°, 45°, 60°, 90°), nevertheless their κ values are the same within the error bars. The missing value for the damaged 0° membrane is assumed to be similar. Obtained values of plain membranes' κ prove the predicted absence[33] of in-plane anisotropy in pristine Si membranes of the same surface orientation at RT, at least down to the thickness of 43.8nm.

The introduction of phononic lattices slightly decreases the thermal conductivity within the pitch range from 140nm down to 100nm, which can be attributed to the increase of the porosity φ or the neck size NS decrease. For 80nm pitch, a very big reduction of κ is observed, which is unproportional to the change of both φ and NS. $\varphi = 0.35$ for 80nm pitch PhM, which is the highest φ value obtained in this work. Different effective medium approximations (EMA)[15,88] were used in order to verify in what membranes the thermal conductivity reduction can be attributed to the filling fraction increase. The Table 4.2 lists the tested models. The formulas for the reduction factor F are given.
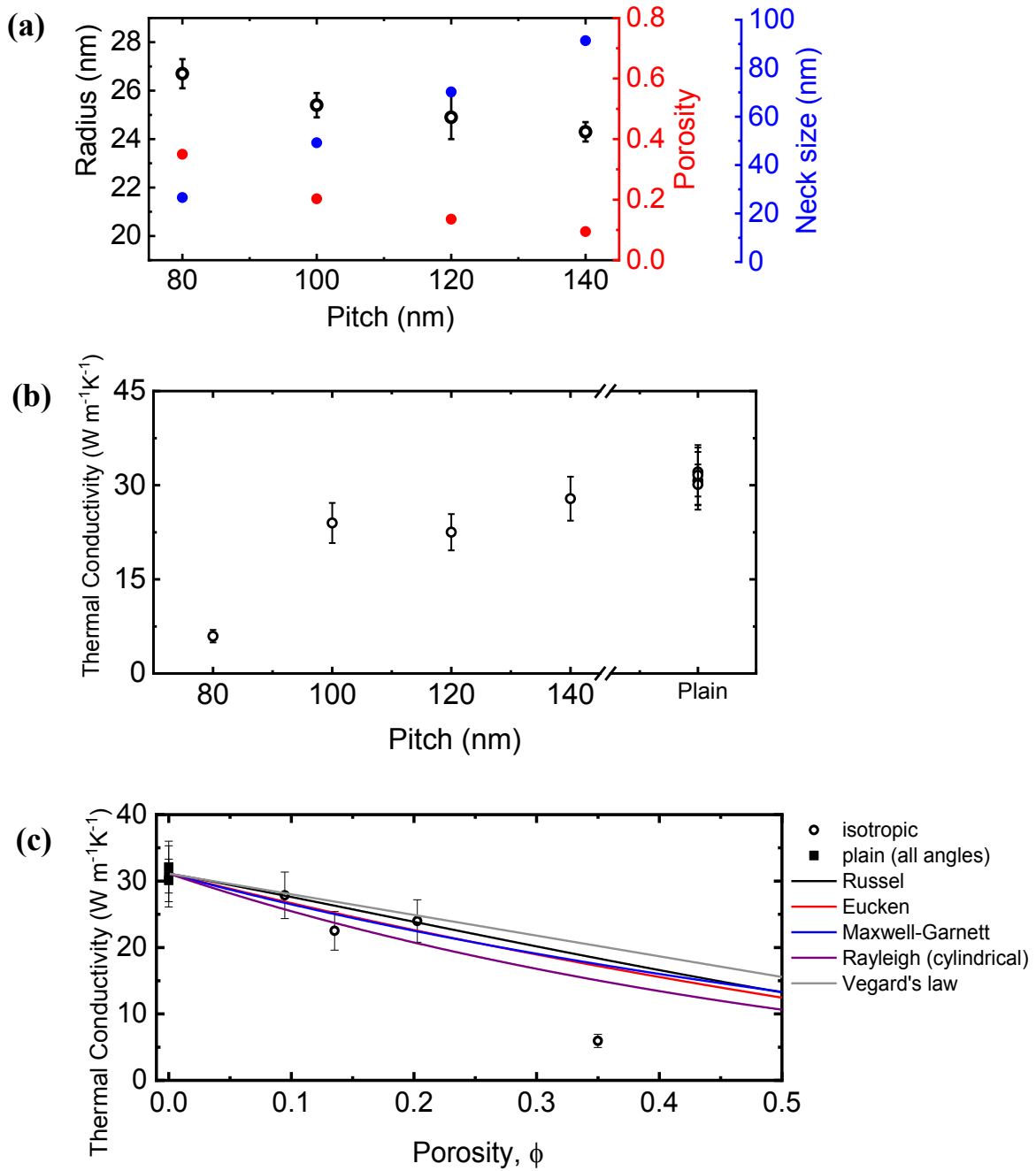
Figure 4.1
Isotropic PhMs' (a) geometrical parameters and (b) thermal conductivity measured with μRT at RT and vacuum conditions. Thermal conductivity for pristine membranes are added for comparison. All membranes belong to the same sample №2 . Isotropic membranes for 80nm and 100nm pitch were measured 2 and 3 times respectively: the averaged values with the maximum error bar are plotted. (c) Thermal conductivity of the same membranes as a function of porosity with the theoretical effective medium approximations' curves.

Table 4.1
Effective medium approximations

Model	Reduction factor, F	Description
Vegard's law	$1-\varphi$	Accounts only for the material removal. Voids shapes and surface area are neglected.
Russel	$\dfrac{1-\varphi^{\frac{2}{3}}}{1-\varphi^{\frac{2}{3}}+\varphi}$	Implies the cubic shapes of voids in a continuous, grid-like matrix.
Eucken	$\dfrac{1-\varphi}{1+\dfrac{\varphi}{2}}$	Extension of Maxwell model for cylindrical voids.
Maxwell-Garnett	$\dfrac{1-\varphi}{1+\varphi}$	Spherical shapes are taken into consideration.
Rayleigh (cylindrical voids)	$1+\dfrac{2\varphi}{-1-\varphi-(0.30584\varphi^4+0.013363\varphi^8)}$	Cylindrical shapes are taken into consideration.

The common approach is that each model expresses the effective thermal conductivity κ of porous or structured material, measured in the experiment, as a conductivity of the bulk or pristine material reduced by factor F: $\kappa_{eff}=\kappa_{bulk}F$. In the case of PhM, we scale to the plain thermal conductivity instead of the bulk one. All the models except Vegard's law (the first row) take into consideration boundaries modifications caused by the shapes of the voids and the change of surface area.

According to Figure 4.1c κ of isotropic membranes with the pitch down to 100nm correspond to the trends of EMA models. Due to relatively large error bars, it is difficult to define which model suits best. However, for 80nm pitch, models overestimate the reduction, which may be interpreted in the following way: as the neck size of isotropic pattern decreases below 25-30nm, the scattering effects, which are not considered in EMA models, start to contribute into κ reduction of the crystalline matrix. The overestimation (by EMA models of the measured thermal conductivity) is observed also for anisotropic patterns (see Figure 4.7a).

4.1.2 PhMs with anisotropic lattices

Results for the series of PhMs with anisotropic patterns from the same sample №2, and partially for samples №1 and №4, are presented in this paragraph. The data from the last two samples is taken (Figure 4.3) in order to substitute the missing data of the damaged membranes from the sample №2, or for the purpose of comparison. As was mentioned in the previous paragraph, our dies (or samples) may have different oxidation level, roughness and contamination (if any) due to individual etching processing motivated by the fragility of the membranes, and due to the exploitation/storage conditions. Hence, only qualitative comparisons of experimental outcomes are possible among the samples. SEM image of fabricated experimental platforms is given once again for convenience in Figure 4.2a. All membranes are 8.9±0.1µm-wide, 200µm-long and 43.8nm-thick. PhMs are completely covered with the lattices of holes in five different configurations, characterised by the aspect ratio r =[1; 1.2; 1.6; 2; 2.5] of the lattice pitches in y- and x- directions. Varying the angle

(0°, 30°, 45°, 60°, 90°) of PhMs orientation (Figure 4.2b) for particular ratio of the lattices, it was possible to measure with µRT several κ-tensors of phononic patterns, and graphically visualize anisotropic heat flow (Figure 4.2d).

The plot from Figure 4.2d gives us a comparison picture of the temperature increase at PhMs centre ΔT_{centr} for all anisotropic patterns and plain PhMs, when 8.45µW of power is absorbed from the incident laser beam. All membranes on this plot are from sample №2, the data of which is listed in Table 4.2. Strictly speaking, only the first quadrant of the plot corresponds to experimentally obtained dependence of ΔT_{centr} vs. the orientation angle θ. However, we can define ΔT_{centr} as a temperature difference between central and end points of the PhM, because we have the ambient temperature in close vicinity of membrane's end even at high ΔT_{centr} according to FEM simulation. In this case, we are legitimate to place the experimentally obtained set of points symmetrically into the third quadrant. The placement of the data into the second and the forth quadrants (hollow points) is just an assumption that, if we had an identical set of the non-diagonalized membranes tilted by 90°, the results would be similar.

The curves on the plot, which are a guide to the eye, were obtained with the ellipse equation in polar coordinates, where major and minor vertices equal to two ΔT_{centr} points for principal orientations (90° and 0°). For r=2, r=1.6 and r=1.2, the vertices coincide with experimental ΔT_{centr}. For r=1 and plain PhMs, the curves are the circles with the radius equal to ΔT_{centr} averaged over the pattern. The motivation for elliptical guide to the eye for $\Delta T_{centr}(\theta)$ in case of large r membranes is supported by the FEM simulation of the T distribution in large-scale membranes, where absorbed at a spot heat leads to characteristic elliptical isotherms (Figure 2.2 in Paragraph 2.1.3). We assume that $\Delta T_{centr}(\theta)$ can be represented with the circle for r=1 even if only two experimental points are available for this pattern, since the results from sample №1 and №4 confirm a rather constant trend for r=1 (Figure 4.3).

As the pitch ratio r increases, the flattening of $\Delta T_{centr}(\theta)$ ellipse increases, which corresponds to the increase κ anisotropy (Figure 4.3) with r. The ratio of principal κ values were found to be up 2.2(for r=2.5) and 1.9(for r=2). Besides 25-fold reduction, comparing to the bulk value, or 5-fold reduction comparing to the pristine 44nm-thick membrane, of the thermal conductivity was observed for r=2.5 pattern: k_{yy}= 6±0.6 Wm^{-1}K^{-1}. This experiment (for the first time to our knowledge) confirms the possibility of artificially inducing high anisotropy of (effective) κ in Si PhMs almost not changing the filling fraction and the diameter of the holes.
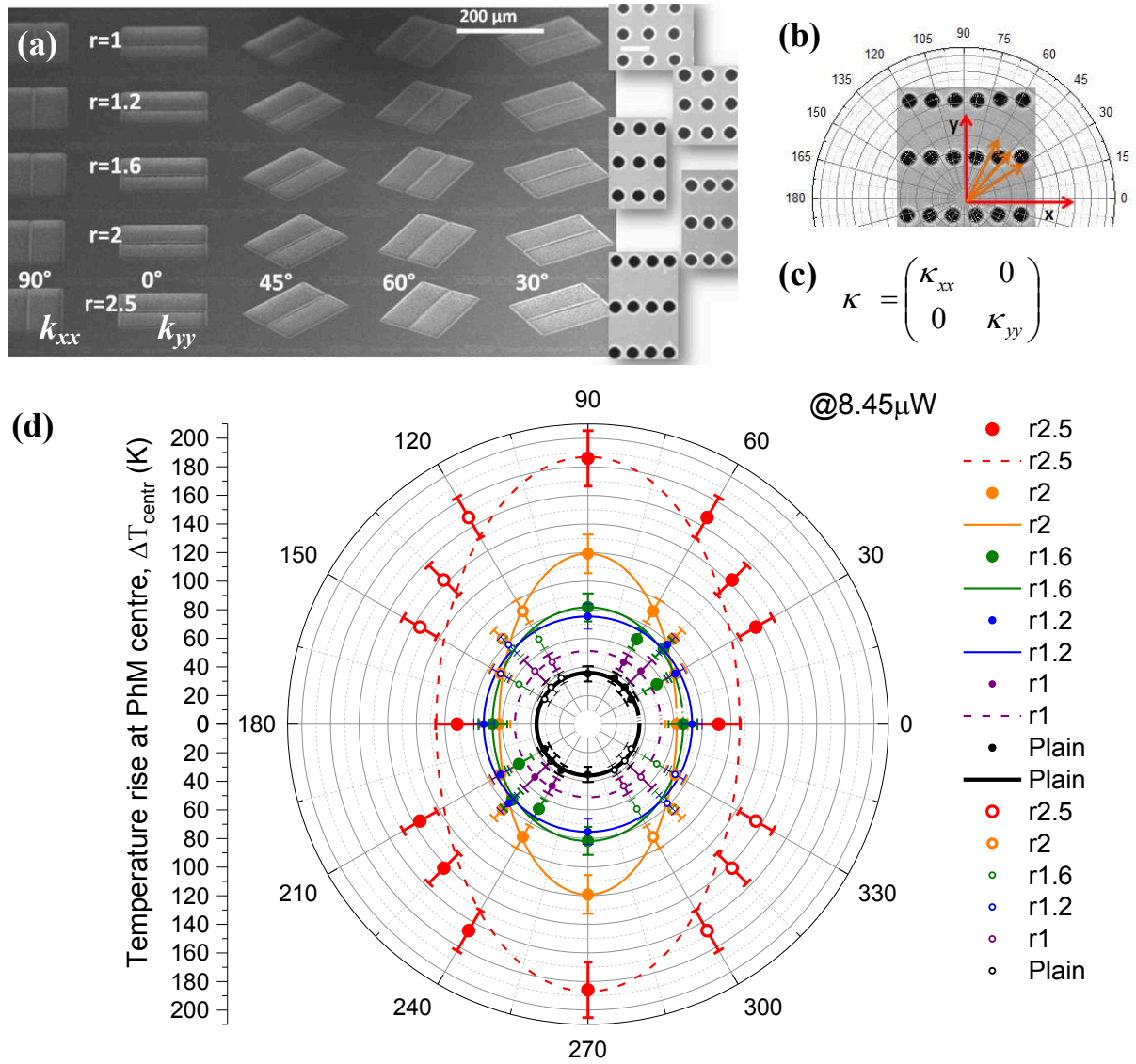
Figure 4.2
(a) SEM image of experimental platform consisted of 25 suspended Si PhMs with 5 configurations of the holes' lattices (SEM images on the right) and 5 angular orientations. (b) Auxiliary sketch showing the principle and tilted orientations of the membranes and the heat flow for each pattern. (c) Diagonal tensor of measured thermal conductivity in each pattern (0° and 90°). (d) Temperature increase ΔT_{centr} caused by the laser heating at the centre of PhMs, reconstructed with FEM model for the measurements obtained 10μm apart membranes' centre by μRT. All the data points are scaled to the same value of absorbed power: $P_{abs} = 8.45$μW. Hollow dots in the 2nd and 4th quadrants are "mirror-extrapolated". Elliptical and circular curves (details are in the text) are a guide to the eye.

Table 4.2
Summary table of experimental results for sample №2. "Times" is the number of measurements per membrane. For Times>1, κ and ΔT_{centr} are taken as an average over the number of outcomes, and the final error for κ and ΔT_{centr} equals to the maximum error of the respective quantity outcomes if this maximum error is bigger than the scatter distance of outcome points, else the final error is equal to the scatter distance.

r	Angle	Times	$\kappa, Wm^{-1}K^{-1}$	$\sigma(\kappa), Wm^{-1}K^{-1}$	ΔT_{centr}, K	$\sigma(\Delta T_{centr})$, K
Plain	30	1	32.1	3.9	34.8	4.1
	45	1	30.7	4.6	36.4	5.5
	60	1	30.1	3.2	37.1	3.8
	90	1	31.6	4.8	35.4	5.3
1.0	45	2	21.6	2.9	52.5	6.1
	60	2	22.4	2.4	49.9	5.4
1.2	0	1	15.4	1.5	72.8	7.1
	30	2	15.6	1.6	71.9	7.5
	45	1	14.2	1.5	78.4	8.0
	90	2	15.4	1.9	75.3	8.8
1.6	0	2	16.9	1.9	66.6	7.4
	30	2	20.3	2.6	55.6	6.4
	45	1	14.9	1.7	74.9	8.4
	60	3	16.3	1.7	68.5	7.1
	90	2	14.2	1.7	81.7	9.8
2.0	0	2	18.0	2.0	62.1	6.8
	30	1	15.8	1.8	70.6	7.8
	45	1	13.3	1.4	84.2	8.7
	60	1	12.3	1.2	91.2	9.0
	90	1	9.4	1.1	119.2	13.5
2.5	0	4	13.1	2	91.3	15.2
	30	1	8.2	0.8	135.6	13.5
	45	1	7.8	0.8	142.5	14.7
	60	1	6.7	0.7	166.8	16.3
	90	3	6.0	0.6	185.9	18.8

On Figure 4.3, the values of κ_{xx} and κ_{yy} correspond to the angles 0° and 90° respectively. If, for a particular pattern, both values are on the same level within the error bar, we conclude of the isotropic thermal transport at RT in the membrane. The plain membrane and r=1 PhM (based on the sample №1 observations) are thermally isotropic. For the patterns with r=[1.2; 1.6], the level of experimental error does not allow to conclude definitely about the anisotropy presence. Finally, as was shown in ΔT_{centr} (θ) representation, the patterns with 2

and 2.5 aspect ratio reveal the anisotropy. The anisotropy for r=2.5 PhM was confirmed twice with the measurements done on samples №1 and №2. The difference among the samples in the absolute values can be attributed to the different roughness formed on the surface of membranes and their cavities or due to BOX overetching along the cavities perimeter. This is possible due to the fact that XeF_2 and HF gas etching processes were performed individually for each sample. This was done for the sake of precautions amid small amount of available cells. Another reason can be attributed to the different native oxidation level of the membranes, which were exposed to different atmospheric conditions. The sample №2 was kept outside of the storage for a long time, and was used many times when the experimental technique was at the stage of adjustment and testing. This could lead to a thicker silica layer for sample №2. According to the study presented in Paragraph 1.2.4 the reduction[19] of κ due to the native oxide is stronger than due to amorphous phase.
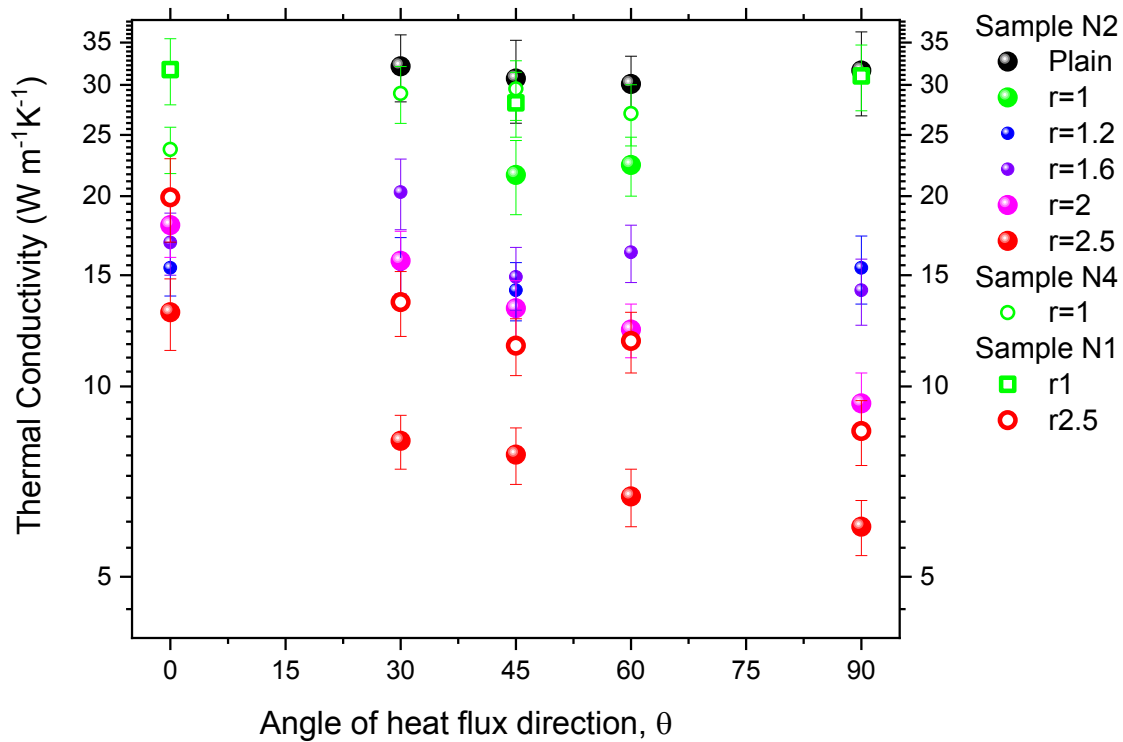
Figure 4.3

Thermal conductivity κ as a function of heat propagation direction (or angle of PhM orientation) for plain membranes and PhMs with five patterns characterised by the different aspect ratio of the pitch. Orientations of 0° and 90° corresponds to principal values κ_{xx} and κ_{yy}. Thermal conductivity values for the intermediate angles are effective in a sense that the they are not in the proper tensor representation.

4.1.3 Unexpected thermal conductivity reduction.

An interesting effect was observed in the results for anisotropic patterns. In order to make it more visible, we plotted the thermal conductivity for the principal orientations vs. the pitch ratio (Figure 4.4b). On the plot (b), the data from the sample №2 is used. The plain

membranes values are plotted as a reference. Figure 4.4a is an illustration for the plot (b). The red and blue arrows indicate the heat flux in x and y directions, initiated by the light absorption at PhMs centre during μRT experiment. The sketch corresponds to 10 membranes with 5 pitch ratio values ($r = p_y/p_x$) and 2 orthogonal principal orientations of the lattices (0° and 90°).

(a)

r = 1   r = 1.2   r = 1.6   r = 2   r = 2.5

(b)

(c)
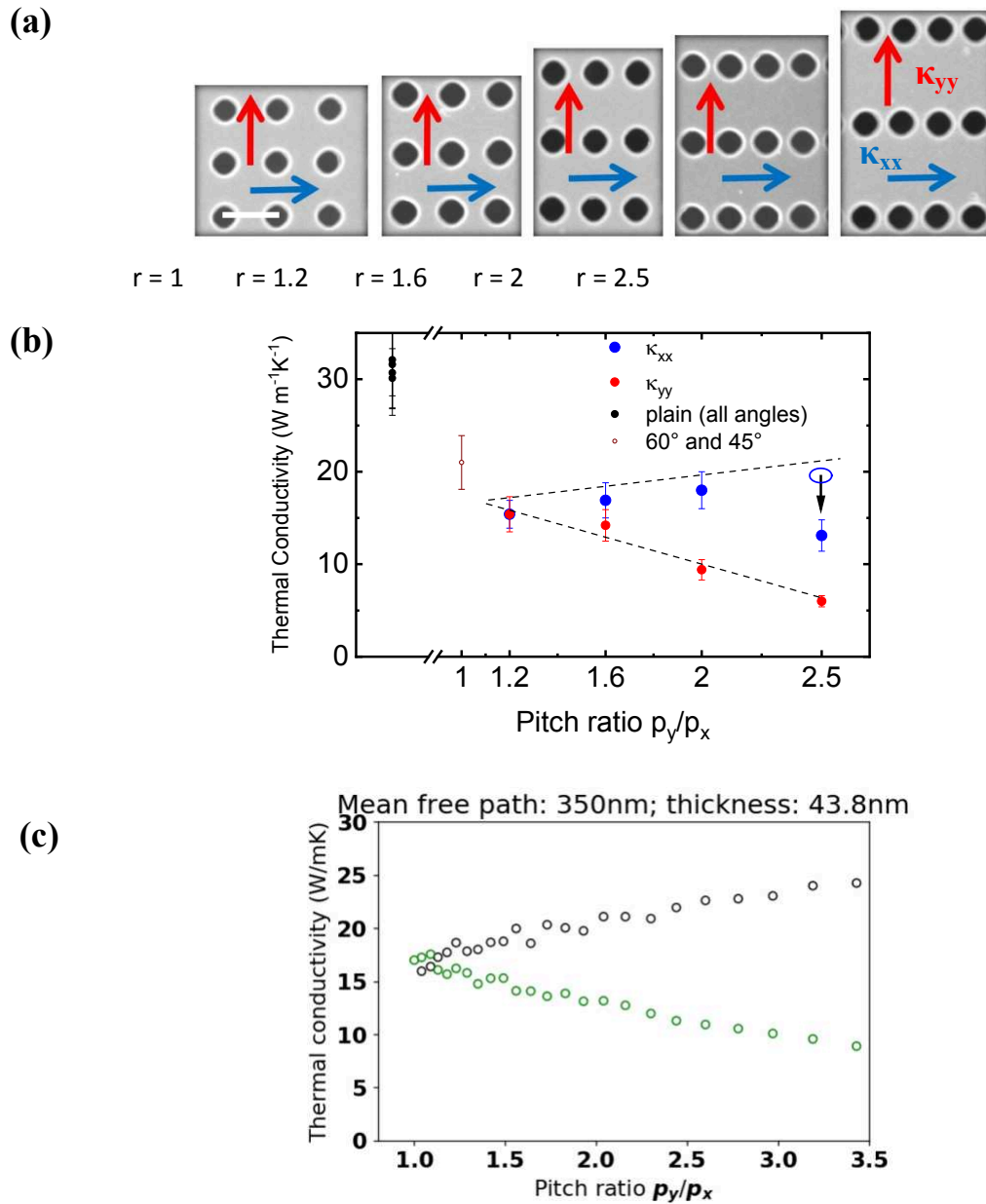
Figure 4.4
(a) Illustration sketch based on SEM scans of 5 phononic lattice patterns (scale bar is 100nm). (b) Measured thermal conductivity as a function of the pitch ratio for plain and anisotropic membranes of the sample №2 with respective directions of the heat flow according to the legend. The black arrow indicates unexpected reduction at r=2.5. Attention: membranes for r=1 in this series are different from isotropic 100nm-pitch membrane, and have slightly different filling fraction. Dashed lines are guide to the eye (c) Monte Carlo ray tracing simulation for anisotropic lattices with fully diffusive phonon scattering. Black points are κ_{xx} and green points are κ_{yy}. The code was written by P.-O. Chapuis, CETHIL (Lyon).

The eigen values κ_{xx} and κ_{yy} were measured respectively for all principal anisotropic membranes except the ones with r=1, which were damaged. The thermal conductivity was obtained for only two membranes of r=1 pattern (with 30° and 60°).

According to the plot (b), as the pitch ratio decreases we observe the divergence of κ_{xx} and κ_{yy} values, starting from r=1.6 (though within error bars). The further ratio increase (to r=2) leads to the larger drop of κ_{yy}, which is reasonable since, for this membrane, the neck on the way of the heat flow decreases. At the same time, κ_{xx} slightly increases, which is also expected due to the further increase of the neck size in this direction. In case of the purely diffusive phononic behaviour it is rather intuitive that this trend is going to continue: if the transverse neck is bigger, the phonons can move with less collisions covering larger distances, which would mean that their mean free path (MFP) is larger. However, as seen from the plot (b) for the pitch ratio r=2.5, the drop of κ_{xx} value occurs, which is controversial from the point of view of purely diffusive regime of phononic heat transport.

Monte Carlo random walks simulation was performed in order to check the trend of the principal values of effective thermal conductivity. The model is based on BTE kinetic picture described in paragraph 1.1.3. One can show that phononic membrane effective thermal conductivity can be expressed as a reduced bulk thermal conductivity (the formula below), which depends on the averaged effective mean free path of PhM. In the diffusive regime, only the geometry of the membrane and the scattering mechanism define this reduction (not the group velocity or the specific heat).

$$F\kappa_{bulk} = \kappa_{mbr} = \frac{3}{2\pi e} \int\limits_{-e/2}^{e/2} dz \int\limits_{0}^{\pi} d\varphi \int\limits_{0}^{\pi} d\theta \Lambda_y(z,\varphi,\theta)\sin^2(\theta)\sin(\varphi) \tag{37}$$

where e is the sample thickness, all other parameters are described in the text.

In the Monte Carlo model the effective MFP $\Lambda_y(z,\varphi,\theta)$ in the direction of the heat propagation (y axis, for example) depends on three geometrical random variables: randomly generated z coordinate along the thickness axis, altitude (θ) and azimuth (φ) angles, which define the initial direction of the phonon. In the fully diffusive case, each simulated phonon moves straight until it encounters the boundary, then it diffusively reflects according to randomly generated θ and φ.

The effective MFP for the single phonon is calculated as the distance between the start and the end locations of the phonon trajectory. The last is assumed to be equal to the length of the bulk MFP. The sketch on Figure 4.5 illustrates this concept. The model runs for several thousand times and then the averaged single phonon effective MFPs yield the value of the membrane thermal conductivity.

Figure 4.4c shows κ_{xx} (black points) and κ_{yy} (green points) as a function of the pitch ratio obtained by the Monte Carlo simulation with fully diffusive scattering approach and the averaged bulk MFP equal to 350nm. The holes in the model are cylindrical. As we see, the κ values obtained are of the same order of magnitude as the ones obtained in the experiment, however κ_{xx} linearly increases with the pitch ratio. This outcome was expected because the simulation is based on the BTE model without any ballistic or quasi-ballistic corrections, and

the possible change in the group velocity is neglected. Even when switching the scattering from diffusive to fully specular, the κ_{xx} trend remains the same.
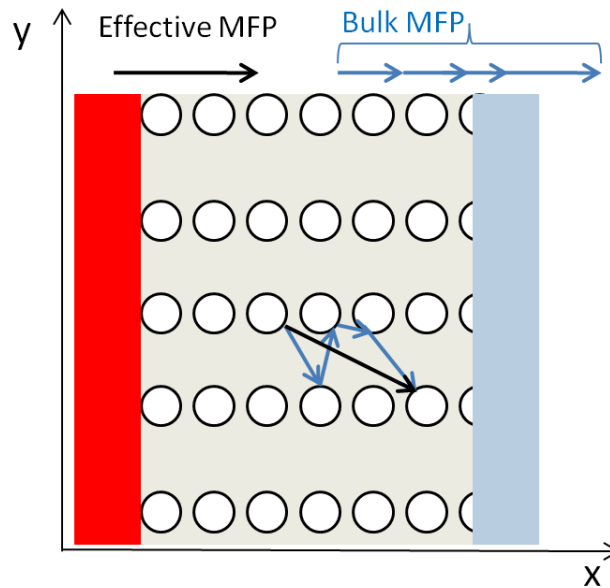

Figure 4.5

Illustration of the effective MFP calculation in Monte Carlo modelling. The top view of the simulation cell is shown in the picture. The circles correspond to the lattice holes. Red and blue bars indicate hot and cold ends of the simulation cell. Blue arrows are trajectory steps of the phonon, which is diffusively scattered on the walls of the holes and top and bottom boundaries of the membrane. Phonon moves until the sum of phonon step vectors' lengths is equal to the bulk MFP. Black vector length is an effective MFP in PhM.

In order to confirm the observed effect of the κ_{xx} reduction at r=2.5 on sample №2, the other available (not-damaged or destroyed) membranes with r=2 and r=2.5 were measured on samples №3 and №1. For samples №1 and №3 (Figure 4.6a), the thermal conductivity values are very close, which could be due to the same storage and exploitation conditions for both samples, and hence the same oxidation and surface contamination level. The membranes with r=2 were damaged on the sample №1 therefore the corresponding values are absent. For at least two samples (№2 and №3), we observe qualitatively the same effect of κ_{xx} reduction. For the sake of visibility, the data for each sample is normalized to κ_{xx}(at r=2.5) point (Figure 4.6b), which allows us to see that the scale of κ_{xx} reduction is the same on both samples. This observation is rather unexpected. The only structural parameter that can be presumably responsible for this effect is the lateral neck size (the neck which is parallel to the direction of the heat flow), which is ≈16nm for the pattern with r=2.5. This size is just an order of magnitude higher than the dominant phonon wavelength (see Paragraph 1.1.2) at RT. In this regard, it would be interesting to check for the level of coherent effects in the geometry of the r=2.5 pattern, using EMD or Landauer approach calculation, which accounts for quasi-ballistic transport in a diffusive limit[11]. Indeed, the simulation findings obtained by EMD (reviewed in Paragraph 1.2.4) showed that when either the thickness of the membrane or the neck size of phononic lattice is close to 10nm, the modification of dispersion relation or DOS can occur.
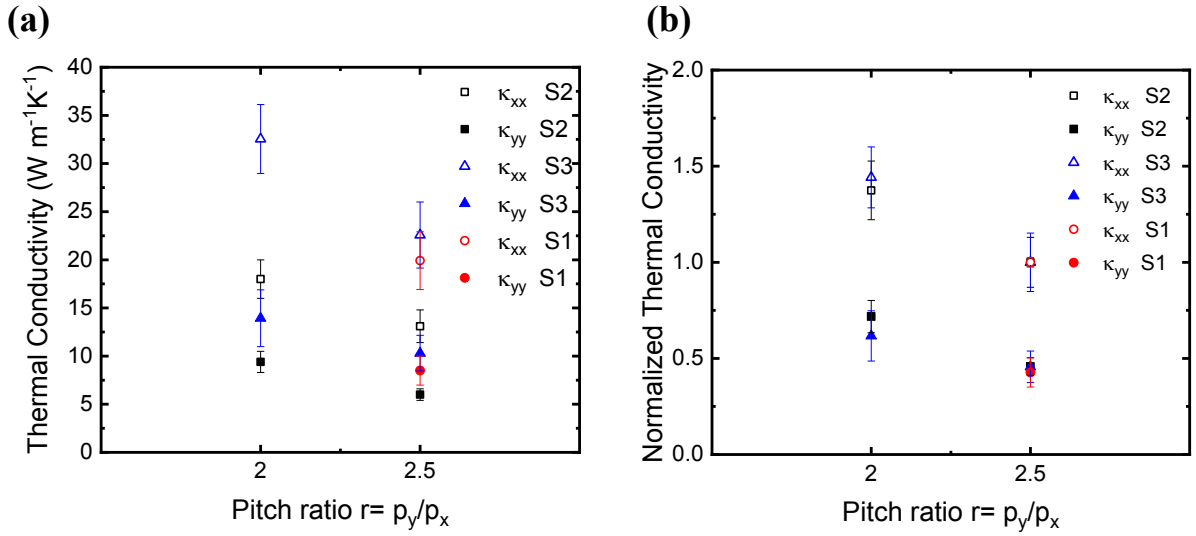
Figure 4.6
Measured thermal conductivity as a function of the pitch ratio for principal orientations of anisotropic PhMs from three different samples. (b) is the same as (a) but for the thermal conductivity normalized to the value κ_{xx} at r=2.5 for each sample.

4.1.4 Thermal conductivity vs. porosity and the neck size

The same effective medium approximations (as in Paragraph 4.1.1) and isotropic membranes κ are plotted, but now adding experimental values for anisotropic series (Figure 4.7a). The porosity picture looks a bit disordered for the anisotropic membranes. On the contrary, when we plot measured thermal conductivity as a function of the neck size (Figure 4.7b), the data seems to be more ordered for all kinds of membranes. This, again, tells us that the change of the scattering rate due to the size effects (and the neck size in particular) plays a big role in the thermal conductivity reduction. It is also interesting that according to MD work[19] introduced in Chapter 1, the amorphous phase makes the neck size a key parameter to control heat transfer (not the distance between the two voids) and a sharp decrease of k is initiated by the minimization of the neck.

The neck size on the plot (b) refers to the neck which is transverse to the direction of the heat propagation. As before, we see the unusual κ_{xx} drop for the patterns r=2.5 (plot b, the last blue point with the neck size 110nm). Plot (c) constructs the dependence of κ vs. the smallest neck in the pattern. In this picture, we see again, that κ_{xx} and κ_{yy} diverge accordingly to the increase of the pitch ratio (or decrease of the smallest neck), except for the case of r=2.5.
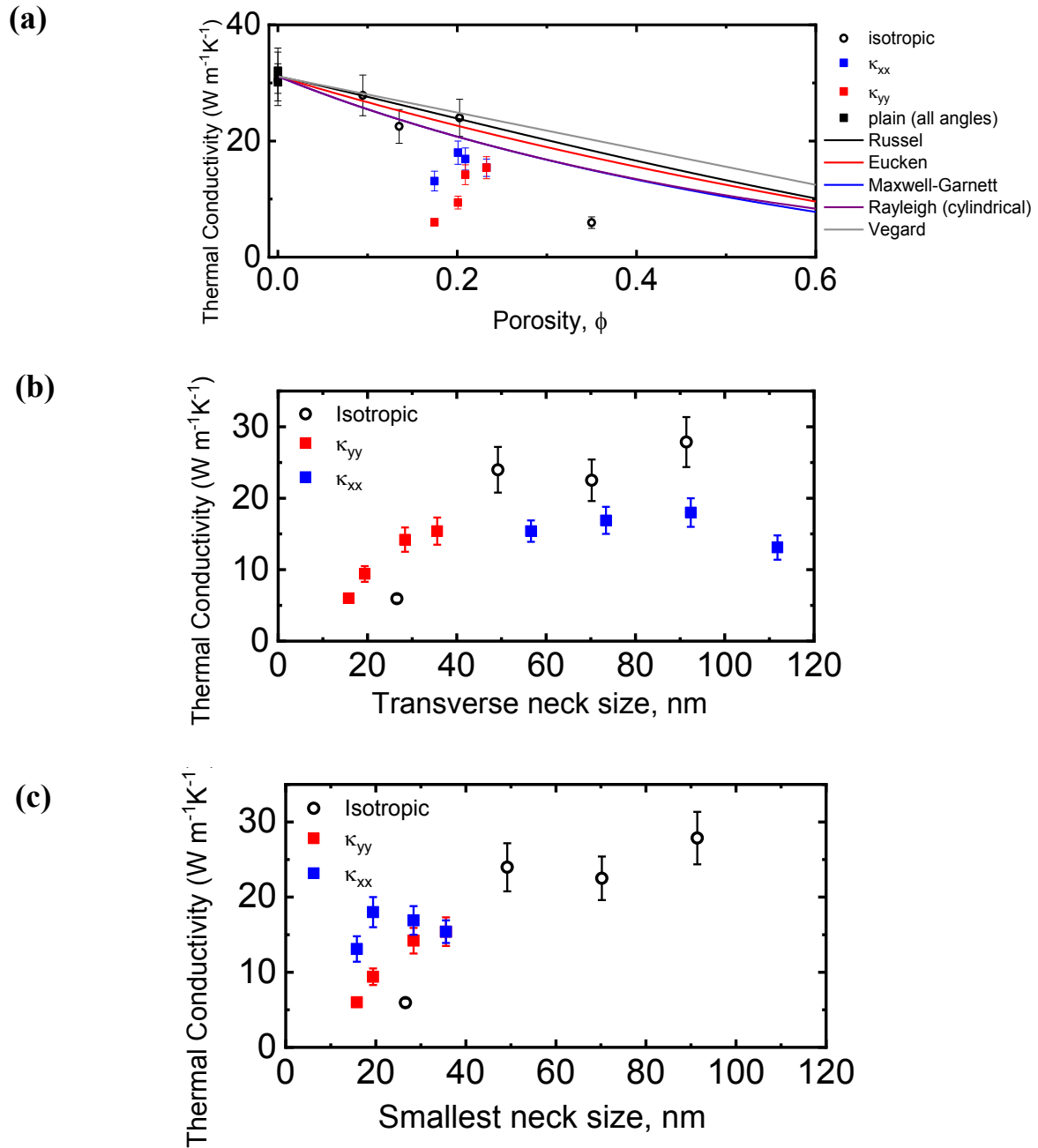
Figure 4.7
Thermal conductivity of PhMs with isotropic and anisotropic patterns as a function of (a) porosity, (b) necks size in the transverse direction relative to the heat flow vector, (c) the smallest neck size in PhM. Theoretical curves in (a) are described in the Table 4.1.

Summarizing the last two paragraphs, we conclude: 1) unexpected drop of κ_{xx} for r=2.5 was observed in three samples; the transverse neck on a way of the heat flux for κ_{xx} with r=2.5 is the widest comparing to all other patterns (with r<2.5); 2) This effect is controversial from the point of view of purely diffusive regime of phononic heat transport, which was proved by Monte Carlo simulations; 3) Presumably the very small size of the lateral neck (≈16nm) can be the reason of κ reduction due to coherent effects contribution. The verification of this assumption possibly can be addressed by EMD or Landauer approach

calculations, which allow for the estimation of the coherent properties changes (DOS, group velocity reduction).

4.2 Possible implementations of the discovered thermal effects

Parameterized FEM Comsol model has been used for the purpose of demonstrating one of the possible implementations of the discovered thermal effects.

Our experiment confirms the possibility to artificially induce high anisotropy of effective κ in Si nanolayers. Moreover, it is important to note that, our membranes were designed with a narrow span of the porosity values (0.175 -0.233) and diameter of the holes in order to show that κ-anisotropy can be developed purely due to the change of the pitch ratio while the area of the phononic lattice unit cell is kept purposefully the same. This implies that there is room for much higher anisotropy induction: when, for example, the unit cell area does not have to be constant, we can fabricate the lattice with r >>2 (r = 8 for instance) keeping the smallest neck value in the range of 20-30nm (the lower value can lead to the effect of wide-neck heat flow reduction, as seen for r=2.5 with the smallest neck of 15.8nm). So far in our experiment, the ratio of principal κ values had been found to be 2.2 (for r=2.5) and 1.9 (for r=2).

4.2.1 Reduction of local T around fragile IC components

The idea was to find within 100nm-thick Si layer (which represents a single tier of 3D IC[89]), such configuration of hot but thermally stable IC modules (no thermal protection is needed), heat sinks (thermal vias) and thermally fragile IC modules (need thermal protection), where the inclusion of anisotropic phononic patterns can play a significant role in the reduction of local T around the fragile components. Figure 4.8 demonstrates the scheme with one of the possible configurations of the mentioned elements, manually found using FEM simulation. The figure also illustrates three cases which were studied; they correspond to the placement of the fragile module into Si layer region a) with the same thermal conductivity as the rest of the plain layer (it implies that no phononic patterning is done);   b) with anisotropic thermal conductivity (which can be achieved via phononic rectangular lattice patterning); c) with reduced isotropic thermal conductivity (isotropic phononic lattice).

Figure 4.9 demonstrates colour maps of the equilibrium temperature distribution in the 100nm×200µm×200µm simulation cell with the periodic boundary conditions attached to the long sides of the cell (those sides are tilted by 45° to x and y axis in the plots), thus creating the condition of continuous IC layer periodically filled with the tiles of the same set of IC modules. The bottom and the top surfaces (perpendicular to z axis) of the cell are thermally insulated. This is a simplified approximation to real cases but valid since in real devices, the vertical heat conduction is far less efficient (oxides, multiple interconnection layers) as in-plane dissipation (silicon, substrate). The heat dissipates from the large modules (2 pieces per cell, the hottest elements on plots) and a fragile module (a circle in the centre of the cell) with the same power density P_{in}=150 W/cm^2. Thermal vias (2 pieces per cell, the coldest elements on plots) sink the heat out of the layer with the same rate: $P_{out} = - P_{in}$. The volume of the cell mostly has isotropic in-plane thermal conductivity value κ_{plain}= 65 Wm^{-1}K^{-1} (typical thermal conductivity value for 100nm-thick silicon thin film[12]). The polygon-shaped area around the fragile elements represents the part of the layer which is supposed to be nanopatterned with the phononic lattices: anisotropic and isotropic lattices in cases (b) and (c) respectively, where in-plane thermal conductibility κ_b =[12 0; 0 55] Wm^{-1}K^{-1} and κ_c =12 Wm^{-1}K^{-1}. In case (a) the polygon area remains untouched, thus having the same thermal volume properties as in the region outside of a polygon with κ_a =κ_{plain}= 65 Wm^{-1}K^{-1}.
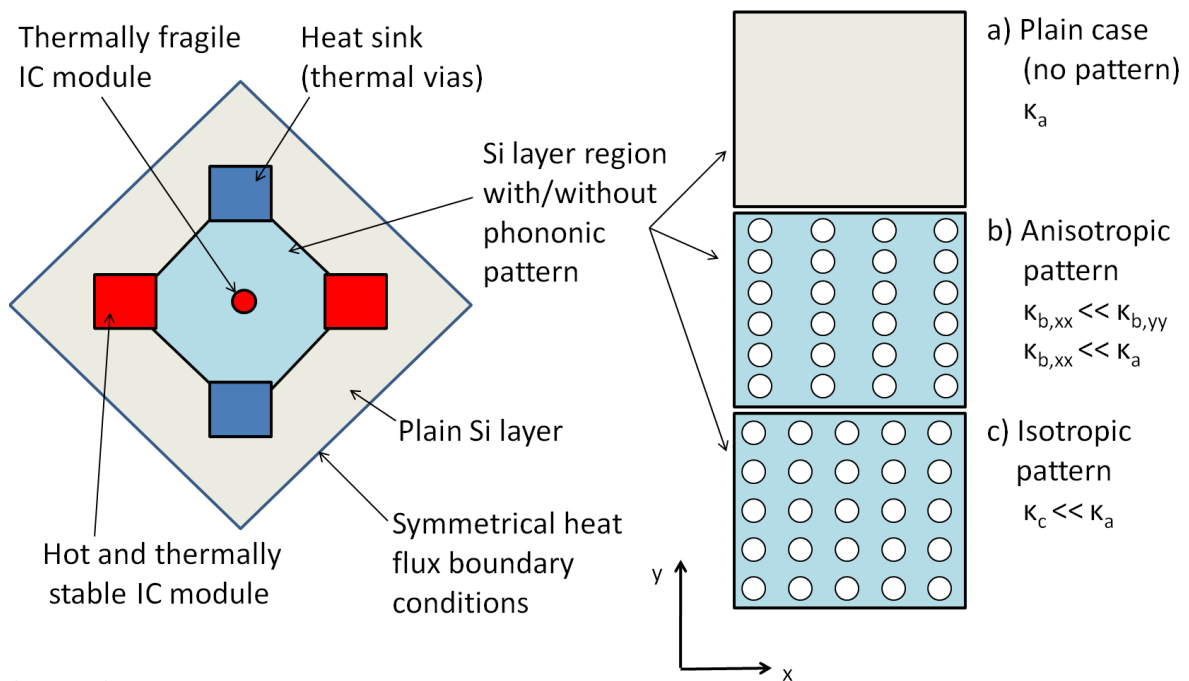
Figure 4.8

Auxiliary scheme of the found arrangement of thermally stable and fragile IC modules, thermal vias and the region with phononic pattern, where the effect of the heat guiding is noticeable. On the right: the sketches for three cases studied by FEM simulation, which correspond to different thermal conductivity settings in the polygon region (blue colour), where the fragile IC module is placed.
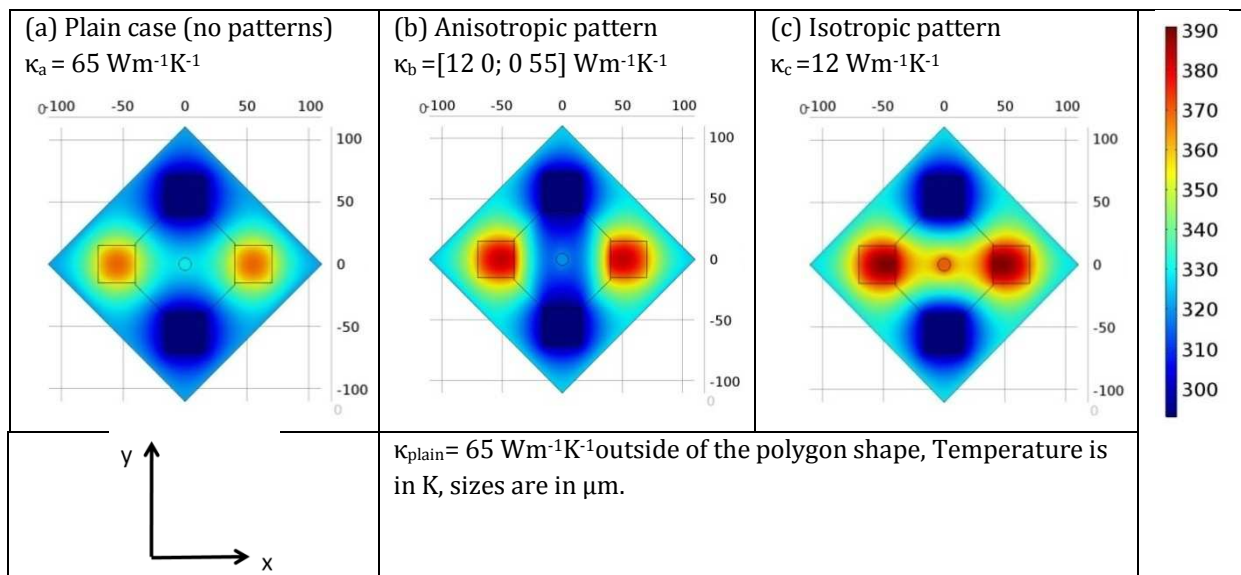
Figure 4.9

FEM simulation of heat dissipation in Si IC layer. (b)The fragile IC module is thermally protected due to decrease of the local T after inducing thermal conductivity anisotropy. (c) Isotropic phononic patterns increases the heating of the fragile module.

Directions of the high κ_b component are parallel to y-axis, this permits the heat to flow preferably from the fragile module to the vias, rather than in perpendicular directions. At the

same time chosen κ_b puts an obstacle for the heat dissipated from the large hot modules. Taking this into account, it is intuitively clear why isotherms bends outward the fragile element perpendicular to the cross-section line (red dashed line) and the region around the centre of the cell become colder. Case (c) is included to demonstrate that needed directional redistribution of the heat flow (like in the case b) does not occur when we use isotropic patterning. Moreover, reduced thermal conductivity value in this case plays the negative role, increasing the temperature around fragile elements.

The temperature at the centre of the fragile module cannot be lower than T of the ambient which is equal to room temperature in our simulations T_{room}=294K. Roughly we can estimate the efficiency of T drop caused by the heat guiding according to expression:

$1 - (T_{guide} - T_{room})/(T_{plain} - T_{room})$

where $T_{guide} = 320$K and $T_{plain} = 330$K are temperature values at the centre of the fragile module for the heat guiding case (with some pattern, which leads to the change of κ) and for the case without pattern.

In our example, this efficiency is $\approx$28%, referring to the ambient T value, thanks to anisotropic κ region placed around the module. A more quantitative picture of the thermal redistribution and fragile region cooling can be found in the next paragraph on the Figure 4.11 (T profile along the cross-section is indicated in Figure 4.10) and Figure 4.12 (temperature at the centre of the cell vs. heat source shift). Remark: the purpose of this modelling was to demonstrate the effect of heat directionality caused by κ-anisotropy (not to bind the modelling with the experimental data of this work), therefore the κ_b =[12 0; 0 55] $Wm^{-1}K^{-1}$ tensor was chosen rather as an efficient target value, which, to our view, can be obtained in fabrication. Besides the results of this modelling require the fabrication and measurements for verification, which has to be based on the fabrication concept of the large-scale membrane (this belongs to the domain of the next part of the project).

4.2.2 Anisotropic patterning as an alternative to IC modules' shifting

Before switching to the description of the next simulation tests, we have to focus on the motivation behind them. Modern thermal management of 3D IC consists of two main levels[90,91]:

1) Low-power design of the logic elements in IC addresses the issue of static (due to the leakage current) and dynamic (e.g. capacitor nodes in logic elements) power consumption.

2) Thermal management strategies are focused on the control of the temperature profile (thermal distribution) across the chip by acting on the layout. Many computational thermally driven optimisation techniques are developed to this day. Almost all of them approach the problem by rearrangement of heat sources (micro architectural optimisation) and/or by improving the heat sink pathways on chip determining the optimal quantity and positions of inter-tier metal thermal vias.

The second level (thermal management strategies) of thermal study particularly concerns the current invention. At the early stages of the IC design, the task is to determine and minimise the spatial temperature distribution caused by the placement of the heat sources within the layout. Simply speaking, when the high-power modules are placed close to each other, the temperature will locally reach higher values than in the case when they are spread apart. Said otherwise, thermal management is achieved at high surface cost.

Moving the modules apart poses an implication onto the performance of the IC, because the modules communicate with each other, and performance can dictate that they have to be kept close to each other: the issue of global signals delay (that exceeds the clock cycle) [89]. This implication means changes in the processor design (Instructions Per Cycles- IPC). In other words, thermally-motivated rearrangements of modules are coupled with Global Wires issues (Interconnection layers, Back-End of Line) and its design in non-trivial way. Besides that, changes in communication latencies affect back the temporal temperature distribution via the timing of block activations.

One can imagine that in some situations for some IC elements arrangements (or at some specific chip areas), it is only sufficient to modify the in-plane thermal properties of interface material (on device layer) around or close to thermally fragile IC elements, not changing the whole joint configuration of chip modules distribution and global wires performance. Therefore, the use of the phononic anisotropic patterning might be an alternative solution (in some situations) to the modules' shifting.
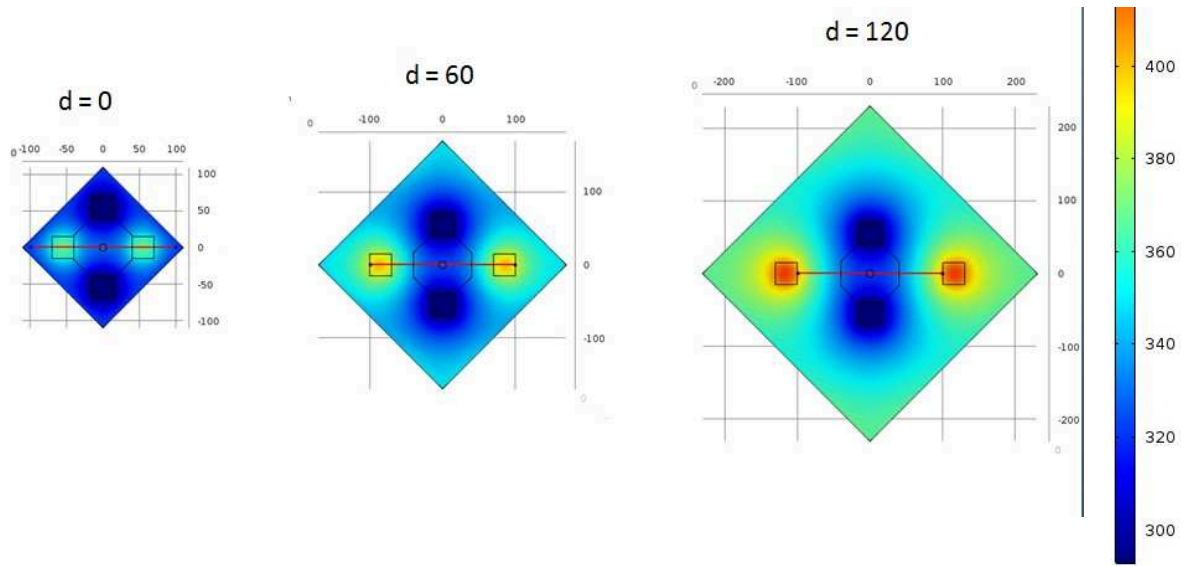
Figure 4.10

Illustration of the heat source shift parameter d, which is the distance between the hot module and the polygon shape. Temperature is in K, sizes are in μm.

But let us see how efficient the patterning over the heat source spatial shift in our configuration is. Both Figure 4.11 (for plain and anisotropic case) and Figure 4.12 (all three cases) show simulation outcomes parameterized by the distance between the heat source and anisotropic pattern. An illustration of the shift parameter can be found above (Figure 4.10). The distance between two hot spots increases proportionally to the size of the simulation cell. Consequently, due to boundary conditions, the overall continuous area of the IC layer increases.

(a) Plain case (no patterns)   (b) Anisotropic pattern
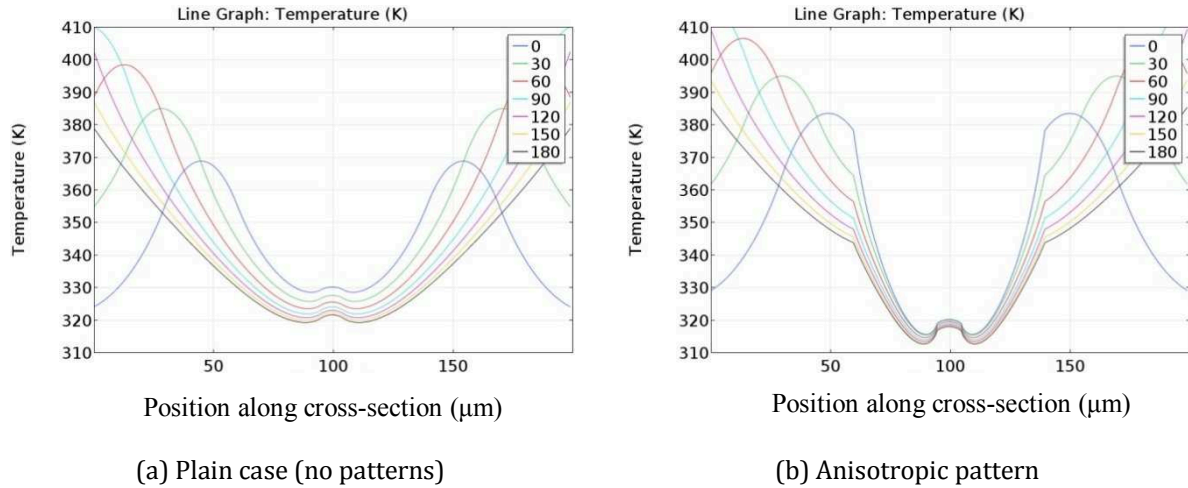
Figure 4.11

Temperature profile along the cross-section (red line on Figure 4.10) obtained in FEM simulation of heat dissipation in Si IC layer. Each T curve corresponds to specific heat source shift.

Figure 4.12 summarizes the main features of the simulation by comparing 3 cases:

1. The case of a plain isotropic material (65 $Wm^{-1}K^{-1}$) which is the reference case (black points).
2. The case of an anisotropic material with 12x55 $Wm^{-1}K^{-1}$ anisotropy (red points).

3. The case of reduced conductivity (12 $Wm^{-1}K^{-1}$) isotropic material (blue points).
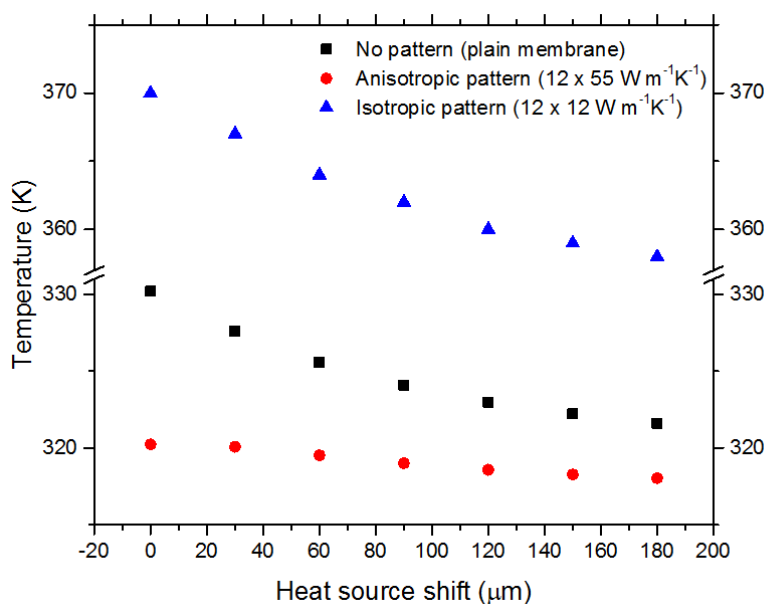
Figure 4.12
Temperature at the centre of the simulation cell vs. heat source shift.

Case 1 shows the common situation when the temperature can be decreased at the cost of heat sources spacing. In case №2, the use of the anisotropic pattern allows even lower temperatures with no additional spacing. Case №3 (blue dots) shows the interest of the study (anisotropy). One could think that just the fact of using a low-thermal conductivity material can protect the fragile component. But, this component has its own self-heating process that needs thermal management, and a low, isotropic, thermal conductance leads to poor thermal evacuation/protection. In other words, only case №2 combines the ability to protect the fragile zone from external heat sources while maintaining its capacity to evacuate its own heat. So-far, in literature only isotropic phononic lattices (leading to case №3) have been proposed.

The configuration of the IC modules discussed above proves that anisotropic patterns and thermal vias are efficient thermal protections to the fragile IC areas (or IC modules), leading to 10K drop in local T due to anisotropic heat redistribution for a thickness of IC layer equal to 100 nm. It can be shown that for even thinner layers, the temperature drop can be even increased.

It is worth noting that this configuration was found by manual trial and error, without systematic computational study, where many crucial geometrical and physical parameters can be analysed (or fitted). Possible list of such parameters: ratio of T increase at the hot elements and T decrease at the fragile ones (dT_{hot}/dT_{fr}), efficiency of anisotropic area shape, IC elements and vias shapes, cell configuration, arrangements of the elements, components of in-plane conductivity tensor, the tilt of the tensor. This implies that there is room for optimization of this technique.

4.3 Conclusions

On the basis of the results on μRT thermal transport characterisation of 8.9±0.1μm-wide, 200μm-long and 43.8nm-thick Si pristine and phononic membranes, the following conclusions are drawn.

The thermal conductivity κ of pristine membranes of the same surface orientation (100) obtained confirms the predicted absence[33] of the in-plane anisotropy at RT, at least down to the thickness of 43.8nm.

The introduction of phononic lattices of holes, with the averaged radius varied from 26.7 ± 0.6nm to 24.3 ± 0.4nm, slightly decreases the effective thermal conductivity within the pitch range from 140nm down to 100nm. According to effective medium approximation models and the accuracy of the measurements, this reduction can be attributed to both the porosity increase and the modification of the scattering boundaries. At the same time, PhM with 80nm pitch, porosity = 0.35 and a neck size NS=26.6nm, reveals a large reduction of κ, which is unproportional to the change of both porosity and NS.

A series of PhMs with anisotropic lattice patterns was studied. The patterns are characterized by the pitch ratio r= [1, 1.2, 1.6, 2, 2.5]. Thanks to the design of the experiment, we were able to estimate the temperature rise at the centre of the membranes for 5 different orientations of the heat flow (0°, 30°, 45°, 60°, 90°) in each pattern. A graphical isotropic/anisotropic visualisation of the heat flow was proposed. As the pitch ratio increases, the flattening of $\Delta T_{centr}(\theta)$ eye guiding ellipse curve increases, i.e. the temperature gradient becomes anisotropic. The ratio of principal κ values were found to be up 2.2(for r=2.5) and 1.9(for r=2). Besides, a 25-fold reduction of the thermal conductivity was observed for r=2.5 pattern: $k_{yy}= 6\pm0.6Wm^{-1}K^{-1}$. This experiment confirms the possibility to artificially induce high anisotropy of κ in Si PhMs almost without changing the filling fraction and the diameter of the holes.

Two-fold anisotropy of κ for PhM with r=2.5 was detected in three samples. For two samples, the absolute values of κ eigenvalues are similar. The variability between the samples can be attributed to the different roughness level formed during the etching processes, performed individually for each sample, or to the different native oxide thickness formed in different atmospheric conditions.

In all samples, where it was possible to measure, unexpected drop of κ_{xx} for r=2.5 was observed (in the direction where transverse neck is the widest compared to the patterns with r<2.5), which is controversial from the point of view of purely diffusive regime of phononic heat transport. The ratio of this reduction is reproducible among different samples. Presumably the very small size of the lateral neck (≈16nm) can be the reason of κ reduction due to coherent effects contribution. In perspective it is suggested to use EMD or Landauer approach calculation to verify this assumption.

Parameterized FEM Comsol model has been used for the purpose of demonstrating the possible implementation of induced anisotropic effects in the area of IC thermal-management. Thermally-motivated rearrangements of modules, conventionally used in thermal-management strategies, are coupled with Global Wires issues in non-trivial way. Our model showed that anisotropic patterns combined with thermal vias is an efficient thermal protection to the fragile IC areas (or IC modules), leading to 28% drop in local T (according

to 1 - (T_{guide} - T_{room})/(T_{plain} - T_{room}) metric) due to anisotropic heat redistribution for a thickness of IC layer equal to 100 nm. The use of the phononic anisotropic patterning might be an alternative solution (in some situations) to the shifting and rearrangements of modules. The perspective systematic computational study, where many crucial geometrical and physical parameters of anisotropic protective heat guiding can be analysed (or fitted), may substantially broaden the horizon of this thermal-management approach.

General conclusions and perspectives

This thesis work was devoted to the development of practical mechanisms for the heat guiding in silicon low-dimensional nanostructures with the specific goal to verify if it is possible to induce sufficiently high in-plane anisotropy of the heat flow in phononic membranes. The motivation had come from both the field of IC thermal management and emerging technology of Si-based thermoelectric devices, where directional heat guiding can play an important role.

The thermal transport experiment based on vacuum μRT measurements of free-standing beam-like (FSBL) membranes with anisotropic lattices of nanoholes was proposed. In order to see at what ratio of anisotropic lattice pitches the difference of $\bar{\bar{\kappa}}$ eigenvalues becomes pronounced, 5 phononic patterns with rectangular unit cell lattices were designed. The patterns are characterized by the lattice pitch ratio (r) with the values: [1, 1.2, 1.6, 2, 2.5]. In order to make the results comparison among the patterns possible, the filling fraction (*ff*) difference was minimized, varying within the small range from 17.5% to 23.4%. This was achieved by keeping the unit cell of anisotropic phononic lattices at the same value $\approx 10000nm^2$, and minimizing the difference of the holes radiuses among the patterns (radiuses vary from $23.6 \pm 0.9nm$ to $27.2 \pm 1.5nm$), which was possible due to EBL dose tests. Each pattern is introduced into five membranes with different PhM orientation angle (0°, 30°, 45°, 60°, 90°). Fast and reliable test-probe method for the assessment of the etched nanoholes quality (and structure) was proposed and extensively utilized during the fabrication process at multiple steps.

For the first time in our lab, it was possible to fabricate phononic membranes with the fully etched holes and complete coverage of membranes' area with phononic lattices. Besides, all four anisotropic patterns were successfully introduced into the suspended membranes. SEM study showed that the smallest neck feature size obtained in this work is $\approx 15.8nm$ (for the pattern with r=2.5), which is close to state-of-the-art fabrication limits. Overall three series with anisotropic, isotropic PhMs and plain membranes were fabricated. All membranes are 8.9±0.1μm-wide, 200μm-long and 43.8nm-thick.

The thermal conductivity of pristine membranes ($\kappa \approx 31\pm5Wm^{-1}K^{-1}$) of the same surface orientation (100) and different angles confirms the predicted absence of in-plane anisotropy at RT, at least down to the thickness of 43.8nm. According to effective medium approximation models and the accuracy of the measurements, the reduction of κ for isotropic PhMs series (with the pitches 140nm, 120nm, 100nm) can be attributed to both the porosity increase and the modification of the scattering boundaries. At the same time PhM with 80nm pitch, porosity = 0.35 and a neck size NS=26.6nm, reveals a big reduction of κ, which is unproportional to the change of both porosity and NS.

During µRT experiment and the analysis of anisotropic PhMs series it was possible to estimate the temperature rise near the membranes centre for 5 different orientations of the heat flow (0°, 30°, 45°, 60°, 90°) in each pattern. By the combined use of Rigorous Coupled Wave Analysis (RCWA), Finite Element Modelling (FEM), the design of the experimental platforms and µRT, it was possible to make a graphical isotropic/anisotropic visualisation of the heat flow in terms of the temperature rise at PhMs centre with respect to the angle of the heat propagation ΔT_{centr}(angle) for the same value of the absorbed power. As the pitch ratio increases, the flattening of ΔT_{centr}(angle) elliptical guiding curves increases. The ratios of the principal κ values were found to be: 2.2(for r=2.5) and 1.9(for r=2). Besides, a 25-fold reduction of the thermal conductivity was observed for r=2.5 pattern: k_{yy}= 6±0.6Wm^{-1}K^{-1}. This experiment confirms the possibility to artificially induce high anisotropy of κ in Si PhMs almost without changing the filling fraction and the diameter of the holes.

These findings open the door to the perspective study based on the large-scale membranes fabricated by the back side laser ablation (Paragraph 2.2.3). The introduction of (designed in this work) anisotropic phononic lattices into the large-scale membranes would allow for the direct measurement of the temperature distribution, which anisotropic shape reconstruction would serve as an important factor of the current experiment reproducibility. Besides, silicon large-scale membranes combined with anisotropic lattices, have a potential to increase the efficiency of Si-based TEG (see Appendix).

A new question had arose in connection with results interpretation, giving room to further theoretical and computational analysis. There is an unexpected drop of the effective thermal conductivity for r=2.5 pattern in the direction of the wide transverse neck (the widest among the patterns with r≤2.5), which is controversial from the point of view of purely diffusive regime of phononic heat transport. BTE-based Monte Carlo random walks model (written by P.-O. Chapuis, CETHIL) confirmed that this experimental outcome cannot be explained with the particle-like picture. Presumably, the very small size of the lateral neck (≈16nm) could be the reason of κ reduction due to the increased contribution of coherent effects.

Purposefully designed parameterized Comsol model demonstrated the possible implementation of the induced anisotropic effects in the area of IC thermal-management. Our model showed that anisotropic patterns combined with thermal vias is an efficient thermal protection to the fragile IC areas (or IC modules), leading to a 28% drop of the T (according to 1 - (T_{guide} - T_{room})/(T_{plain} - T_{room})) in the thermally fragile module due to anisotropic heat redistribution (when the thickness of IC layer is equal to 100nm). The use of the phononic anisotropic patterning might be an alternative solution (in some situations) to the shifting and rearrangements of modules, which are used conventionally in thermal-management strategies. The perspective systematic computational study, where many crucial geometrical and physical parameters of anisotropic heat guiding can be optimized (or fitted), may substantially broaden the horizon of this thermal-management approach. At the same time, there is a need to fabricate the prototype platform, which can demonstrate experimentally the effect of the heat protection by the anisotropic phononic patterns.

Overall the research introduced in this manuscript demonstrates that anisotropic phononic lattices of nanoholes and the thermal properties they induce in Si layer (membranes) are a promising topic from both physical (phononic transport effects) and application (TEG, IC thermal management) perspectives.

Appendix

Lithographic efficiency contest

Until recently EBL's high writing resolution was considered as an unbeatable advantage, reaching sub-10nm limit (2 nm isolated feature size and 5 nm half-pitch in hydrogen silsesquioxane resist[92]). Conventional clean-room techniques allow to access features sizes down to 15 nm (15.8 nm was obtained in this work). Notwithstanding this remarkable resolution advantage of EBL, the recent developments in photolithography imply that the optical methods challenge EBL in a lithographic efficiency contest. Thus, the combination of multiple patterning with immersion approaches[93] pushes the optical lithography down to 20 nm (which is comparable with conventional EBL). Promising extreme ultra violet lithography EUVL (UV wavelength of 13.5 nm is used) reaches 13 nm half-pitch resolution, however this type of lithography has multiple drawbacks (mask defects, high energy 93eV photons create short noise) and still requires an additional development.

While optical approach deals mainly with the resolution issues, EBL's main improvement strategy is a writing speed. The most promising rising EBL technology is the multi-beam approach (multi-beam electron lithography), developed by Mapper[94]. The main idea is to split the low-voltage (5kV) wide electron beam into tens of thousands beamlets[95], then each beamlet independently passes through the a pair of MEMS deflectors, which manipulate the beamlet (switching it on and off). Developers claim that their EBL tool based on such parallel writing will reach 40wph speed (wph is wafers per hour by a single e-beam litho-cell) in the nearest future, what is comparable to the output of the modern industrial optical litho-cells (60-90wph).

Perspectives of anisotropic heat flow in thermoelectrical application

Silicon large-scale membranes, which novel method of fabrication was described in Paragraph 2.2.3, combined with anisotropic lattices of nanoholes studied in this work, has a potential to increase the efficiency of Si-based TEG. The main idea of already proposed scheme[96] (figure A1) for κ-anisotropic TEG, is the implementation of a generic structure based on a silicon thin film, in which heat propagation is laterally redirected from the hot pillar sites (pink and red dash line) to the cold pillar sites (blue) via the introduction of anisotropic phononic patterns and possible directionally-dependant band-structure and group velocity modification occurred at a very small thickness. The second assumption was disproved by this work thermal experiments on pristine beam-like membranes at a RT. However, the first factor (pattern introduction) is feasible according to the results of the current experiment and Comsol simulation. Instead of the proposed by the scheme multi-diameter phononic structure, we can apply anisotropic lattices patterns with similar characteristics, which were used in this work (for r=2 for example). Although the concept,

introduced on the figure, is not very accurate about the shape of the isotherms, the general idea seems to be highly physical, especially with the experimental outcome of the current work, demonstrating that it is possible to induce thermal anisotropy in phononic membranes.
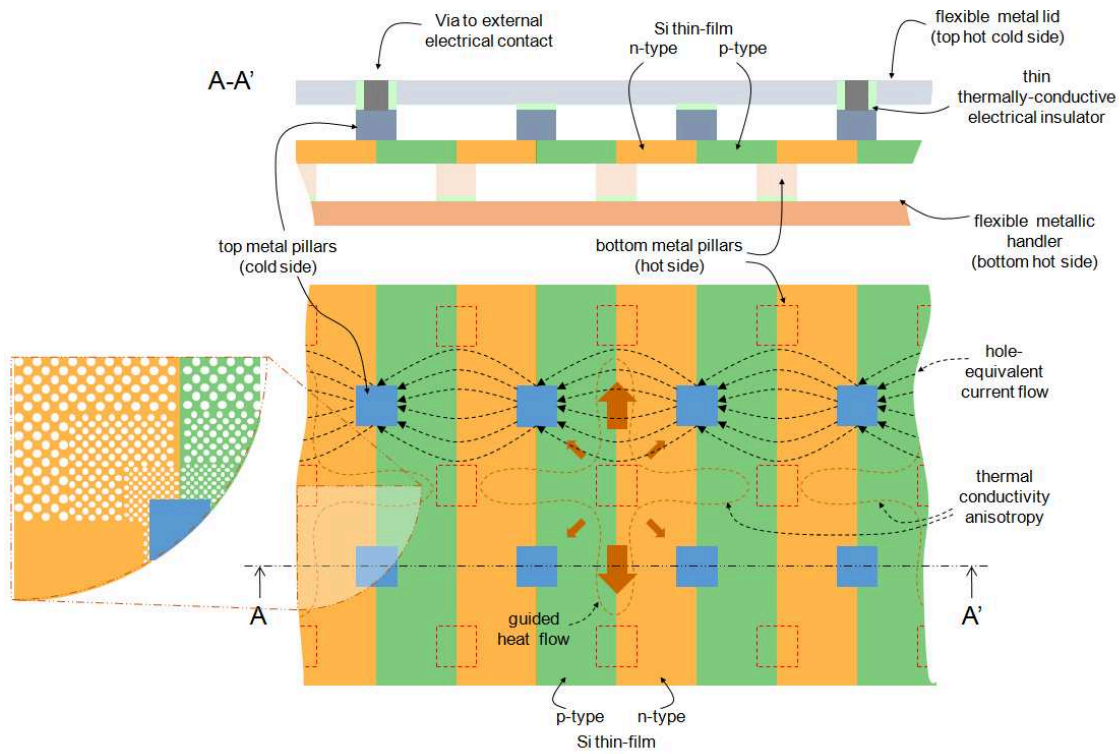

Figure A1
The sketch[96] of the hypothetical thermoelectrical converter based on large-scale free-standing membrane, patterned with multiple dissimilar phononic regions that anisotropically redirect the heat flux, maintaining higher temperature gradient between hot and cold pillar sites.

List of the used abbreviations in alphabetic order

BSS	Beam step size
CDF	Cumulative distribution function
DPSS	Diode-pumped solid-state laser
DoFL	Dots-on-the-fly
EBL	Electron-beam lithography
EDX	Electron dispersive x-ray (spectroscopy)
EMA	Effective medium approximation
EMD	Equilibrium molecular dynamics
EPD	End-point detection
ER	Etching rate
FEM	Finite element method
FIB	Focused ion beam
FSBL	Free-standing beam-like
HAADF	High-angle annular dark-field imaging
HF	Hydrofluoric acid.
IC	Integrated circuit
ICP-RIE	Inductively Coupled Plasma - Reactive Ion Etching
LPCVD	low-pressure chemical vapour deposition
NS	Neck size
PhC	Phononic crystal
PhM(PM)	Phononic membrane
RCWA	Rigorous coupled-wave analysis
RIE	Reactive ion etching
SOI	Silicon on the box
STEM	Scanning transmission electron microscope
SThM	Scanning thermal microscopy
TDTR	Time domain thermo reflectance
TEG	Thermoelectric generation
UC	Unite cell
ff	filling fraction
μRT	micro Raman Thermometry

Scientific outcome

Conferences:

1. S. Didenko et al., Thermal conductivity in Si 2D phononic membranes studied by Raman Thermometry. Thermal NanoSciences and NanoEngineering, GDRe Workshop, Villeneuve d'Ascq, France (23-24 November 2017). Oral presentation.
2. S. Didenko et al., Thermal conductivity of Si 2D phononic membranes studied by MD simulations and Raman thermometry. Eurotherm Seminar №108, Nanoscale and Microscale Heat Transfer V, Santorini, Greece (26-30 Sept 2016). Oral presentation.
3. D. Zhou, S. Didenko et al., Fabrication of large-scale free-standing Si membranes using laser ablation. Eurotherm №111, Nanoscale and Microscale Heat Transfer VI, Levi, Lapland, Finland (2-7 December 2018). Poster.

Patent application

July 2018 - submission of a patent application (declaration d'invention), based on PhD project outcome and additional modelling addressing thermal management in 3D IC: "Silicon Anisotropic Thermal Conduction for Thermal Management of Integrated Circuits"

Publications

1. M. Verdier, D. Lacroix, S. Didenko, J. F. Robillard, E. Lampin, T. M. Bah, and K. Termentzidis. "Influence of Amorphous Layers on the Thermal Conductivity of Phononic Crystals." Physical Review B 97, no. 11 (March 21, 2018): 115435.
2. M. Haras, V. Lacatena, T. M. Bah, S. Didenko, J. F. Robillard, S. Monfray, T. Skotnicki, and E. Dubois. "Fabrication of Thin-Film Silicon Membranes With Phononic Crystals for Thermal Conductivity Measurements." IEEE Electron Device Letters 37, no. 10 (October 2016): 1358–61.
3. T. M. Bah, S. Didenko, S. Monfray, T. Skotnicki, E. Dubois, J. F. Robillard. "Performance evaluation of silicon based thermoelectric generators interest of coupling low thermal conductivity thin films and a planar architecture." Solid-State Device Research Conference, Dresden, Germany, september 3-6, 2018, Session C2L-E - Sensors and Reliability, 226-229, ISBN 978-1-5386-5402-6.

Study activities

Summer school "PHONON SCHOOL 2017: Wave phenomena and phonon thermal transport" held in Oleron island, France, from September 3rd to 8th, 2017.

Les formations d'école doctorale: 61 crédits.

Bibliography

1. Shi, L. *et al.* Evaluating Broader Impacts of Nanoscale Thermal Transport Research. *Nanoscale Microscale Thermophys. Eng.* **19**, 127–165 (2015).

2. Solid State Physics. Von N. W. Ashcroft und N. D. Mermin; Holt, Rinehart and Winston, New York 1976, XXII, 826 Seiten. *Phys. Unserer Zeit* **9**, 33–33 (1978).

3. Lattice vibration, physics tutorial: http://www.tutorsglobe.com/homework-help/physics/lattice-vibration-75520.aspx, active 05/02/2019.

4. McConnell, A. D. & Goodson, K. E. THERMAL CONDUCTION IN SILICON MICRO- AND NANOSTRUCTURES. *Annu. Rev. Heat Transf.* **14**, 129–168 (2005).

5. Kai Hock, Photons and phonons, University of Liverpool, http://hep.ph.liv.ac.uk/~hock/Teaching/2010-2011/3-photons-phonons.pdf. Active by 12/02/2019.

6. Chan L. Tien. Microscale Energy Transfer. *CRC Press* Available at: https://www.crcpress.com/Microscale-Energy-Transfer/Tien/p/book/9781560324591. (Accessed: 12th February 2019)

7. Bourgeois, O. *et al.* Reduction of phonon mean free path: From low-temperature physics to room temperature applications in thermoelectricity. *Comptes Rendus Phys.* **17**, 1154–1160 (2016).

8. Tian, Z., Lee, S. & Chen, G. COMPREHENSIVE REVIEW OF HEAT TRANSFER IN THERMOELECTRIC MATERIALS AND DEVICES. *Annu. Rev. Heat Transf.* **17**, 425–483 (2014).

9. Lee, J. *et al.* Investigation of phonon coherence and backscattering using silicon nanomeshes. *Nat. Commun.* **8**, 14054 (2017).

10.   Glassbrenner, C. J. & Slack, G. A. Thermal Conductivity of Silicon and Germanium from 3\ifmmode^\circ\else\textdegree\fi{}K to the Melting Point. *Phys. Rev.* **134**, A1058–A1069 (1964).

11.   Jeong, C., Datta, S. & Lundstrom, M. Thermal conductivity of bulk and thin-film silicon: A Landauer approach. *J. Appl. Phys.* **111**, 093708 (2012).

12.   Chávez-Ángel, E. *et al.* Reduction of the thermal conductivity in free-standing silicon nano-membranes investigated by non-invasive Raman thermometry. *APL Mater.* **2**, 012113 (2014).

13.   Sondheimer, E. H. The mean free path of electrons in metals. *Adv. Phys.* **1**, 1–42 (1952).

14.   Maire, J. *et al.* Heat conduction tuning using the wave nature of phonons. *ArXiv150804574 Cond-Mat* (2015).

15.   Alaie, S. *et al.* Thermal transport in phononic crystals and the observation of coherent phonon scattering at room temperature. *Nat. Commun.* **6**, 7228 (2015).

16.   Morita, M., Ohmi, T., Hasegawa, E., Kawakami, M. & Ohwada, M. Growth of native oxide on a silicon surface. *J. Appl. Phys.* **68**, 1272–1281 (1990).

17.   Tang, J. *et al.* Holey Silicon as an Efficient Thermoelectric Material. *Nano Lett.* **10**, 4279–4283 (2010).

18.   Neogi, S. *et al.* Tuning Thermal Transport in Ultrathin Silicon Membranes by Surface Nanoscale Engineering. *ACS Nano* **9**, 3820–3828 (2015).

19.   Verdier, M. *et al.* Influence of amorphous layers on the thermal conductivity of phononic crystals. *Phys. Rev. B* **97**, 115435 (2018).

20.   Haras, M. *et al.* Fabrication of Thin-Film Silicon Membranes With Phononic Crystals for Thermal Conductivity Measurements. *IEEE Electron Device Lett.* **37**, 1358–1361 (2016).

21.   V. Lacatena. Fabrication and thermal characterization of phononic engineered silicon membranes for thermoelectric applications. PhD thesis. (IEMN, Lille 1, 2016).

22.   M. Massoud. Experimental characterization of heat transfer in nanostructured silicon-based materials. PhD Thesis. (L'INSA de Lyon, 2016).

23.   Anufriev, R., Maire, J. & Nomura, M. Reduction of thermal conductivity by surface scattering of phonons in periodic silicon nanostructures. *Phys. Rev. B* **93**, 045411 (2016).

24.   Hopkins, P. E. *et al.* Reduction in the Thermal Conductivity of Single Crystalline Silicon by Phononic Crystal Patterning. *Nano Lett.* **11**, 107–112 (2011).

25.   Kim, B. *et al.* Thermal conductivity manipulation in single crystal silicon via lithographycally defined phononic crystals. in *2012 IEEE 25th International Conference on Micro Electro Mechanical Systems (MEMS)* 176–179 (2012). doi:10.1109/MEMSYS.2012.6170122

26.   Cahill, D. G. Thermal conductivity measurement from 30 to 750 K: the 3ω method. *Rev. Sci. Instrum.* **61**, 802–808 (1990).

27.   Ftouni, H. *et al.* Thermal conductivity measurement of suspended Si-N membranes from 10 K to 275 K using the 3 ω -V ö lklein method. *J. Phys. Conf. Ser.* **395**, 012109 (2012).

28.   Massoud, A. M. *et al.* Native-oxide limited cross-plane thermal transport in suspended silicon membranes revealed by scanning thermal microscopy. *Appl. Phys. Lett.* **111**, 063106 (2017).

29.   Gomès, S. *et al.* Application of scanning thermal microscopy for thermal conductivity measurements on meso-porous silicon thin films. *J. Phys. Appl. Phys.* **40**, 6677 (2007).

30.   Scanning thermal microscopy: A review - Gomès - 2015 - physica status solidi (a) - Wiley Online Library. Available at: https://onlinelibrary-wiley-com.buproxy.univ-lille1.fr/doi/full/10.1002/pssa.201400360. (Accessed: 12th December 2018)

31. Regner, K. T. *et al.* Broadband phonon mean free path contributions to thermal conductivity measured using frequency domain thermoreflectance. *Nat. Commun.* **4**, ncomms2630 (2013).

32. Luo, Z. *et al.* Anisotropic in-plane thermal conductivity observed in few-layer black phosphorus. *Nat. Commun.* **6**, ncomms9572 (2015).

33. Aksamija, Z. & Knezevic, I. Anisotropy and boundary scattering in the lattice thermal conductivity of silicon nanomembranes. *Phys. Rev. B* **82**, (2010).

34. Soitec. https://www.soitec.com/en.

35. Bruel, M., Aspar, B. & Auberton-Hervé, A.-J. Smart-Cut: A New Silicon On Insulator Material Technology Based on Hydrogen Implantation and Wafer Bonding*1. *Jpn. J. Appl. Phys.* **36**, 1636 (1997).

36. Lecture 21, EE 441 Spring 2009: Tadigadapa. http://php.scripts.psu.edu/users/c/a/cao5021/ee/441/Lecture_21_-_Advanced_Plasma_Etching_Con.pdf.

37. Mark A. McCord, Stanford University. *SPIE Handbook of Microlithography, Micromachining and Microfabrication*.

38. Fundamentals of Microfabrication and Nanotechnology, Three-Volume Set. *CRC Press* Available at: https://www.crcpress.com/Fundamentals-of-Microfabrication-and-Nanotechnology-Three-Volume-Set/Madou/p/book/9780849331800. (Accessed: 30th November 2018)

39. Flamm D. L. Feed gas purity and environmental concerns in plasma etching: Part I. *Solid State Technol* (1993).

40. P, M. N. *Mems*. (Tata McGraw-Hill Education, 2008).

41.   Sledzinska, M., Graczykowski, B., Alzina, F., Santiso Lopez, J. & Sotomayor Torres, C. M. Fabrication of phononic crystals on free-standing silicon membranes. *Microelectron. Eng.* **149**, 41–45 (2016).

42.   Koshelev, K. *et al.* Comparison between ZEP and PMMA resists for nanoscale electron beam lithography experimentally and by numerical modeling. *J. Vac. Sci. Technol. B Nanotechnol. Microelectron. Mater. Process. Meas. Phenom.* **29**, 06F306 (2011).

43.   Success story of CSAR 62 - Allresist EN - ALLRESIST GmbH – Strausberg, Germany. Available at: http://www.allresist.com/research-development/success-story-of-csar-62/. (Accessed: 26th November 2018)

44.   He, Y., Donadio, D., Lee, J.-H., Grossman, J. C. & Galli, G. Thermal Transport in Nanoporous Silicon: Interplay between Disorder at Mesoscopic and Atomic Scales. *ACS Nano* **5**, 1839–1844 (2011).

45.   Zen, N., Puurtinen, T. A., Isotalo, T. J., Chaudhuri, S. & Maasilta, I. J. Engineering thermal conductance using a two-dimensional phononic crystal. *Nat. Commun.* **5**, 3435 (2014).

46.   D. Zhou, S. Didenko et al., Fabrication of large-scale free-standing Si membranes using laser ablation. Eurotherm №111, Nanoscale and Microscale Heat Transfer VI, Levi, Lapland, Finland (2-7 December 2018).

47.   Shchepetov, A. *et al.* Ultra-thin free-standing single crystalline silicon membranes with strain control. *Appl. Phys. Lett.* **102**, 192108 (2013).

48.   Shah, V. A. *et al.* Electrical properties and strain distribution of Ge suspended structures. *Solid-State Electron.* **108**, 13–18 (2015).

49.   M. Haras. Non-conventional thermoelectrics based on thin-film silicon technologies.

50.   Lopez, J. Le micro-usinage par laser et ses applications. *Photoniques* 46–50 (2012). doi:10.1051/photon/20126046

51.   Gamaly, E. G., Rode, A. V., Luther-Davies, B. & Tikhonchuk, V. Ablation of solids by femtosecond lasers : Ablation mechanism and ablation thresholds for metals and dielectrics. (2015). Available at: /paper/Ablation-of-solids-by-femtosecond-lasers-%3A-Ablation-Gamaly-Rode/a5c227f875ff558f7fffbaeadcdc61b5bbe03cf5.   (Accessed: 9th December 2018)

52.   Trasobares, J. *et al.* High speed e-beam lithography for gold nanoarray fabrication and use in nanotechnology. *Beilstein J. Nanotechnol.* **5**, 1918–1925 (2014).

53.   Lacatena, V. *et al.* Phononic engineering of silicon using "dots on the fly" e-beam lithography and plasma etching. *Microelectron. Eng.* **121**, 131–134 (2014).

54.   Micro chem. NANO ^{TM} PMMA and Copolymer, data sheet.

55.   Home: Vistec - We understand E-Beam. Available at: http://www.vistec-semi.com/. (Accessed: 20th December 2018)

56.   ZEON CHEMICALS - Electronic Materials - Homepage - Electronic Home. Available at: http://www.zeonchemicals.com/ElectronicMaterials/. (Accessed: 26th November 2018)

57.   Positive E-Beam Resists AR-P 6200 (CSAR 62), manufacturing process sheet, Allresist EN - ALLRESIST GmbH – Strausberg, Germany.

58.   ImageJ, Image Processing and Analysis in Java: https://imagej.nih.gov/ij/, visited 22/02/2019.

59.   Kinetics and Growth of Silicon Dioxide, L. Filipovic, Topography Simulation of Novel Processing Techniques: http://www.iue.tuwien.ac.at/phd/filipovic/node29.html, active 02/02/2019.

60.   H. Fujiwara. Spectroscopic Ellipsometry: Principles and Applications. *Wiley.com* Available at: https://www.wiley.com/en-us/Spectroscopic+Ellipsometry%3A+Principles+and+Applications-p-9780470016084. (Accessed: 16th January 2019)

61.   Jellison, G. E. Optical functions of silicon determined by two-channel polarization modulation ellipsometry. *Opt. Mater.* **1**, 41–47 (1992).

62.   Canavese, G. *et al.* Polymeric mask protection for alternative KOH silicon wet etching. *J. Micromechanics Microengineering* **17**, 1387 (2007).

63.   Yang, C.-R., Chen, P.-Y., Yang, C.-H., Chiou, Y.-C. & Lee, R.-T. Effects of various ion-typed surfactants on silicon anisotropic etching properties in KOH and TMAH solutions. *Sens. Actuators Phys.* **119**, 271–281 (2005).

64.   Boukai, A. I. *et al.* Silicon nanowires as efficient thermoelectric materials. *Nature* **451**, 168–171 (2008).

65.   Brazzle, J. D., Dokmeci, M. R. & Mastrangelo, C. H. Modeling and characterization of sacrificial polysilicon etching using vapor-phase xenon difluoride. in *Proceedings of the IEEE International Conference on Micro Electro Mechanical Systems (MEMS)* 737–740 (2004).

66.   Bruker Corporation: https://www.bruker.com/products/surface-and-dimensional-analysis/3d-optical-microscopes/3d-surface-metrology/overview.html, 22/01/2019.

67.   Passi, V. *et al.* Anisotropic vapor HF etching of silicon dioxide for Si microstructure release. *Microelectron. Eng.* **95**, 83–89 (2012).

68.   Bals, S., Kabius, B. C., Haider, M., Radmilovic, V. & Kisielowski, C. Annular dark field imaging in a TEM. *Solid State Commun.* **130**, 675–680 (2004).

69. Reparaz, J. S. *et al.* A novel contactless technique for thermal field mapping and thermal conductivity determination: Two-Laser Raman Thermometry. *Rev. Sci. Instrum.* (2014). doi:10.1063/1.4867166

70. Wagner, M. R. *et al.* Two-Dimensional Phononic Crystals: Disorder Matters. *Nano Lett.* **16**, 5661–5668 (2016).

71. Wolf, I. D. Micro-Raman spectroscopy to study local mechanical stress in silicon integrated circuits. in (1996).

72. Specifications: https://static.horiba.com/fileadmin/Horiba/Company/About_HORIBA/Readout/R07E/RE07-11-052.pdf, active 31/01/2019.

73. Doerk, G. S., Carraro, C. & Maboudian, R. Temperature dependence of Raman spectra for individual silicon nanowires. *Phys. Rev. B* **80**, 073306 (2009).

74. Balkanski, M., Wallis, R. F. & Haro, E. Anharmonic effects in light scattering due to optical phonons in silicon. *Phys. Rev. B* **28**, 1928–1934 (1983).

75. Klemens, P. G. Anharmonic decay of optical phonon in diamond. *Phys. Rev. B* **11**, 3206–3207 (1975).

76. Si Photodiode, FDS1010, 350 - 1100 nm, 10 mm x 10 mm active area: https://www.thorlabs.com.

77. Byrnes, S. J. Multilayer optical calculations. *ArXiv160302720 Phys.* (2016).

78. Vuye, G. *et al.* Temperature dependence of the dielectric function of silicon using in situ spectroscopic ellipsometry. *Thin Solid Films* **233**, 166–170 (1993).

79. Palik, E. D. *Handbook of optical constants of solids. II II.* (Academic Press, 1998).

80. Kaspar, F. G. Diffraction by thick, periodically stratified gratings with complex dielectric constant. *JOSA* **63**, 37–45 (1973).

81. "Rigorous coupled-wave analysis," Wikipedia, the free encyclopedia. 01/02/2019. *FR3029355 - 2016-06-03 BOPI 2016-22*

82. Khosrofian, J. M. & Garetz, B. A. Measurement of a Gaussian laser beam diameter through the direct inversion of knife-edge data. *Appl. Opt.* **22**, 3406–3410 (1983).

83. The beginner's guide on spot size of laser beam: https://www.gentec-eo.com/blog/spot-size-of-laser-beam, 01/02/2019.

84. Mounted Continuously Variable ND Filter: https://www.thorlabs.com/thorproduct.cfm?partnumber=NDC-100C-2M, 02/02/2019.

85. Si Photodiode, FDS1010, 350 - 1100 nm, 10 mm x 10 mm active area: https://www.thorlabs.com.

86. N. Kravchenko, Methods for processing measurement results, Tomsk Polytechnic University:

http://portal.tpu.ru:7777/departments/kafedra/tief/method_work/method_work2/lab1/Labs MechMolecFiles/obrabotka_0.pdf, active 03/02/2019.

87. Liu, W. & Asheghi, M. Thermal conduction in ultrathin pure and doped single-crystal silicon layers at high temperatures. *J. Appl. Phys.* **98**, 123523 (2005).

88. Pietrak, K. & Wiśniewski, T. S. A review of models for effective thermal conductivity of composite materials. *J. Power Technol.* **95**, 14–24 (2014).

89. Iqbal, M. A., Macha, N. K., Danesh, W., Hossain, S. & Rahman, M. Thermal Management in Fine-Grained 3-D Integrated Circuits. *ArXiv180303727 Cs* (2018).

90. Zhan, Y., Kumar, S. V. & Sapatnekar, S. S. Thermally Aware Design. *Found. Trends® Electron. Des. Autom.* **2**, 255–370 (2007).

91. Pedram, M. & Nazarian, S. Thermal Modeling, Analysis, and Management in VLSI Circuits: Principles and Methods. *Proc. IEEE* **94**, 1487–1501 (2006).

92.   Manfrinato, V. R. *et al.* Resolution Limits of Electron-Beam Lithography toward the Atomic Scale. *Nano Lett.* **13**, 1555–1558 (2013).

93.   Wu, B. & Kumar, A. Extreme ultraviolet lithography and three dimensional integrated circuit—A review. *Appl. Phys. Rev.* **1**, 011104 (2014).

94.   Mapper, designs and manufactures. https://mapper.nl/technology/.

95.   Servin, I. *et al.* Ready for multi-beam exposure at 5kV on MAPPER tool: lithographic and process integration performances of advanced resists/stack. in (eds. Resnick, D. J. & Bencher, C.) 94231C (2015). doi:10.1117/12.2085915

96.   DUBOIS EMMANUEL, R. J.-F. GENERATEUR THERMOELECTRIQUE, FR3029355 - 2016-06-03 (BOPI 2016-22), Patent.

Résumé de thèse en anglais

This thesis work is devoted to the development of practical mechanisms for the heat guiding in silicon low-dimensional nanostructures. The motivation comes from both the field of IC thermal management and emerging technology of Si-based thermoelectric devices, where directional heat guiding can play an important role.

A series of micrometre-sized thermal characterisation platforms was designed and fabricated. The objective is to study experimentally the feasibility of artificially-induced in-plane anisotropy of effective in Si patterned membranes. The design of experiment that relies on varying the angle of heat flow (0°, 30°, 45°, 60°, 90°) with respect to patterns' lattices is used. By the combined use of micro Raman Thermometry, Rigorous Coupled Wave Analysis (RCWA) and Finite Element Modelling (FEM) it was possible to measure the thermal gradient, membrane conductance and determine effective thermal conductivities. The isotropic/anisotropic character of the heat flow is clearly demonstrated. The patterns are characterized by the lattice pitch ratio (r) with the values: [1, 1.2, 1.6, 2, 2.5]. The ratios of the principal values were found be up 2.2 (for r=2.5) and 1.9 (for r=2). Besides, 25-fold reduction of the thermal conductivity, as compared to the bulk value, was observed for r=2.5 pattern: $k\_yy = 6\pm0.6$ W/(m K). This experiment confirms the possibility to induce artificially high anisotropy of in Si PhMs almost not changing the filling fraction and the diameter of lattice nanoholes. The causes of origins and possible applications of the observed thermal effects are discussed. Finally, purposefully designed parameterized FEM model demonstrated the possible implementation of the induced anisotropic effects in the area of IC thermal-management.

Résumé de thèse en français

Ce travail de thèse est consacré au développement de mécanismes pratiques pour le guidage de chaleur dans des nanostructures de silicium de faible dimension. Les applications vont du domaine de la gestion thermique des circuits intégrés aux technologies et matériaux thermoélectriques émergents à base de Si, dans lesquels le guidage thermique de la chaleur peut jouer un rôle important.

Une série de plates-formes de caractérisation thermique de taille micrométrique a été conçue et fabriquée. L'objectif est d'étudier expérimentalement la faisabilité d'une anisotropie de conductivité thermique dans le plan, induite artificiellement, des membranes nanostructurées en Si. L'expérience repose sur la variation de l'angle du flux de chaleur (0°, 30°, 45°, 60°, 90°) par rapport aux réseaux de motifs. En combinant la thermométrie Raman, la modélisation optique (Rigorous Coupled Wave Analysis) et la modélisation par éléments finis (FEM), il a été possible de mesurer le gradient thermique, la conductance de la membrane et de déterminer les conductivités thermiques effectives. Le caractère isotrope / anisotrope du flux de chaleur est clairement démontré. Les motifs sont caractérisés par le rapport des pas de répétitions du réseau suivant les deux directions principales (r) avec les valeurs: [1, 1.2, 1.6, 2, 2.5]. Le rapport d'anisotropie des conductivités thermiques est mesuré à 2.2 (pour r = 2.5) et 1.9 (pour r = 2). En outre, une réduction d'un facteur 25 de la conductivité thermique, par rapport à la valeur du matériau massif a été observée pour le motif r = 2.5: $k\_yy = 6\pm0.6$ W/(m K). Cette expérience confirme la possibilité d'induire artificiellement une anisotropie élevée de dans des membranes en silicium. L'origine et les applications possibles des effets thermiques observés sont discutées. Enfin, un modèle FEM paramétré conçu à dessein a démontré la mise en œuvre possible des effets anisotropes induits dans le domaine de la gestion thermique des circuits intégrés.